Femtosecond Optical Nonlinearities in ZnSe and Characterization of ZnSe/GaAs Heterostructures

by

David J. Dougherty

B.S.E.E., University of Southern California (1990)

Submitted to the Department of Physics
in partial fulfillment of the requirements for the degree of

Doctor of Philosophy

at the

MASSACHUSETTS INSTITUTE OF TECHNOLOGY

June 1997

Signature of Author .....
Department of Physics
6 March 1997

Certified by .....
Professor Erich Ippen
Elihu Thomson Professor of Electrical Engineering and Professor of Physics
Thesis Supervisor

Accepted by .....
Professor George F. Koster
Chairman of Graduate Committee

Femtosecond Optical Nonlinearities in ZnSe and Characterization of ZnSe/GaAs Heterostructures

by

David J. Dougherty

Submitted to the Department of Physics
on 6 March 1997, in partial fulfillment of the
requirements for the degree of
Doctor of Philosophy

Abstract

ZnSe is an important material for fabricating laser diodes in the blue spectral region. Understanding its bulk optical and interface transport properties can lead to improved device design. Because ZnSe is a II-VI semiconductor, it can also serve as a useful comparison to the body of knowledge about III-V semiconductor nonlinear optics. This thesis describes ultrafast pump-probe and modulation spectroscopy experiments to address these issues.

Pump-probe experiments were performed to investigate the nonlinear optical mechanisms in ZnSe. Frequency doubling of pulses from a modelocked Ti:sapphire laser provided 60 fs probe pulses tunable across the ZnSe bandgap. For above band pumping and large carrier injections, screening of the Coulomb attraction between electron-hole pairs was seen to be the dominant probe absorption saturation mechanism.

By using a below band pump and doped ZnSe films, the carrier distributions were heated by free carrier absorption without population density changes. The intraband carrier cooling dynamics were thus isolated and relaxation times of 500 fs for electrons and 900 fs for holes were measured in N and P-type samples respectively. A delayed heating response was also seen in the N-type samples. This is due to electrons returning from the satellite L-valley in the conduction band and a $L - \Gamma$ scattering time of 1.8 ps was determined. By tuning the pump photon energy it was also possible to measure the energy of the L-valley minimum to lie 1.31 eV above the Γ-valley. This is arguably the most accurate measurement of this quantity so far. An instantaneous bleaching was also seen and attributed to the optical Stark effect. Dense electron plasmas were observed to cause a factor of two decrease in the interband repulsion.

Characterization of ZnSe/GaAs heterojunctions were carried out with contactless electro- and photo-reflectance modulation spectroscopy techniques. Fields much larger than can result from modulation doping effects were measured. This points to large interface charges in the 10^{12} cm^{-2} range. The electro-reflectance technique unambiguously determined the sign of the charges to be negative for both n-type GaAs and intrinsic GaAs substrates. This leads to large conduction band bending on the GaAs side of the junction and formation of a large effective barrier for electrons to enter the ZnSe. This barriers' existence was confirmed by photoreflectance saturation intensity measurements and a new technique using a tunable pump to directly measure the conduction band offset at the interface. These results demonstrate that band bending due to interface charges must be taken into account for understanding carrier transport in ZnSe based devices using GaAs substrates.

Additional pump-probe experiments were performed to extend the conventional photoreflectance measurements. The mechanism of photoreflectance techniques is screening of built-in surface fields by surface trapping of minority carriers. This reduction in the electric field changes the Franz-Keldysh contributions to the refractive index and, therefore, the sample reflectivity. Pump-probe experiments were performed to time resolve these subpicosecond trapping dynamics for the first time. A simple model is proposed for explaining these results which shows that this technique may be used as a non-contact method for measuring surface trap densities and recombination velocities. Extension of this technique to the technologically important Si/SiO2 interface would be straightforward due to the bandstructure transitions used.

Thesis Supervisor: Professor Erich Ippen
Title: Elihu Thomson Professor of Electrical Engineering and Professor of Physics

Contents

List of Figures

Acknowledgments

I would like to thank Prof. Erich Ippen for his advice on experimental matters and his insight into current research. The freedom he has given me to pursue many different research topics has been the most valuable part of my graduate education, and was possible because of his wide range of knowledge in nonlinear optics and his quick understanding of new ideas. I have appreciated his words of encouragement and his sense of humor over the past six years.

Without Prof. Leslie Kolodziejski's enthusiasm, cheerfulness, and high standards, this work would not have been possible. She makes you feel good about having to measure more samples. I would like to thank her for producing excellent films, often on short notice, and for being a reminder of what life is like outside of grad school.

This thesis has benefitted greatly from the attention of my Physics Department co-advisor, Prof. Millie Dresselhaus. I would like to thank her for her careful reading and many suggestions. Her solid state class provided me with the background to pursue the modulation spectroscopy experiments in Part I. Thanks also to Prof. Irwin Pless for being on my thesis comittee, and for his patience throughout this process of finishing things up.

Charlie Hultgren taught me most of what I know about operating lasers and how to do experiments - just do it. Thanks for introducing me to W. S. Burroughs, Fassbinder, Joy Division, and the Bradford. Much of what I've learned at MIT has come from losing arguments to Gadi Lenz about solid state physics, integrated optics, and Led Zeppelin trivia. Siegfried Fleischer is probably the best engineer I' ll ever know. The time we spent discussing lasers, signals and systems, circuit theory, and nonlinear optics when we should have been working on our experiments, did probably delay my graduation six months, but it helped me keep one foot back in the world of electrical engineering.

Lynn Nelson has helped me in countless ways, from lending equipment to just sharing what she knows about fiber lasers. I'm sure she will be successful at whatever she decides to do after MIT. Jody House was a tremendous help in learning about ZnSe and characterization.

Without her I may have fallen through the cracks in trying to pursue projects off the mainstream of research in each of our groups.

I leave the lab in the competent hands of Dr. Gunter Steinmeyer, who I have been glad to know over the past year. I expect Eric Thoen to maintain the tradition of excellent (loud) music in the lab. Thanks also to William Wong, another member of the late-shift, for keeping things entertaining and for his irrepressible energy. I'll always remember Nick Ulman for being an icon of decisiveness and an inspiration to the rest of us. Steve Stephanides has been a good friend since USC, and I hope he finishes Med Scool soon and gets back to CA so we can have a beer. I thank Edward Lizine for bestowing the many nuggets of wisdom he has gained through his years in Boston and at MIT.

Finally, thanks to my parents and to Mike for their love, understanding, and support. Most of all, thank you, Renee, for giving me the best reason of all for finishing this thing. I could'nt have done it without you.

Part I

Electro-reflectance Characterization of ZnSe/GaAs heterostructures

Chapter 1

Semiconductor heterojunctions and ZnSe/GaAs interfaces

Zinc Selenide (ZnSe) is a wide bandgap II-VI semiconductor with many potential uses in opto-electronics[1]. With a 2.67 eV direct bandgap, ZnSe and its alloys with sulfur, cadmium, and magnesium are strong candidates for fabrication of laser diodes in the blue and green regions of the spectrum. Shorter wavelengths lead to smaller diffraction-limited spot sizes and are thus desirable for high density optical storage technologies such as CD ROM and, in the future, photo-refractive devices. ZnSe light emitting diodes (LEDs) may find applications in flat-panel displays. The lattice constant of ZnSe is 5.67 Å, which is very similar to that of GaAs, 5.65 Å [2]. This close lattice match makes GaAs an ideal substrate material for ZnSe-based devices. This is a major advantage, since GaAs is commercially available in high quality wafers and the potential exists for straight-forward integration with GaAs electronics. Because ZnSe is transparent to GaAs optical emission, interesting possibilities exist for combining ZnSe and GaAs opto-electronic devices in smart pixel optical interconnections[3].

Spurred by these applications, several investigations of lasing action in ZnSe quantum well structures were conducted using optical pumping [4, 5]. Electrical pumping was hindered by the inability to obtain high enough p-type doping for good, low resistance p-n junctions. Successful LEDs were constructed using Li as an acceptor[6], but the hole concentrations were not sufficient to obtain the population inversion necessary for lasing. The discovery by Park et. al. [7] in 1990

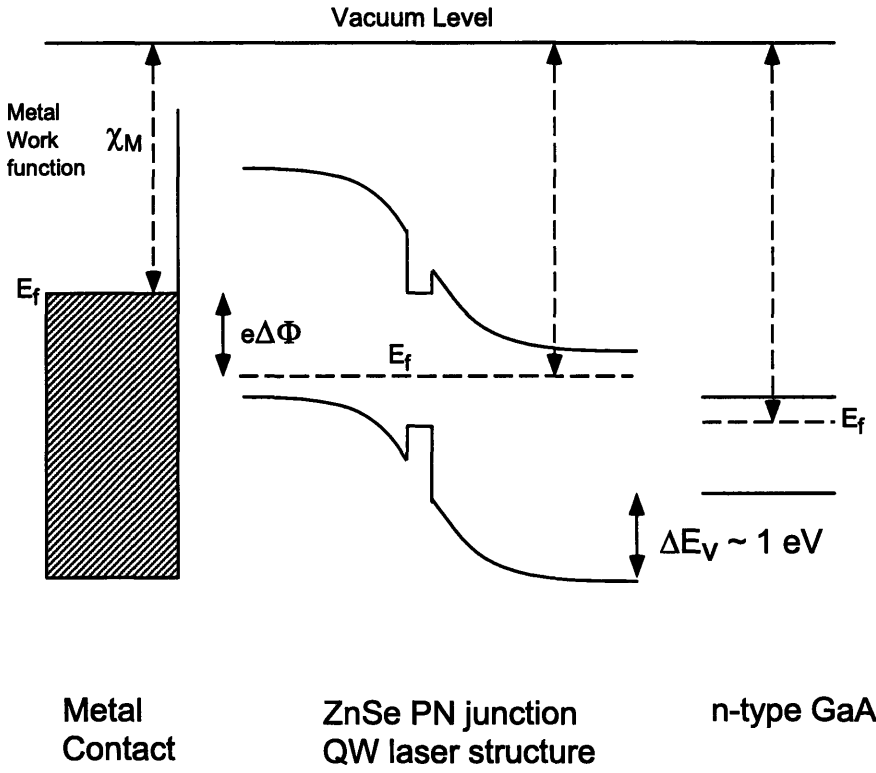

Figure 1-1: Making electrical contacts to a ZnSe laser structure is difficult due to a lack of compatible materials. Because of the large valence band offset between ZnSe and GaAs and the lack of any metals with large enough work function, large barriers for hole transport are formed if either material is used for the p-type ZnSe contact. Most designs use a metal with an graded superlattice for the p-contact, and GaAs for the n-contact.

of the ability to achieve high acceptor concentrations in the 10^{17} cm^{-3} range using an atomic nitrogen source, paved the way for fabrication of high quality ZnSe p-n junctions. Within a year, the first successful ZnSe-based electrically pumped laser diode was demonstrated [8]. Development of more advanced structures, such as separate confinement heterostructures (SCH) for improved optical guiding [9] lead to improved device performance. Unfortunately, device lifetimes were found to be limited by optical degradation due to dislocation formation[10]. The lifetime of ZnSe devices is slowly improving, with the record for room temperature laser operation standing at about 1 hour. The short lifetimes of ZnSe-based laser diodes remain the biggest obstacle for wide-spread use in mass market applications such as compact-disk players.

Another problem is the inability to form ohmic electrical contacts to p-type ZnSe [11].

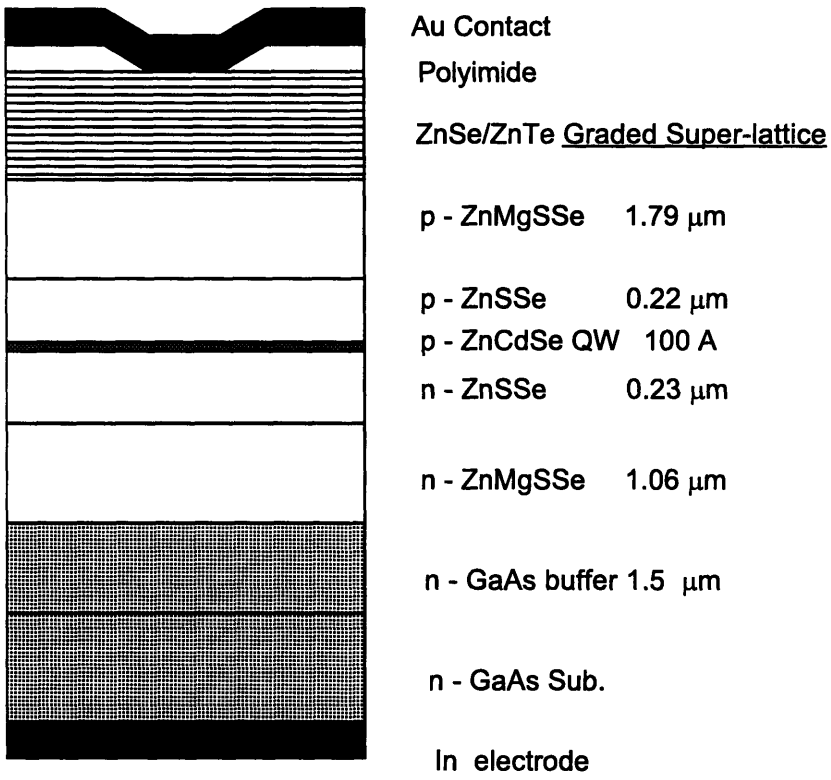

Figure 1-2: Diagram of a typical ZnSe quantum well laser diode structure. A graded bandgap ZnTe/ZnSe superlattice is used to gradually reduce the large Schottky barrier for holes at the top p-type contact.

Figure 1-1 shows a ZnSe p-n junction laser structure which is to be put in contact with a metal and GaAs. The main question is which material should be used for contacting the p-ZnSe. The 1.42 eV bandgap of GaAs is much less than that of ZnSe. When a ZnSe/GaAs heterojunction is formed, most of the bandgap mismatch is taken up in the valence band, resulting in an approximately 1 eV barrier, ΔE_v, for holes trying to enter the ZnSe from the GaAs. Large barriers exist for holes entering ZnSe from metal contacts as well. No metal exists with a large enough work function to position the Fermi level close enough to the ZnSe valence band edge to form an ohmic contact. The strategy used by most researchers is to use a metal, such as gold, for the p-ZnSe contact and n-type GaAs for the n-ZnSe contact. This is because the conduction band offset between ZnSe and GaAs is only about 0.1 to 0.3 eV. To minimize the effect of the Schottky barrier formed with the metal contact, graded ZnTe/ZnSe superlattices

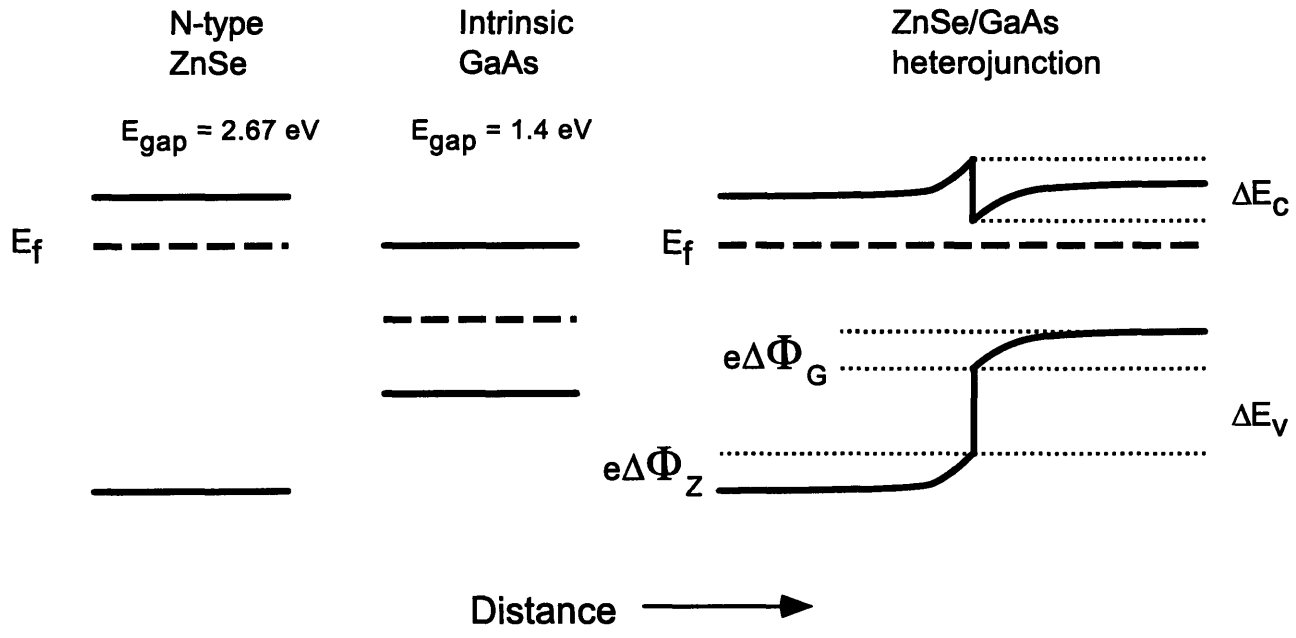

Figure 1-3: The left side diagram shows the bandgaps and Fermi levels for isolated ZnSe and GaAs material. When the materials joined to form a junction, as in the right diagram, the band offsets determine the line-up of the conduction and valence bands. Charge transfer from the ZnSe results in an electric field across the junction which bends the bands as shown. The total barrier between the materials is due to both the band offsets and the band bending.

are used. The bandgap of ZnTe is 2.3 eV[2], less than ZnSe, and thus enabling a better metal contact[12]. By growing interleaved thin layers of ZnTe and ZnSe, and gradually changing their relative thicknesses, an artificial material is created with an effective band gap which is slowly increased with distance from the metal until it matches bulk ZnSe. An example of a ZnSe-based SCH laser structure incorporating a graded superlattice is shown in Fig. 1-2.

Most of the attention of devices designers has been on the p-type contact in order to reduce the operating voltages of the devices which are on the order of 5 to 10 volts, even with these heroic measures. Less attention has been given to the n-type ZnSe/GaAs heterojunction. Figure 1-3 depicts the situation when two semiconductors with different bandgaps, such as ZnSe and GaAs, are put into contact with each other. These band diagrams show the energy levels of the bottom of the conduction band and the top of the valence band as a function of position. For separated materials, as shown on the left, the bands are flat. To be able to draw the band

diagram of the materials in physical contact, knowledge of the band offsets and the electrostatic potential is needed. As mentioned above, the alignment of the conduction and valence bands is given by the band offsets which are fundamental parameters determined by the microscopic atomic bonding between the materials. The electrostatic potential arises because, in order to achieve equilibrium, a single Fermi level must be attained across the heterojunction. For the example in Fig. 1-3, the Fermi levels of the separated materials (left hand schematic) lie near the conduction bands so both materials are n-type. When they are joined, as shown in the right schematic, electrons from the ZnSe will spill over the junction into lower energy states on the GaAs side. This process continues until the electric fields, set up by the separation of the electrons from their positive donor ions on the ZnSe side, are strong enough to oppose any more transfer. The resulting electric potential makes the energy of the electrons vary with distance from the junction and causes the 'bending' of the band diagram in the left hand plot. The electrostatic potential, $\Phi(x)$, is found by solving the Poisson equation on either side of the junction

$$\nabla^2\Phi = \frac{e}{\epsilon}\left[n - p - (N_d^+ - N_a^-)\right] \tag{1.1}$$

with boundary conditions that $\Phi = 0$ far into the bulk on either side, and that Φ and the displacement, $\vec{D} = \epsilon\vec{\mathcal{E}}$, are continuous at the junction. Here, the free carrier densities are functions of the potential as

$$\begin{aligned} n(x) &= n(E_c(x) - E_f) = N_c^{\pm} F_{\frac{1}{2}}(E_c^{\pm} - e\Phi(x) - E_f) \\ p(x) &= p(E_f - E_v(x)) = N_v^{\pm} F_{\frac{1}{2}}(E_f - E_c^{\pm} + E_g^{\pm} + e\Phi(x)) \end{aligned} \tag{1.2}$$

where the notation $\pm$ indicates that parameters are to be taken for the GaAs ($x > 0$) and ZnSe sides ($x < 0$) respectively. $E_g^{\pm}$ refers to the bandgap on either side of the junction, and $E_c^{\pm}$ refers to the conduction band energy far into the bulk on either side as determined by the doping. The Fermi energy E_f serves as the reference energy and can be set to zero. N_c and N_v are the density of states factors for the conduction and valence bands, and the function $F_{\frac{1}{2}}(x)$ is the Fermi integral for three dimensions.

The total potential energy barrier, E_b, for electrons to enter the ZnSe from the GaAs is determined by the conduction band offset as well as the band bending on the GaAs side of the

junction

$$E_b = \Delta E_c - e\Phi_G. \tag{1.3}$$

Fig. 1-3 represents the case of an ideal heterojunction with no surface trap states and no interface surface charge. In this case, the band bending acts to reduce the barrier formed by the conduction band offset. The electric field on the GaAs side of the junction points into the GaAs from the space charge region of positive donor ions on the ZnSe side. The transfer of electrons from a larger to a narrower bandgap material at a heterojunction is called modulation doping. With a voltage applied to the heterojunction (positive contact to the ZnSe for electron injection to the ZnSe) the energy barrier will have an important effect on the current flow. The current, according to Sze [13], will be exponential in the voltage as

$$J \propto \exp(\tfrac{qV - E_b}{kT}) \tag{1.4}$$

since electrons must be thermionically emitted into the ZnSe over the barrier. Thus the energy barrier causes the heterojunction to act like a diode and will cause increased operating voltages for a given current necessary to drive a device such as a laser.

The goal of this study is to investigate the electronic structure of ZnSe/GaAs heterojunctions, an experimental technique which can be used to determine the electrostatic potential, $\Phi(x)$, in each material and is specific to the interface is required. In the field of semiconductor devices, current-voltage (I-V) and capacitance-voltage (CV) methods are standard for evaluating the transport properties of bulk materials and various junctions between materials. Barrier heights, material doping, and interface charges can be measured with these techniques [13, 14].

The drawback with these transport methods is that electrical contacts to the sample are required. Formation of ohmic contacts to wide bandgap semiconductors can be problematic, requiring high doping densities. In the case of P-type ZnSe, as mentioned previously, ohmic metal/semiconductor junctions are not possible. In principle, metal/ZnSe contacts could be characterized independently and incorporated into structures with a large spatial separation between the contact junction and the ZnSe/GaAs interface under study. Because of the finite mismatch (0.27%) [15, 16] in the lattice constants of ZnSe and GaAs, epitaxial films of ZnSe are under compressive strain. For layer thicknesses below about 1500 Å, this strain can be

accommodated in the ZnSe lattice. Above this thickness, the ZnSe film will relax by formation of dislocations in order to achieve its slightly larger lattice dimensions. Thus, in order to study the ZnSe/GaAs heterojunction without complications from dislocations and lattice defects, the ZnSe layer must be kept thinner than 1500 Å. In this case, however, surface states created at a metal surface contact will almost certainly cause depletion layers and band bending across the heterojunction. This will complicate interpretation of CV and I-V measurements. A non-contact technique is therefore required.

Electron and optical spectroscopy are non-contact methods, and studies have been performed on the ZnSe/GaAs heterojunction using these techniques. The most important of these have been the x-ray photo-emission spectroscopy (XPS) studies of Prof. Franciosi's group [17, 18, 19]. In the XPS technique, x-ray are used to photo-eject electrons from the material. By analyzing the energies of the emitted electrons, information of the energy levels of the bands from which they were ejected can be obtained. By comparing the separation in energy of the electrons emitted from Ga core and Zn core atomic states, they were able to measure the valence band offset at the heterojunction. The energy resolution of XPS spectroscopy is low and the width of the electron distributions collected for each band is on the order of 1 eV. The researchers claim about a 70 meV resolution for detecting small shifts in the distributions. Despite this low resolution, they were able to determine that the valence band offset can be adjusted from about 1.2 eV down to 0.6 eV by changing the relative concentrations of Zn and Se in the molecular beams used to grow the ZnSe film [19]. The beam pressure ratio (BPR) is defined as [Zn]/[Se]. For BPR values near 1, the ZnSe surface at the start of the growth is Zn rich and large values of ΔE_v are obtained. This is the most common situation, and results in the best quality ZnSe films. At BPR values near 0.1, the surface is Se rich, and ΔE_v is lowered to near 0.6 eV. Experiments incorporating Ge in the growth of the first few monolayers resulted in even lower valence band offsets of about 0.44 ± 0.07 eV. The material quality in these low valence band offset regimes was found, by the authors, to be poor as measured by lack of excitonic features in the PL and absorption spectra. Improvement in the material quality was obtained by only using low BPRs in the growth of the first few monolayers. This set the band offsets. Continuing the rest of the growth at high BPRs then resulted in better quality films while still retaining the low valence band offset.

This observation of growth-dependent band offsets is very important for ZnSe device design. Even in the high BPR regime, these authors quote valence band offsets from 1.2 eV [19] to 0.78 eV [17]. In addition, the scattering in their data appears to be about 100 meV. This implies conduction band offsets anywhere from 50 meV up to 470 meV. The XPS technique requires in situ measurement of the ZnSe films, which must be kept thinner than 5 monolayers (30Å) in order to prevent secondary scattering of the electrons ejected from the underlying GaAs. Also, since synchrotron x-ray sources are not widely available, a simpler table-top method for investigating band offsets would be useful. A novel photo-reflectance technique capable of extracting the conduction band offset is a major result of this thesis work, and will be described in Chapter 4.

Based on I-V measurements of LEDs, Rennie et. al. [20] have claimed conduction band offsets up to 0.6eV between n-ZnSe and n-GaAs. Band bending was not accounted for in these measurements, and thus the assignment of the entire energy barrier responsible for their high operating voltages to the conduction band offset is not justified. Using AlGaAs and ZnCdSe buffer layers between the GaAs and ZnSe, the researchers were able to lower the effective barrier and reduce the operating voltage of their LED from 17 V to 6.5V. But, again, this reduction could just as well be due to lower interface state densities.

Yeganeh et. al. [21] have used surface second harmonic generation to investigate the ZnSe/GaAs heterojunction. in bulk materials with inversion symmetry, such as glass or Si, second order non-linear optical processes like second harmonic generation (SHG) cannot occur. An interface between two materials breaks this symmetry, and an effective surface non-linear susceptibility, $\chi^{(2)}$, appears. Thus, surface SHG can be used as an interface specific optical probe. Since both ZnSe and GaAs are non-centrosymmetric crystals, each has its own $\chi^{(2)}$ susceptibility for SHG besides that of the interface. By using proper polarization selection rules, however, the SHG from the interface of a ZnSe/GaAs junction can be separated from the bulk contributions. Using a tunable pump laser, these authors observed a resonance in the surface SHG at the two-photon energy 2.72 eV. They attributed the resonance to a spatially indirect 'cross-over' transition from the ZnSe valence band to a bound quantum well state formed on the GaAs side of the junction by band bending. The transition is diagrammed in Fig. 1-4.

As a mechanism providing band bending strong enough to support this bound state, the

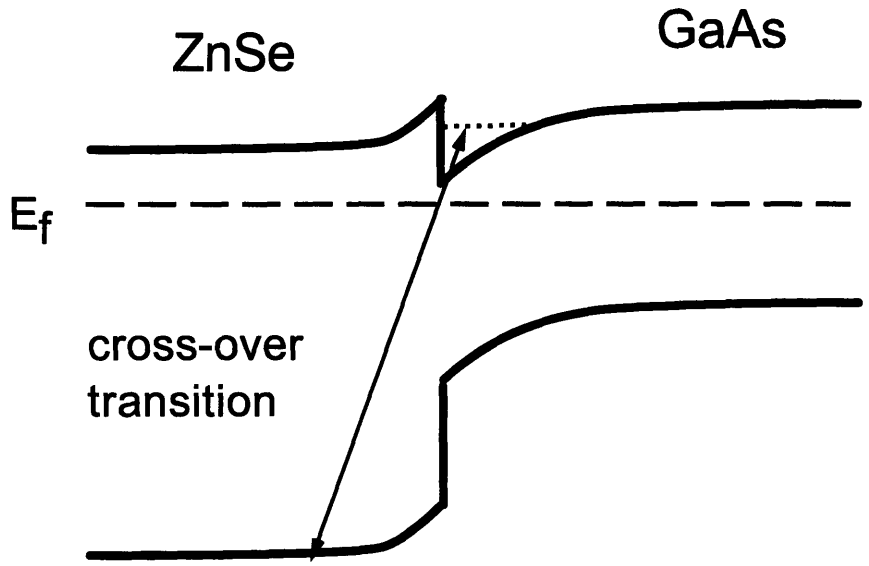

Figure 1-4: Band bending as determined by surface second harmonic studies. Diffusion of Ga and Zn across the junction results in formation of quantum well states at the interface and removal of any conduction band barrier.

authors invoked a diffusion process whereby Ga and Zn diffuse across the interface during the growth [22, 23]. Since Ga is a donor in ZnSe and Zn is an acceptor in GaAs, this forms a modulation-doped p-n junction with potentially very high (10^{19} cm^{-3}) dopant densities localized to within 100 Å on either side of the junction. This diffusion is supposedly due to charge imbalance in the interface bonding leading to very large electric fields. These field, then, enhance the normal material diffusion coefficient until the are screened [24, 25]. Cross-over transitions from the ZnSe valence band to the GaAs conduction band, were previously invoked by Kassel et. al. [26, 27], to explain features in electro-reflectance data. These authors also suggested that their results indicated strong band bending due to interdiffusion. It will be shown in chapter 4 that the cross-over transition seen by Kassel is in fact due to the GaAs alone. Their often referenced analysis of the band offsets at the ZnSe/GaAs junction therefore falls apart. For the MBE technique, the low substrate temperature employed is believed to result in little interdiffusion[28]. Hermans et. al. [29] have attributed excess free carriers in nominally undoped ZnSe to diffusion of Ga across the junction, but only at high growth temperatures. At lower ZnSe growth temperatures of about 640K, the diffusion process was

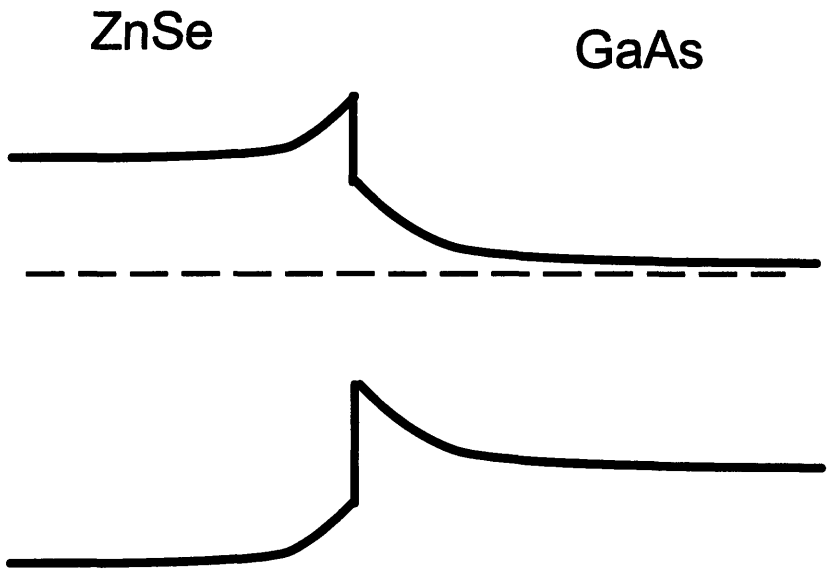

Figure 1-5: Interface traps accumulate electrons and create a negative surface charge. Electric fields in both materials point toward the interface causing the band bending shown which acts to create a large conduction band barrier.

found to be drastically reduced. Growth temperatures of about 560K were used for the ZnSe samples grown for this work.

Returning to the surface SHG results, the resonance seen at 2.72 eV seems to be real, and associated with the interface. No attempt at determining magnitude or sign of the field at the interface was attempted, however. This result seems to show that electric fields pointing into the GaAs (equivalent to a positive interface charge) are possible at the ZnSe/GaAs heterojunction. The band bending, in this case, can support bound states and is, therefore, strong enough to completely remove the energy barrier between the materials, as shown in Fig. 1-4.

A surface trap model for the band bending at the ZnSe/GaAs interface has been proposed by Pagès et. al. [30] based on Raman scattering measurements. An enhancement of the LO phonon scattering on the GaAs side of the junction was seen and attributed to electric fields generated by a depletion region caused by Fermi level pinning by trap states at the interface. Under illumination with the above-band laser, the enhancement was reduced in accord with a flattening of the bands. The band bending diagram for this case is shown in Fig. 1-5. Here, the band bending actually increases the barrier between the materials. This may account for

the large conduction band offsets invoked by Rennie [20]as discussed above. Direct evidence for band bending due to interface traps will be presented in Chapter 3 using electro-reflectance methods.

The experimental results for the electronic structure of the ZnSe/GaAs interface appear quite confusing. The band offsets have been shown to vary with growth conditions. A simpler technique for estimating the band offsets is therefore necessary for routine characterization of structures. Band bending at the interface has also been demonstrated to play a major role in the barrier heights at the interface. The techniques used so far, however, have been only indirectly sensitive to the electric fields at the junction. Electroreflectance (ER) and photoreflectance (PR) spectroscopy are a well known tools for direct characterization of the electric fields near semiconductor interfaces. Part I of this thesis is devoted to an in-depth ER and PR investigation of ZnSe/GaAs interfaces as a function of doping and surface reconstruction. The theory of ER and PR spectra will be discussed in Chapter 2, and results using this analysis will be presented in Chapter 3. A new technique, which is an extension of PR using a tunable pump laser, will be developed in Chapter 4 as a method for directly measuring barrier heights and conduction band offsets at semiconductor junctions.

Chapter 2

Electro-reflectance spectroscopy

2.1 Introduction

Electro-reflectance (ER) spectroscopy is a unique optical technique which is sensitive to electric fields in materials[31, 32]. In ER methods, changes in the dielectric constant of materials caused by presence of electric fields are monitored by a reflected probe beam. Modulations in the measured reflected power are recorded as a function of probe photon energy, yielding a modulation spectrum which can be analyzed in terms of well established theoretical lineshapes to extract the electric field magnitude and direction. Because the probe beam is used in reflection, it samples the material under test near dielectric discontinuities such as at the surface or at interfaces between materials. Thus ER spectroscopy is well suited to the study of band bending near heterojunctions.

This chapter will outline the general theory of ER spectroscopy as well as explain some of the details needed to interpret the data presented in Chapters 3 and 4. Historically, the theory of ER spectroscopy was developed for the purpose of determining the energies of high symmetry critical points in semiconductor band structures. In this regard, ER techniques are a form of modulation spectroscopy[33]. These band structure aspects of modulation spectroscopy will be discussed first as they reveal which transitions give rise to ER signals and why the modulation spectra are localized in energy for a given semiconductor. However, in general, the concern of this work is with the opposite situation: characterization of built-in electric fields in terms of a known bandstructure. This is the motivation for much of the current work in this field 30

years after its introduction, and much progress has been made in developing ER methods for measuring fields in materials [34]as well as devices such as heterojunction bipolar transistors (HBTs) [35, 36]and metal-oxide-semiconductor (MOS) transistors[37, 38].

Next, the problem of direct interband optical transitions in the presence of an electric field will be solved in order to introduce the so called electro-optic functions which give the lineshape of the observed modulation spectra. Two experimental methods for ER, contactless electro-reflectance (CER) and photoreflectance (PR) will be described and compared with emphasis on how they complement each other. Data obtained for the simple case of an N-type GaAs surface will be presented to illustrate the theory, and a particularly clear example of Franz-Keldysh oscillations found in the PR spectrum of a ZnSe/GaAs double hetero-structure will be used to show how electric field strengths can be accurately extracted from ER spectra. Finally, the important issue of spatial averaging will be discussed. With this conceptual framework in place, the ER spectra of ZnSe/GaAs heterostructures presented in Chapter 4 can be easily interpreted and the new technique of internal photo-emission PR developed in this thesis work can be appreciated.

2.2 Critical Points and Modulation Spectroscopy

Throughout the 1960's and early 1970's, with the general symmetry properties becoming well understood, and powerful numerical methods being brought to bear, the theory of semiconductor bandstructure was in need of new experimental techniques both to verify results and provide certain input parameters such as critical point energies and effective masses[33, 39]. Although electrical transport measurements such as magneto-resistance and cyclotron resonance and optical spectroscopies such as photo-luminescence and absorption can yield information on the bands lying near the Fermi energy, higher lying transitions are more difficult to characterize. Linear optical measurements like reflection, absorption , and ellipsometry can determine the dielectric constant of a solid; however, the dielectric constant is often a smooth function of photon energy because several transitions at different locations in the Brillouin zone may be contributing. Singularities in the joint density of states for one transition may only result in a small change in slope of the reflectivity or absorption at that energy.

Modulation spectroscopies get around this problem by effectively measuring the derivative of the joint density of states. The imaginary part of the dielectric constant for interband direct transitions can be obtained by summing the oscillator strength for each transition consisting of pairs of Bloch states where the initial state k-vector equals the final state k-vector at a given photon energy. This integral over k-space can be expressed as an integral over constant energy surfaces and energy as

$$\mathrm{Im}\,\varepsilon(\omega) = \frac{1}{2\pi\omega}\sum_{ij}\int dS_{\omega_{ij}} d\omega_{ij} F_{ij}\delta\left(\omega_{ij}(\vec{k}) - \omega\right) \tag{2.1}$$

Here, the discrete sum is over pairs of bands i and j , F_{ij} is the interband oscillator strength, and $\hbar\omega_{ij}(\vec{k})$ is the interband energy separation at wavevector $\vec{k}$. The integral over energy can be formally evaluated because of the delta function to give

$$\mathrm{Im}\,\varepsilon\,(\omega) = \frac{1}{2\pi\omega}\sum_{ij}\int_{\omega_{ij}=\omega}\frac{dS_{\omega_{ij}} F_{ij}}{\left|\vec{\nabla}_k\omega_{ij}(\vec{k})\right|}. \tag{2.2}$$

This expression suggests that the energy dependence of the dielectric constant should show strongest features near energies where the gradient term in the denominator for one of the interband transitions is equal to zero. If the oscillator strength is constant for a given allowed interband transition, Eq. 2.2 can be expressed as

$$\mathrm{Im}\,\varepsilon\,(\omega) = \frac{4\pi^2}{\omega}\sum_{ij} F_{ij}\Omega_{ij}(\omega_{ij} - \omega) \tag{2.3}$$

where Ω_{ij} is the joint density of states for the $i \rightarrow j$ transition. Since F is often only a very slowly varying function of energy, the structure in the optical properties of a solid are determined by the band structure through the joint density of states. A critical point is a location in the Brillouin zone where the interband energy is expanded in a power series in k as

$$\omega_{ij}(\vec{k}) = \omega_g + \frac{\hbar}{2}\left(\frac{k_x^2}{\mu_x^*} + \frac{k_y^2}{\mu_y^*} + \frac{k_z^2}{\mu_z^*}\right) + ..., \tag{2.4}$$

where x, y, and z refer to the principal axes of the reduced effective mass tensor. This point can be either a maximum, minimum, or saddle-point depending on the signs of the effective

masses in the various directions.

For spherical bands and μ^* positive (a M_0 critical point such as the fundamental gap in a direct gap semiconductor), $\mathrm{Im}\,\varepsilon(\omega)$ given by Eq. 2.2 can be easily evaluated for ω near ω_g using Eq. 2.4 and shown to have the form

$$\mathrm{Im}\,\varepsilon(\omega) \propto \frac{F}{\omega}\,\mathrm{Re}\,(\omega-\omega_g)^{\frac{1}{2}} + \frac{C}{\omega} \tag{2.5}$$

where C represents the contribution from all other transitions and is slowly varying in energy. The joint density of states near an M_0 critical point can thus be expressed as

$$\Omega(\omega) \propto \mathrm{Re}\,(\omega-\omega_g)^{\frac{1}{2}} + C. \tag{2.6}$$

If one of the masses in Eq. 2.4 is negative, a M_1 critical point results. The constant energy surfaces are hyperboloids and Eq. 2.2 can be evaluated by assuming the energy dispersion remains parabolic and by cutting the integral off at the Brillouin zone boundary. In this case the joint density of states is given by an expression similar to Eq. 2.6

$$\Omega(\omega) \propto C - \mathrm{Re}\,(\omega_g-\omega)^{\frac{1}{2}}\,. \tag{2.7}$$

Schematic plots of Ω near M_0 and M_1critical points are shown in Fig. 2-1. The density of states for the other two types of three dimensional critical points, M_3 and M_2, which occur for the other two combinations of signs in the effective masses in Eq.2.4, are the same as those for M_0 and M_1 respectively, only with the energy axes flipped around ω_g. The band structure of GaAs is shown in Fig. . The fundamental band gap transition (1.42eV) marked at the zone center is of type M_0. The transition from the valence band to the L-valley near the Λ point is the so called E_1transition (2.9 eV) and is of type M_1. Note how the bands track each other along the $\Gamma - L$ symmetry axis indicating that one of the masses in Eq.2.4 is negative.

The above expressions for the joint density of states hold the key to the success of modulation spectroscopy in determining critical point energies. As stated above, $\mathrm{Im}\,\varepsilon(\omega)$ often does not show large variations near a critical point. This is because the constant C in Eqns. 2.6 and 2.7 ,which is the joint density of states due to other interband transitions, can be quite

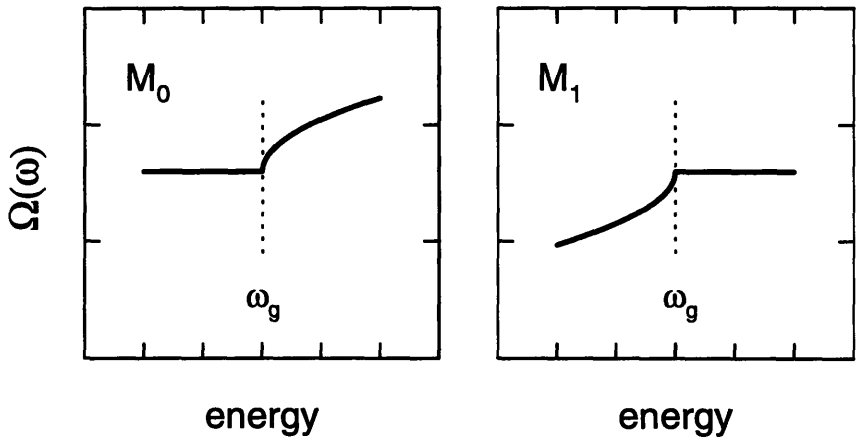

Figure 2-1: Joint density of States function, $\Omega(\omega)$, plotted near an M_0 and an M_1 critical point with a gap energy ω_g.

large. In modulation spectroscopy, the sample is subjected to some form of stress described by a parameter ξ. Various methods for perturbing the solid lead to different forms of modulation spectroscopy such as piezoreflectance (ξ =strain), thermoreflectance (ξ =temperature), or electro-reflectance (ξ =electric field strength). The energies, $E\left(\vec{k}\right)$, of the Bloch states of the solid can be expected to change slightly in response to any of these perturbations. In particular, the critical point energies will shift. The resulting change in the joint density of states for a M_0 point is given by

$$\Delta\Omega(\omega) = \frac{d\Omega(\omega)}{d\xi}\Delta\xi \propto \left[-\frac{1}{2}(\omega-\omega_g)^{-\frac{1}{2}}\frac{d\omega_g}{d\xi} + \frac{dC}{d\xi}\right]\Delta\xi. \tag{2.8}$$

The first term in the brackets blows up at ω_g indicating that changes in the dielectric constant will be dominated by the contribution from transitions with their critical points near ω. Thus, Eq. 2.8 predicts that strong features should be observed in the differential reflectance spectrum, which is proportional to the changes in the dielectric constant, for energies near ω_g. The exact modulation spectrum obtained may be different from that given by Eq. 2.8 which assumes a rigid shift of the band structure with ξ. Piezo-reflectance and thermoreflectance spectra may be modelled in this way. Electric fields; however, modify both the spectrum of the density of

states as well as the oscillator strength (interband matrix element). The arguments presented here still generally hold, and ER signals are found near critical point energies. The subsequent sections of this chapter will explain the modulation lineshapes resulting from application of electric fields to semiconductors.

One final experimental detail to note is that the perturbation can be applied as a periodic function of time ($\Delta\xi(t) = \Delta\xi \cos 2\pi\upsilon t$). The changes in the sample reflectivity will then impose a small periodic, narrow-band modulation on the probe beam intensity. Using suitable electronic techniques such as filtering and lock-in amplification, this small AC signal from the probe detector can be detected and changes in reflected power as small as 10^{-6} can be measured.

2.3 Optical absorption in the presence of a uniform electric field

Electro-reflectance (ER) spectroscopy uses electric fields to modulate the dielectric constant in semiconductors. To understand the observe modulation spectra, ΔR/R, the problem of optical absorption in the presence of an electric field needs to be solved. The general theory of the effects of electric fields on semiconductor dielectric functions for arbitrary critical points and field directions was worked out by Aspnes [40, 41, 42]. Since detailed analysis of ER lineshapes is only required for the fundamental bandedge of GaAs for the experiments in this thesis, the simpler problem of an electric field along the <100> symmetry axis for a spherically symmetric M_0 critical point with parabolic dispersion will be discussed. This theory is essentially the same as that presented originally by Tharmalingram [43]. Additional simplifications of both this analysis and the more general solution of Aspnes include neglecting of excitonic (electron-hole Coulomb attraction) effects and of spatially non-uniform electric fields. Non-uniform field effects will be important for this work and will be discussed at the end of this Chapter. The magnitude of the electric field strength is assumed to be such that the energy scale of the spectral features in ΔR/R , $\hbar\theta$ (called the electro-optic energy), which will be introduced below, is $> \Gamma$, the phenomenological broadening parameter due to scattering processes and thermal effects. This range of electric fields is known as the Franz-Keldysh regime [44]. The fields are not so high that interband tunnelling rates are significant, however.

The starting point for calculation of the optical properties of semiconductors is the Elliot

formula[45] for the imaginary part of the dielectric constant

$$\mathrm{Im}\,\varepsilon\left(\hbar\omega\right) = \frac{4\pi^2 e^2}{m^* \omega^2} \left|\hat{\epsilon} \cdot \mathbf{P}_{cv}\right|^2 \sum \left|\Phi_i\left(r=0\right)\right|^2 \delta\left(E_i - \hbar\omega\right). \tag{2.9}$$

The real part of the dielectric constant can be calculated from this expression via Kramers-Kronig relations. Here $\hat{\epsilon}$ is a unit vector in the direction of the electric field and $\mathbf{P}_{cv}$ is the $\vec{k}$-independent momentum matrix element between the lattice periodic parts of the conduction and valence band wavefunctions. The summation is over all states with energies E_i. $\Phi_i\left(\vec{r}\right)$ is the envelope of the wavefunction of the electron-hole pair in relative coordinates. The Elliot formula indicates that the optical absorption is proportional to the probability of finding the electron and hole at the same position in space. In the absence of an external potential and neglecting Coulomb effects, the envelope functions Φ_i are plane waves whose value at $r = 0$ is unity. Thus the absorption is simply proportional to the density of states.

An electric field affects both the spectrum of energy eigenstates E_i, and the wavefunction envelopes. The crystal Hamiltonian becomes, with the field, $\mathcal{E}$, pointing along the positive z axis,

$$H = H_0 - e\mathcal{E}z \tag{2.10}$$

where H_0 is the unperturbed Hamiltonian,

$$H_0 = \frac{p^2}{2m_0} + V(\vec{r}), \tag{2.11}$$

and $V(\vec{r})$ is the periodic potential of the lattice. Since the linear potential in Eq. 2.10 varies slowly over a unit cell, the envelope approximation may be used to find the new wavefunctions. The envelope Hamiltonian to be solved is

$$\frac{p_e^2}{2m_e^*} + \frac{p_h^2}{2m_h^*} + e\mathcal{E}\left(z_e - z_h\right) = \frac{P^2}{2(m_e^* + m_h^*)} + \frac{p^2}{2\mu^*} + e\mathcal{E}z \tag{2.12}$$

where the right hand side shows the separation into center of mass and relative coordinates. Since the composite particle (electron-hole pair) has no charge, the center-of-mass motion is unaffected by the potential and the pair moves as a free particle. The relative coordinate

Schrödinger equation is

$$\left[\frac{\hbar^2}{2\mu^*}\left(\frac{\partial^2}{\partial x^2}+\frac{\partial^2}{\partial y^2}+\frac{\partial^2}{\partial z^2}\right)-e\mathcal{E}z+E_i\right]\Phi_i(\vec{r})=0 \tag{2.13}$$

where Φ_i is the envelope wavefunction to be inserted into Eq. 2.9. By separating variables and using the substitution

$$\begin{aligned}\xi &= \frac{e\mathcal{E}z-E_{i_z}}{\hbar\theta} \\ (\hbar\theta)^3 &= \frac{e^2\mathcal{E}^2\hbar^2}{2\mu^*},\end{aligned} \tag{2.14}$$

the z-coordinate part of Eq.2.13 can be shown to be equivalent to the Airy equation

$$\frac{d^2\Phi_i(\xi)}{d^2\xi}=\xi\Phi_i(\xi). \tag{2.15}$$

Thus, the solution to Eq. 2.13 is given by

$$\Phi_i(\vec{r})=\frac{1}{2\pi}\frac{e^{ik_x x+ik_y y}}{L}\sqrt{\frac{e\mathcal{E}}{\hbar\theta}}Ai(\frac{e\mathcal{E}z-E_{i_z}}{\hbar\theta}), \tag{2.16}$$

with total energy E_i given by

$$E_i=\frac{\hbar^2k_x^2}{2\mu^*}+\frac{\hbar^2k_y^2}{2\mu^*}+E_{i_z}. \tag{2.17}$$

The electron-hole pair is free along the x and y axes and so the wavefunction resembles a plane wave in these directions characterized by the quantum numbers $k_x$and k_y. Along the z axis, the electric field acts to accelerate the electron and hole, thus mixing the original Bloch function eigenstates with wavevector k_z. Φ_i in this direction is given by an Airy function of the first kind characterized by E_{i_z}, the energy (kinetic + potential) in the z component of the pairs's motion. The parameter $\hbar\theta$, the "electro-optic energy" which is a function of the electric field strength, sets the energy scale in the problem, and the square root factor ensures that Φ_i is properly normalized to 1 over the sample volume.

Before the Elliot formula is evaluated to determine the absorption, it is instructive to get some physical insight in the above solution. From the left side of Eq.2.12 it is evident that the

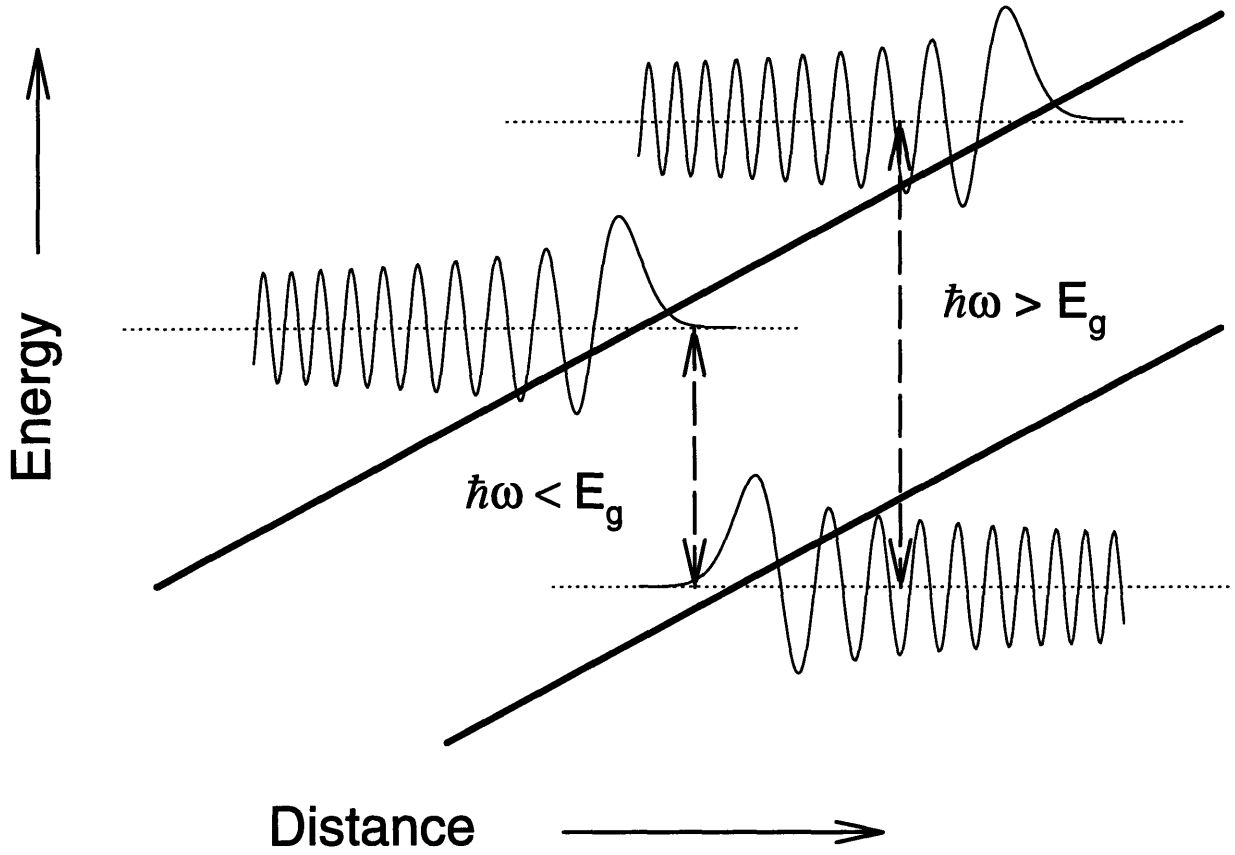

Figure 2-2: Envelope wavefunctions for electrons and holes in a linear potential. Tunneling beyond the classical turning points results in finite absorption below the gap.

electron and hole coordinates may be separated without going to CM and relative coordinates as required for the Elliot formula. In this case, the electron and hole wavefunctions are individually seen to be given by Airy functions. Figure 2-2 plots a few of these wavefunctions against the band diagram of the linear potential introduced by the electric field. Classically, in a uniform electric field, electrons and holes enter from minus and plus infinity, respectively, are slowed by the electric field until they reach the turning point of their trajectory, and are accelerated back to where they started. The turning point along the z-axis is obtained by setting $\xi = 0$ in Eq. 2.14. The wavefunctions represent the addition of some simple quantum concepts to these classical trajectories. The kinetic energy of each particle increases with distance away from its turning point and is reflected in the period of the Airy function's oscillation which may be taken as the De Broglie wavelength of the particle at each point along the z axis. The exponential tail of the Airy functions represents the ability of the particles to tunnel slightly beyond the turning points.

Optical absorption is proportional to the overlap of these electron and hole wavefunction envelopes. The zero of energy is taken as the energy of the wavefunction whose turning point occurs at z=0. The absorption at energy $\hbar\omega$ is then determined by the overlap of the hole wavefunction which has its turning point at z=0, and the electron wavefunction with energy $\hbar\omega - E_g$. All other transitions are redundant. Note that the complete set of eigenfunctions to the Airy equation are shifted versions of the same function as seen in Eq. 2.16. This simply reflects the fact that although translational symmetry is broken by the electric field, the position defined as $z = 0$ which in turn defines the zero of energy, $E_{i_z} = 0$, are still arbitrary. Figure 2-2 illustrates that because of the exponential tails, there is a small overlap of the wavefunctions for $\hbar\omega < E_g$. Thus the electric field induces a finite absorption below the band gap energy. For $\hbar\omega > E_g$, the spatial oscillations in the wavefunctions lead to oscillatory structure in the absorption spectrum. These spectral oscillations are called Franz-Keldysh (FK) oscillations after the theorists who first addressed the problem of electric field effects on optical absorption [46, 47]. The absorption is proportional to

$$|\langle\Phi_e|\Phi_h\rangle|^2 = \left|\int dz\, \mathrm{Ai}(\frac{e\mathcal{E}z - E_{i_z}}{\hbar\theta_e})\, \mathrm{Ai}(-\frac{e\mathcal{E}z}{\hbar\theta_h})\right|^2 . \tag{2.18}$$

Using a property of the Airy functions,

$$\int_{-\infty}^{+\infty} dt\, \mathrm{Ai}(t+x)\, \mathrm{Ai}(\alpha t+y) = \frac{1}{(1-\alpha^3)^{1/3}}\, \mathrm{Ai}(\frac{y-\alpha x}{(1-\alpha^3)^{1/3}}) \quad for\ \alpha < 1, \tag{2.19}$$

expression 2.18 can be evaluated as

$$|\langle \Phi_e | \Phi_h \rangle|^2 \propto \mathrm{Ai}^{\,2}\left(\frac{-E_{i_z}}{\hbar\theta}\right) \propto |\Phi_i\,(\vec{r}=0)|^2\,, \tag{2.20}$$

which shows the connection between the intuitive wavefunction overlap picture and the Elliot formalism of Eq. 2.9.

Formula 2.9 will now be evaluated to determine $\mathrm{Im}\,\varepsilon\,(\hbar\omega)$. Plugging Eq.2.16 into Eq. 2.9 and explicitly writing out the sum over states, results in

$$\mathrm{Im}\,\varepsilon\,(\hbar\omega) = \frac{4\pi^2 e^2}{m^*\omega^2}\,|\hat{\epsilon}\cdot\mathbf{P}_{cv}|^2\ \frac{1}{2\pi}\frac{e\mathcal{E}}{\hbar\theta}\iint_{-\infty}^{\infty} dk_x dk_y \int_{-\infty}^{\infty} \frac{d\epsilon_z}{\hbar\theta}\,\mathrm{Ai}^{\,2}\left(\frac{-\epsilon_z}{\hbar\theta}\right)\delta\left(E_g+\epsilon_x+\epsilon_y+\epsilon_z-\hbar\omega\right). \tag{2.21}$$

The integral over ϵ_z collapses because of the delta function, and the 2D integral over k_x and k_y can be transformed into the expression

$$\int_0^{\infty} d\epsilon_\perp\,\mathrm{Ai}^{\,2}\left(\frac{\epsilon_\perp + E_g - \hbar\omega}{\hbar\theta}\right), \tag{2.22}$$

which can be evaluated using another standard Airy function formula for the indefinite integral

$$\int^{t} du\,\mathrm{Ai}^{\,2}(u) = t\,\mathrm{Ai}^{\,2}(t) - \mathrm{Ai}^{\,\prime 2}(t)\,. \tag{2.23}$$

The prime in Eq. 2.23 denotes a derivative. The final result is

$$\mathrm{Im}\,\varepsilon\,(\hbar\omega) = \frac{2\pi e^2}{m^*\omega^2}\,|\hat{\epsilon}\cdot\mathbf{P}_{cv}|^2\left(\frac{2\mu^*}{\hbar^2}\right)^{\frac{3}{2}}(\hbar\theta)^{\frac{1}{2}}\left[\mathrm{Ai}^{\,\prime 2}(\eta) - \eta\,\mathrm{Ai}^{\,2}(\eta)\right],$$

with

$$\eta \;=\; \frac{E_g - \hbar\omega}{\hbar\theta} \tag{2.24}$$

$$(\hbar\theta)^3 = \frac{e^2\mathcal{E}^2\hbar^2}{2\mu^*}.$$

In the limit $\mathcal{E} \to 0$,

$$\lim_{\mathcal{E}\to 0} \operatorname{Im}\varepsilon(\hbar\omega) = \frac{2e^2}{m^*\omega^2}\left|\hat{\epsilon}\cdot\mathbf{P}_{cv}\right|^2\left(\frac{2\mu^*}{\hbar^2}\right)^{\frac{3}{2}}\sqrt{\hbar\omega - E_g}\,U(\hbar\omega - E_g), \tag{2.25}$$

which is the standard absorption spectra of free electron hole pairs (U is a unit step function). ER spectroscopy measures the difference in the dielectric constant induced by the electric field $\mathcal{E}$

$$\Delta\varepsilon = \varepsilon(\hbar\omega, \mathcal{E}) - \varepsilon(\hbar\omega, 0). \tag{2.26}$$

. Using a form of the Kramers-Kronig relation valid for this difference quantity

$$\Delta\varepsilon_1(\omega) \simeq \frac{1}{\pi\omega^2}\mathcal{P}\int_{-\infty}^{\infty} d\omega' \frac{\omega'^2}{\omega' - \omega}\Delta\varepsilon_2(\omega'), \tag{2.27}$$

the final results for the changes in the dielectric constant induced by the electric field are

$$\Delta\varepsilon(\hbar\omega) = \Delta\varepsilon_1 + i\Delta\varepsilon_2 = \frac{2e^2}{m^*\omega^2}\left|\hat{\epsilon}\cdot\mathbf{P}_{cv}\right|^2\left(\frac{2\mu^*}{\hbar^2}\right)^{\frac{3}{2}}(\hbar\theta)^{\frac{1}{2}}\left[G(\eta) + iF(\eta)\right], \tag{2.28}$$

where,

$$\begin{aligned} F(\eta) &= \pi\left[\mathrm{Ai}'^2(\eta) - \eta\,\mathrm{Ai}^2(\eta)\right] - \sqrt{-\eta}U(-\eta) \\ G(\eta) &= \pi\left[\mathrm{Ai}'(\eta)\,\mathrm{Bi}'(\eta) - \eta\,\mathrm{Ai}(\eta)\,\mathrm{Bi}(\eta)\right] + \sqrt{\eta}U(\eta). \end{aligned} \tag{2.29}$$

F and G are the electro-optic functions and are plotted in Fig. 2-3. The function Bi is the Airy function of the second kind which blows up at $+\infty$, and the primes denote derivatives with respect to the argument.

These (dimensionless) electro-optic functions F and G were introduced by Aspnes in Ref. [40] and are the starting point for the discussion of electric field effects in more complicated situations. Although the derivation presented here was for a simple symmetrical M_0 critical point, F and G also show up in the expressions for other critical points and for arbitrary field alignment and mass tensor symmetry. Information on the size of the electric field is contained

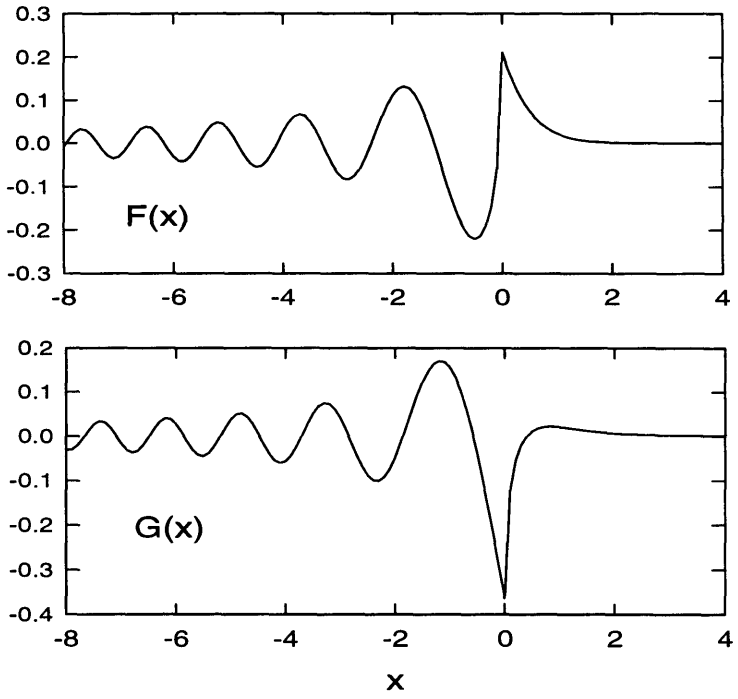

Figure 2-3: The dimensionless electro-optic functions F(x) and G(x). x<0 corresponds to $\hbar\omega > E_g$.

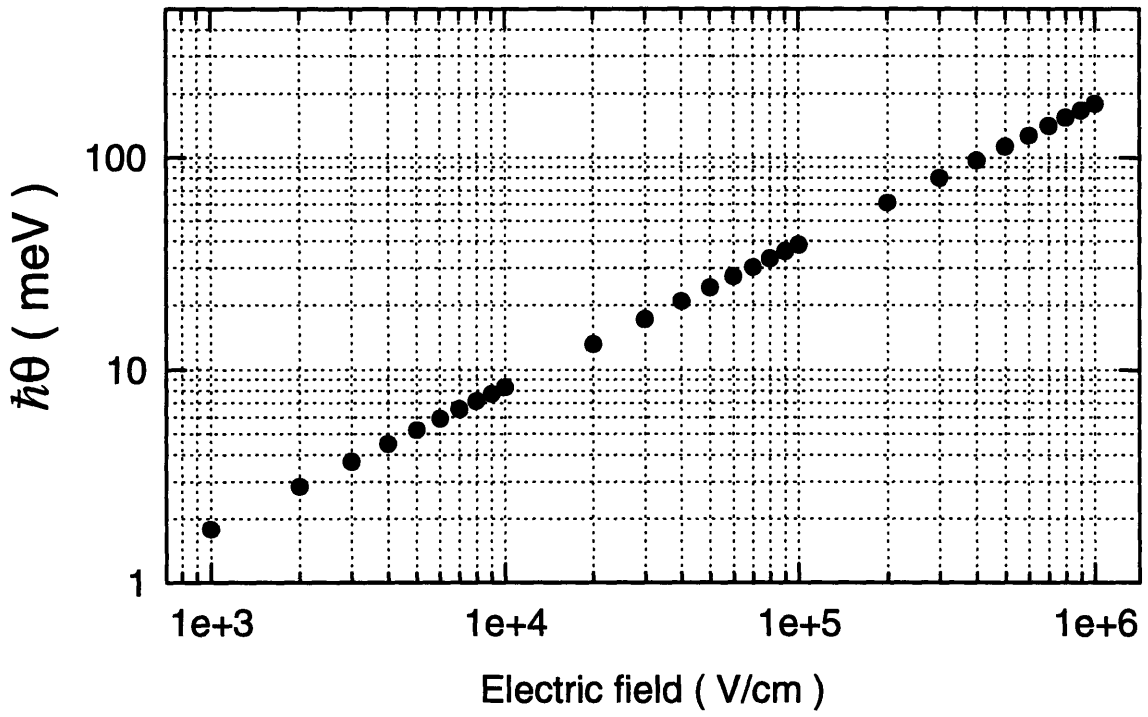

Figure 2-4: The electro-optic energy parameter $\hbar\theta$ as a function of electric field evaluated using the GaAs conduction band mass ($m_c^* = 0.067m_0$).

in the period of the above band Franz-Keldysh oscillations. For reference, figure 2-4 shows the energy scale parameter, $\hbar\theta$, as a function of electric field using the GaAs effective electron mass.In this work, the interest is in using small external AC fields to slightly perturb large static built-in fields resulting from band bending. The quantity of interest is

$$\Delta\hat{\varepsilon}\left(\hbar\omega\right) = \Delta\varepsilon\left(\hbar\omega, \mathcal{E}_{DC} + \tfrac{1}{2}\mathcal{E}_{AC}\right) - \Delta\varepsilon\left(\hbar\omega, \mathcal{E}_{DC} - \tfrac{1}{2}\mathcal{E}_{AC}\right). \tag{2.30}$$

For $\mathcal{E}_{AC} \ll \mathcal{E}_{DC}$,

$$\Delta\hat{\varepsilon}\left(\hbar\omega\right) = \frac{\partial}{\partial\mathcal{E}}\Delta\varepsilon\left(\hbar\omega, \mathcal{E}\right)\Big|_{\mathcal{E}_{DC}}\left(\mathcal{E}_{AC}\right) \tag{2.31}$$

where $\Delta\varepsilon$ is the deviation from flat-band ($\mathcal{E} = 0$) given by Eq.2.26. By taking derivatives of Eq. 2.28 with respect to the electric field, Eq. 2.31 can be put in the form

$$\Delta\hat{\varepsilon}\left(\hbar\omega\right) = \Delta\hat{\varepsilon}_1 + i\Delta\hat{\varepsilon}_2 = \frac{2e^2}{m^*\omega^2}\left|\hat{\epsilon}\cdot\mathbf{P}_{cv}\right|^2\left(\frac{2\mu^*}{\hbar^2}\right)^{\frac{3}{2}}\left(\hbar\theta_{DC}\right)^{\frac{1}{2}}\left[\hat{G}\left(\eta_{DC}\right) + i\hat{F}\left(\eta_{DC}\right)\right]\frac{\mathcal{E}_{AC}}{\mathcal{E}_{DC}} \tag{2.32}$$

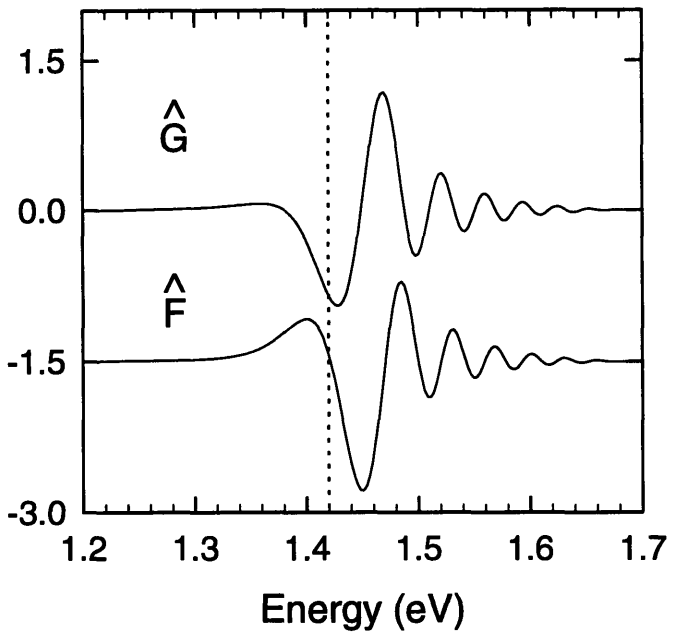

Figure 2-5: Functions $\hat{F}$ and $\hat{G}$ used for spectra obtained by modulating an existing electric field.

which is similar to Eq.2.28, but with two new functions defined by

$$\begin{aligned} \hat{F}(\eta) &= \frac{\pi}{3}\left[\mathrm{Ai}'^{2}(\eta) + \eta\,\mathrm{Ai}^{2}(\eta)\right] \\ \hat{G}(\eta) &= \frac{\pi}{3}\left[\mathrm{Ai}'(\eta)\,\mathrm{Bi}'(\eta) + \eta\,\mathrm{Ai}(\eta)\,\mathrm{Bi}(\eta)\right]. \end{aligned} \tag{2.33}$$

These functions are plotted in figure 2-5. The energy scale has been explicitly evaluated to correspond to the GaAs bandedge ($E_g = 1.42$ eV, $\mu^* = 0.067m_0$). The functions have been convolved with a Lorentzian broadening factor of width k_BT =26 meV and $\hbar\theta$ was chosen equal to k_BT, which implies an electric field equal to 5.5×10^4 V/cm.

The changes in the dielectric constant predicted by Eq.2.28 are a complicated non-linear function of the electric field strength. The theory outlined here is a non-perturbative solution relying only on the effective mass approximation, which is valid as long as the potential due to

the electric field varies slowly over a unit cell. The induced changes in the optical properties of the affected transitions can be quite large. In GaAs, fields on the order of 10^5V/cm can result in reflectivity changes of a few percent. This may seem to be a weak perturbation, but it is only because the index of refraction of GaAs near the bandedge is large (~ 3.4) and is mostly due to higher energy transitions in the near UV region. For GaAs at $\sim$1.42 eV, $\Delta R/R \simeq .38\Delta n$.Thus, only a 4% change in reflectivity is caused by an index change of 0.1. Considering that the near band edge states affected by the field contribute only about 0.1 to the index, the relative changes caused by the field are on the order of unity.

For small fields in a wide bandgap material ($\hbar\omega < E_g$ and $\hbar\theta < E_g$ which implies $\eta \to \infty$), $G(\eta) \sim \eta^{-5/2}$. This means that $\Delta\varepsilon_1 \sim (\hbar\theta)^3$ or $\mathcal{E}^2$. This is the DC Kerr effect, an index change proportional to the square of the field. Note, this result is quoted by Aspnes in Ref. [44]. An attempt to verify this result using asymptotic forms from Antosieswicz [48] yielded the result $G(\eta) \sim \eta^{-1}$ and $\Delta\varepsilon_1 \sim (\hbar\theta)^{3/2}$ which is linear in $\mathcal{E}$. Either the form quoted by Antosiewicz for $\mathrm{Bi}'(z)$ for large z is incorrect, or Aspnes has neglected this leading, linear term (representing the linear $\chi^{(2)}$ electro-optic effect) because it is of more complicated symmetry than the quadratic term. The symmetry for these near band gap contributions, however, appears to be the same as for the optical absorption. Perhaps $\chi^{(2)}$ processes are dominated by higher lying transitions of lower symmetry (m3 point group), and this calculation is only relevant for the quadratic Kerr effect.

Now that the dielectric constant is known, it remains to calculate its effect on the reflectivity. The linear reflection coefficient at normal incidence on a material surface is given by

$$R = \left|\frac{K - K_0}{K + K_0}\right|^2 \tag{2.34}$$

where K and K_0 are the light propagation wavevectors in the material and in free space, respectively. K_0 is assumed to be real, while K may be complex to allow for material absorption. The changes in the reflectivity are expressed in terms of the Seraphin coefficients [31]

$$\frac{\Delta R}{R} = \alpha\Delta\varepsilon_1 + \beta\Delta\varepsilon_2 \tag{2.35}$$

where

$$\alpha = \frac{2n_0 n\left[n^2 - 3k^2 - n_0^2\right]}{\left[(n+n_0)^2 + k^2\right]\left[(n-n_0)^2 + k^2\right]\left[n^2 + k^2\right]} \tag{2.36}$$
$$\beta = \frac{2n_0 k\left[3n^2 - k^2 - n_0^2\right]}{\left[(n+n_0)^2 + k^2\right]\left[(n-n_0)^2 + k^2\right]\left[n^2 + k^2\right]}.$$

n and k refer to the real and complex parts of the material index of refraction defined by $\sqrt{\varepsilon} = \sqrt{\varepsilon_1 + i\varepsilon_2} = n + ik$. The coefficient α defined here is not to be confused with the absorption coefficient for optical intensity, α_0,

$$\alpha_0(abs) = \frac{4\pi k}{\lambda} = \frac{2\pi\varepsilon_2}{\lambda n}. \tag{2.37}$$

Both Seraphin coefficients, α and β, are functions of photon energy for a material. Near the bandedge of most semiconductors $n >> k$, so that the reflectivity changes are dominated by $\Delta\varepsilon_1$, the real part of the dielectric constant. This is, again, due to the fact that absorption on higher energy transitions, with very large densities of states, can make significant contributions to the real part of the dielectric constant far away from resonance due to the slow roll-off of the ω^{-1}factor in the Kramers-Kronig integral. Note that $\beta = 0$ for $k = 0$. These expressions apply for a uniform perturbation of the dielectric constant in space throughout the medium. When the perturbations are restricted to regions near the surface on the order of a wavelength, significant modifications such as mixing of the real and imaginary components of the dielectric constants can occur. These issues will be dealt with at the end of this chapter.

2.4 Methods of ER spectroscopy

In the early days of ER spectroscopy, when the goal was bandstructure determination, electrode pads were formed on the sample in either a transverse ($\vec{\mathcal{E}}$ parallel to the surface) or longitudinal ($\vec{\mathcal{E}}$ perpendicular to the surface) geometry [31]. The electric field in the sample, being externally applied, was either known or irrelevant. The major interest was in figuring out symmetries of the effective mass tensors and energies of critical points [39]. The goal here is to modulate built-in DC fields with small AC external fields and extract the DC electric field magnitudes from the modulation spectra through $\hbar\theta$. The two techniques that are of interest, here, are contactless

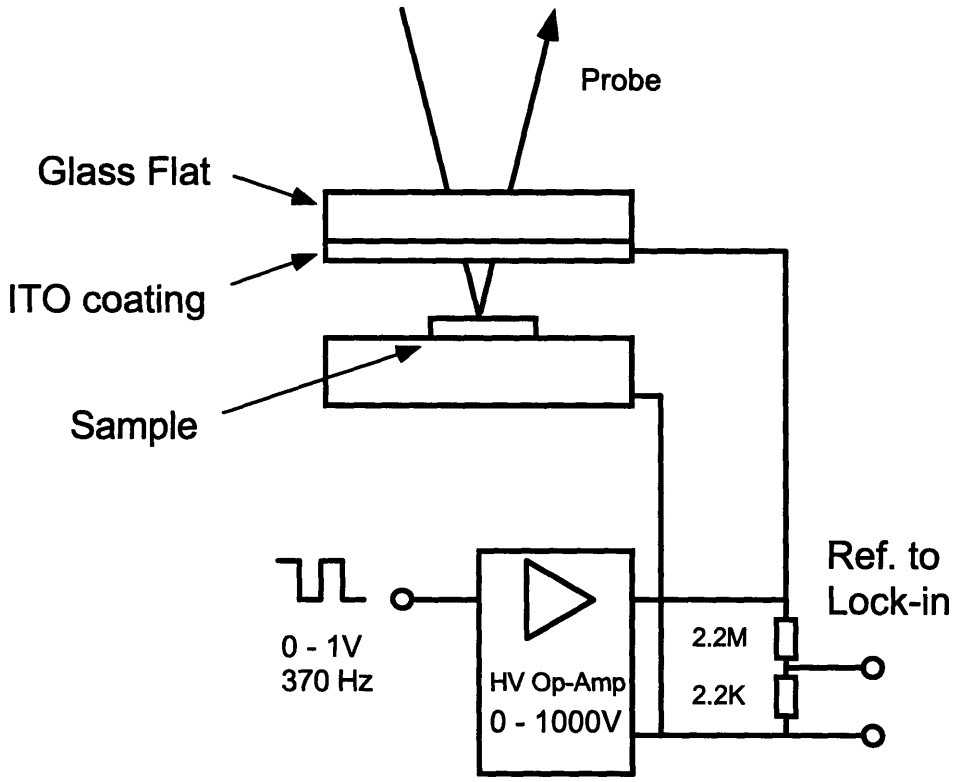

Figure 2-6: CER set-up.

electroreflectance (CER) [49] and photoreflectance (PR) [35]. Neither of these methods require forming of electrical contacts and both are used in a longitudinal configuration, so they are ideal for characterizing interface electric fields.

CER is the more straightforward of the two techniques, and it will be discussed first. Figure 2-6 shows the basic set-up. The sample is simply placed between two electrode plates. The top electrode is a glass flat with a transparent conductive coating on one side such as indium-tin-oxide (ITO). The plates are brought together as close as possible without making contact or causing arcing. A high voltage amplifier is used to drive a several hundred volt square wave at a few hundred Hz across the plates. With a plate separation on the order of 1mm, fields on the order of 1kV/cm to 10kV/cm can be created in the material. A probe beam from a white light source such as a tungsten lamp filtered though a monochromator is bounced off the sample through the top plate to monitor the reflectivity modulation.

The major advantage of CER is that because the direction of the modulating field is known,

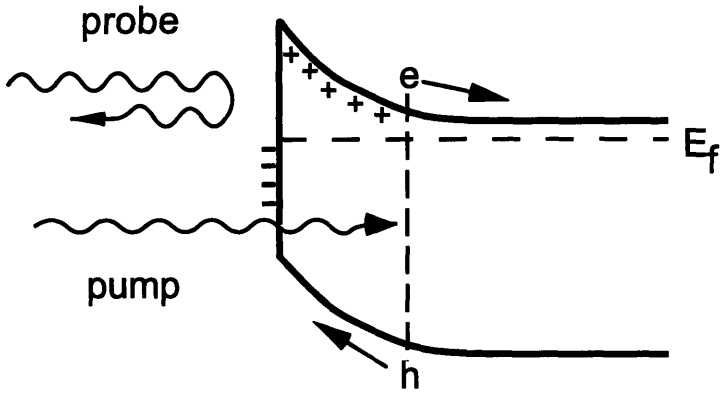

Figure 2-7: Mechansim of PR. Photo-generated minority carriers screen surface fiel due to trapped majority carriers.

the sign of the built-in field can be determined. The F and G functions shown in Fig.2-3 give $\Delta\varepsilon$ for an increase in the electric field. In principle, by observing the sign of the modulated reflectivity spectrum in relation to these functions, it is possible to infer whether the AC field is increasing or decreasing the total electric field strength in the material. Because $\Delta R/R$ is very small, lock-in detection is used on the signal coming from the probe detector. Phase shifts in the high voltage amplifier and the probe detector circuit can therefore lead to errors in the observed sign of the modulation. To avoid these problems, a voltage divider is used to derive a reference signal from the actual voltage applied to the plates and care is taken to ensure that the detector has adequate bandwidth. In practice, sign determination from the observed spectrum is complicated by non-uniform field effects as well as Fabry-Perot interferences from different layers in thin film structures. However, when used with photoreflectance, these extra sign flips can be easily taken into account as will be shown in the next section and Chapter 3.

In photoreflectance, a low intensity laser is used to alter the band bending at semiconductor surfaces. Figure 2-7 shows the band diagram of an N-type semiconductor near the surface. Surface states trap electrons creating a negative surface charge, and therefore a surface electric field which is screened at some distance into the bulk material. Photo-generated minority carriers (holes) are drawn to the surface where they combine with the trapped electrons. This

reduces the surface charge, and therefore the surface field. The changes in the electric field are detected by the probe just as in the CER technique.

This explanation for the mechanism for PR can be supported by some simple calculations and experimental observations. It might, at first, be supposed that free electron-hole pairs created by the pump could cause the probe modulation either through field screening due to free carriers or by entirely different physical processes such as changes in the plasma frequency or Fermi level (bandfilling). For absorption lengths of $\sim 1\mu m$, and carrier lifetimes of $\sim$1 ns appropriate for a good quality direct bandgap semiconductor, and pump intensities of 1 mW/cm^2 at a photon energy of 1.6 eV, a photogenerated carrier density of only about $10^{11}cm^{-3}$ is achieved. This density is too low by a factor of a million to cause the typically observed signal sizes through bandfilling or plasma effects. The Debye screening length

$$L_D = \sqrt{\frac{\epsilon_0 \varepsilon kT}{e^2 n}} \tag{2.38}$$

at a carrier density of $10^{11}cm^{-3}$ is about 12 μm which is too long to affect surface fields which may already be screened to within 0.1μm or less of the surface by the background majority carrier doping. For surface traps, however, the lifetime can be a millisecond or even longer which is sufficient to allow the minority carriers to completely cancel the surface charge in some cases. Two experimental observations clearly indicate the mechanism of surface trapping in PR. The first is the pump intensity dependence. At high pump intensities, all of the available traps can be emptied. Beyond this point the surface fields cannot be reduced further and the probe signal saturates as in the right plot of Fig. 2-8. The left plot in Fig. 2-8 shows a typical dependence of the PR signal on chopping frequency. The signal has a first order roll-off at about 200 Hz which demonstrates the extremely long lifetimes of surface traps compared to bulk recombination processes.

An important feature of the PR method is that the photo-generated carriers produced by the pump always act to reduce the electric fields in the material through screening. Only the magnitude of the interface fields can be determined by PR, unlike CER where the sign of $\Delta R/R$ depends on the direction of the AC field with respect to the built-in DC field. Often, however the extracting the sign of the surface charge from the sign of a CER trace is complicated as

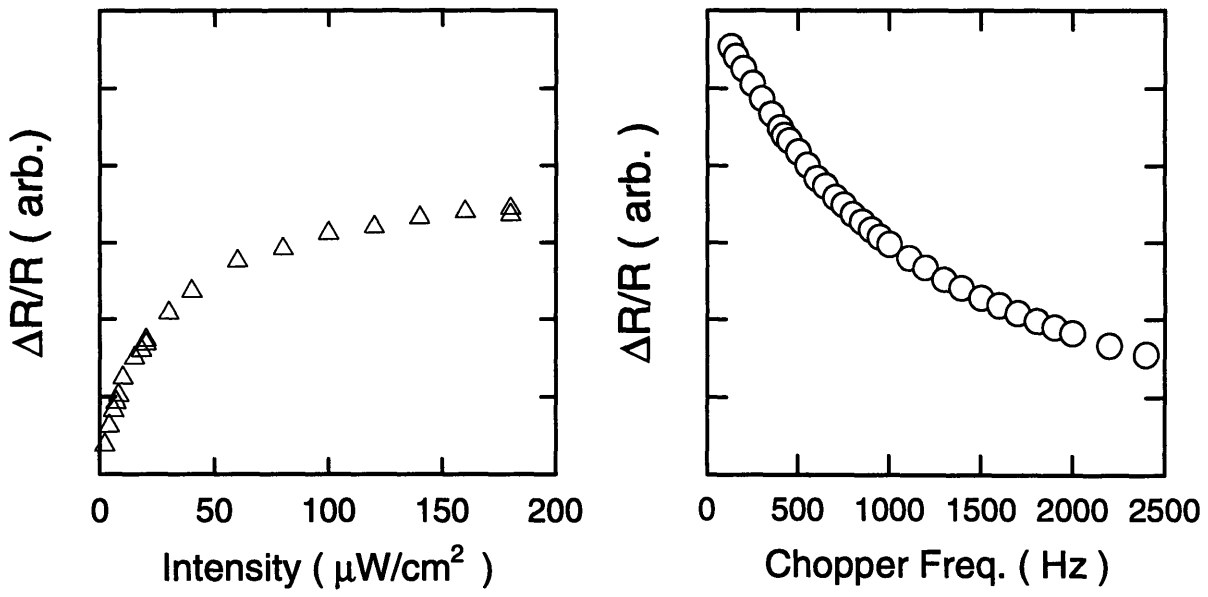

Figure 2-8: Typical intensity (right plot) and chopping frequency (left plot) dependence for PR signals.

discussed above. By comparing the CER trace to a PR trace, the direction for which the AC field opposes the DC field can be found. Another advantage of PR is that it can be used to selectively excite one material in a structure by proper choice of pump photon energy. This idea is pursued in Chapter 4 where PR is used as a new technique for measuring conduction band offsets.

2.5 Example ER spectra

Figure 2-9 shows PR and CER spectra taken for a Si doped (n-type) GaAs substrate. The band bending in this case is similar to fig. 2-7 with a negative surface charge due to trapped electrons and a field pointing toward the surface. The top plot shows spectra from the fundamental bandedge at 1.42 eV. The top trace is the PR spectra using a HeNe laser as a pump ($\hbar\omega = 1.95$ eV). Except for the large spike right at the band gap, the spectrum resembles -$\hat{G}$ and is consistent with the pump laser decreasing the surface field. The CER spectrum is almost identical to the PR spectrum showing that PR is indeed a form of ER. With the positive lead from the HV amplifier connected to the top, transparent electrode and a 0-700V square wave applied, the

AC field points into the sample and opposes the built-in field. The excitation, in this case, acts to reduce the DC field, and, therefore the spectrum has the same sign as the PR trace. This correspondence is observed for the E_1 transition as well (bottom plot). By fitting the observed lineshape to -$\hat{G}$, the magnitude of the field was found to be 3×10^4V/cm.

The negative spike seen at the bandedge is attributed, in the PR literature, to excitonic effects [50]. The Coulomb potential leading to a bound electron-hole pair states was not included in the Hamiltonian (Eq. 2.12) used to derive the electro-optic functions. Excitons states are susceptible to electric fields, however, and will cause modification of the samples optical properties. Because the exciton wavefunction is localized in space, its modulation lineshape will be different. Often a first or second derivative of a Gaussian or Lorentzian is observed, but no general analytic theory exists for this case. The binding energy of an exciton in GaAs is only about 4 meV. At room temperature, excitonic features in the linear absorption and reflection spectra are completely washed out due to thermal broadening. The derivative nature of the ER technique allows these weak components to be resolved. Due to this small binding energy, an electric field on the order of 10^3 V/cm needed to ionize the excitons. Throughout most of the space-charge region near the surface of the sample the exciton states are destroyed. At a certain distance into the bulk, the surface fields will be screened sufficiently to allow them to exist. Interference between light reflected from this region and the rest of the space charge region causes additional complications in unraveling the exitonic spectra [51]. Fortunately, these exciton signals are limited to the bandedge and contribute relatively less at high surface fields.

Figure 2-10 shows a nice example of a spectrum exhibiting many Franz-Keldysh oscillations. This trace will be used to show an often used method for accurately determining the electric field responsible. The measurement was performed on a ZnSe/GaAs double heterostructure and the spectrum shown is, again, of the GaAs bandedge. From asymptotic expressions for the Airy functions, the following formula can be derived for the positions in energy of the extrema of the oscillations [34] :

$$m\pi = \phi + \frac{4}{3}\left(\frac{\hbar\omega_m - E_g}{\hbar\theta}\right)^{3/2}. \tag{2.39}$$

Here, m=1,2,3...is an index for the extrema, ϕ is an arbitrary phase factor, and $\hbar\omega_m$ is the energy of the mth extrema. By plotting $\frac{4}{3\pi}(\hbar\omega_m - E_g)^{3/2}$as a function of m and determining

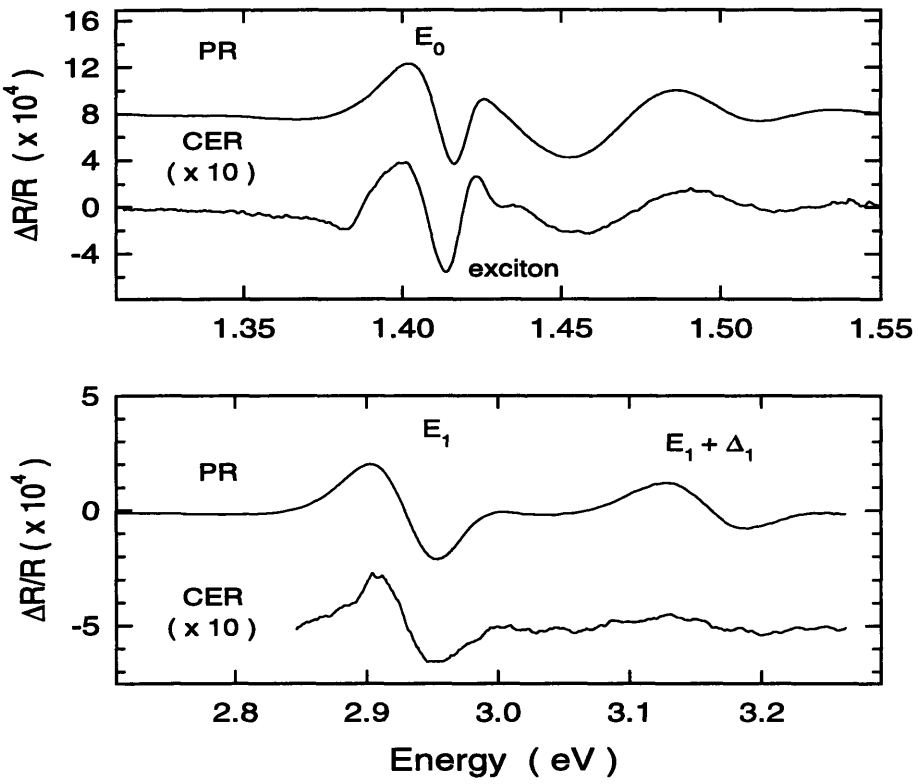

Figure 2-9: PR and CER spectra for an n-type GaAs surface. Top: Bandgap signal, type M_0. Bottom: E_1 transitions, type M_1.

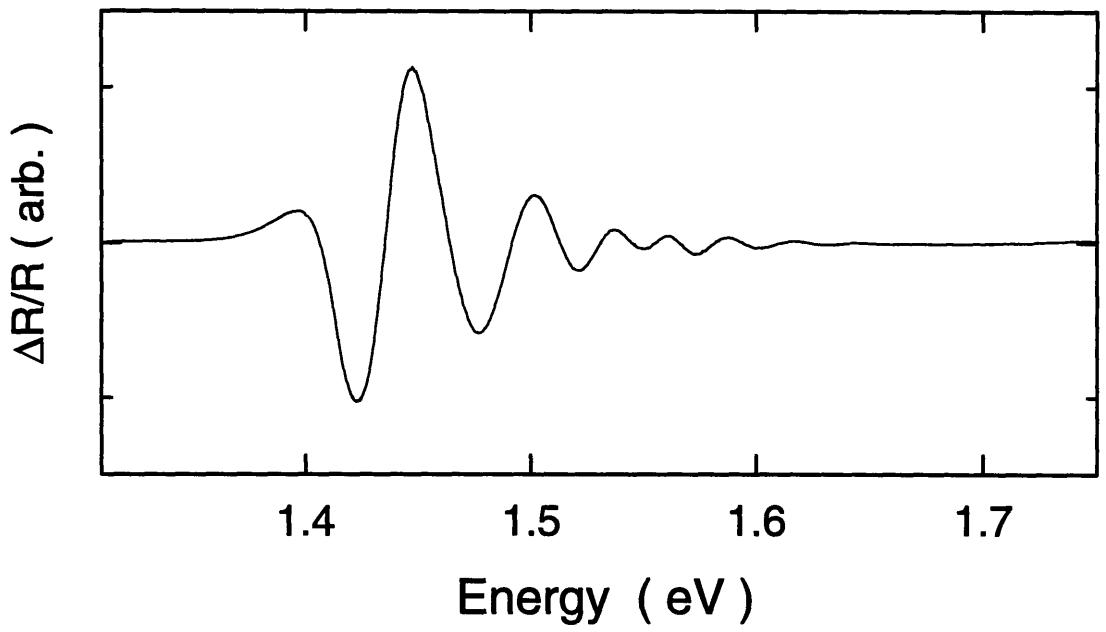

Figure 2-10: PR spectra exhibiting Franz-Keldysh oscillations.

the slope via a least squares fit, $\hbar\theta$ and, thus, the electric field can be obtained. This procedure is plotted in figure 2-11 and the field is found to be 7.5×10^4 V/cm.

2.6 Non-uniform field effects

The expression given in Eq. 2.35 for the reflectivity change assumes a spatially uniform perturbation of the dielectric constant, i. e. the value of the bulk dielectric constant is assumed to be only slightly changed. Often the changes in the dielectric constant occur only in a narrow region near the surface which can be much smaller than a wavelength in the material. This situation is sketched in Fig. 2- 2, showing the spatial variation of the dielectric constant at a surface. The modifications to the reflection coefficient, in this case, include phase changes in the reflected light due to mixing of the real and imaginary parts of the sample response and a spatial average over the dielectric constant perturbation. Both of these modifications are important since they affect the lineshape of the observed modulation spectrum and will impact determination of the magnitude and sign of the interface electric fields. The solution of this problem was first presented by Aspnes and Frova , and their derivation will be briefly outlined

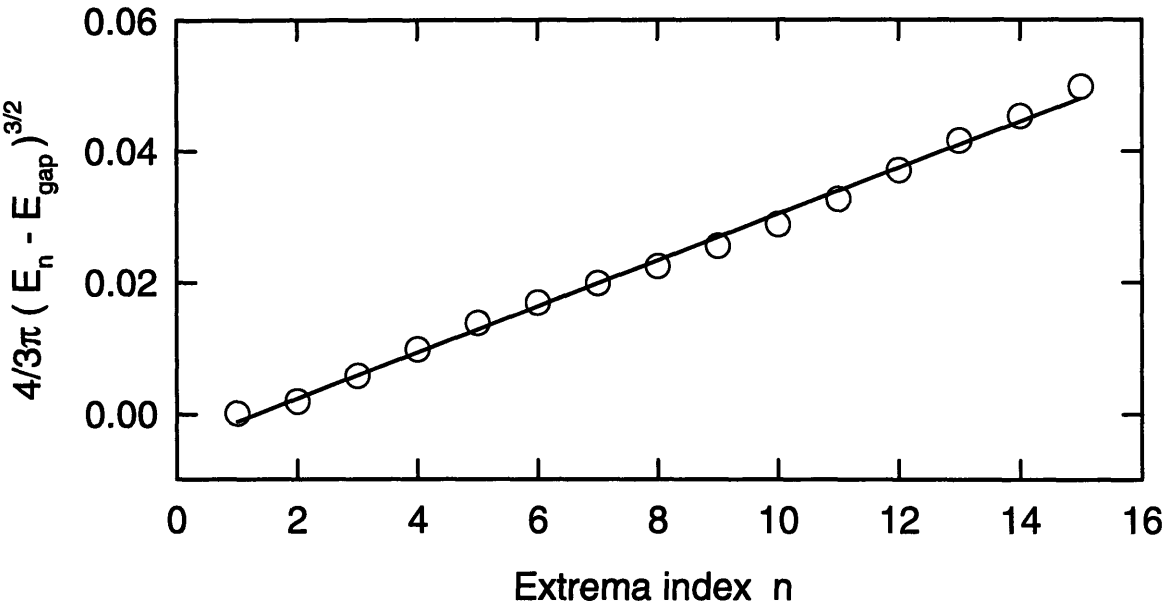

Figure 2-11: Plot of extrema indices to determine $\hbar\theta$ from FK oscillations.

here for reference.

To account for spatial variation in $\Delta\varepsilon$, the wave equation for the propagation of the optical field in the material must be solved

$$\nabla^2\mathcal{E} + \frac{\omega^2}{c^2}\left[\varepsilon + \Delta\varepsilon\left(x\right)\right]\mathcal{E} = 0. \tag{2.40}$$

The solid is assumed to extend from $x = 0$ to $x = +\infty$. In the spirit of the WKB approximation, a trial solution for the wave propagating in the positive x direction of the form

$$\mathcal{E} = \mathcal{E}_0 \exp\left(ikx + i\phi\left(x\right)\right). \tag{2.41}$$

When this solution is plugged into the wave equation, an equation for $\phi'\left(x\right)$ is found

$$i\phi'' + 2k\phi' - \phi'^2 = -\tfrac{\omega^2}{c^2}\Delta\varepsilon. \tag{2.42}$$

The prime denotes differentiation with respect to x. Since ϕ arises from $\Delta\varepsilon$, the third term on the left hand side, ϕ'^2, is of second order and will be neglected. Eq. 2.42 can then be solved for

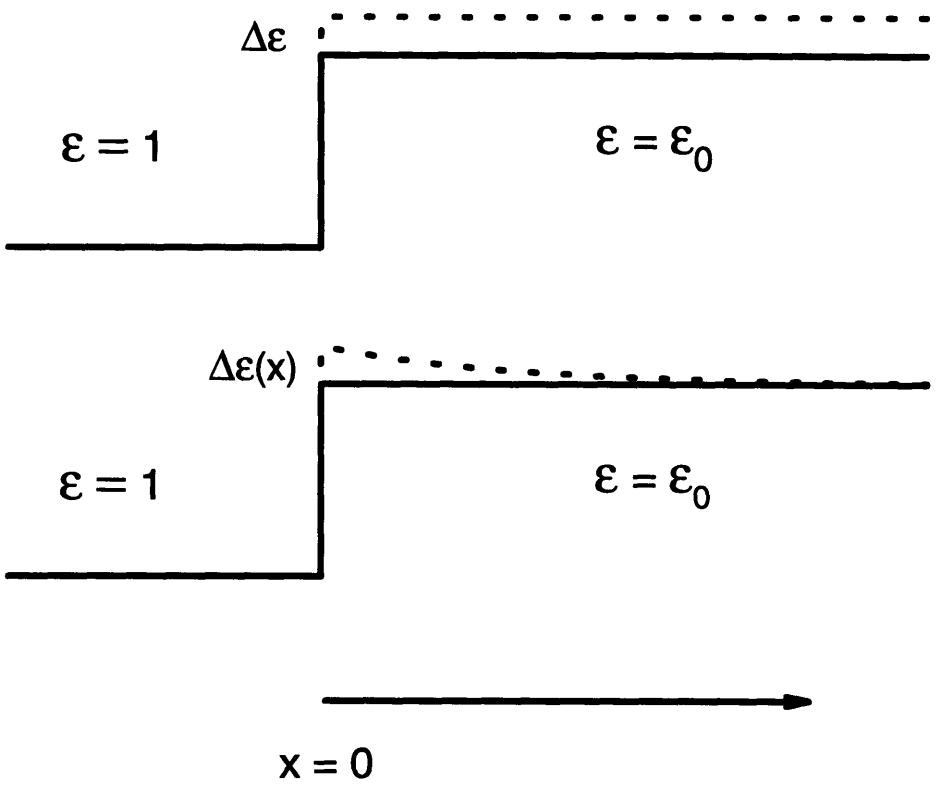

Figure 2-12: Dielectric discontinuity at a material surface. Dashed lines show the induced pertubation to the dielectric constant in the uniform (top plot), and non-uniform cases (bottom plot).

ϕ' as

$$\phi'(x) = -\frac{ik^2}{\varepsilon}\int_x^\infty \Delta\varepsilon(x')\, e^{2ik(x'-x)}dx' \tag{2.43}$$

which can be verified by direct substitution. Now, ϕ' is a modification of the propagation wavevector k. Therefore, the reflectivity is

$$R = \left|\frac{k+\phi'(x=0)-k_0}{k+\phi'(x=0)+k_0}\right|^2 \tag{2.44}$$

where k_0 is the propagation constant of the ambient material ($x < 0$). This equation is the same as Eq.2.34. From this expression, relative changes in the reflectivity are obtained in exactly the same manner as for the bulk case,

$$\frac{\Delta R}{R} = \alpha\langle\Delta\varepsilon_1\rangle + \beta\langle\Delta\varepsilon_2\rangle, \tag{2.45}$$

where the Seraphin coefficients are the same as before, and the spatially averaged change in the dielectric constant is given by

$$\langle\Delta\varepsilon\rangle = -2ik\int_0^\infty \Delta\varepsilon(x)\, e^{2ikx}dx. \tag{2.46}$$

$\langle\Delta\varepsilon\rangle$ reduces to $\Delta\varepsilon$ when $\Delta\varepsilon$ is independent of x. The $-2ik$ and exponential factor cause a mixing of the real and imaginary parts of the sample response. This is most evident when $\Delta\varepsilon$ is limited to a distance W from the surface such that $2kW \ll 1$ with k real:

$$\langle\Delta\varepsilon\rangle = -2ik\int_0^W \Delta\varepsilon(x)\, dx. \tag{2.47}$$

Here, the real and imaginary parts of $\Delta\varepsilon$ have completely changed roles. Note also that the reflectivity will be determined by the spatially averaged perturbation.

The Eq. 2.46 is valid for any spatially localized change in the dielectric constant and is therefore completely general. Some of the consequences for ER measurements will be described next. At the fundamental gap of most semiconductors, $\alpha \gg \beta$ and the reflection changes are controlled mainly by the real part of the dielectric response of the sample. Eq. 2.46 shows that as the electric field in the material becomes limited to the surface due to screening, the

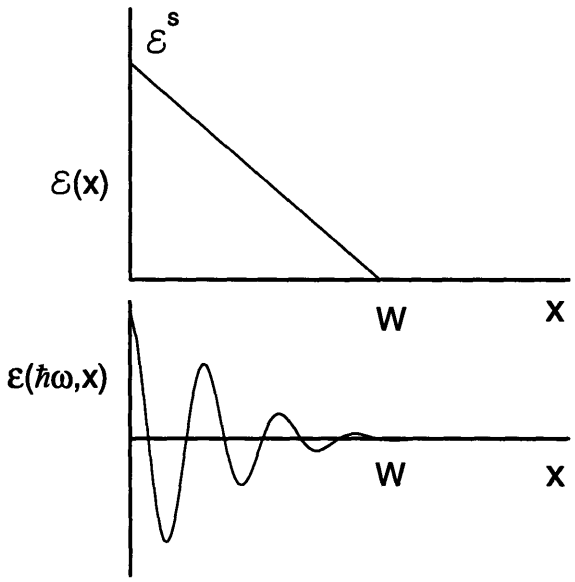

Figure 2-13: Top diagram: electric field vs. distance in the depletion region. Bottom diagram: $\Delta\varepsilon\left(\hbar\omega\right)$ depends on distance through the electric field dependence of the electro-optic functions. Spatial averging causes damping of higher energy FK oscillations.

spectrum of $\Delta R/R$ will be described by a combination of both the electro-optic functions G and F. The spatial averaging inherent in the integration over the perturbation also leads to damping of the Franz-Keldysh oscillations. The top diagram in 2-13 shows the electric field near a semiconductor surface due to a surface charge when the depletion approximation (discussed further below) holds. The bottom picture shows the spatial dependence of $\Delta\varepsilon$ at a given probe energy, $\hbar\omega$. The spectral FK oscillations are mapped onto the spatial coordinate through the spatially varying electric field, $\mathcal{E}\left(x\right)$, which appears in the argument of the electro-optic functions in Eq. 2.28. If the probe energy is sufficiently far above the bandedge so that G and F have made several spectral oscillations, $\Delta\varepsilon\left(\hbar\omega,\mathcal{E}\left(x\right)\right)$will oscillate rapidly in space, and integrating over x will lead to cancellations that reduce $\langle\cdot\varepsilon\rangle$. Thus, nonuniform fields lead to damping of the spectral Franz-Keldysh oscillations even when $\hbar\theta > \Gamma$.

These conclusions apply for the case of modulation from flat-band:

$$\Delta\varepsilon\left(\hbar\omega,\mathcal{E}\right)=\varepsilon\left(\hbar\omega,\mathcal{E}\right)-\varepsilon\left(\hbar\omega,0\right). \tag{2.48}$$

In the case of modulation of a large built-in DC field, the quantity of interest is

$$\Delta\varepsilon\left(\hbar\omega, \mathcal{E}_{DC}, \mathcal{E}_{AC}\right) = \varepsilon\left(\hbar\omega, \mathcal{E}_{DC}+\mathcal{E}_{AC}\right) - \varepsilon\left(\hbar\omega, \mathcal{E}_{DC}-\mathcal{E}_{AC}\right), \tag{2.49}$$

and the situation is a little more complex. The evaluation of Eq. 2.49 outlined next essentially parallels that found in Ref. [52].

At the surface of a semiconductor, the electric field in the space charge region is given by Poisson's equation,

$$\nabla \cdot \mathcal{E} = \frac{\rho}{\varepsilon_0}, \tag{2.50}$$

where, in the depletion approximation, $\rho = e\left[N_d - N_a\right]$. N_d and N_a are the donor and acceptor concentrations in the material. The surface charge, σ, is accounted for as a boundary condition on $\mathcal{E}(x)$ at the surface by $\mathcal{E}(x=0) = \mathcal{E}^s = \frac{\sigma}{\varepsilon_0}$. The electric field is then given by

$$\mathcal{E}(x) = \mathcal{E}^s\left[\frac{W-x}{W}\right] \tag{2.51}$$

with the depletion width, $W = \sigma/\rho$ simply determined by charge balance. Applying $\mathcal{E}_{AC}$ will change both the surface field and the depletion width slightly. Evaluating Eq. 2.49 using Eq. 2.46 and $\mathcal{E}(x)$ above results in

$$\left\langle \Delta\varepsilon\left(\hbar\omega, \mathcal{E}_{DC}, \mathcal{E}_{AC}\right)\right\rangle =$$

$$-2ik\left[\int_0^{W+\Delta W} \Delta\varepsilon\left(\hbar\omega, \mathcal{E}\left(x-\Delta W\right)\right) e^{i2kx} dx\right.$$

$$\left. - \int_0^{W-\Delta W} \Delta\varepsilon\left(\hbar\omega, \mathcal{E}\left(x+\Delta W\right)\right) e^{i2kx} dx\right] \tag{2.52}$$

where the electric field spatial dependence is given by the functional form in Eq.2.51 and $W+\Delta W$ and $W-\Delta W$ are the depletion widths for surface fields of $\mathcal{E}^s_{DC}+\mathcal{E}^s_{AC}$ and $\mathcal{E}^s_{DC}-\mathcal{E}^s_{AC}$,

respectively. Changing variables, Eq. 2.52 becomes

$$\begin{aligned}\langle \Delta\varepsilon\left(\hbar\omega, \mathcal{E}_{DC}, \mathcal{E}_{AC}\right)\rangle \;=\; & \\ & -2ike^{2ik\Delta W}\left[\int_{-\Delta W}^{W}\Delta\varepsilon\left(\hbar\omega,\mathcal{E}\left(x\right)\right)e^{i2kx}dx\right. \\ & \left.-\,e^{-4ik\Delta W}\int_{\Delta W}^{W}\Delta\varepsilon\left(\hbar\omega,\mathcal{E}\left(x\right)\right)e^{i2kx}dx\right].\end{aligned} \tag{2.53}$$

Now the approximation $k\Delta W \ll 1$ is made and terms of order ΔW^2 are neglected to get

$$\begin{aligned}\Delta\varepsilon\left(\hbar\omega, \mathcal{E}_{DC}, \mathcal{E}_{AC}\right) \;=\; & \\ & -2ik\left[\int_{-\Delta W}^{\Delta W}\Delta\varepsilon\left(\hbar\omega,\mathcal{E}\left(x\right)\right)e^{i2kx}dx\right. \\ & \left.-\,4ik\Delta W\int_{0}^{W}\Delta\varepsilon\left(\hbar\omega,\mathcal{E}\left(x\right)\right)e^{i2kx}dx\right].\end{aligned} \tag{2.54}$$

Next, some quantities normalized to the surface electric field are defined

$$\begin{aligned}\chi &= \mathcal{E}/\mathcal{E}^s_{DC} \\ x &= W(1-\chi) \\ \eta^s_{DC} &= \left(E_g-\hbar\omega\right)/\hbar\theta^s_{DC} \\ \left(\hbar\theta^s_{DC}\right)^3 &= e^2\left(\mathcal{E}^s_{DC}\right)^2\hbar^2/2\mu^* \\ \xi &= \mathcal{E}^s_{AC}/\mathcal{E}^s_{DC} = \Delta W/W.\end{aligned} \tag{2.55}$$

Additionally, to absorb some of the factors in Eq. 2.28, the constant

$$B = \frac{2e^2\hbar^2}{m^*}\left|\hat{\epsilon}\cdot\mathbf{P}_{cv}\right|^2\left(\frac{2\mu^*}{\hbar^2}\right)^{\frac{3}{2}} \tag{2.56}$$

is defined. Finally, the integration variable is changed from space to electric field via the linear

relation 2.51:

$$\langle \Delta\varepsilon\left(\hbar\omega, \mathcal{E}_{DC}, \mathcal{E}_{AC}\right)\rangle = -4ikB\frac{\varepsilon_0}{\rho}\frac{\left(\hbar\theta^s_{DC}\right)^{1/2}}{(\hbar\omega)^2}\mathcal{E}^s_{AC} \times \left[\frac{1}{2\xi}\int_{1-\xi}^{1+\xi}\chi^{1/3}\left(G\left(\frac{\eta^s_{DC}}{\chi^{2/3}}\right)+iF\left(\frac{\eta^s_{DC}}{\chi^{2/3}}\right)\right)e^{i2kW(1-\chi)}d\chi\right.$$

$$\left. + 2ikW\int_0^1\chi^{1/3}\left(G\left(\frac{\eta^s_{DC}}{\chi^{2/3}}\right)+iF\left(\frac{\eta^s_{DC}}{\chi^{2/3}}\right)\right)e^{i2kW(1-\chi)}d\chi\right]. \quad (2.57)$$

The response is composed of two parts. The first integral is the 'surface' term, and the second is the 'average' term. A physical interpretation of Eq. 2.57 is sketched in Fig. 2-14. Here, the electric field is plotted against distance from the surface for the case when the AC field points along, and against the built-in DC field. Eq. 2.46 can be interpreted as dividing up the total dielectric perturbation into 'blocks' and summing them up with the correct phase. The circles in Fig. 2-14 are meant to represent these dielectric blocks. In the case of modulation of a large built-in field considered here, the average dielectric response will be determined by the difference between the field arrangement with the AC field positive and negative. In Eq. 2.57, the spatial sum is converted to a sum over electric field values. Up to a field value of about $\mathcal{E}^s_{DC}$ (for $\mathcal{E}^s_{AC}$ small), each value of the electric field occurs when the AC field points towards or away from the surface. The only difference is the distance from the surface where each value occurs. These 'blocks' or 'slabs' of dielectric are account for in the 'average' term. Thus, the AC field can be thought of as moving the dielectric blocks closer to or further from the surface. The resulting phase changes are the origin of the $2ikW$ factor in the second integral of Eq. 2.57 which undoes the complex factor originally introduced in Eq. 2.46. The integration over all field values down to zero will cause damping of the higher energy FK oscillations. As $2kW$ becomes large, this term will dominate over the first term. At very large $2kW$, the exponential factor in the integral will result in cancellation everywhere except very near the surface, thus yielding the simple uniform field result of Eq. 2.28.

The first term in Eq. 2.57 is the result of integrating over the left over white circles in Fig. 2-14. These values of the electric field occur only when the AC field adds to the DC field and only very near the surface. Therefore, these blocks will have their real and imaginary parts switched as in Eq. 2.46. Since the electric field varies little in this region, the first term simply

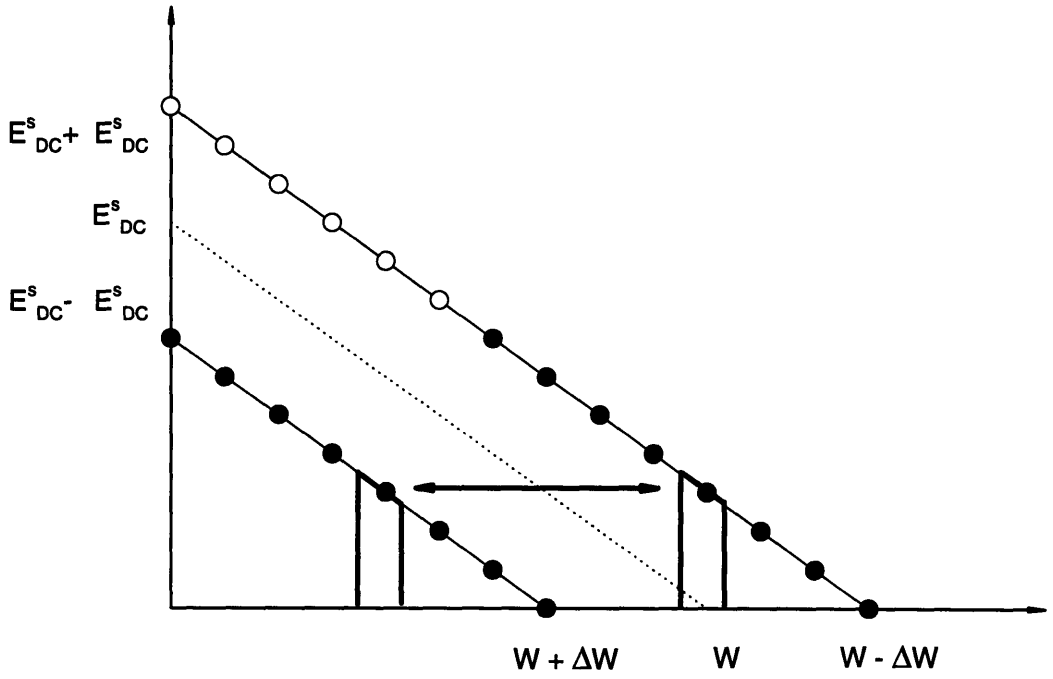

Figure 2-14: A physical interpretation of the calculation of surface effects in modulation as described in the text. The circles represent 'slabs' of dielectric which are summed, taking into account the proper optical phase, to give the total average dielectric response. The filled circles correspond to the 'bulk' term. As the AC field is turned on and off, these slabs can be imagined to just translate in space giving a phase change in the response. The open circles represent the 'surface' term. These slabs are turned on when the AC field is on are are limited to a region close to the surface.

samples the electric field at the surface. This is why the first integral is called the 'surface' term. If the modulation depth, ξ, becomes large, then some averaging will occur which will cause some damping of FK oscillations. In the limit $2kW \rightarrow 0$ this surface term will dominate, and if $\xi \rightarrow 1$ it will correspond to Eq. 2.47.

An important result of this analysis is that the spectral dependence is controlled by η^s_{DC} in Eq. 2.57. The means that it is the *surface* DC field, and not some average value, that will control the Franz-Keldysh oscillations [50]. This is a fortunate occurrence and is very useful for using ER as a characterization tool.

For heavily doped semiconductors, fields will be screened very close to the surface. For $1 \times 10^{18}\text{cm}^{-3}$ n-type GaAs, the width of the space charge region may be on the order of 300Å for a field of 4×10^5 V/cm yielding a value of $2kW \approx 2$ for wavelengths near the bandedge.

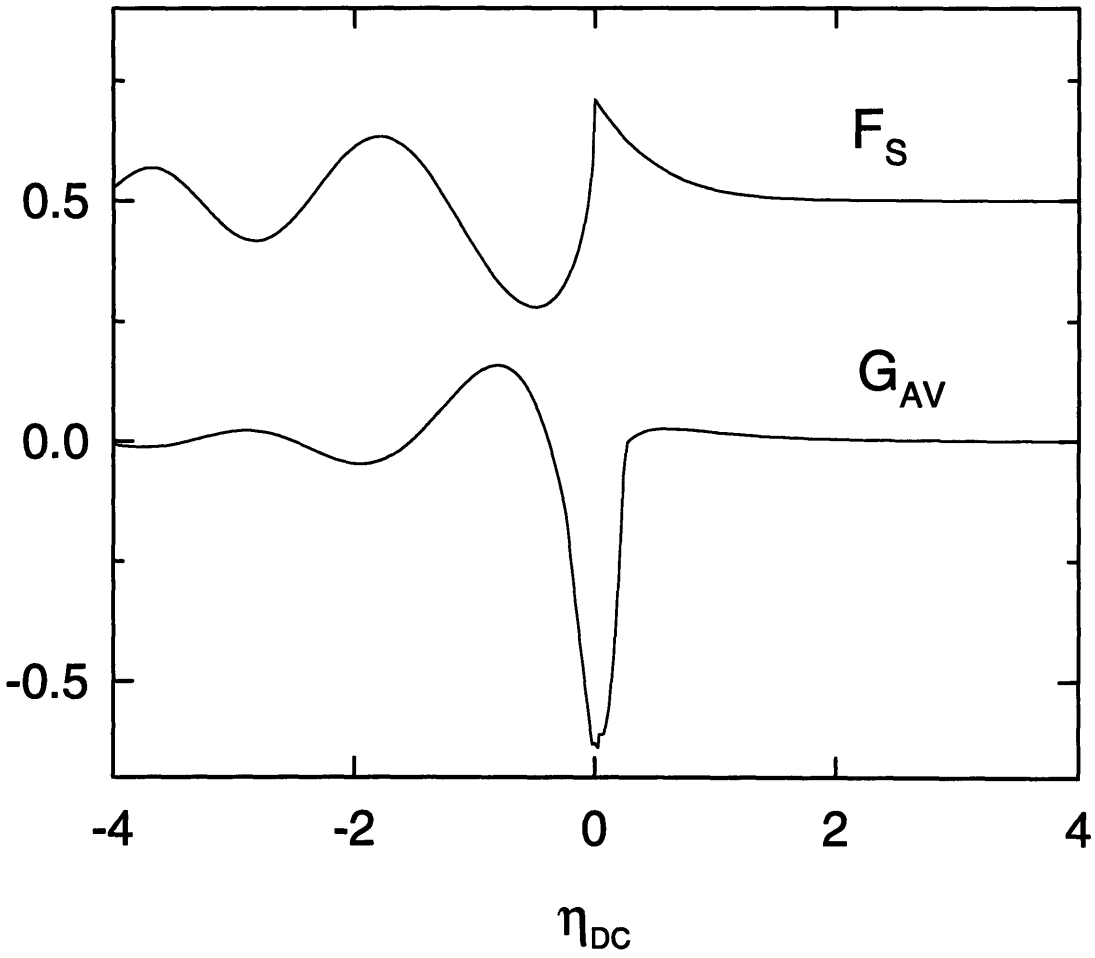

Figure 2-15: Plots of the 'surface' and 'average' lineshape functions contributing to the real part of $\langle \Delta\varepsilon \rangle$. Note how the FK oscillations of the average term, G_{AV}, are damped by the spatial variation.

Both terms in Eq. 2.57 will be significant. Since the Seraphin coefficient $\alpha \gg \beta$, the reflectivity changes will be determined by the real part of $\langle \Delta\varepsilon \rangle$. The spectral dependence of the real part of the first term in Eq. 2.57 is given by F, and will be denoted F_s, while that of the second term is determined by G, and will be called G_{AV}. Figure 2-15 plots these two functions in order to compare their relative sizes. The total modulation spectrum will be given by the sum of these terms. G_{AV} shows significant damping due to spatial averaging. These results will have impact on the lineshape analysis for n-type samples in the next chapter.

2.7 Summary

This chapter has outlined the basic theory of ER spectroscopy with the main goal of explaining the lineshapes of modulation spectra. Critical points and bandstructure were discussed first to explain why ER modulation is observed only near certain energies in semiconductors. The problem of optical absorption in a uniform electric field was solved to introduce the electro-optic functions which determine the dielectric constant and detailed shape of the modulation spectra around the critical point energies. The main feature of these functions are the spectral oscillations called Franz-Keldysh oscillations, whose period can be used to determine the magnitude of the electric field in the material. A careful analysis of surface effects on the lineshapes was also presented. An important result of this analysis is that even if the electric fields show significant variation near the interface, the period of the FK oscillations will be determined by the surface value of the field. Figure 2-16 summarizes the predicted lineshape functions for several experimental conditions that are encountered in ER spectroscopy.

Two experimental techniques, contactless electro-reflectance, CER, and photoreflectance, PR, were introduced and the mechanisms of field modulation were discussed. PR was seen to rely on surface trapping of photo-generated carriers, and the consequences for the power and frequency dependence of the response were briefly considered. These aspects of PR will be important in chapter 5 for explaining the tunable pump PR experiments. The complementary nature of PR and CER and their usefulness in determining the sign of electric fields will be seen more clearly in the next chapter.

	Re($\Delta\varepsilon$)	Im($\Delta\varepsilon$)	Eq. #
uniform field, modulation from flatband	$G(\hbar\omega)$	$F(\hbar\omega)$	3.29
uniform field, modulation of built-in field	$\hat{G}(\hbar\omega)$	$\hat{F}(\hbar\omega)$	3.33
spatially varying field (kW<<1), modulation from flatband	$F(\hbar\omega)$	$G(\hbar\omega)$	3.29 (3.46)
spatially varying field, modulation of built-in field	$F_s(\hbar\omega)$+ $G_{av}(\hbar\omega)$	$G_s(\hbar\omega)$ + $F_{av}(\hbar\omega)$	3.57

Figure 2-16: Lineshape functions in various experimental situations.

Chapter 3

Conventional ER spectroscopy of ZnSe/GaAs heterojunctions

3.1 Introduction

With the general theory of CER and PR spectroscopy outlined in Chapter 2, results for ZnSe/GaAs interfaces will now be presented. The ER experiments and analysis discussed in this chapter are conventional in that the goal is to measure electric fields in the semiconductors using the lineshape functions introduced in the previous chapter. In the next chapter, the PR technique will be used in a new fashion where the pump, rather than the probe, energy dependence of the reflectivity changes will be important.

The experiments will concentrate on the GaAs side of the junction. The magnitude, and especially the sign, of the electric fields at the junction will allow the band bending at the junction to be worked out. Looking at the ER spectra of the ZnSe are of less importance for several reasons. The first is that because thin epitaxial films of ZnSe will be studied, the probe beam will be reflected from the air/ZnSe surface as well as the ZnSe/GaAs interface. Both the imaginary, as well as, the real part of the changes in the ZnSe dielectic constant will affect the measured modulation spectrum. This is not a fundamental problem. With careful characterization of the wavelength dependence of the linear absorption and index, the spectra could be unraveled [53]. Interpretation of the ZnSe spectrum does, however, suffer from more experimental uncertainty than the GaAs spectrum. Second, in finding the minimum energy configuration

of charges, some electrons from the n-type ZnSe will drop into the GaAs (modulation doping) and some will be trapped on surface states at the air/ZnSe surface. The field structure in the ZnSe may not be due only to the heterojunction fields, therefore. Finally, the ZnSe spectra are not as detailed as the GaAs spectra, and do not show FK oscillations. This is because the bandedge of ZnSe is dominated by excitonic effects. The binding energy of excitons in ZnSe is approximately 20 meV, as opposed to 4 meV in GaAs. At room temperature, the effects of Coulomb attraction on the bandedge states is quite significant. Thus, the wavefunctions used in Chapter 2 are not appropriate and FK oscillations do not appear in the same way [54]. These Coulomb effects will appear again in the pump-probe studies of ZnSe presented in Part III.

In any event, the GaAs results provide enough information to distinguish between the qualitatively different pictures of the GaAs/ZnSe junction band bending predicted by the diffusion and trap models. Specifically, large, negative interface charges will be shown to dominate the bending. In Chapter 1, modulation doping effects were shown to result in an effective positive charge due to the donor ions seen by the GaAs side of the junction. This caused the conduction band to bend up, cancelling some of the conduction band potential barrier between the materials due to the conduction band offset. A negative charge results in the bands bending down, increasing the barrier.

The samples studied in these experiments will be described next. Presentation of CER and PR spectra will follow, and will be divided into two parts. The doping of the GaAs side of the junction will be shown to have the most pronounced effect on the junction fields. This is evident in Fig. 3-1 which is shown for comparison. Proper understanding of these spectra requires taking into account different physical details in each situation, and so the n-type and undoped GaAs samples will be discussed in separate sections. At the end of the chapter, the possible origins of the interface charges will be described.

3.2 Sample structures

The ZnSe films examined in these experiments were grown by MBE. Several micron thick GaAs buffer layers were first grown on GaAs substrates to provide good quality, low defect nucleation surfaces for the ZnSe growth. Use of the GaAs buffer layers allowed samples with different

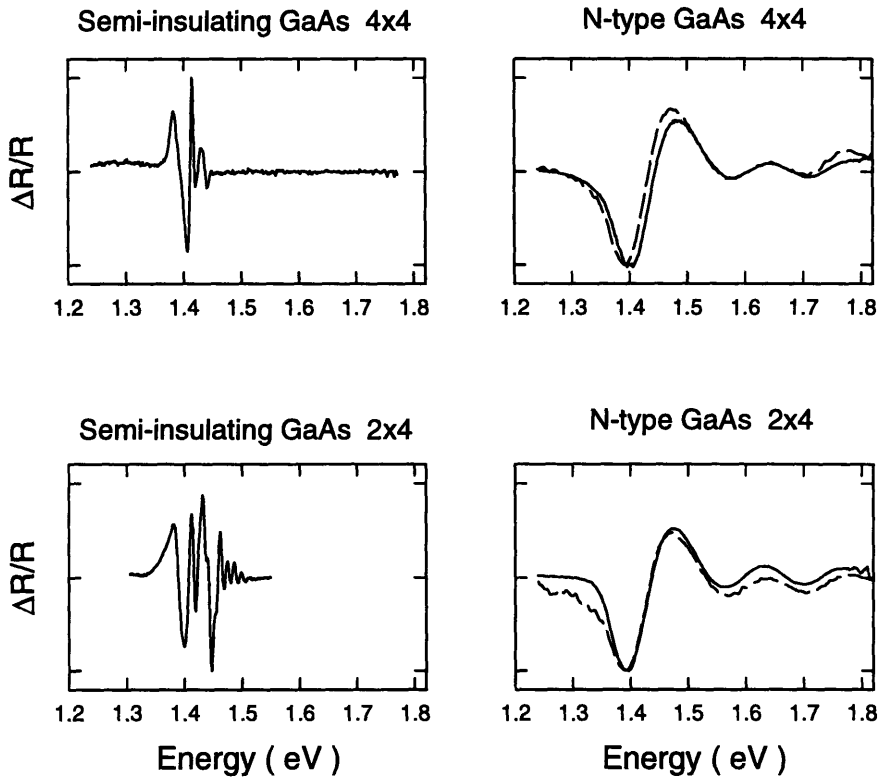

Figure 3-1: CER (dashed lines) and PR (solid lines) spectra of ZnSe/GaAS heterojunctions for different GaAs surface reconstructions and doping.

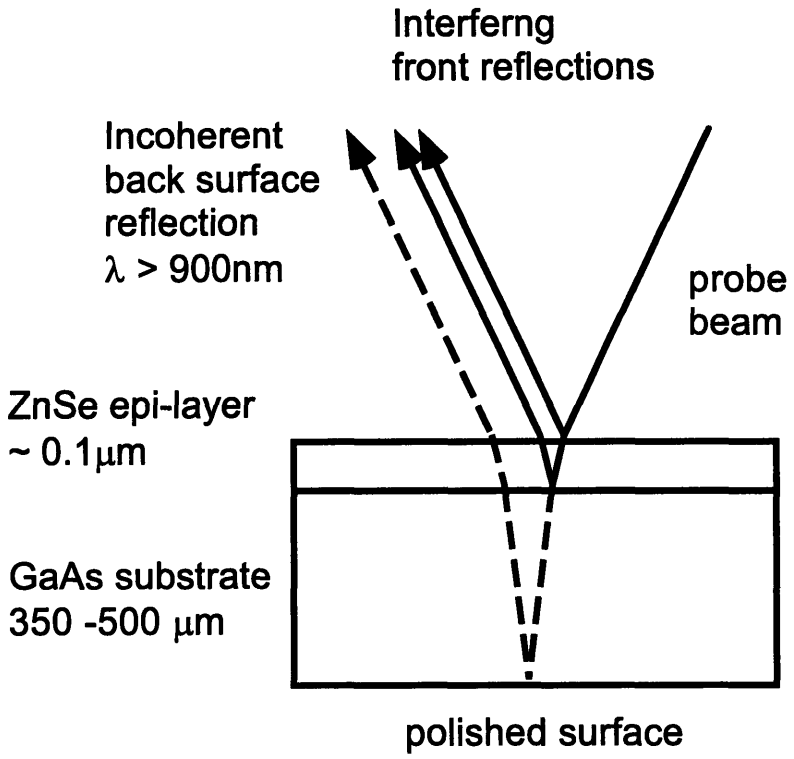

Figure 3-2: Multiple reflections from ZnSe thin film samples.

GaAs surface reconstructions to be fabricated. Proper choice of surface reconstruction has been shown to minimize defects at the interface and lead to better quality films [55]. The ZnSe was left unintentionally doped which results in about 10^{16} cm^{-3} n-type material. The ZnSe layer thicknesses were kept at about 1000Å as a compromise between preventing the ZnSe from relaxing and moving the air/ZnSe surface as far away from the junction as possible. Four main samples will be discussed in this chapter which differ in the GaAs surfaces on which they were grown. The samples are: i44 - semi-insulating GaAs with a 4×4 surface reconstruction, i24 - semi-insulating GaAs with a 2×4 surface reconstruction, and n44 and n24 which are the same as the first two, only with $10^{18}cm^{-3}$ n-type GaAs. The buffer layers and the underlying substrates have the same doping to prevent the formation of another (homo-) junction at the substrate/buffer layer boundary.

The 2.67 eV bandgap of ZnSe means that it is transparent to light at the 1.42 eV bandgap of GaAs. In addition, because ER modulation occurs only near critical points, no signals from

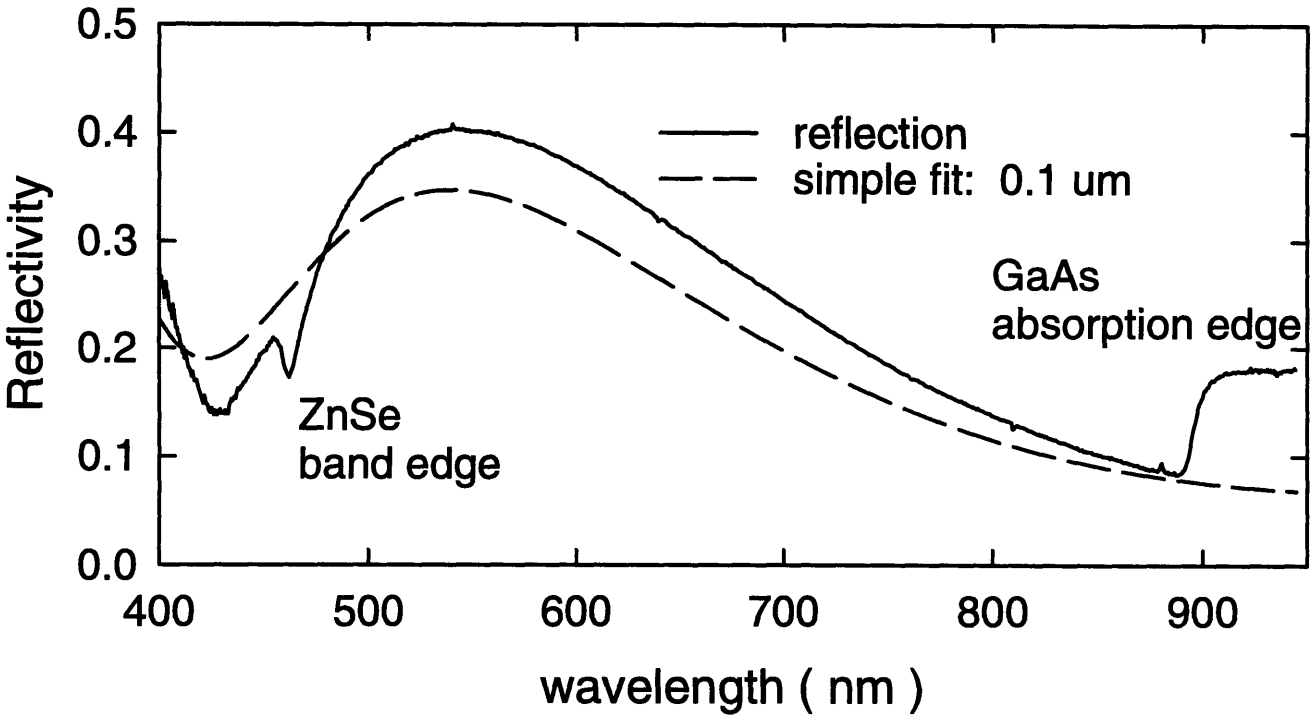

Figure 3-3: Solid line shows the reflectivity of a 1000Å ZnSe thin film. Dashed line is a fit using the Fabry-Perot formula with ZnSe dispersion included.

the ZnSe occur on top of the GaAs modulation spectrum. Studying the GaAs bandgap ER in these samples is thus the same as for bare GaAs surfaces except for one difference shown in Fig. 3-2. The probe will reflect off the air/ZnSe as well as the ZnSe/GaAs interface causing interference. This is evident in the sample reflectivity shown in Fig. 3-3. Near 500 nm, the reflectivity is maximum, indicating that the two reflected fields are in phase. Near 900 nm, the reflectivity is minimum indicating the front and rear reflections are 180° out of phase. This flips the sign of reflectivity changes on the GaAs interface and has to be taken into account in order to determine the direction of the junction electric field by CER. The step in reflectivity near 900 nm is due to light reflected off the back of the 500μm thick GaAs substrate. Because the absorption of the GaAs is very high (10^4 cm^{-1}) at the bandgap (874 nm), light reflected from the back surface does not appear unless its frequency is tuned substantially below-band. This is not an interference effect since the free spectral range of a 0.5mm GaAs etalon is much less than the probe bandwidths of 1-2 nm used in these measurements. Effects due to these

back surface reflections are important for the semi-insulating GaAs samples.

3.3 n-type GaAs results

Figure 3-4 shows the CER and PR spectra for samples n24 and n44, again. The spectra show oscillations with a very long period indicating the presence of a large electric field at the interface. The reflectivity changes, $\Delta R/R$, are about 1% for both of these samples. This signal size is quite large for ER, and it also points to large electric fields. The two spectra are almost identical which reinforces the fact that PR and CER essentially measure the same quantity.

The magnitudes of the interface fields will be estimated by associating the traces in Fig. 3-4 with the $\hat{G}$ lineshape function of the previous chapter. This is a reasonable start for the analysis as the reflectivity changes are due to the real part of the dielectric constant, and the data traces have minima almost at the bandedge energy of 1.42 eV. The magnitude of the fields obtained by this analysis indicate that triangular quantum well states are formed on the GaAs side of the interface in the valence band. The analysis of Chapter 2, is therefore not strictly valid. An outline of how to construct a theory to cover this case will be outlined. Although the magnitude of the fields can only be estimated, the conclusion that extremely large fields occur at the interface is only underscored by these necessary modifications.

Before the magnitude of the fields are discussed, their direction will be determined since this will have the biggest impact on the total barrier height between the materials. In the configuration used here, both the PR and the CER spectra have the same sign. A positive signal means that the reflectivity goes up (more light received on the detector) when the excitation, pump light or plate voltage, is turned on. The positive plate for the CER trace was the ITO coated glass flat in front of the ZnSe. The plate field, then, points into the GaAs on the positive part of the drive cycle. Since the photo-carriers always act to reduce the field, the fact that the CER signal has the same sign as the PR signal means that the plate field is opposing the built-in field when it points into the GaAs. This, in turn, reveals that the GaAs interface electric field points toward the interface from the GaAs bulk and indicates the presence of a negative interface charge density. It must be stressed that this determination of the sign is not affected by thin film interferences or by modifications to the wavefunctions used in Chapter 3

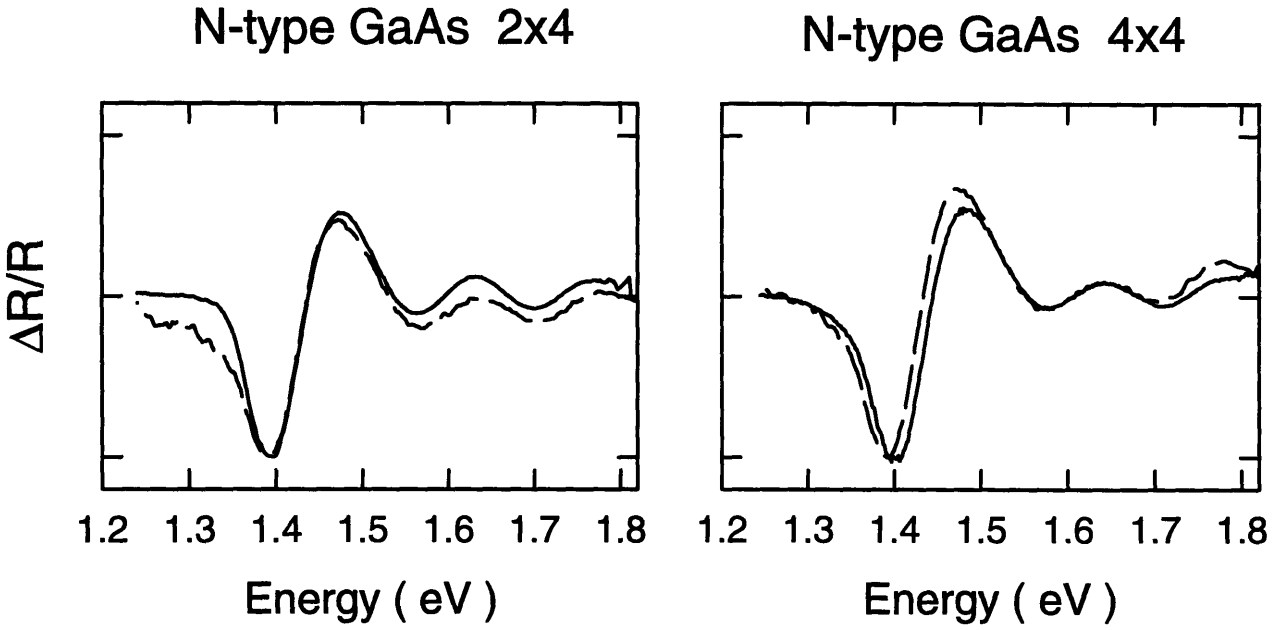

Figure 3-4: PR (solid lines) and CER (dashed lines) of the GaAs bandedge for two ZnSe/n-GaAs samples.

due to quantum confinement or excitonic effects. This is because the direction of the field is contained in the relative sign between the PR and CER traces. All of these other complicated effects influence the PR and CER traces in the same way, and can only modify the shape or the overall sign of both traces together.

To estimate the field magnitude, the same analysis as used in Fig. 2-11 is performed. The energies of the maxima and minima of the oscillations are plotted in Fig. 3-5 using Eq. 2.39. The slope of the linear fit determines $\hbar\theta$, and therefore the electric field magnitude. Electric fields of 8.8×10^5 V/cm and 7.8×10^5 V/cm are found for n44 and n24, respectively, corresponding to surface charge densities of 6.6×10^{12} cm^{-2} and 5.8×10^{12} cm^{-2}. In both plots in Fig. 3-5, the higher extrema deviate from the linear fit predicted by Eq. 2.39. This suggests that the oscillations in the modulation spectra are not pure free-carrier FK transitions.

With the sign and magnitudes of the interface charges estimated, Poisson's equation (Eq. 1.1) can be solved for the potential in the vicinity of the junction. Surface charges on the air/ZnSe surface are neglected in this calculation. Fermi statistics are used for calculating the charge density from the potential at each point in space, and a 200 meV conduction band

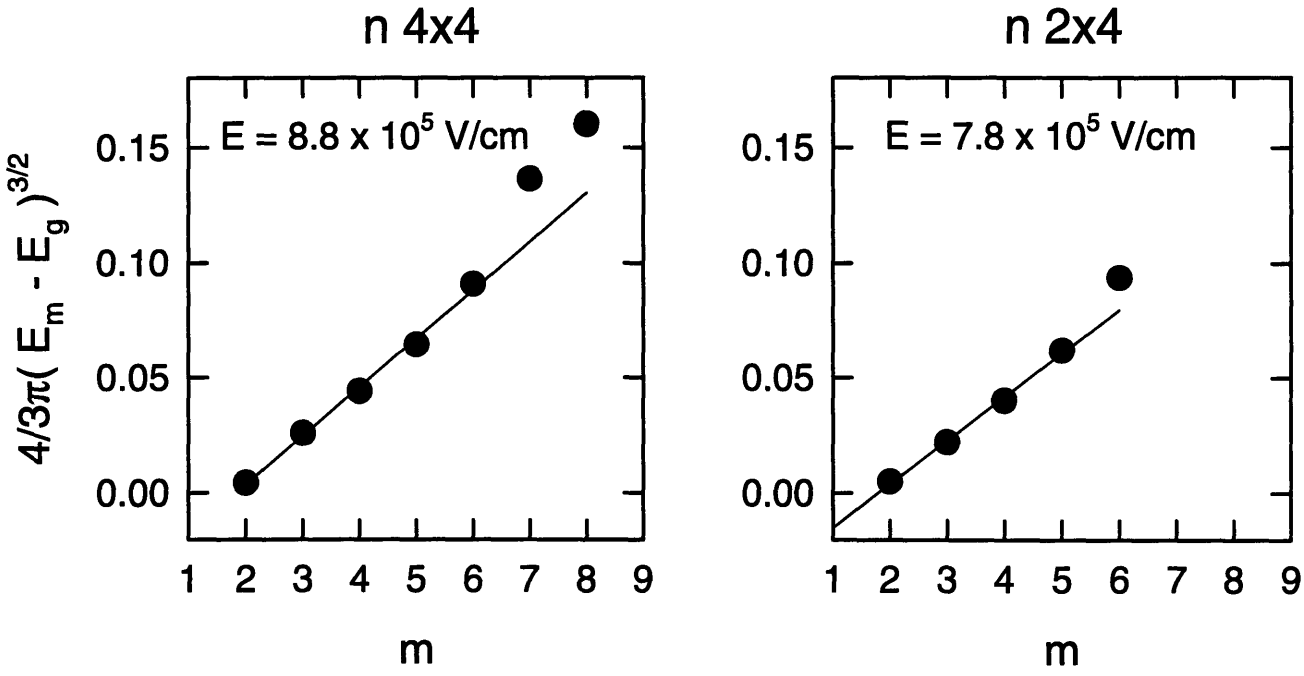

Figure 3-5: Plots of extrema energies to determine $\hbar\theta$ for ZnSe samples n24 and n44.

offset is used. A value of 200 meV was chosen to match the results presented in chapter 4. The result for sample n44 is shown in Fig. 3-6 Comparing this structure to the ideal junction modulation doping case shown in Fig 1-3, it is obvious that the negative interface charge has a dramatic effect. The conduction bands on both sides of the junction are bent down as electrons are repelled from the negative charge. This creates a very large potential barrier for electrons entering the ZnSe from the GaAs. The band bending contribution, in fact, is almost 2.5 times the barrier due to the fundamental conduction band offset, taken here to be 200 meV.

Because of the high doping in the GaAs, the interface fields are screened within about 300Å into the GaAs bulk. The non-uniform field theory of Chapter 3 is therefore applicable. The functions G_{AV} and F_S presented at the end of Chapter 3, were calculated to deal with the band bending seen in these n-type samples. Under the theory of that section, the observed modulation spectrum should be given by the sum of these two functions. Inspection of Fig. 3-4 seem to show that this is not the case, since the contribution from F_S would cause a positive bump in the traces just below the bandgap at about 1.4 eV.

The reason for this discrepancy, as well as the poor fit at high energies in Fig. 3-5, lies in

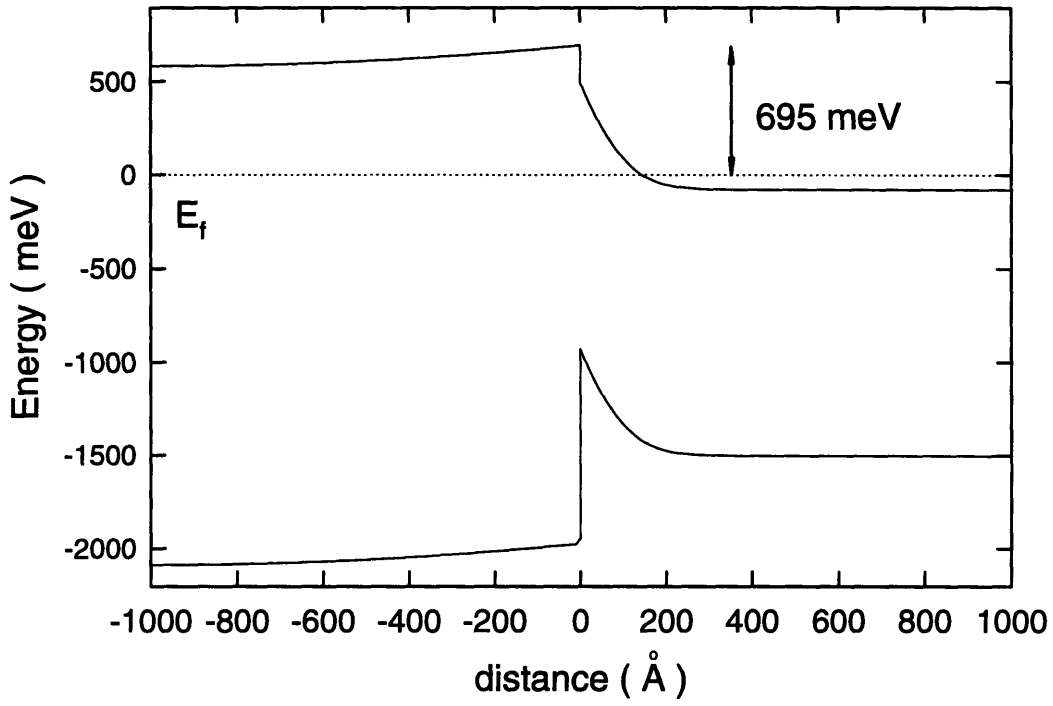

Figure 3-6: Band bending at the ZnSe/ n-GaAs interface due to a large negative surface charge density as detected by ER.

the structure of the valence band in Fig. 3-6. The band bending causes a triangular potential well to be formed for holes . The 100Å distance scale of the well is on the order of the De Broglie wavelength of carriers near the bandedge, and results in quantum mechanical bound states. These states do not have to be taken into account in evaluating the charge density when solving the Poisson equation since the Fermi level remains far enough away from the valence band that almost no holes are present. At larger interface fields the GaAs valence band may bend below the ZnSe valence band and the bound states may become populated with holes. At this point, both the Schrödinger and Poisson equations must be solved together, as is also the case of inversion in the theory of reversed biased field effect transistors (FETs). It would seem, however, that inversion can only happen for externally applied fields because if the Fermi level is so close to the valence band, the trap states on the interface must be mostly empty. Thus there will be no large surface charge and no large electric field to cause the inversion.

Although the band bending can be calculated classically as in Chapter 1, the bound hole states will affect the optical transitions monitored by the probe in the ER measurements. Transitions between bound and free states in PR spectroscopy have been invoked before in previous work in the field, but no theoretical attempt to characterize the lineshapes has been published [56, 57]. An outline of the calculations necessary to deal with this situation will be presented next.

The first step is to determine the envelope wavefunctions for the bound holes and the electrons. A simplification of the problem is to assume that the potential is due to a half-infinite uniform electric field for x>0 and an infinite potential barrier at x=0. This is appropriate due to the large valence band offset (~1.2 eV). Neglect of the flat band regions beyond 300Å in Fig. 3-6 will only affect the spectrum at energies well below the band gap. The model potential and sketches of the wavefunctions are shown in Fig. 3-7.

Both the hole and electron wavefunctions can be obtained from solutions to the uniform field case. The holes will be discussed first. Away from x=0, the potential is linear and the wavefunction,Φ_n^h, will be an Airy function of the first type (Ai) since the wavefunction must vanish at $x = +\infty$. At $x = 0$, Φ_n^h must vanish and this introduces a quantization of the energy

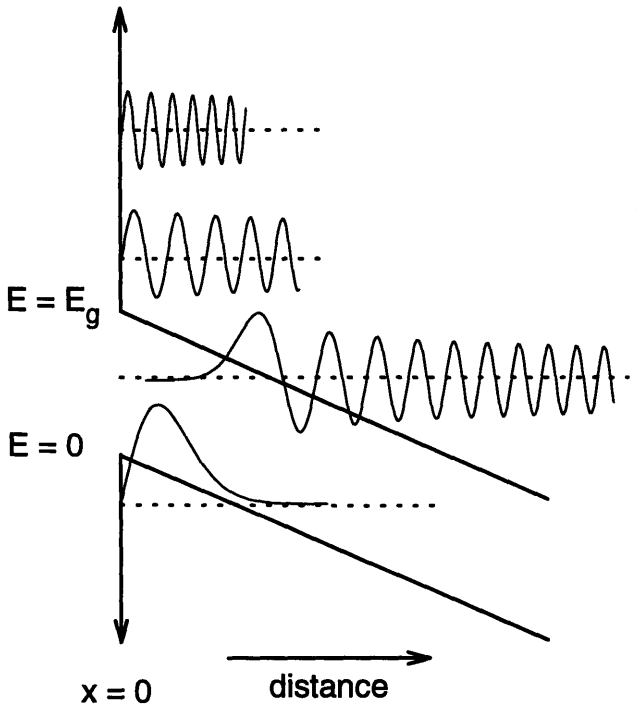

Figure 3-7: Strong electric fields at a surface create a bound valence band state.

levels. The wavefunction are given by

$$\Phi_n^h(x) = N_n^h \,\mathrm{Ai}\left(\frac{e\mathcal{E}x - E_n^h}{\hbar\theta_h}\right) U(x) \tag{3.1}$$

with $\hbar\theta_h$ using the hole effective mass. N_n^h is a normalization constant and U is the unit step function. The quantized energy levels are given by

$$-\frac{E_n^h}{\hbar\theta_h} = z_n\,, \quad n = 1, 2, 3\ldots \tag{3.2}$$

where z_n in the n^{th} root of $\mathrm{Ai}(z)$ on the negative real axis. Only the $n = 1$ state is necessary for the potential of Fig. 3-6.

The electron wavefunctions form a continuous spectrum, and are therefore functions of both space and energy. They must also vanish at $x = 0$, and are given by

$$\Phi^e(x, E_c) = N^e(E_c)\left[\mathrm{Ai}\left(\frac{-E_c - e\mathcal{E}x}{\hbar\theta_e}\right) + C\,\mathrm{Bi}\left(\frac{-E_c - e\mathcal{E}x}{\hbar\theta_e}\right)\right] U(x) \tag{3.3}$$

where

$$C = -\frac{\mathrm{Ai}\left(\frac{-E_c}{\hbar\theta_e}\right)}{\mathrm{Bi}\left(\frac{-E_c}{\hbar\theta_e}\right)} \tag{3.4}$$

and $N^e(E_c)$, and $U(x)$ are the normalization constant and step function.

The absorption depends on the projections of these wavefunctions on each other as shown by Eq. 2.18 and 2.20 is proportional to

$$\mathrm{Im}\left(\varepsilon(\hbar\omega)\right) \propto \int_0^\infty d\epsilon_\perp \left| \int_0^\infty dx \Phi_1^h(x)\, \Phi^e\left(x, E_g + E_1^h + \epsilon_\perp - \hbar\omega\right)\right|^2 \tag{3.5}$$

. After, obtaining the imaginary part of $\Delta\varepsilon$, the real part must be found by a Kramers-Kronig transform. Both of parts of $\Delta\varepsilon$ must then be used in Eq. 2.46 since the spatial scale of the wavefunctions and resulting changes to the dielectric constant are on the order of the wavelength of light in the material, $\lambda/2\pi n$. Because of the limits on the integrals in these equations, and the normalization conditions above, they cannot be evaluated analytically. Attempts at numerical integration of the modulation spectra will not be attempted here.

Although these extensions to the theory of ER are necessary for a correct description of the

problem and experimental data, they emphasize the fact that large electric fields are present in these n-type GaAs samples. Besides these two samples, several other ZnSe/n-GaAs structures with dopings from 6×10^{17} to 1×10^{18} cm^{-3} were studied. Spectra similar to Fig. 3-4 and large negative surface charges were observed in all cases. Possible origins of these charges will be discussed at the end of this chapter. Again, it must be emphasized, that the determination of the sign of the field at the junction is not affected by the neglect of these quantum confinement effects.

3.4 Semi-insulating GaAs results

In contrast to the ZnSe films grown on n-type GaAs, samples grown on semi-insulating GaAs show much smaller interface fields. Like the n-GaAs samples, negative interface charges are also found on both the 2×4 and 4×4 reconstructed GaAs samples. Before the experimental results are presented, an effect due to reflections off the back of the samples will be described.

Because the carrier concentration is very low in the semi-insulating samples, the screening length is very long. At $n_e = 10^{10}$ cm^{-3}, the Debye length is 44 μm. Figure 3-8 is a sketch of the band diagram of the samples showing how the field from the interface extend much further into the bulk than for the n-type case. At energies sufficiently below the band gap, the absorption becomes small enough for light to reflect off the back surface of the 500μm thick GaAs substrate. The impact on the measured ER spectra is diagrammed in Fig. 3-9. The step in the reflectivity below 1.38 eV marks the onset of the back surface reflection. Note that the actual bandedge is at 1.42eV. Modulating the electric fields in the GaAs can change the transmission of this light by electro-absorption - changes in the imaginary part of the dielectric constant whose spectrum is given by the F function. Only the small tail of the F function in Fig. 3-9 that extends below the substrate absorption edge will give rise to a measured signal. Because the fields extend to such a long distance in the semi-insulating substrates, the small absorption changes due to electro-absorption can integrate up and lead to changes in the total measured sample reflectivity which are comparable to the front surface ER signals.

Electro-absorption contributions are evident in the data shown in Fig. 3-10. The middle and bottom plots are of the PR spectrum of the 4×4 reconstructed semi-insulating GaAs sample.

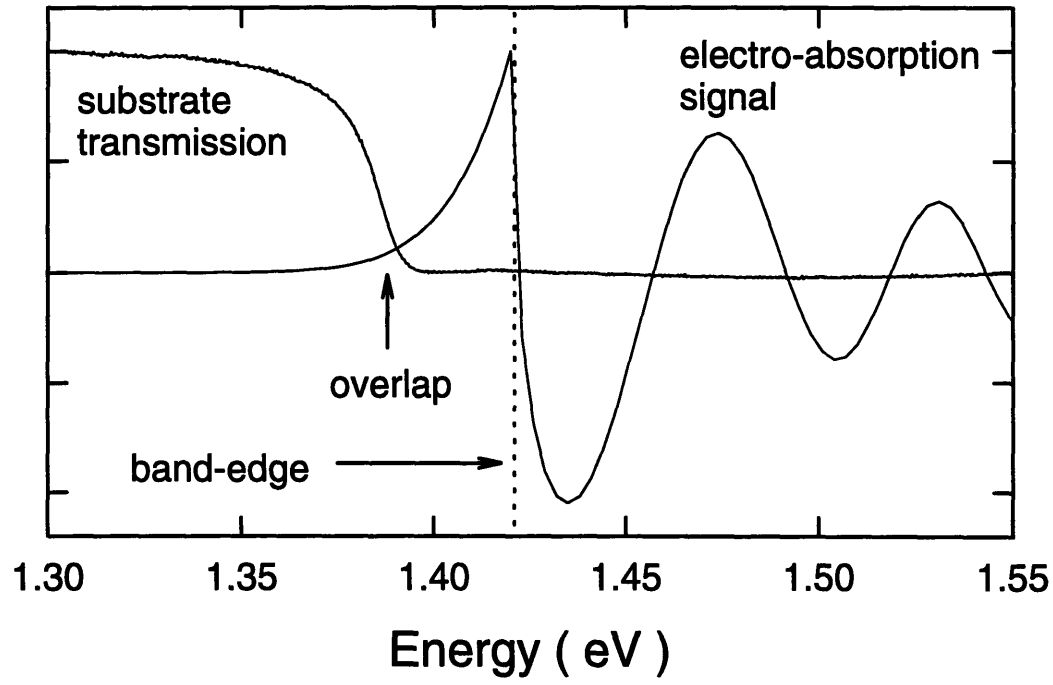

Figure 3-8: Band diagram for a ZnSe/ SI-GaAs interface. Low carrier concentration in the GaAs results in very long screening lengths and electro-absorption of the the back surface reflection.

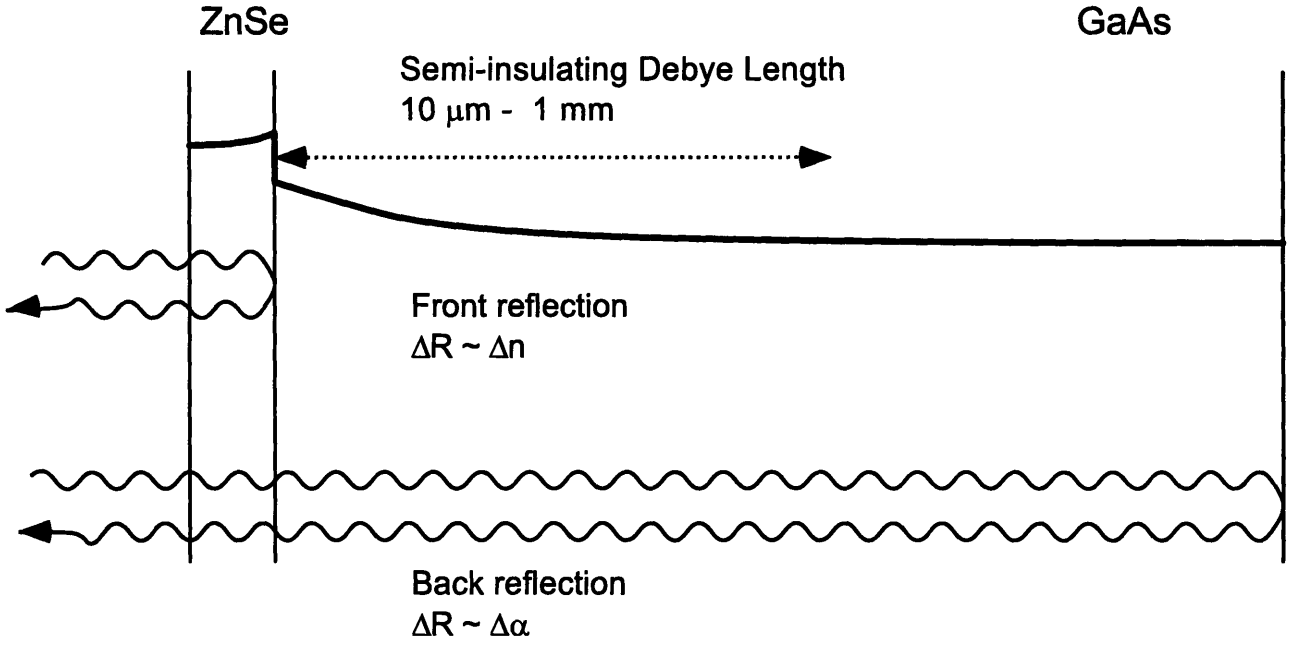

Figure 3-9: Reflection spectrum and electro-absorption modulation lineshape. The GaAs substrate is transparent below 1.38eV. Probe light with be modulated with a spectrum given by the product of these functions.

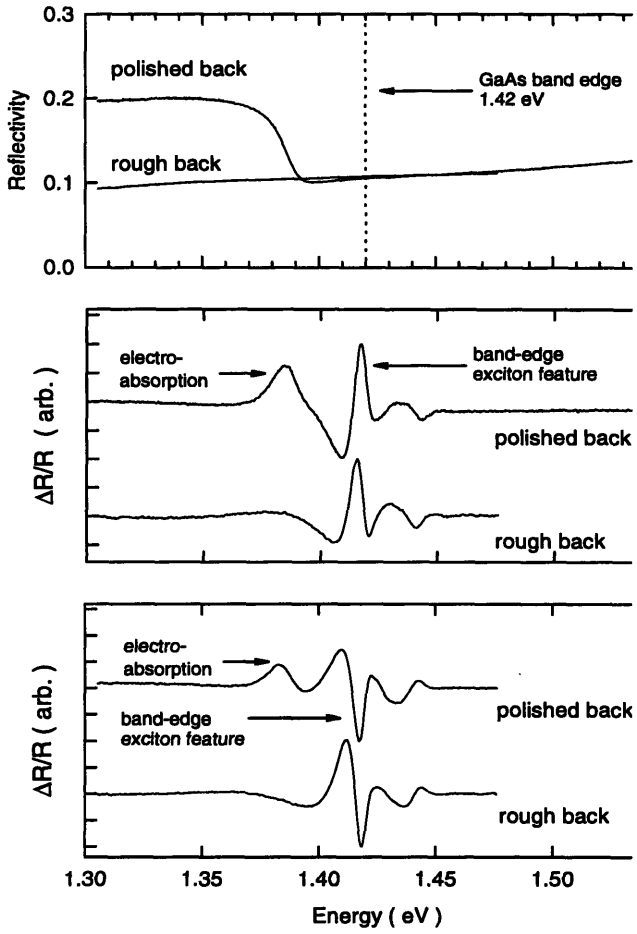

Figure 3-10: Effects of back surface roughening. Top plot: Sample reflectivity. Middle plot: PR spectrum for sample i44 showing electro-absorption bleaching feature. Bottom plot: i44 again on a different spot on the wafer.

The top traces in these two plots show PR signals taken at different places on the wafer. Both traces show a positive bump at 1.38 eV which corresponds to the step in the reflectivity. These bumps look like the overlap of the tail of the electro-absorption F spectrum with the transmission edge as in Fig. 3-9. The pump beam reduces the electric fields which reduces the absorption at energies below the bandgap. This lets more light through the sample and results in a positive change in the reflectivity as observed.

Conclusive proof of this effect comes from repeating the measurements after roughening the polished rear surface of the substrates. The roughening was accomplished simply by gently rubbing the samples' back surface against some 9μm grit polishing film. The rough surface scatters the probe very effectively and eliminates the reflection as seen in the top plot of Fig. 3-10. The bottom traces in the middle two plots show the actual PR spectra of the two pieces. The spectra are essentially the same except for a sign difference due to thickness variations in the ZnSe layer. The electro-absorption does not take part in these front surface interferences because the substrate is thicker than the coherence length of the probe light. This fact actually makes this feature useful for determination of the sign of the electric fields when it is observed in CER experiments and it will be exploited here. This effect has not been reported or discussed in the literature though it appears to be quite significant in interpreting ER lineshapes on low doped samples. The reason the effect does not occur for the n-type GaAs substrates is that the fields are screened so close to the surface that the front surface probe reflection already samples the whole space charge region. Thus, the light reflected from the back surface has no relative material volume advantage and is negligible.

With its back surface roughened, PR and CER were performed on the 2×4 semi-insulating GaAs sample and the results are shown in Fig. 3-11. The PR and CER traces are almost identical. The fact that they have the same sign indicates that the built-in field points toward the interface from the GaAs, just as in the n-type case. The magnitude of the field is much smaller, however. Figure 3-12 plots the energy of the extrema to determine $\hbar\theta$. The field is found to be 4.2×10^4 V/cm.

Analysis of the 4×4 semi-insulating sample is a little more complicated. The PR and CER spectra are shown in Fig. 3-13. The data shown here are for the sample before the back surface was roughened. The electro-absorption feature is therefore present in both traces. Identifying

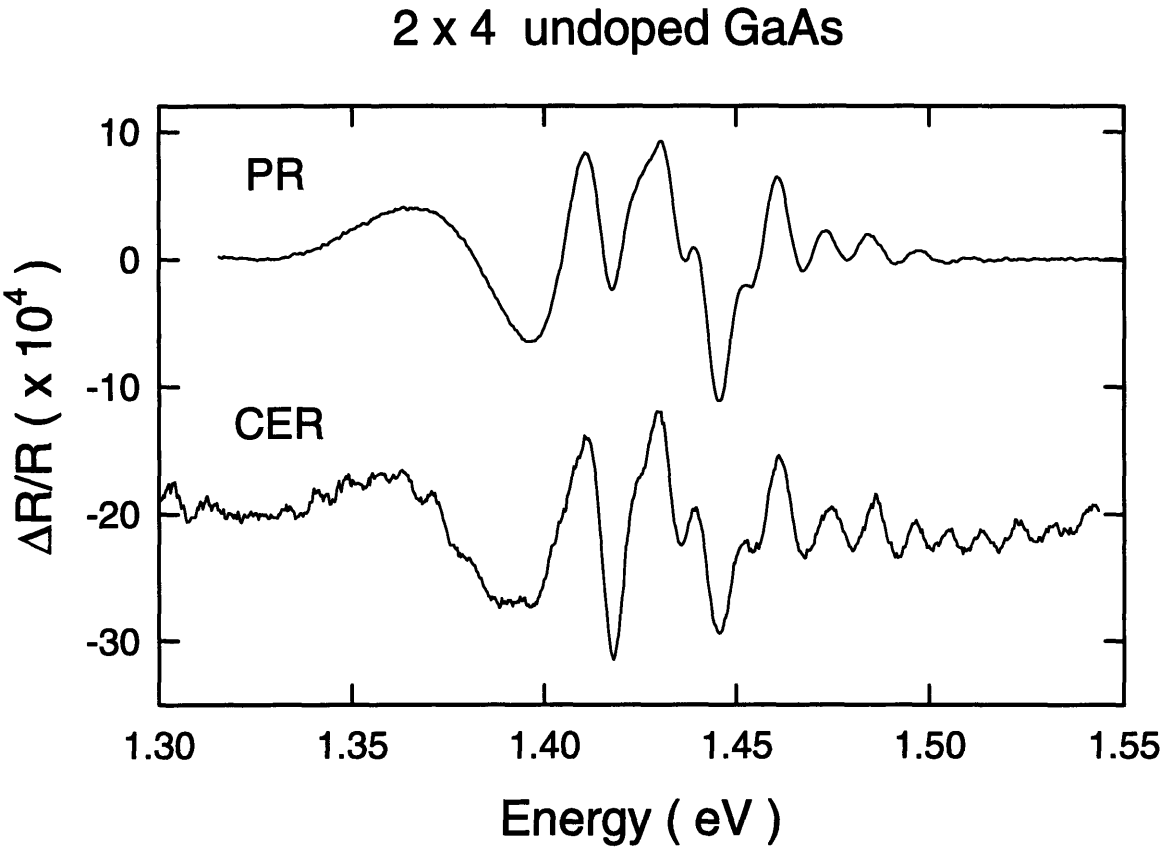

Figure 3-11: PR and CER for sample i24. Traces show same sign indicating negative interface charge density.

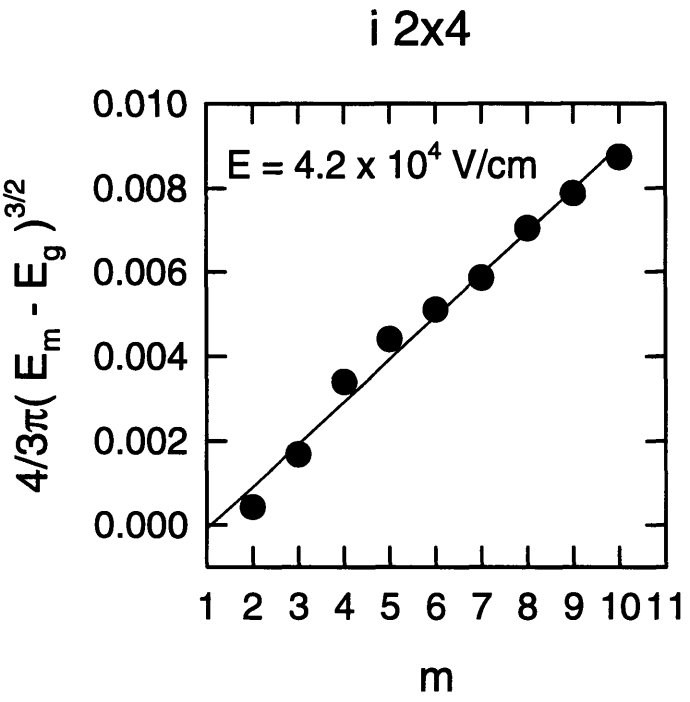

Figure 3-12: Extrema plot for sample i24 to extract the interface electric field on the GaAs side of the junction.

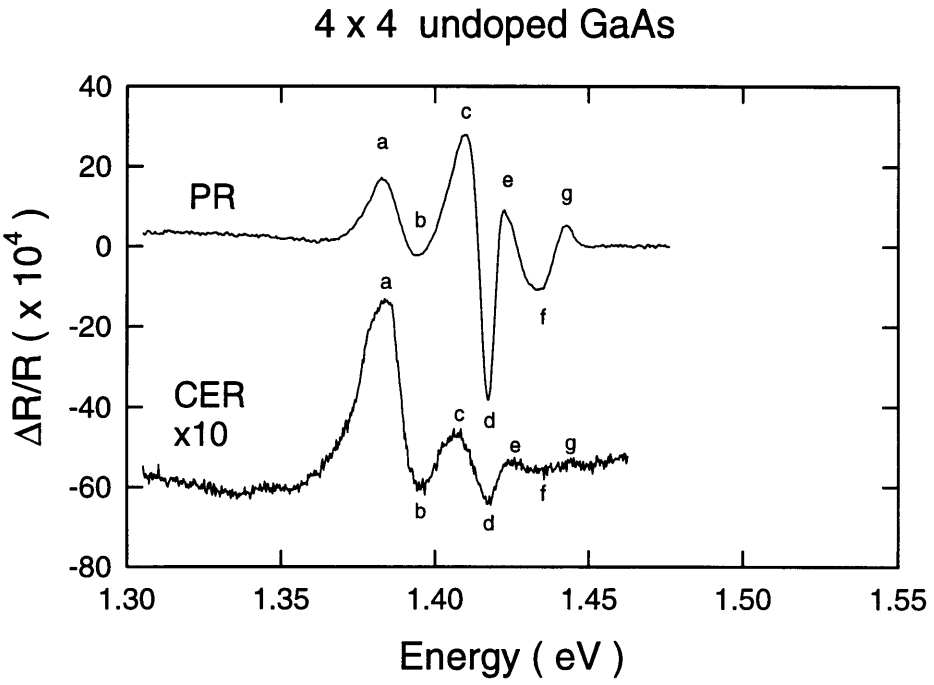

Figure 3-13: PR and CER spectra for the ZnSe/ 4×4 semi-insulating GaAs sample. Back surface is polished resulting in electro-absorption peaks at 1.38 eV. The back substrate surface has been roughened.

oscillations with the letter indexes shows that the ER components of the two traces have the same sign. This, again, implies negative interface charge. The 'd' peak is the exciton signal which masks one of the ER extrema between 'c' and 'e'. The peaks at 'f' and 'g' can, however, be used for a very crude estimate of 3.5×10^4 V/cm for the interface field. The sign of the charge determined from the PR/CER comparison is corroborated by the electro-absorption signal as well.

CER is generally less sensitive than PR. Apparently, the AC fields created by the plates result in smaller modulation than the minority carrier trapping induced by the pump in PR. This may have to do with mis-alignment of the plates which results in the strength of the modulating field varying across the probe beam spot. The CER signal for i44 could not be found when the sample had its back roughened. Some plate alignment is necessary to achieve small separations without coming too close to the sample to cause shorting or arcing. Pick-up of the drive signal from the high voltage op-amp is another source of background noise. To obtain the CER trace in Fig. 3-13 , it was necessary to first find the large electro-absorption signal. Averaging for approximately 1.5 hours (550 points @ 10 sec/pt) was needed to bring out the small ER oscillations. Attempts to measure the roughened samples were not successful.

The negative charge densities observed here, are in contrast to the results of Ref. [21] which show strong evidence of interface well states in the conduction band. This discrepancy will be discussed further in the discussion section at the end of this chapter.

Using the estimated interface fields, the band bending can be calculated. Figures 3-14 and 3-15 plot the band diagrams for ZnSe on semi-insulating GaAs with a 4.2×10^4 V/cm interface field corresponding to a 3×10^{11} cm^{-2} negative surface charge density. Because of the extremely long screening length, the conduction band solution has structure on very small and very long length scales. Note the distance scales in the two figures compared to Fig. 3-6. Numerical techniques to solve Poisson's equation must use a sophisticated adaptive grid to model this case. The solution presented here was calculated analytically assuming that the 1000 Å, 10^{16} cm^{-3} n-type ZnSe layer is completely depleted. The GaAs was treated as intrinsic - the only charges present being free electrons and holes. In this case, the Poisson equation can be integrated directly to yield an expression for the distance from the interface as a function of the potential. To screen the negative charge on the interface, holes must be created on the

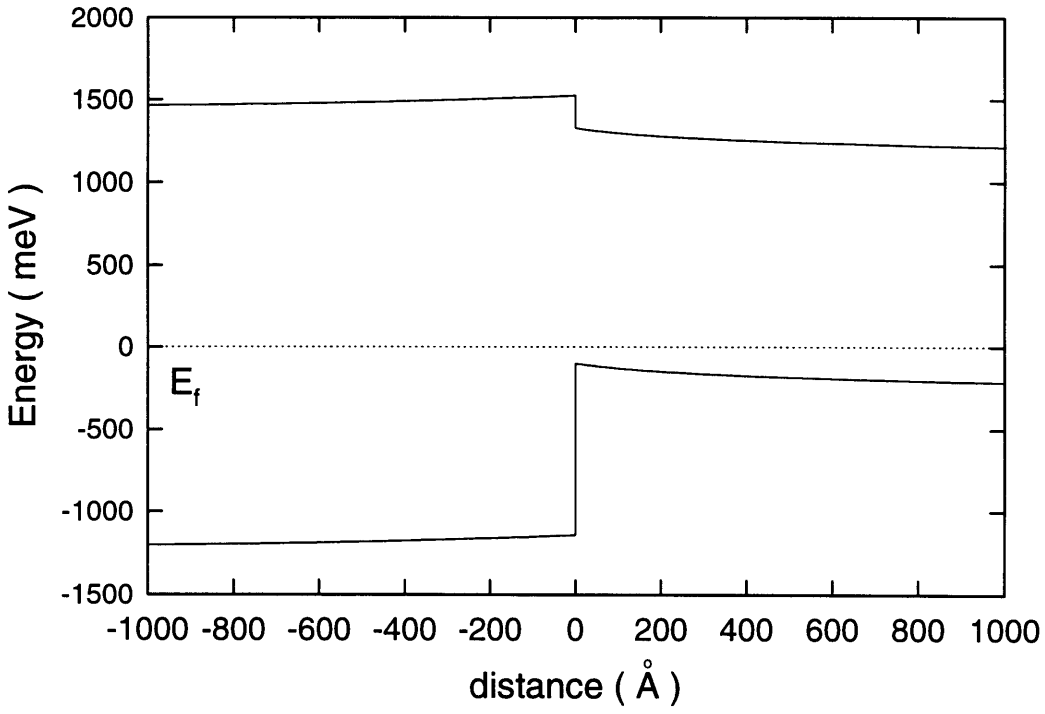

Figure 3-14: Band bending at a ZnSe/SI-GaAs interface due to a negative $3\times10^{11}\mathrm{cm}^{-2}$ interface charge.

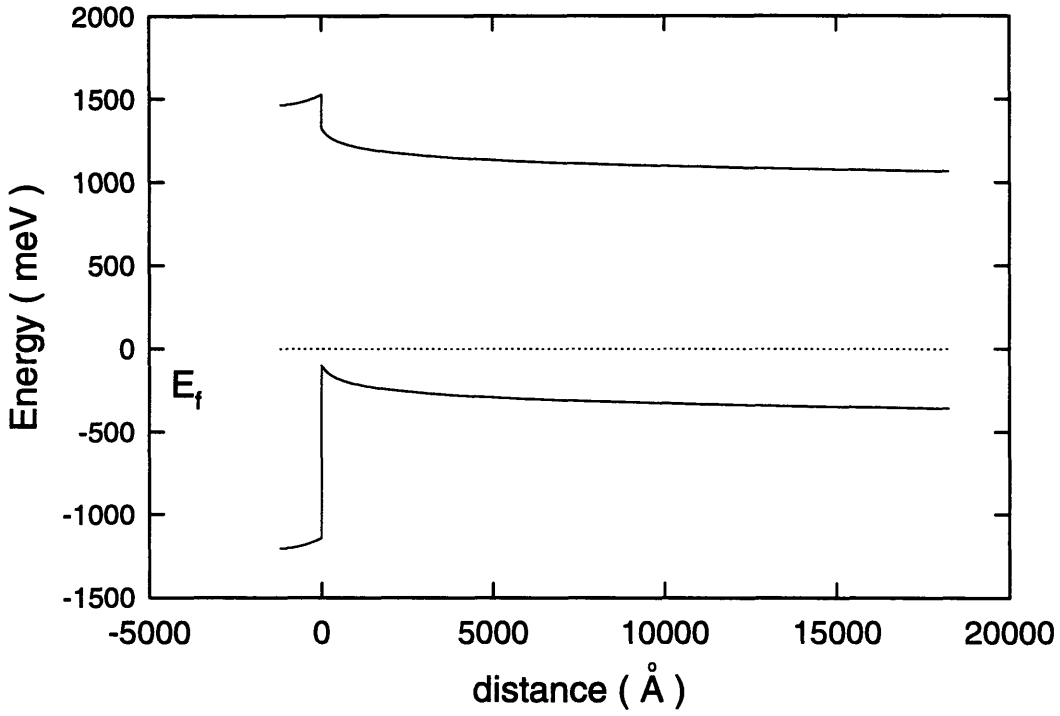

Figure 3-15: Larger scale view of the ZnSe/SI-GaAs interface.

GaAs side of the junction. Thus, the Fermi level is near the valence band of the GaAs. The Fermi level does not reach its bulk position at mid-gap until about 50 μm into the GaAs. The negative charges, although much smaller than for n-type GaAs, again cause the conduction band to bend down from the interface. The barrier is mostly due to the conduction band offset between the materials. Because the band bending doesn't shield the conduction band offset as the ideal junction modulation doping solution predicts, finding negative charge on the interface is a significant new experimental observation with implications for device design.

3.5 Discussion

The analysis of the CER and PR results in this study has focused on the electrostatics of the junction with no mention made of the origins of the charges. The two main explanation of the charges are interface traps and interdiffusion of ions across the junction. The interdiffusion model is outlined in Chapter 2. It suggests that Zn diffuses into the GaAs and Ga diffuses into the ZnSe during the growth process. Since Zn is an acceptor in GaAs and Ga is a donor in ZnSe, a p-n junction is formed at the interface resulting in the surface fields. In the trap model, surface charge is created at the junction in the same way as at an air/semiconductor surface - surface states, perhaps due to unfulfilled bonds, trap majority carriers.

The data presented in this chapter support the trap model. The main argument is the huge difference in the fields between the n-type and semi-insulating GaAs samples. Supposedly, ions are driven across the interface by very large fields due to mismatch of bonding within the first few atomic layers at the interface. If this is so, then all samples should show similar size electric fields. A volume density of 10^{18} cm^{-3} results in only one out of every thousand unit cells containing an ionized donor. It seems implausible that such a small charge density can affect the hypothetical diffusion process on a single mono-layer spatial scale. Doping in the n-type samples, therefore, cannot account for the difference in field sizes within the diffusion model.

The diffusion model also predicts that the field points in the opposite direction as observed in the GaAs. Band bending would then act to lower the effective barrier between the materials. The sign determination presented here is independent of any specific model of the band bending and is a solid experimental result upon which any model should be based.

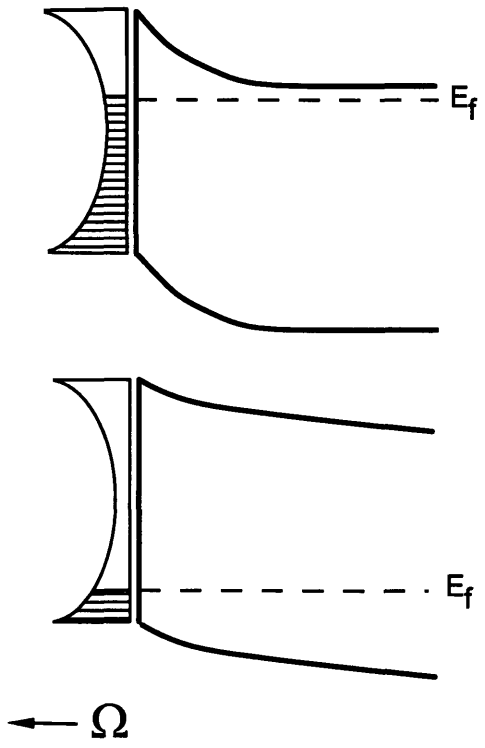

Figure 3-16: Surface traps with density of states $\Omega(E)$ fill until equilibrium is reached with the bulk. Top: N-type GaAs. Bottom: SI -GaAs, surface states act as acceptors . The Fermi level eventually is at mid-gap far into the bulk due to the long Debye length.

The trap model can account for both the magnitude and sign of the observed fields. The top plot of Fig. 3-16 shows a density of surface states similar to that which is often measured by C-V methods on Si-SiO_2 interfaces. In the n-type GaAs samples, electrons will minimize the free energy of the system by falling into the lower energy surface states creating a surface charge. This is shown by the middle plot. In the semi-insulating case, there are no free electrons. States within a few kT of the valence band will act as surface acceptors, holding a valence electron while creating a free hole. The band bending in this case is similar to the n-type case, but the charge density will be smaller since only those states close to the valence band edge will become occupied.

With regard to the different GaAs surface reconstructions studied, no dramatic effect is observed. The 4×4 sample has a larger field of the two n-type samples, and the 2×4 sample has the larger field of the SI samples. Apparently, any differences on the surface state densities due to the initial GaAs surface during growth are small. Other factors such as the ratio of species in the molecular beams (beam pressure ratio) and the temperature may have a greater impact on the MBE growth. It may be that in addition to neutral surface trap states, a density of fixed charges due to the nature of bonding at the interface may also be present. This charge could be swamped by the large population of trapped electrons in the n-type samples, but may be important for the low-doped cases. Indeed, one SI GaAs sample, presented in the next chapter, will be seen to have a positive interface charge causing the conduction band to bend up as in Fig. 1-3 in Chapter 1. Further work is necessary to reveal under what conditions positive or negative interface charges as found on ZnSe/SI-GaAs heterojunctions.

The trap model is also preferred based on the inherent limitations of the available experimental techniques. In the uniform field theory of ER, no detailed information on the spatial distribution of the fields is really possible. Because of this lack of resolution, the trap model simply lumps all of the charges causing the electric fields into a localized surface charge density. The diffusion model, instead, suggests a spread out volume charge density within ~100Å of the interface. References [27] and [26] reports complicated band bending near the junction along with values for diffusion lengths for the Zn and Ga. How this information is obtained from the published ER spectra is not explained. In this thesis, the simplest model for the interface will be adopted until experimental results force a more complicated theory to be considered.

The exact form of the band bending is of secondary importance, anyway. The most important result of this chapter is the evidence for large effective conduction band barriers between the ZnSe and the GaAs. The new PR method introduced in the next chapter is designed to measure these barriers directly. It will provide confirmation of the general picture of the ZnSe/GaAs heterojunction laid out in this chapter.

Chapter 4

Tunable pump PR and conduction band offsets

The previous chapter described an analysis of the ZnSe/GaAs heterojunction based on conventional ER techniques. The primary focus was on the material spectral response measured by varying the energy of the *probe* beam. Theoretical lineshape analysis was used to determine the electric field which, in turn, was used to infer a plausible model of the charge density at the interface. Numerical solutions of Poisson's equation then led to the realization of large Schottky barriers at the junction. Although this is the standard usage of the ER method, it is indirect and requires experience and familiarity with the theory in order to draw conclusions.

This chapter will present an entirely different approach to using PR spectroscopy. The main interest will be on the *pump* energy dependence of the PR signals. The ZnSe bandedge PR response will be used as a probe to detect the migration of electrons between the materials. The exact PR lineshape and the structure of the electric fields in the ZnSe are not necessary for these measurements, and are difficult to determine, in any event, because of excitonic effects. The probe wavelength will in fact be held fixed on a PR signal peak. This is the first use of PR to directly measure carrier transport.

Usually, the pump photon energy is unimportant for PR spectroscopy so long as light is absorbed in the material to create minority carriers. There have only been a few investigations that have made use of this degree of freedom in PR. Most have been directed toward obtaining

PR spectra for conventional analysis. For instance, Badakshan et. al. [58, 59] used two pump lasers at widely separated wavelengths with different absorption lengths in the semiconductor under study. By using both pumps and chopping out of phase, they were able to discern small PR signals from buried layers from those caused by large surface fields. Pollack et. al. performed an experiment which is the precursor to the methods developed in this work [60]. They used a tunable pump source to determine the absorption spectrum of quantum well structures by tracking the size of the PR signal while the pump was tuned across the bandedge exciton peaks. PR was just the means to get information on a different physical property of the semiconductor. This method was dubbed 'photoreflectance excitation spectroscopy' (PRE) in exact analogy to the relation between photoluminescence spectroscopy (PL) and photoluminescence excitation spectroscopy (PLE).

The new twist of the experiments described here is that the pump will be used to excite one material while the probe monitors a PR signal from the other. The probe modulation is therefore dependent on carriers moving across the heterojunction. By exciting carriers (electrons) at different energies, 'electron spectroscopy' of the junction potential barrier can be performed. This is the principle behind a standard photo-conductive technique - internal photo-emission spectroscopy (IPE) [61, 62, 63]. By optically detecting the arrival of the electrons across the barrier, the use of electrical contacts and specially designed structures, necessary for photo-current methods can be avoided. Thus, the work presented in this chapter is, essentially, a combination of the PRE and IPE techniques.

A description of these tunable pump experiments will be presented by first examining a single ZnSe/GaAs sample. Supporting experiments designed to confirm the method and demonstrate certain precautions will be discussed. Arguments will also be made that these results actually measure the conduction band offset at the heterojunction. Next, results for several different ZnSe films grown on n-type and SI GaAs will be shown. Finally, the chapter will conclude with a very elementary theory of the observed pump wavelength dependences.

4.1 ZnSe PR signals and electron transport

Figure 4-1 shows the layer structure and conventional GaAs bandgap CER and PR spectra

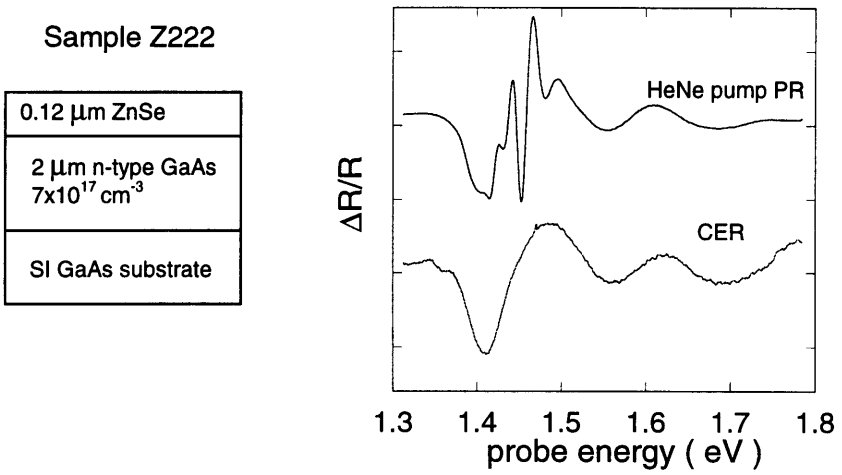

Figure 4-1: Left: structure of sample Z222. Rightt: CER and PR spectra at the GaAs bandedge showing a large electric field due to a negative interface charge.

of a ZnSe/GaAs heterojunction sample. The samples will be denoted by their growth run number in this chapter for brevity. Z222 is a 0.12 μm ZnSe film grown on a 4×4 n-type GaAs buffer layer doped to $7\times10^{17}cm^{-3}$. The n-type buffer layer was grown on a SI GaAs substrate. The large short period oscillations seen in the PR trace arise from fields due to interface traps at this homojunction. No samples with uniformly doped GaAs buffer layers and substrate show this signal. Aside from this, the spectra are very similar to the results for the n-GaAs samples of the preceding chapter (Fig. 3-4). The PR and CER spectra have the same sign. Taking into account the orientation of the AC field from the electrode plates, this indicates a negative surface charge at the junction with a conduction band barrier between the materials. An electric field strength of 2.3×10^5 V/cm was determined from the FK oscillations and used to calculate the band bending shown in Fig. 4-2.

In order to see what else could be learned about the structure, PR measurements around the ZnSe bandgap energy of 2.67 eV were performed. The results obtained with several different pump lasers are shown in Fig. 4-3. The top trace is actually of a bare Si doped GaAs film and is presented to demonstrate that the PR signals at 2.9 eV and 3.1 eV , seen in all of the

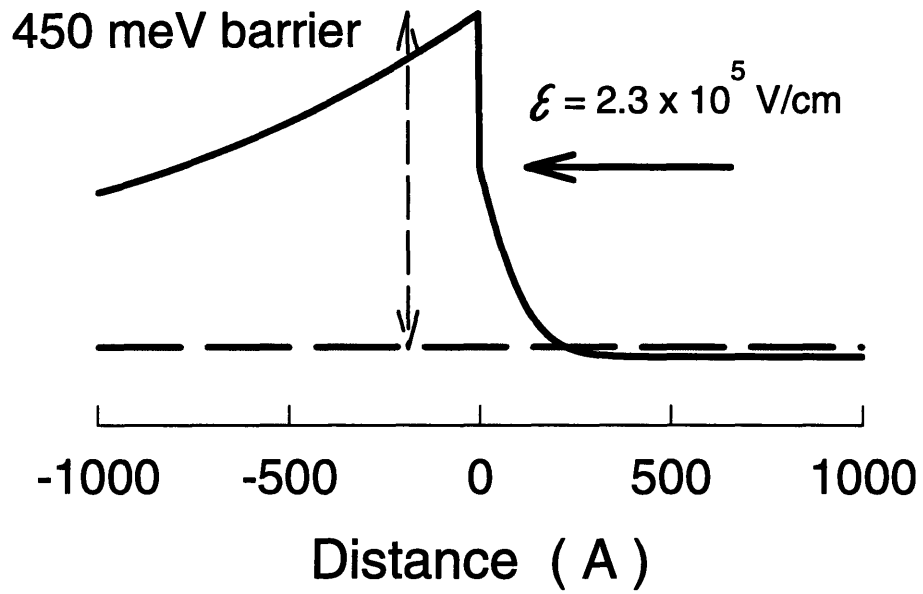

Figure 4-2: Band bending calculated from Z222 PR and CER results. Conduction band offset of 200 meV was used.

traces, originate from GaAs transitions. These are the GaAs E_1 and $E_1+\Delta_1$ signals due to transitions from the heavy hole and split-off valence bands to the conduction band L-valley near the Λ critical point (see Chap. 2, Fig. and Fig. 2-9). The Λ point is a type M_1 critical point. An earlier ER investigation of the ZnSe/GaAs heterojunction mistakenly associated this signal with supposed spatially-indirect transitions from the ZnSe valence band to the GaAs conduction band [26]. The researchers then used this transition energy with the known band gaps of the two materials to determine the band offsets. The observations in Fig. 4-3 cast serious doubt on the conclusions of this highly referenced paper. As a last point, note that PR signals can be observed at probe energies much higher than the pump energy. Here a laser diode at 1.80 eV (688nm) was used. So long as carriers are created, field screening will affect transitions at all critical points in the bandstructure.

The next trace from the top in Fig 4-3 is of sample Z222. A UV HeCd laser at 3.8 eV (325 nm) was used to created electron-hole pairs in both the ZnSe and GaAs materials. With carriers in both materials, screening of fields on both sides of the junction occurs and PR spectra are observed for the GaAs E_1 transition and, now, for the ZnSe E_0 transition as well. The ZnSe spectrum is composed of basically one oscillation, due to excitonic effects, and is therefore not

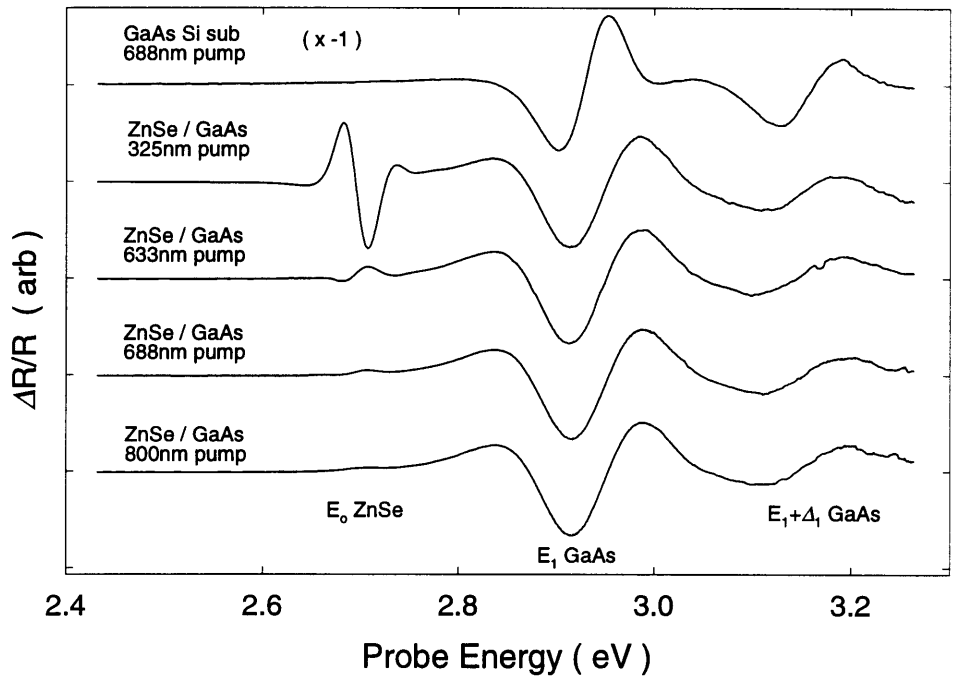

Figure 4-3: PR in the blue spectral region taken with various pump lasers. Top trace: n-type GaAs sample for reference (with sign flipped). Bottom traces: sample Z222 (ZnSe/n-GaAs structure) showing GaAs and ZnSe PR signals.

useful for the extrema analysis of Eq. 2.39.

The bottom three traces are also of sample Z222, but with pump photon energies decreasing towards the GaAs bandedge. As expected, when the pump photon energy drops below the ZnSe bandgap and electron-hole pairs are no longer created directly in the ZnSe, the ZnSe PR signal becomes much smaller. As the pump is tuned to lower energies, the signal becomes smaller still. The GaAs transitions are largely unaffected as long as $\hbar\omega_{pump} > 1.42$ eV.

This seems reasonable, but one must wonder why any ZnSe PR signals are observed at all for $\hbar\omega_{pump} < E_g$. Figure 4-4 shows the situation for pump photon energies below the ZnSe bandgap. The pictures sketch the band diagrams at the junction with the built-in and photo-carrier electric fields shown by horizontal arrows. The top diagram is for pump photon energies above the GaAs bandgap, but below the energy necessary to create electrons with enough kinetic energy to surmount the potential barrier at the interface. The photo-electrons are thus confined to the GaAs side of the junction. The minority holes are attracted to the negative interface charge and fall into traps. This sets up a field opposing the built-in field, but, according to 1-D electrostatics, only in the GaAs material. No screening of fields should occur in the ZnSe, and therefore, no ZnSe PR signal should be observed.

The bottom diagram shows the situation when the pump does have enough energy to create electrons that can escape into the ZnSe. Electrons moving into the ZnSe can be trapped at either the air surface or bulk defect traps and set -up a screening field in the ZnSe. The ZnSe PR signals in the bottom traces of Fig. 4-3 actually measure, for the first time, screening due to carriers transported between two materials.

4.2 Preliminary results

The conclusions of the last section and Fig. 4-4 suggest that the barrier height at the junction can be measured by observing the size of the ZnSe PR signal as the pump is tuned in the energy range intermediate to the two material bandgaps. Before results of this experiment are presented, some preliminary measurements must be discussed. These will serve partly to add support for the electron transport conclusion, and partly to explain some precautions that must be taken into account.

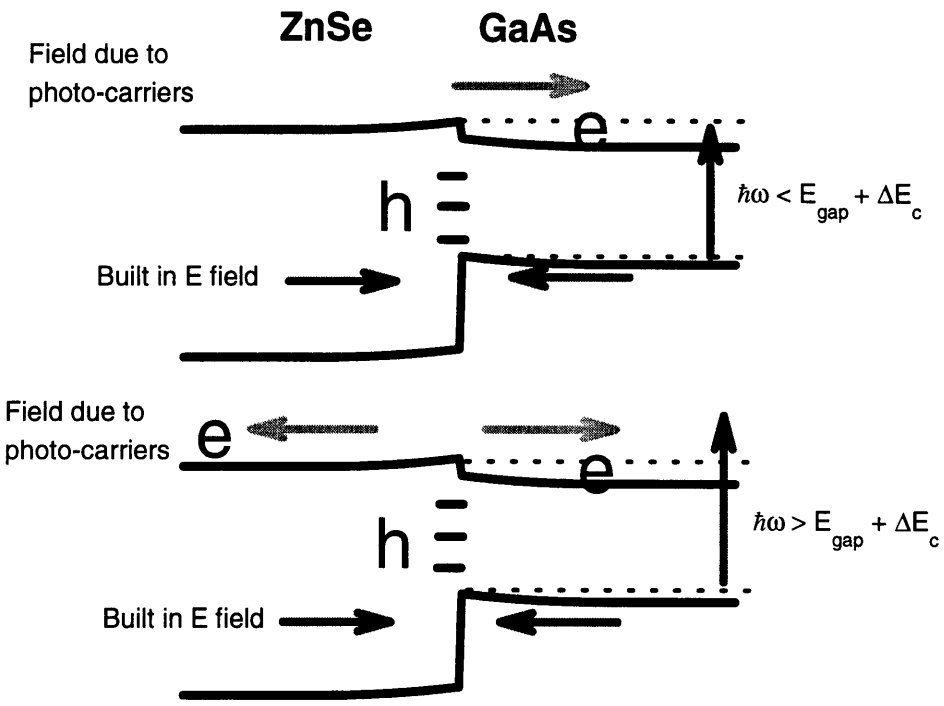

Figure 4-4: Band diagrams of the ZnSe junction showing screening action of photocarriers generated with a pump below (top) and above (bottom) the photon energy necessary for electrons to cross the junction barrier.

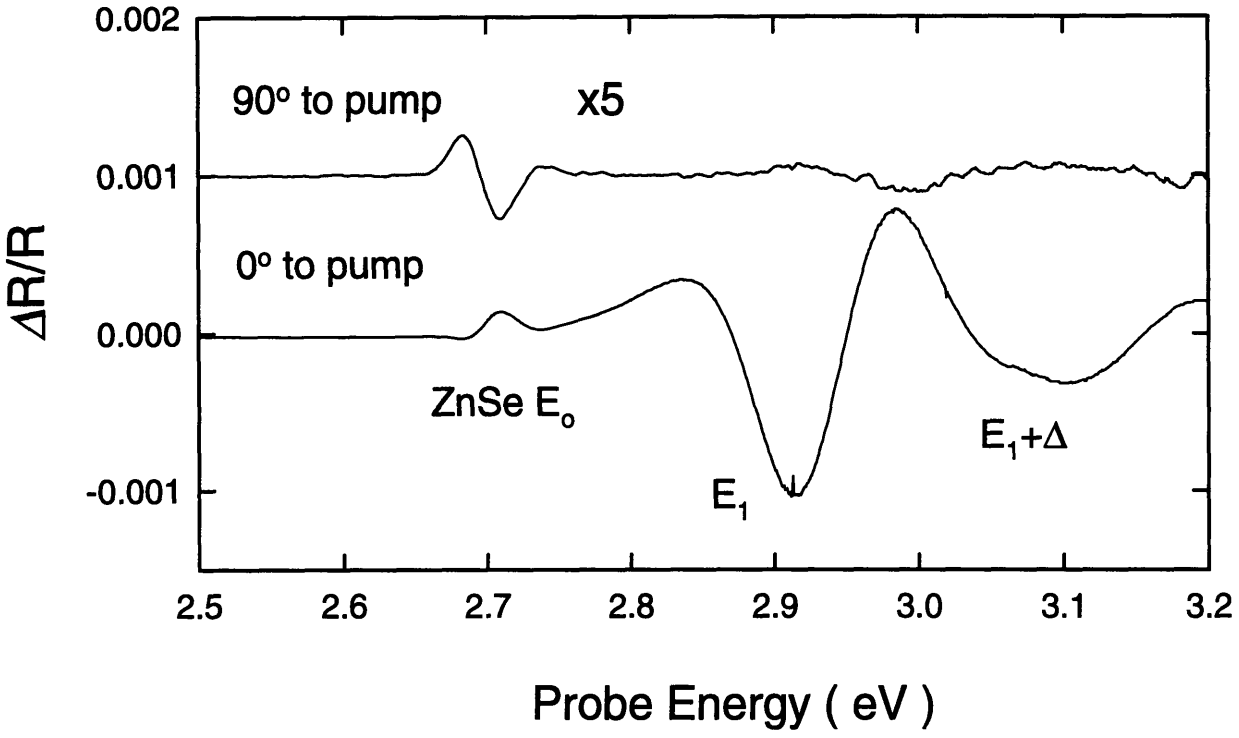

Figure 4-5: PR spectra of Z222 chopping at 800Hz showing the out-of-phase component of the ZnSe signal.

In figure 4-3 the ZnSe PR signals for the below band pumps are quite small and ride on a background from the tail of the GaAs signals. This is not a favorable experimental situation. Fortunately, it is possible to measure the ZnSe signal in a background free way. Figure 4-5 shows PR traces for Z222 taken with the 688nm laser diode chopped at 800 Hz. The traces were taken with the lock-in amplifier set at 90° and 0° to the chopped pump beam. The phase of the pump was determined by removing a colored glass filter in front of the probe detector and measuring the scattered pump light. From these two components, the GaAs E_1 signal is seen to be almost completely in phase with the pump. By varying the chopping frequency, it was found that the E_1 signal is able to follow the pump up to about 2.5 kHz. The ZnSe signal, however, has a significant out-of-phase component. Plotting the phasors constructed from these components in Fig. 4-6, the phase lag is found to be 44°. By setting the lock-in 90° to the E_1 signal, the ZnSe signal can be measured background free. If the ZnSe PR signal originates at the front surface, there is no reason why the time constant should be the same

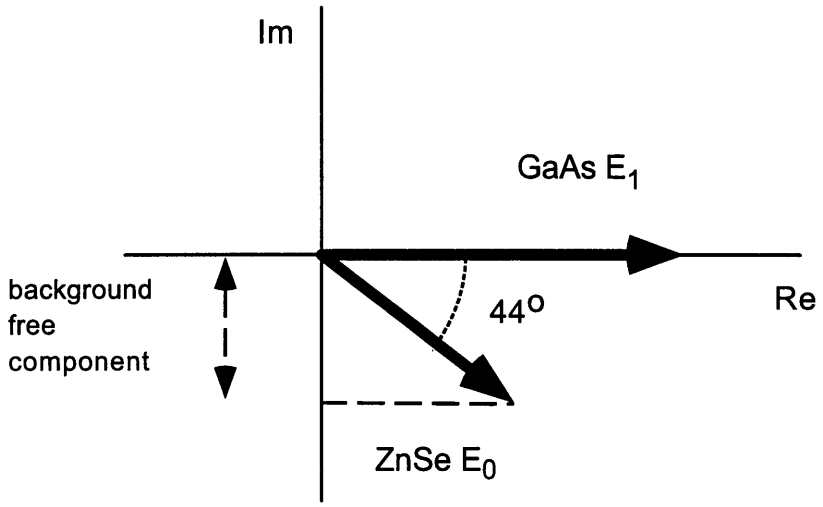

Figure 4-6: Phasor relation between the ZnSe and GaAs PR signals of Fig.

as for the GaAs since the trap states can lie at different energies and have different densities. Even if the ZnSe signal arises from the interface traps, they lie at different energies with respect to the bandedges of the two materials and, therefore, may have different escape rates. For the purposes of this experiment, it is simply fortuitous that the time constants are different and that the ZnSe signal is slow enough that it can be exploited at modest chopping frequencies. Franz-Keldysh and excitonic signals have been separated in a similar manner in Ref. [64].

Another important feature of the PR technique is the pump intensity dependence. As discussed in Chapter 2 (Fig. 2-8), at high intensities the pump may fill all of the available trap states causing the signal to saturate. The pump intensity dependence of the ZnSe PR signal was measured using the HeNe and the HeCd laser. The intensity was determined by using a small pinhole of known diameter and measuring the power in the center of the pump beam spot. A thermo-pile detector was used to calibrate a silicon photodiode power meter in order to accurately compare the power levels at 325 nm and 633 nm. The results are shown in Fig. 4-7 . Note the difference in scales between the top and bottom plots. The saturation intensity increases by a factor of 250 for the HeNe pump.

This makes intuitive sense in the transport picture. Electrons created with sufficient energy must enter the ZnSe before they relax to the bottom of the GaAs conduction band. The large opposing electric field reduces the fraction of arriving electrons further. Assuming that a

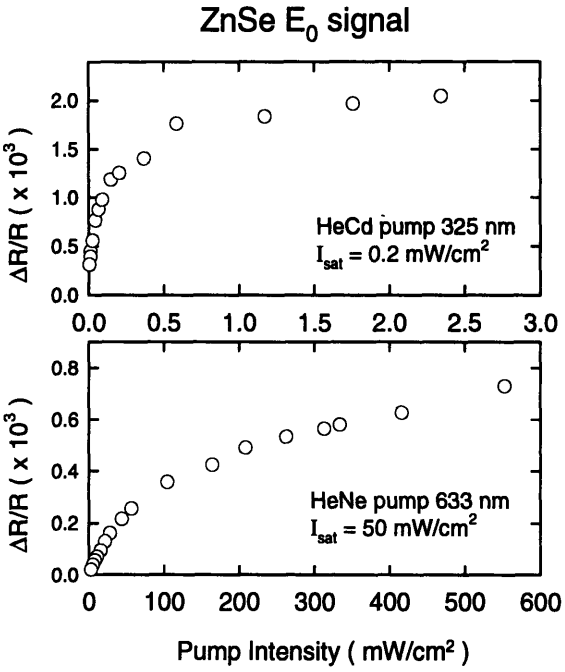

Figure 4-7: PR pump intensity dependencies of the ZnSe signal using a HeCd laser (top) and a HeNe laser (bottom).

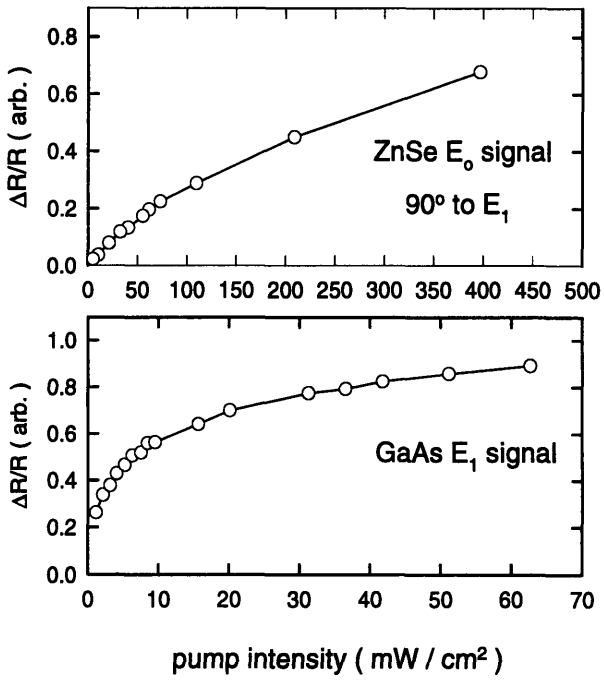

Figure 4-8: GaAs E_1 and ZnSe E_0 PR intensity dependences using a 688nm (1.80 eV) laser diode.

carrier in either material has the same probability of finding a trap state before recombination, a branching ratio can be estimated from the observed power dependences. The absorption length in the GaAs at 2.0 eV is taken as 0.5μm and the HeCd beam is assumed to be completely absorbed in the ZnSe layer. Taking the width of the space charge region of the GaAs side of the junction to be ~500Å, I estimate only 10% of the electrons generated in the GaAs are eligible to cross the junction. Electrons generated in regions of high electron concentration will be rapidly scattered to the bottom of the band. Finally, accounting for the differences in photon fluxes at the two pump wavelengths, a probability of roughly 2% is estimated for electrons at the junction to enter the ZnSe.

Figure 4-8 shows a comparison of the power dependences of the ZnSe and GaAs signals using the 688nm laser diode. Again, the ZnSe saturation intensity is much larger than the ~1 mW/cm^2 necessary to fill the GaAs junction traps. 50 mW/cm^2 is actually a very high

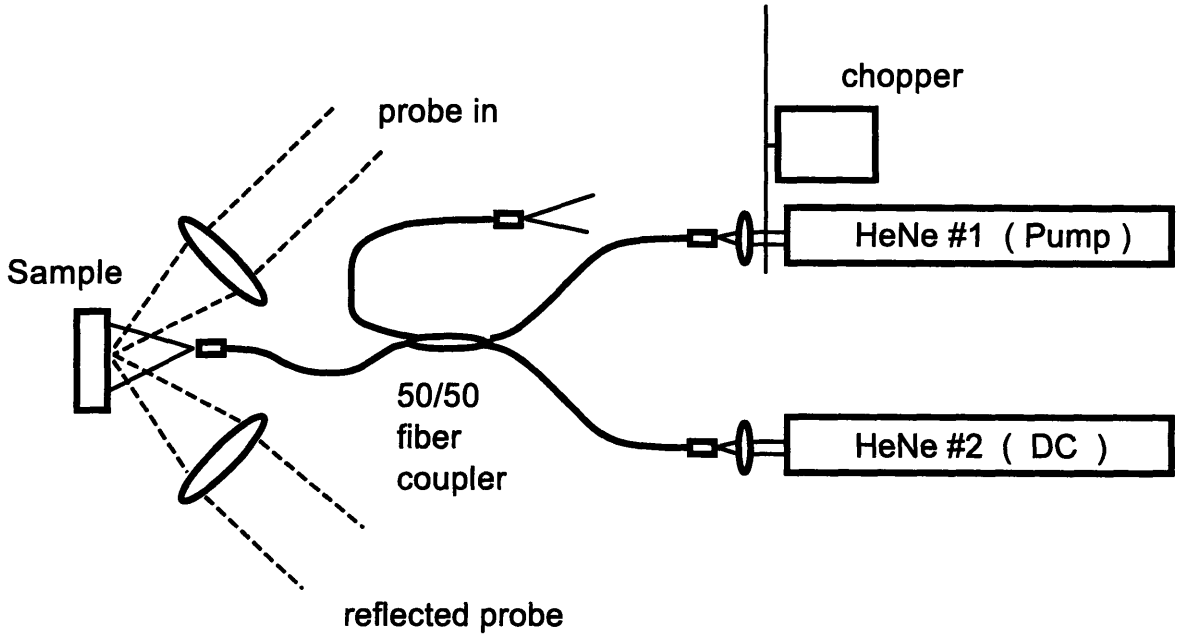

Figure 4-9: Experiment to measure effects high intensities on band bending. DC laser is used to saturate the PR signal while the pump laser is used to record a PR spectrum to measure the field.

saturation intensity for a PR signal. Measurement of the power dependence alone is a good indicator of the existence or lack of a barrier at the junction.

Below the saturation intensity the signal is proportional to the absorbed pump, and therefore, to the number of photo-carriers present. In order to use the PR signal as a probe of the electron population transferred to the ZnSe, the pump intensity must be in the linear regime. This is the most important fact to take into account for the tunable pump experiments described in the next section.

Figure 4-8 raises one final issue which must be addressed. From the plot, it is obvious that to obtain the best signal to noise for the measurement, a pump intensity just below the saturation intensity should be used. This maximizes the signal while remaining linear in the absorbed pump power. The ZnSe saturation intensity, however, is much greater than the GaAs saturation intensity. Completely emptying the surface traps may alter the band bending, and therefore any conclusions drawn on the barrier height. To prove that this is not a problem, the experiment pictured in Fig. 4-9 was performed. Two HeNe lasers, a pump laser and a

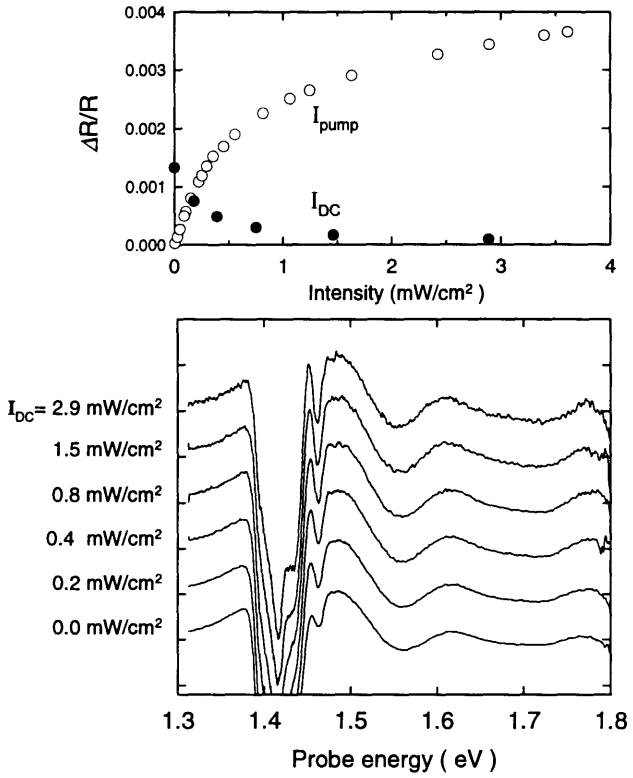

Figure 4-10: Top: White circles - intensity dependence of GaAs PR signal for Z222. Black circles - DC laser saturating signal with the pump fixed at 0.25 mW/cm^2. Bottom: GaAs PR spectra taken at the DC laser intensities in the top plot. No evidence for band flattening is observed from the FK oscillation period.

saturating (DC) laser were used. The purpose of the unchopped DC laser is to fill the junction traps in an attempt to bias the sample. The pump laser was then used to record the PR spectrum as before. Changes in the PR spectrum would indicate changes in the field strength and band bending at the junction. Figure 4-10 shows the results. The white circles in the top plot mark the intensity dependence due to the pump laser with the DC laser blocked. The GaAs PR bandgap signal was monitored. The black circles mark the signal size as the DC laser intensity is increased. The intensity of the pump laser was held at 0.25 mW/cm^2. As I_{DC} exceeds the saturation intensity, the signal is rapidly quenched in a nice mirror image of the pump laser dependence. The bottom plot presents PR spectra measured at each of the I_{DC} values marked by the black circles in the top plot. Clearly, even at 2.9 mW/cm^2, much larger than the 0.25 mW/cm^2 saturation intensity, the spectrum oscillations maintain their period

and shape. Evidently, the charge controlled by the traps represents a small perturbation of the total interface charge density. The band bending is therefore not affected.

4.3 Tunable-pump PR and conduction band offsets

Using the tricks learned in the experiments of the last section, the barrier height measurement will now be described. The conduction band offset is expected to be at most 300 meV based on previous results. A tunable pump laser is therefore required in the range from the GaAs band gap energy of 1.42 eV to about 2 eV. Ti:sapphire is a widely tunable solid state laser which is ideally suited for this experiment. The Ti:sapphire laser used here was tunable from 840 nm (1.48 eV) to 710 nm (1.75eV); limited by the reflectivity bandwidth of the dielectric cavity mirrors. The laser was designed primarily to operate modelocked and serve as a source of ultrashort pulses. CW operation is, of course possible, but a laser designed specifically for widely tunable narrow linewidth operation could use multi-stack mirrors and a tuning range closer to the 690nm - 1 μm gain spectrum of the Ti:sapphire material.

To extend the tuning range, a 688nm laser diode and a HeNe laser were also used to provide two more data points at 1.8 eV and 1.96 eV. A 50/50 single mode fiber coupler was used to combine the beams from the lasers and ensure that the pump light distribution was the same for all of the pump sources. The fiber also served as a convenient variable attenuator to reduce and control the intensity at the sample. At each wavelength, the power was measured at the output of the sample port to avoid errors in the pump intensity due to the wavelength dependence of the coupling ratio. With these precautions, repeatable measurements of the PR signal size could be made when switching between sources.

Light from a quartz-tungsten-halogen lamp filtered through a 1/2 or 1/4 m monochromator served as a probe beam. The probe was guided with lenses and loosely focussed on the sample. The reflection from the sample was then collected and focussed on a 9 mm^2 silicon detector. At the chopping frequencies of a few hundred Hz and above, the lamp is essentially shot-noise limited. The signal-to-noise ratio is thus determined by the amount of probe light reaching the detector. Use of the large NA 1/4m monochromator greatly helps in this regard. Probe bandwidths of 1-2 nm were sufficient to resolve almost all PR spectra. Narrower slits on the

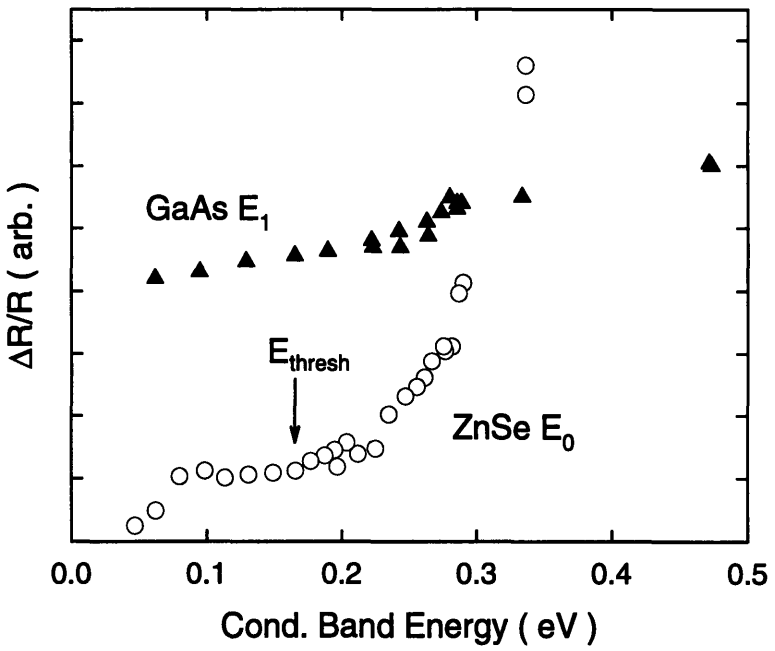

Figure 4-11: Pump energy dependence of the GaAs E_1 and ZnSe E_0 PR signals. Pump energy is plotted as excess electron energy in the GaAs conduction band. The GaAs signal simply follows the GaAs absorption spectrum. The ZnSe signal shows a threshold energy for electron escape into the ZnSe at about 160 meV above the bottom of the GaAs conduction band.

spectrometers only limit the probe power and thus the S/N. A simple transimpedance circuit with a low input bias current OPA-111 FET op-amp from Burr-Brown was used to amplify the detector signal. The feedback resistance was chosen high enough so that the typical probe power used (~4μW) resulted in a 5-6 V output bias. Higher resistances only drive the output to the power supply rail and limit the amount of probe light that can be used. Note, that considering feedback resistor Johnson noise and photo-current shot-noise, the S/N ratio will be shot-noise limited above 50mV of DC output bias.

Figure 4-11 shows the wavelength dependence of the ZnSe PR signal as the pump is tuned. The pump energy is plotted as excess electron energy in the GaAs conduction band

$$E_c = \frac{\hbar\omega_p - E_g}{1 + \frac{m_e^*}{m_h^*}} \tag{4.1}$$

for the determination of the barrier threshold energy. The ZnSe PR signal was measured at the positive and negative peaks (457.7 and 462.1 nm) seen in Fig. 4-3 and subtracted in order to further reduce background from the E_1 signals and scattered pump light.

The dark triangles are measurements of the GaAs E_1 signal. The data was taken at much lower pump powers in order to stay in the linear regime (see Fig. 4-8). The GaAs signal is thus proportional to the absorbed pump light, and is, in fact, a measurement of the GaAs absorption spectrum. This is photoreflectance excitation spectroscopy [60] (PRE). The kink evident at 0.25 eV may be due to the onset of the split-off band absorption. Generally, no pronounced spectral features are observed, however.

The white circles represent the magnitude of the ZnSe PR signal. From the GaAs bandedge (0.0 eV), the ZnSe signal appears as the pump tunes across the absorption edge. This is shifted from the band gap energy by bandfilling due to the high n-type doping. The signal remains constant up to about 0.15 eV, but then dramatically increases indicating the crossing of a threshold. This is exactly the same behavior as is observed in photo-current IPE methods [61, 62]. In these measurements the yield is given by the expression

$$Y = a + b\,(E_c - E_{thresh})^2 \tag{4.2}$$

where E_c is given by Eq. 4.1 and E_{thresh} is the threshold energy for transport across the junction. The constant a represents a wavelength independent contribution to the photo-current, or in this case the PR signal, from thermal emission over the barrier. Subtracting off this level, and performing a least squares fit of $\sqrt{Y}$ to a linear function, the threshold energy from Fig. 4-11 is found to be 160 meV $\pm$ 20 meV.

IPE spectroscopy of a heterojunction usually involves fabrication of a special p-n junction in order to maximize the collected current and to control band bending which may cause formation of other barriers. A typical band diagram of such a structure is shown in Fig. 4-12. The quantity of interest is the conduction band offset, ΔE_c. From the diagram, however, determination of ΔE_c from E_{thresh} requires knowledge of the barrier reduction due to the band bending, Φ_b :

$$\Delta E_c\,(pn\ junction) = E_{thresh} + \Phi_b + \chi_{im.} \tag{4.3}$$

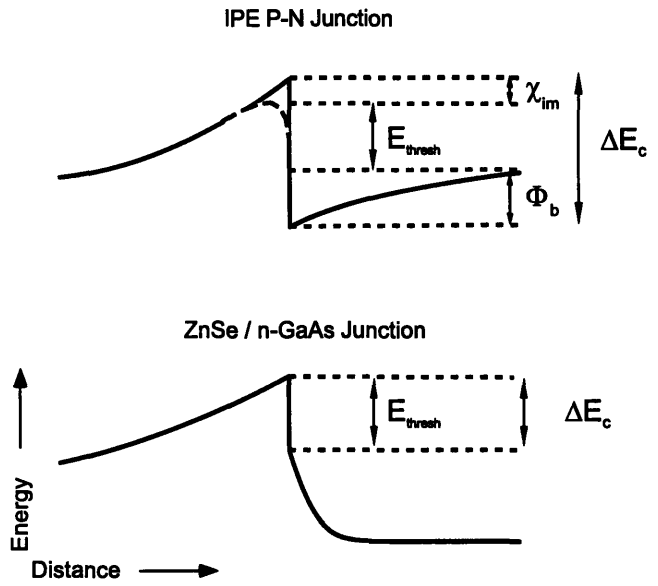

Figure 4-12: Barrier energy parameters for determining conduction band offsets for (top) a conventional IPE p-n junction, and (bottom) a ZnSe/n-GaAs heterojunction.

In the most precise measurements, the term χ_{im}, which represents the barrier reduction due to image charge effects as the electron enters the barrier material, is included. For the fields estimated on the ZnSe side of the junction (2×10^4 V/cm), this term is only about 10 meV which is less than the experimental uncertainty. It will not be included in the conduction band offsets analyses in this work.

The bottom diagram in Fig. 4-12 is the conduction band bending determined from conventional PR and CER methods in the previous chapter. From the shape of the conduction band due to the negative interface charge it is apparent that the minimum energy needed to excite an electron across the barrier is found by absorbing a pump photon right at the junction on the GaAs side. Thus, for the ZnSe/GaAs heterojunctions studied here,

$$\Delta E_c\,(ZnSe/GaAs) = E_{thresh}, \tag{4.4}$$

and the conduction band offset is directly given by the threshold energy. The spatial form of the band bending will affect the functional form of the yield, but not the threshold energy.

4.4 n-type GaAs results

The results for Z222 serve as a model against which other samples can be compared. Figures 4-13 and 4-14 outline the results of the same series of experiments for two other ZnSe/n-GaAs samples. The upper left plot of figure 4-13 shows the layer structure of sample Z223. The sample consists of a 0.12 μm thick undoped ZnSe layer grown on an n-type GaAs buffer layer. This sample was grown as part of a nucleation investigation unrelated to this work. The ZnSe growth was initiated on a 4×4 Ga surface formed with a nitrogen source on. Presumably GaN may form at the interface. The effect on these interface measurements, however, is seen to be minimal in the CER and PR spectra of the upper right-hand plot. Large, long period oscillations occur very similar to those found for Z222, and the n-GaAs samples of the previous chapter, n24 and n44. Again, a negative surface charge dominates the interface as seen from the signs of the CER and PR signals. The HeNe pump intensity dependence shown in the bottom left plot, indicates a fairly large saturation intensity implying that the electrons cross the junction with difficulty. This suspicion is confirmed by the threshold behavior in the tunable pump plot on the bottom right side. The threshold energy, which is the same as the conduction band offset, is found to be 180 meV±20 meV.

Sample Z194 shown in Fig. 4-14 is also very similar to Z222 and Z223. The CER and PR traces again indicate a negative surface charge leading to exposure of the conduction band offset as a barrier. The relatively high saturation intensity of 10 mW/cm^2 follows the model. The conduction band offset for this sample is measured to be 180 meV ± 20 meV.

Both of these samples show very similar behavior to that of Z222. The agreement between the observed field sizes, interface charge signs, and conduction band offsets strengthens confidence in the model of the ZnSe/GaAs interface set forth in this and the previous chapter. Repeating these measurements for the pair of samples n24 (ZnSe on 2×4 reconstructed n-type GaAs) and n44 (ZnSe on 4×4 reconstructed GaAs) would have been ideal for further confirmation. Unfortunately, the ZnSe signals in these samples had a fast time constant like the GaAs

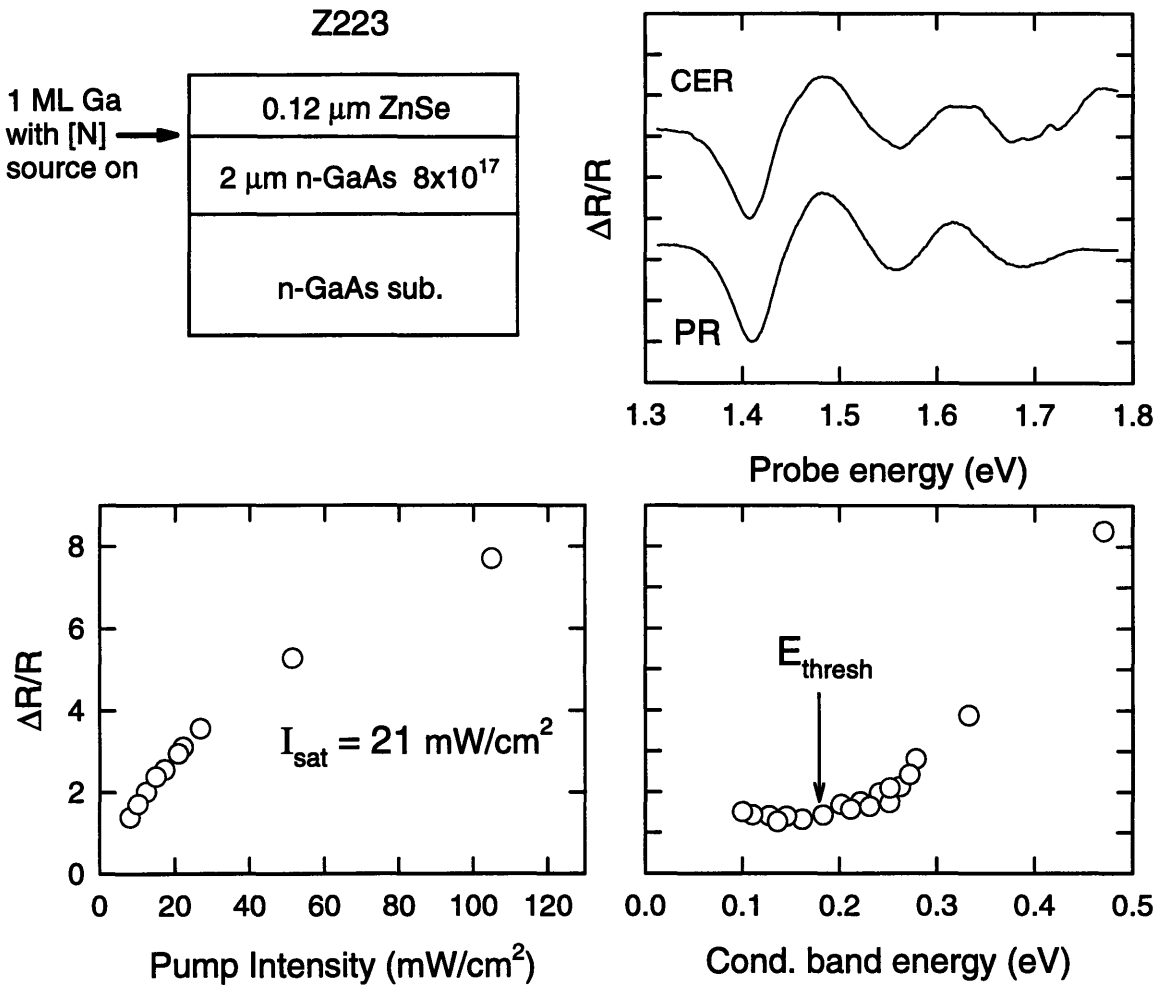

Figure 4-13: Top left: Sample structure of Z223. Top right: CER and PR spectra of the GaAs bandedge. Signs indicate negative interface charge. Lower left: Pump intensity dependence indicates a large saturation intensity suggesting a barrier at the junction. Lower right: Tunable pump PR determination of the conduction band offset. ΔE_c =180 meV.

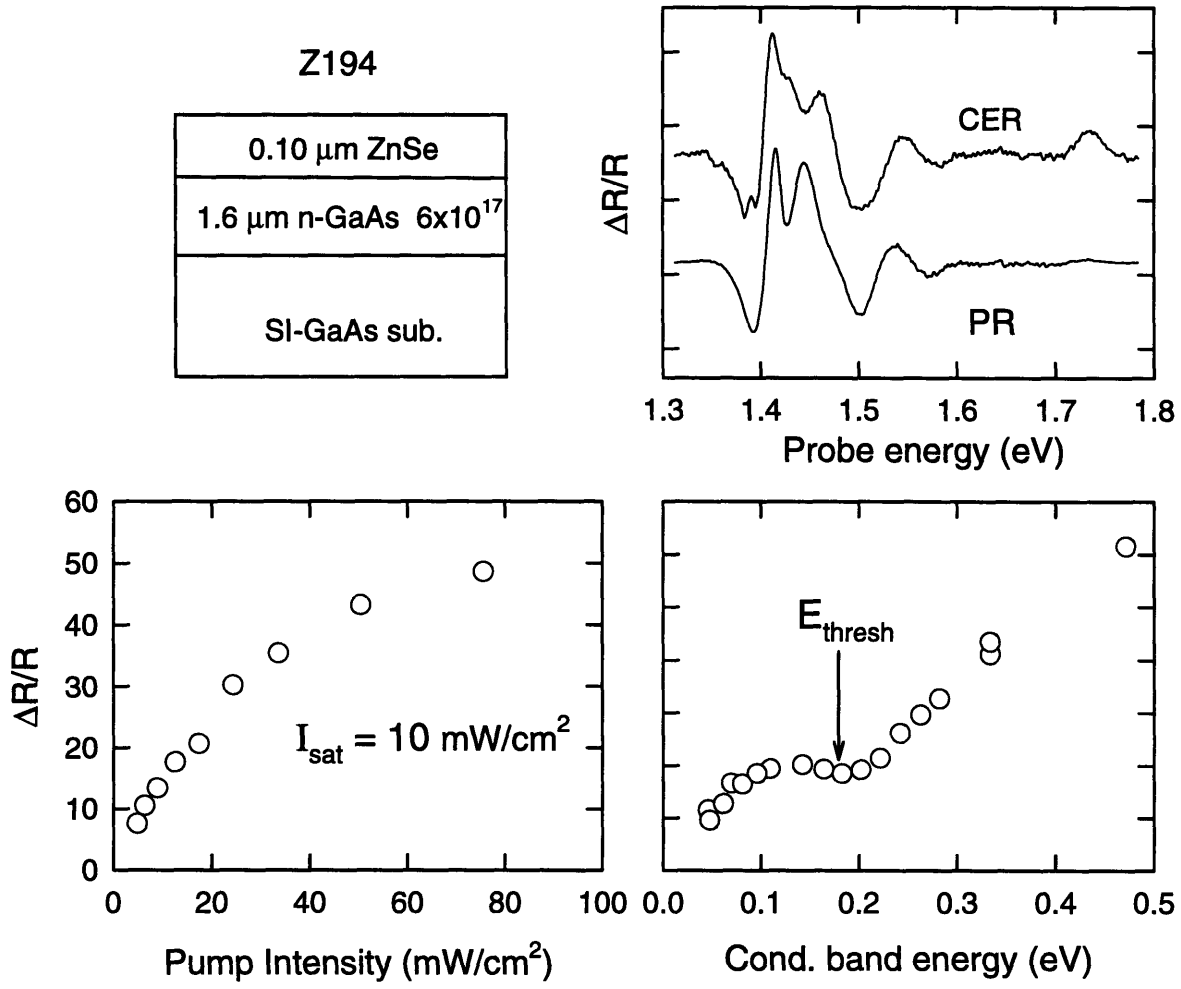

Figure 4-14: Top right: Sample structure of Z194. Top left: CER and PR spectra of the GaAs bandedge indicating negative interface charge. Lower left: HeNe pump intensity dependence of ZnSe PR signal showing a large saturation intensity. Lower right: Tunable pump PR determination of the conduction band offset. ΔE_c =180 meV.

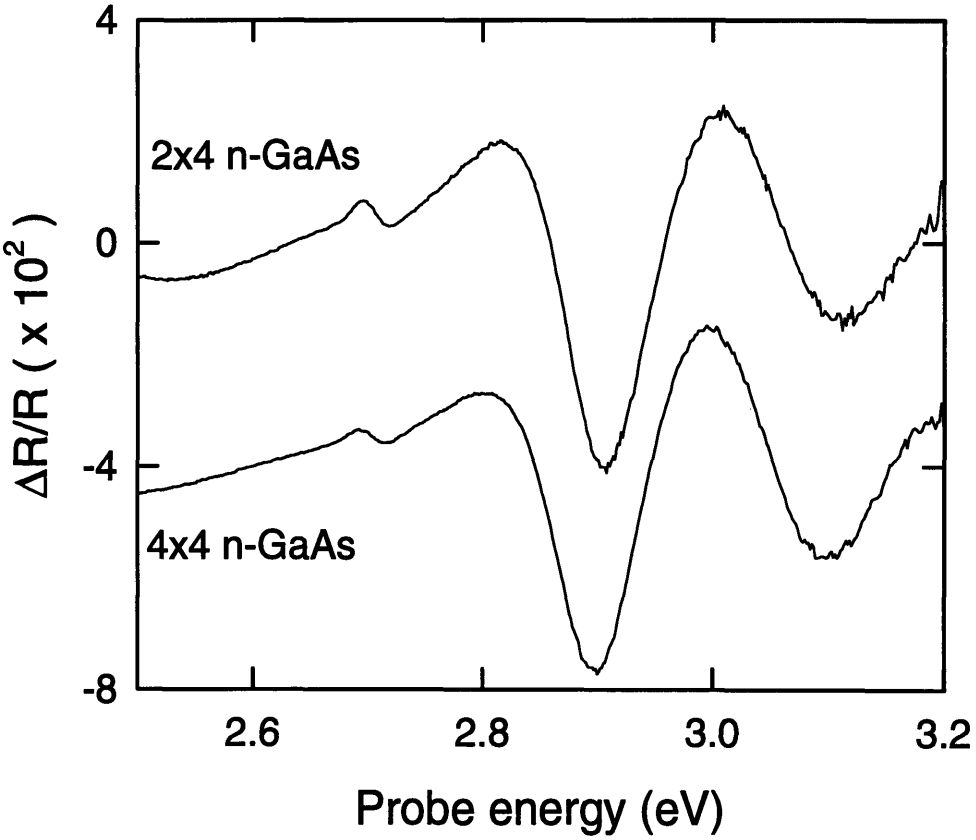

Figure 4-15: PR spectra of samples n24 and n44 taken with a HeNe laser. ZnSe and GaAs signals are in phase with the pump out to high frequencies prohibiting the tunable pump measurements.

signals. No phase lag which could be exploited for background free measurements was found out to 3kHz chopping frequency, which was as fast as the mechanical chopper and the detector could go. PR measurements obtained with a HeNe laser of the ZnSe E_0 and the GaAs E_1 transitions are shown in Fig. 4-15 for reference. The ZnSe signal is present indicating electron transport across the junction.

4.5 Comparison of junctions with positive and negative interface charge

All of the ZnSe/GaAs heterojunctions presented so far have had negative interface charge densities. Even the two SI-GaAs samples in the preceding chapter were found to have negative interface charge. Other studies of ZnSe/SI-GaAs junctions have found samples with fields on the GaAs side pointing into the bulk, giving rise to band bending which shields the conduction band offset. One ZnSe/SI-GaAs sample in this work was found with fields pointing into the bulk (i.e. there was a positive interface charge density). The ZnSe layer for this sample was 0.5μm thick, however, and was therefore relaxed. In order to compare this sample to the others, it was necessary to also measure a 0.5 μm thick ZnSe film grown on n-GaAs with a negative interface charge. Creation of dislocations at the junction may be thought to disrupt the lattice enough so that electrons from the GaAs could find low energy pathways into trap states on the ZnSe side of the junction. Failure to observe threshold behavior in the tunable pump experiments may not have anything to do with the actual band bending. The results of this section show that this is not the case, and that the junction model developed so far holds even for relaxed, thick ZnSe films, such as must be used in almost any practical application.

Figure 4-16 shows the PR and CER spectra of sample Z345. The spectra differ enough so that firm conclusions cannot be drawn as in previous cases, but it does appear as if the spectra have opposite signs in looking at the features near the bandedge. Opposite sign CER and PR imply fields pointing toward the junction. This could mean a positive interface charge, or it could simply result from modulation doping effects. In any case, the band bending will counteract the conduction band offset and will lower the threshold energy between the materials.

This conclusion is supported by the intensity dependence and band offset measurements shown in Fig. 4-17. The left plot compares the saturation intensity of Z345 to sample Z350, a 5000Å thick ZnSe film grown on an n+ GaAs substrate. The much lower saturation intensity for Z345 (SI-GaAs) indicates that the electrons have no trouble entering the ZnSe from the GaAs side. The saturation intensity of sample Z350 is comparable to those found earlier. The left plot shows the pump energy dependence of the ZnSe PR signals. While the n-GaAs sample shows the familiar threshold behavior, the curve for Z345 is flat indicating no threshold energy

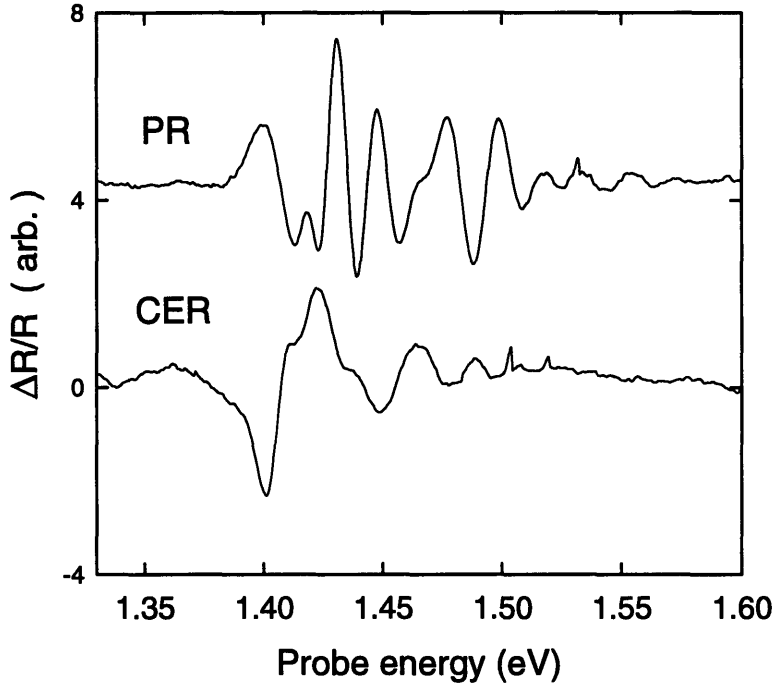

Figure 4-16: PR and CER traces for a 5000 Å ZnSe film grown on SI-GaAs. Opposite digns of signals indicates positve interface charge.

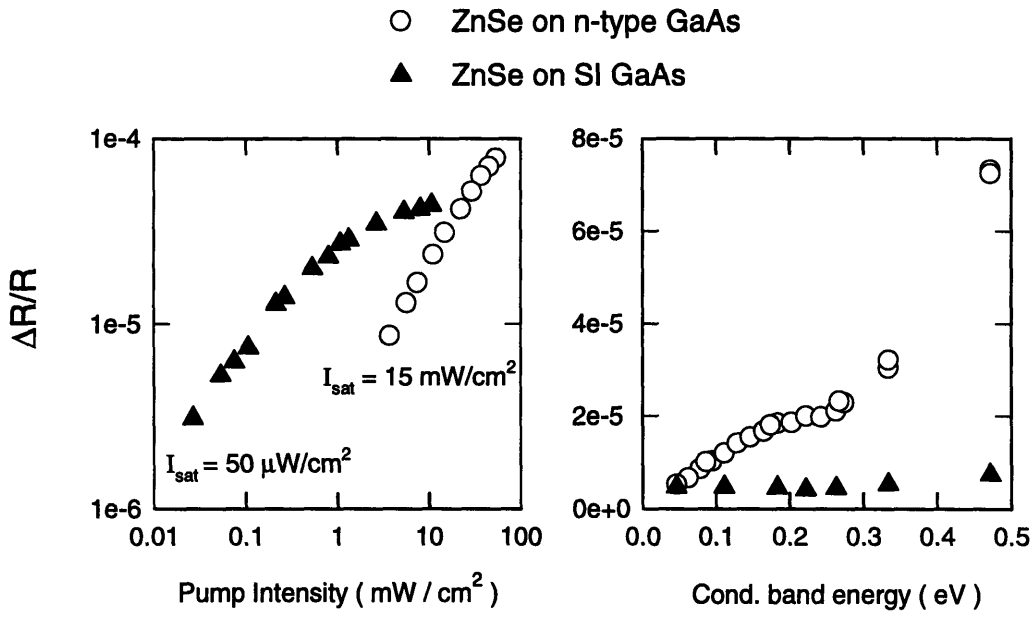

Figure 4-17: Comparison of ZnSe PR results for samples with positive and negative interface charges. Left plot: Comparison of saturation intensities. Right: Tunable pump measurements. SI GaAs sample shows no threshold and a much lower saturation intensity indicating no conduction barrier between the ZnSe and the GaAs.

to overcome and no barrier between the materials.

4.6 Semi-insulating GaAs samples

Finally, conduction band offset results for the two ZnSe/SI-GaAs samples measured in chapter 3 are presented in this section. Both of these samples were found to have a negative interface charge. The ZnSe PR spectra for these sample are shown in Fig. 4-18. Because the GaAs E_1 signals were much smaller than found for the n-GaAs samples, the pump energy dependence could be measured despite the fact that very fast time constants were observed. The conduction band potential barrier caused by the interface charge is directly evident in the pump energy dependence of the ZnSe PR signals. Figure 4-19 shows the results for the 2×4 reconstructed sample (i24). The data are noisy, but appear to show a threshold of about 110 meV ± 30 meV.

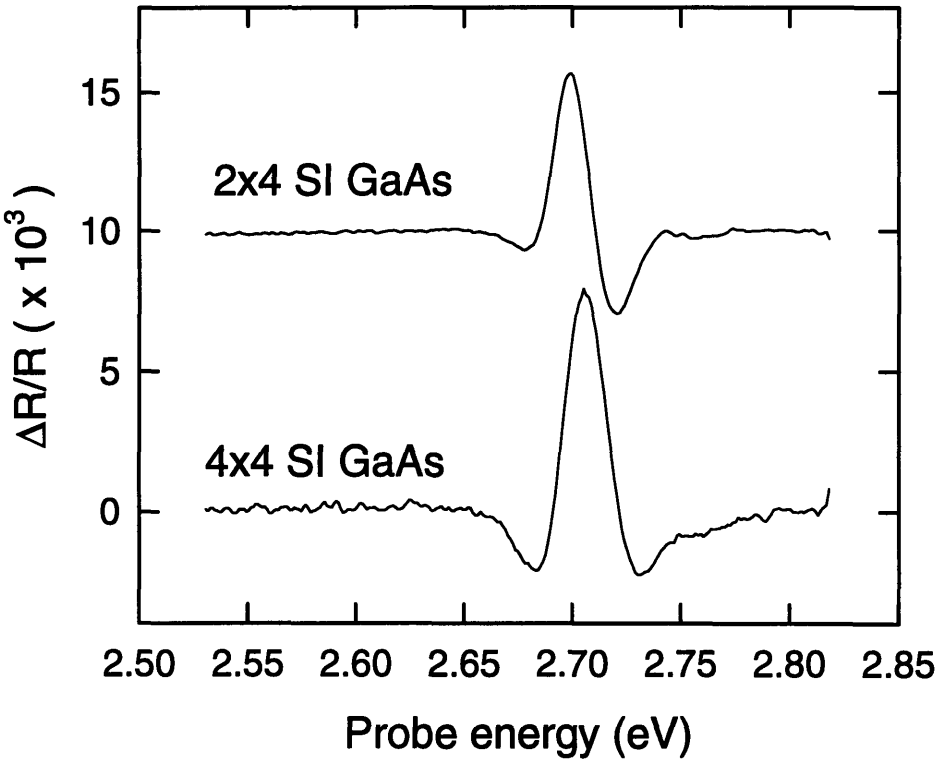

Figure 4-18: PR traces of the ZnSe bandedge of samples i24 and i44 (ZnSe on 2x4 and 4x4 SI GaAs) taken with a HeNe laser.

Data for sample i44, shown in Fig. 4-20, is the clearest example of this technique found so far. Again, a threshold of about 110 meV is found. The reason for the observation of lower conduction band offsets for the SI-GaAs samples is not clear. The thermal excitation background in both of these samples is relatively much lower than for the n-GaAs data. Excitation across the barrier from the high energy tail of the electron distribution in the heavily doped samples appears to cause this background.

1

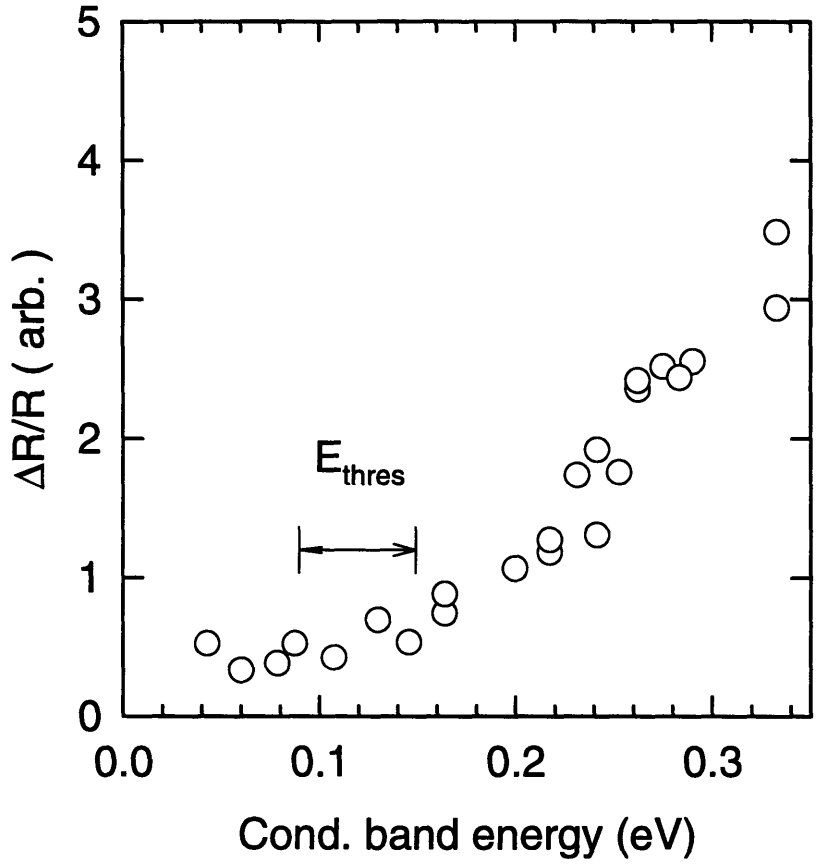

Figure 4-19: Tunable pump PR plot for sample i24 with estimated threshold energy as shown.

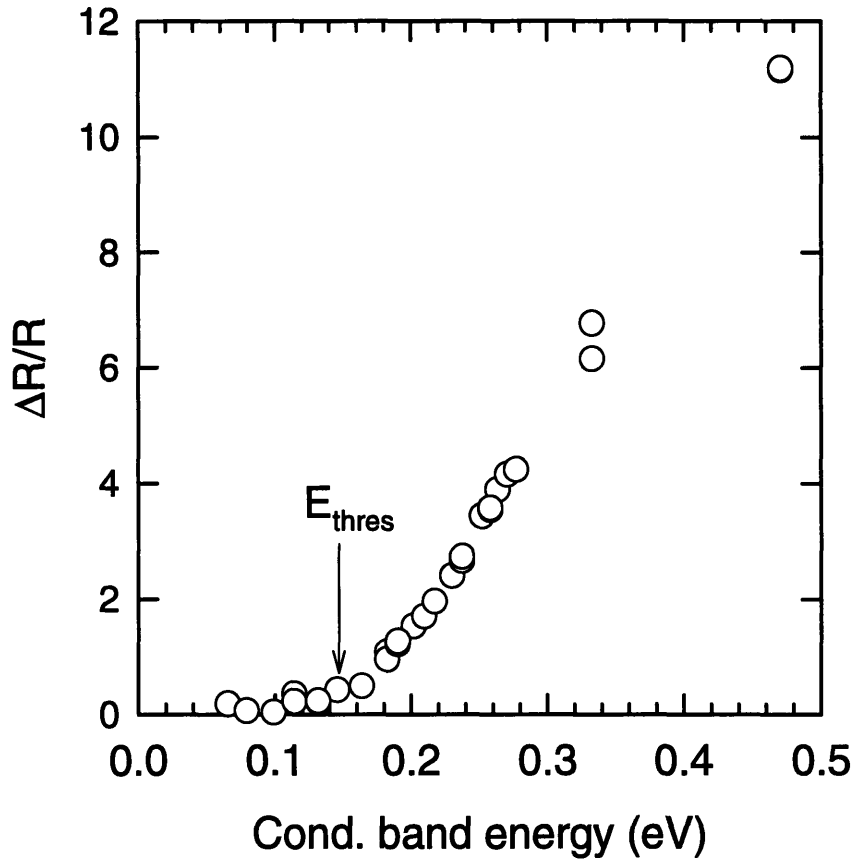

Figure 4-20: Tunable pump PR plot of sample i44 showing sharp threshold at 0.12 eV above the bandedge.

Chapter 5

Conclusion

Table 5.1 summarizes the results of the ER and PR measurements performed in Chapters 3 and 4. Every sample grown on n-type GaAs was observed to have very large electric fields present at the heterojunction on the GaAs side. Using both CER and PR measurements, the direction of the field was found to point toward the interface on the GaAs side. This suggests a that the interfaces have a large negative surface charge. With the field pointing towards the junction, the bands on the GaAs side bend down with distance away from the ZnSe, and the tunable pump barrier height measurements directly determine the conduction band offset. The observed values are significantly lower than the band offsets reported by Kassel et. al. [26]. As discussed in Chapter 3, their mis-assignment of the GaAs E_1 transition as some sort of spatially indirect cross-over transition seems to cast doubt on their results. The conduction bands offsets obtained by the tunable-pump PR method generally fall between 160 and 200 meV. Sample

Z350 from table 5.1 showed a threshold energy closer to 250 meV.

Sample	thickness	GaAs doping	GaAs	E. Field	Charge	Offset
	(μm)	(cm^{-3})	recon.	(V/cm)	sign	(meV)
Z222	0.12	n-type 7×10^{17}	4×4	2.2×10^{5}	-	160
Z223	0.12	n-type 8×10^{17}	4×4	2.3×10^{5}	-	180
Z194	0.10	n-type 6×10^{17}	4×4	1.0×10^{5}	-	180
n44	0.10	n-type 1×10^{18}	4×4	8.8×10^{5}	-	NA
n24	0.10	n-type 1×10^{18}	2×4	7.8×10^{5}	-	NA
Z350	0.50	$1\times10^{18}(n^{++}$sub)	4×4	9.5×10^{5}	-	250
i44	0.10	SI	4×4	4.2×10^{4}	-	110
i24	0.10	SI	2×4	3.5×10^{4}	-	110
Z345	0.50	SI	4×4	2.8×10^{4}	+	NA

(5.1)

(5.2)

The semi-insulating GaAs samples showed much smaller electric fields at the junction. The GaAs electric fields for two samples, i24 and i44 of Chapter 3, were unambiguously shown to point towards the interface by PR and CER measurements. Thus, the band bending for these samples is the same as found for the n-type GaAs samples with the band bending adding to the potential barrier. This picture was confirmed by the tunable-pump measurements which found threshold energies of about 110 to 120 meV above the GaAs conduction band. The CER and PR results for sample Z345, discussed at the end of Chapter 4, suggest that the GaAs electric fields, in this case, point into the GaAs, consistent with modulation doping or a positive interface charge. The bands on the GaAs side would then be expected to bend up, acting to remove the barrier presented by the conduction band offset. This was confirmed in the tunable-pump measurements where no threshold behavior was observed, indicating that the photo-electrons created in the GaAs have no trouble entering the ZnSe. The much lower ZnSe PR saturation intensity found for this sample also supports this picture.

Based on these results, several conclusions may be drawn. The size of the GaAs electric fields seems to be determined primarily by the doping. It is hard to see how doping at 10^{18} cm^{-3} could affect inter-diffusion of ions across the junction which is supposedly driven by electric fields due to charge imbalances on the first one or two monolayers of material at the junction and which is claimed to result in doping densities above 10^{19} cm^{-3} localized within 100 Å of the junction [24, 25]. If interdiffusion were the dominant source of the observed fields and band bending, the n-type and semi-insulating samples would, thus, be expected to give similar ER and PR results. In addition, the sign of the electric field was observed to be opposite to that expected for a p-n junction formed by Ga donors in ZnSe and Zn acceptors in GaAs.

The more mundane model of surface traps controlling the band bending, therefore seems more appropriate. The lower fields for the semi-insulating GaAs samples would then simply be due to the presence of fewer free electrons to be trapped at the surface. Semi-insulating GaAs is formed by doping with mid-gap donor and acceptor ions [65] to pin the Fermi level near half-the band gap. Depending on the nature of the interface states, either electrons or holes could be formed on the interface due to charge exchange with these mid-gap donors and acceptors. This could explain the observation of electric fields pointing both towards and away from the interface in different SI-GaAs samples.

On a microscopic level, these results do not give much information on the exact nature of the interface charges. No other characterization techniques, however, would fare any better. Buried interfaces severely restrict the available surface analysis techniques. In fact, it is not even known if the surface traps have anything to do with the ZnSe at all. They could be present on the GaAs before the ZnSe growth is started. In situ PR measurements could determine if this is the case. Such further detailed analysis, however, misses the point. These results are important because of the implications for transport in devices. Further research should be directed towards eliminating these surface charges and reducing the potential barriers to electron conduction between the GaAs and ZnSe. The CER and PR experimental framework set-up in this thesis seems to be the best way to characterize the band bending since these techniques are the only optical, contactless methods which can directly give the field magnitude and sign.

The interface trap densities on the n-type GaAs samples were not observed to be strongly dependent on the GaAs surface reconstruction. Only small differences were seen between the 2x4

and 4x4 reconstructed GaAs samples. More work is necessary to determine if these differences are really due to the initial GaAs surface structure. More mundane factors such as growth temperature, beam pressure ratios, and growth rate may be more important. Annealing has been observed to reduce large electric fields observed in ZnSe/GaAs double-heterostructure samples [66], and may lead to a simple solution to this band bending problem.

The nature of the band bending observed was fortunate, in one sense, because it allowed the tunable-pump PR barrier height measurement to directly determine the conduction band offsets. Some variation was observed, which may possibly be expected given the results of Refs [19, 17]. All of the band offsets were observed to be significantly less than the 300 meV value often quoted in the literature. The results for samples Z345 and Z350 are significant because the ZnSe layers were relaxed. The observation of a threshold energy for the n-type GaAs sample (Z350) shows that dislocations do not effect the barrier height between the materials.

Besides the specific experimental results for the ZnSe/GaAs interfaces that were obtained, several new experimental techniques were developed in the course of this work. The use of CER and PR together to determine the sign of electric fields is a fairly straight forward idea, but is not generally appreciated in the literature. This may be due to the fact that researchers generally know the origins of the electric field in the samples under study, and that often the focus is on characterizing energy of levels in quantum wells or of bandgap energies rather than the fields themselves. This combination of measurements is useful because complications due to spatially non-uniform fields, thin film interferences , and presence of bound states alter the observed lineshapes from those predicted by the simple, uniform field theory of Chapter 2. Using PR to determine which direction of the CER field results in reduction of the built-in field can circumvent all of these difficulties.

The tunable pump technique represents a new method for measuring barrier heights at junctions. It is simple to implement compared to x-ray synchrotron photo-emission experiments, and is non-destructive and contactless. Extension to other interesting materials systems, such as InGaP/ZnSe, InGap/GaAs, or infra-red semiconductors such as the antimonides, should be straight forward. For materials with band gaps closer in energy than for ZnSe and GaAs, more care need to be taken in the filtering of the pump beam since color glass filters are not very sharp in wavelength. A 1/4m double-monochromator would be the ideal probe source for these

measurements. The second, synchronized spectrometer would be used for filtering before the probe detector. Pump detunings as small as can be achieved in photo-luminescence excitation (PLE) methods could then be achieved. An alternative solution is to find higher energy PR signals for the barrier material (such as the E_1 or E_2 transitions) that ,hopefully, are far removed from the other material's bandgap. This is a major advantage of PR as opposed to PL.

An auto-tuning pump laser would also be a major improvement. Much of the spread in the data points can be eliminated attributed to low frequency variations in the pump power rather than probe-shot noise. This is especially true when background signals due to scattered pump light or other PR transitions are present. Stabilizing the pump and performing multiple scans would reduce this problem. The trick of using the chopping frequency and lock-in phase to distinguish between overlapping PR signals does not always work. A vibrating mirror in the probe monochromator could be used for rapid scanning over the PR signal being monitored. Tuning the lock-in to the sum or difference of the probe scanning and pump chopping frequencies would then eliminate the background signal.

Part II

Time-Resolved Photoreflectance of GaAs surfaces

Chapter 6

Time resolved PR of GaAs

In this chapter, the mechanism of photo-reflectance will be investigated in more detail by time resolving the surface trapping of the injected minority carriers. The samples studied were simple GaAs bulk substrates and epilayers. Several sub-picosecond studies of GaAs reflectivity have been made in the past [67, 68, 69], and the observed signals were attributed to carrier dynamics, plasma effects, and changes in band-filling due to diffusion. The experiments described here show that the dominant response near the GaAs critical points is due to screening of surface electric fields.

As discussion in Part I, PR signals may be conveniently 'time-resolved' simply by changing the chopper frequency since the frequency response is so slow. An experiment using a digital oscilloscope to look at the probe modulation in the time domain on a micro-second timescale has been reported [70]. These slow time responses are associated with deep surface traps. The equilibration times with the bulk free carriers are slow because the escape time from a trap is an exponential function of the trap binding energy. Shallower traps can equilibrate much faster. The micro-second experiments time resolve the net transfer of charge to the surface and not the time it takes for an individual hole to be captured.

The pump-probe technique used to measure fast processes with ultrashort pulses will be described briefly first. This chapter will thus serve as a bridge to the ultrafast carrier dynamics studies in Part III. Experimental results for GaAs will then be discussed. Finally, some ideas on the application of these results will be presented at the end of the chapter.

6.1 Pump-Probe Spectroscopy

Ultra-short ($\tau_p < 100$ fs) light pulses produced by modelocked lasers can be used to time-resolve processes that occur too quickly for electronic circuits. The beam from the pulsed laser is split using a beam splitting mirror into a pump beam and a probe beam. The two beams are then separately focussed onto the same spot on the sample. The purpose of the pump pulse is to excite the sample causing changes in its absorption or refractive index. The probe pulse is used to measure these changes either in transmission or reflection. By reflecting the probe beam from a mirror on a movable stage before it hits the sample, the relative arrival time between the pump and probe pulses at the sample can be varied. Thus, the probe can be set to intercept the sample at a fixed time delay behind the pump and to interrogate the state of the sample at that point in time. By measuring the modulation induced on the probe by the pump as the stage is scanned, the sample dynamics can be mapped out using only low frequency detection of the probe. The timing of the pulses is depicted in Fig. 5.1.

If the excitation of the sample is small enough, it will be linear in the pump intensity. The time response, r(t), of the induced change in the optical properties is obtained by convolving the pump intensity profile, $I_p(t)$, with the sample impulse response, A(t) (which is assumed to be causal),

$$r(t) = \int_{-\infty}^{\infty} dt' A(t') I_p(t - t'). \tag{6.1}$$

The probe pulse following at delay, τ, is modulated by this response and the resulting total pulse energy is measured with a slow detector

$$S(\tau) = \int_{-\infty}^{\infty} dt I_{pr}(t - \tau) r(t). \tag{6.2}$$

By making suitable variable changes, one can show that this is equivalent to

$$S(\tau) = \int_{-\infty}^{\infty} dt A(t + \tau) \int_{-\infty}^{\infty} dt' I_{pr}(t') I_p(t - t'). \tag{6.3}$$

Thus the pump-probe trace, $S(\tau)$,can be thought to be the result of the sample response,

$A(\tau)$,being driven by the cross-correlation waveform of the pump and probe. The cross-correlation width of the pump and probe combined determines the time resolution of the system. If both pulses are very short, the pump probe trace will simply be the sample impulse response mapped onto the delay, τ.

6.2 Experimental results

The laser used for these time-resolved PR (TRPR) experiments was a modelocked Ti:Sapphire laser producing 100 fs pulses and operating in the wavelength region from 840 nm to 960nm. By second harmonic generation (SHG) in a nonlinear beta-barium-borate (BBO) crystal, either the pump or the probe beam could be converted to the blue spectral region in the range 420-480nm. More on the laser, and pump-probe set-up details will be left to the chapters on carrier dynamics in Part III.

Figure 6-2 shows a reflection pump-probe traces using a IR pump pulses and SHG blue probe pulses at energies of 2.963 eV (418 nm), 2.925 eV (424 nm), and 2.917 eV (425 nm). The sample is a 3μm thick GaAs epi-layer doped n-type at 3×10^{16}cm^{-3} with Si. The substrate is SI GaAs. The pump and probe were focussed with a fused silica lens to an approximately 20 μm spot. The pump power was 2.5 mW resulting in a 2.8×10^{17} cm^{-3} density of injected carriers. The probe power was 200μW. The traces are composed of a fast negative step which drops with the integral of the pump pulse and slow step with 5-6 ps rise time. The sign of the slow component varies with probe energy. The negative step seen at all probe energies represents a reduction of the refractive index, and is consistent with an increase in the plasma frequency due to the injected carriers. The top plot of Fig. 6-3 shows the 425 nm trace with a fit generated by convolving a 1 ps exponential plus a step response with the system cross correlation. The dynamics are evidently non-exponential. The bottom plot shows the same data at short time delays with the measured system cross-correlation to emphasize that the response is due to two competing step responses: one that turns on instantaneously, and one that turns on slowly.

At this point, many physical mechanisms for the index non-linearity can be imagined. One possibility is that some of the photo-generated electrons and holes are scattered to high energy states in the conduction and valence bands by carrier-carrier collisions. Figure 6-4 shows the

bandstructure of GaAs with the pump and probe transitions marked. Electrons scattering to the L-valley would be detected by the probe on the E_1 transition. The dynamics would then, presumably, be due to inter-valley scattering processes.

The correct interpretation of these results becomes apparent when the magnitude of the slow rising component is plotted against the probe wavelength as in Fig. 6-5. The solid curve is an experimental conventional PR trace of the E_1 transition taken with a HeNe laser and a lamp. The excellent agreement between these spectra identify the index non-linearity as resulting from the Franz-Keldysh effect. The slow rising component in the pump-probe trace is therefore measuring the screening dynamics of the built-in surface field.

6.3 Free carriers vs. Traps

Having established that the reflectivity changes are due to the Franz-Keldysh effect, it is still necessary to prove that the dynamics are due to surface trapping in order for the experiment to be called 'time-resolved photoreflectance' or TRPR. The photo-injected free carrier plasma will of course screen electric fields without having anything to do with the surface. A quick estimation of the time and length scales involved will resolve the issue.

At a doping density of 3×10^{16} cm^{-3} and a surface charge density of 10^{11} cm^{-2}, the surface field is 50 kV/cm and the depletion width is about 400 Å. After optical injection at 4×10^{17} cm^{-3}, the Debye length is about 70 Å. The probe, however, only senses changes in the dielectric constant within about 100 Å of the surface due to the extremely high absorption in GaAs at 2.9 eV [59, 31]. The situation is illustrated in Fig. **??**. Thus, holes must be physically trapped on the surface in order to reduce the electric fields sensed by the probe.

The time scales for free carriers to reach electrostatic equilibrium can be estimated by either the dielectric relaxation time, $\tau = \sigma/\epsilon$, or the inverse plasma frequency, $\tau = 2\pi\omega_p^{-1}$. In both cases τ is much less than 100 fs, much too short to account for the several picosecond rise-time seen in Fig. 6-3.

6.4 Modelling

The disparity in length and time scales between the screening behavior of free carriers and the observed response greatly simplifies analysis of the problem. Instead of having to solve the full device equations [13], a quasi-static picture seems appropriate. The number of electrons trapped on the surface, N_e, is governed by a rate equation involving the total number of traps, N_{trap}, rate constants κ_p and κ_n , and the free electron and hole densities at the surface

$$\frac{dN_e}{dt} = \kappa_n(N_{trap} - N_e)n(z=0,t) - \kappa_p N_e p(z=0,t). \tag{6.4}$$

The surface free carrier densities are calculated by solving the Poisson equation

$$-\nabla^2\Phi = \frac{e}{\epsilon}\left[p - n + N_d^+\right] \tag{6.5}$$

with degenerate Fermi statistics and subject to boundary conditions involving the trapped surface electrons, and the optically injected carriers

$$\Phi'(z=0,t) = \frac{e}{\epsilon}N_e(t)\ ,\ p(z=\infty,t) = p_{inj}\ ,\ n(z=\infty,t) = n_{inj}. \tag{6.6}$$

The potential and free carrier densities are time dependent only through the changing surface charge density. Because the equilibration time of the electrons and holes via drift and diffusion are extremely fast on the short length scales we are considering, the surface free carrier densities will adiabatically follow the surface field.

The rate equation (Eq. 6.4) is to be integrated numerically by a Runge-Kutta method with the Poisson Eq. being solved at each time step. The structure of these equations is very similar to simple population dynamics which yield non-exponential solutions with rise times controlled by the initial populations.

The goal of this model is to account for the dynamics shown in Figs 6-7 - 6-9. The traces in Fig. 6-7 are the TRPR components of the pump-probe response taken at different power levels and normalized to unity in order to compare their time dependence. As the pump is increased, the trapping proceeds faster. This can be seen more clearly in Fig. 6-8 where the circles and triangles represent the 40% and 80% rise times of the traces in Fig. 6-7. Fig. 6-9 shows

the magnitude of the TRPR component at 20 ps delay versus pump power. The saturation of the signal size is intuitively in agreement with the rate equation model described above. The saturation is not due self-bleaching of the pump pulse since the maximum injected carrier densities are estimated to be only 6×10^{17} cm^{-3} and the pump is 50 meV above the band edge. The pump saturation intensity was found to vary for different spots on the sample indicating spatially varying surface state densities. This may lead to applications in characterization which will be briefly described next.

6.5 Future work

If data such as in Fig. 6-3, and 6-7 can be fit quantitatively through the material parameters κ_p, κ_n,and N_{trap}, the TRPR may become a useful non-contact tool for characterizing surface treatment procedures. Repeating these experiments for silicon would be very interesting because of the sophisticated washing, etching, and oxide deposition technologies used in electronic device fabrication. The E_1 transition in Si lies at about 3.4 eV [31] and is accessible by SHG of Ti:sapphire or modelocked laser diode pulses. The fact that Si is an indirect gap semiconductor does not matter for the pump. Eventually, it would be interesting to try and build an instrument to image surface state densities. The use of a laser as a probe in PR allows high spatial resolution and sensitivity. The drawback with using a laser in the conventional method of PR is that data analysis is done on the PR spectrum requiring a widely tunable source. Learning to extract surface densities from the dynamics is an important result of this work since power and time dependences can be measured rapidly at each point in an imaging system, and tuning is not required.

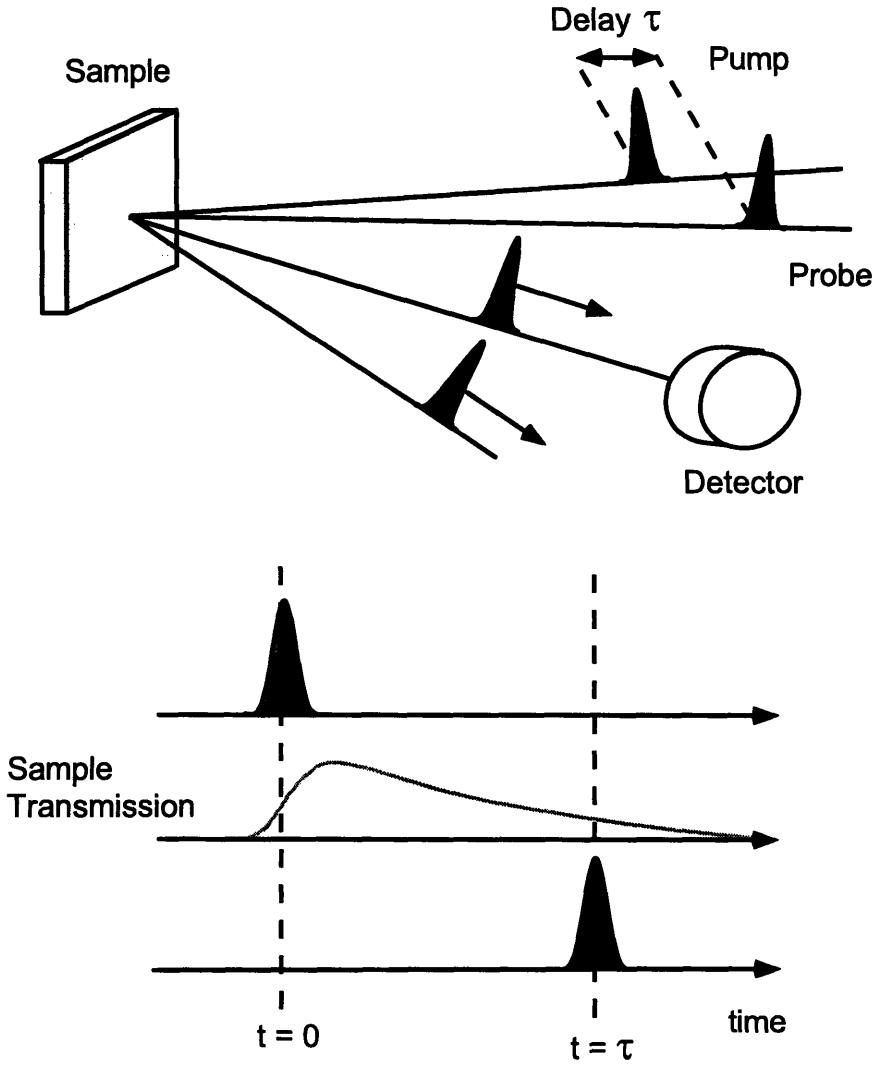

Figure 6-1: Top: Reflection pump -probe experiment. Bottom: Timing diagram showing how probe intercepts the sample dynamics always at the same point for a given delay, τ, in the path length.

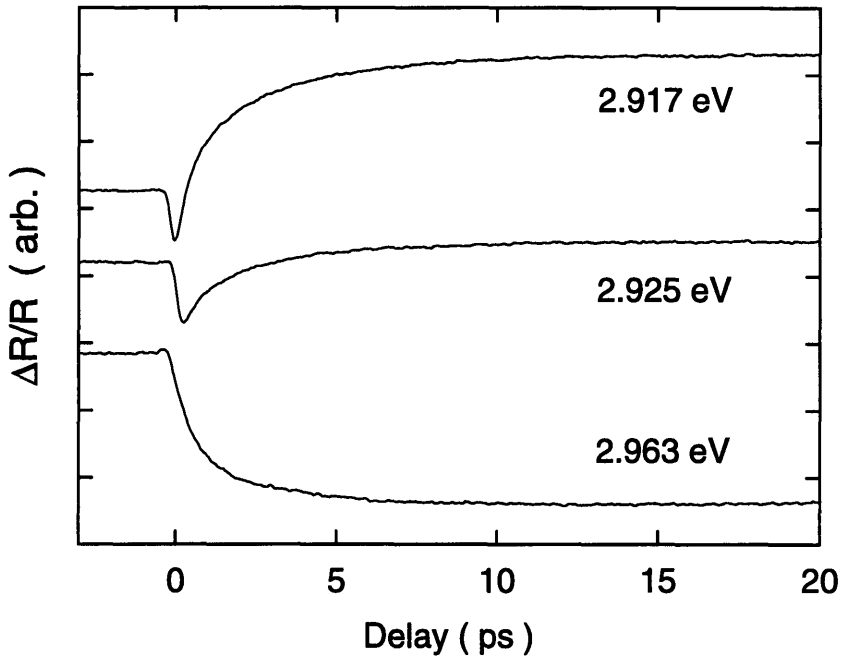

Figure 6-2: IR pump - Blue probe reflectivity traces for a $3x10^{16}$ cm^{-3} n-type GaAs epilayer.

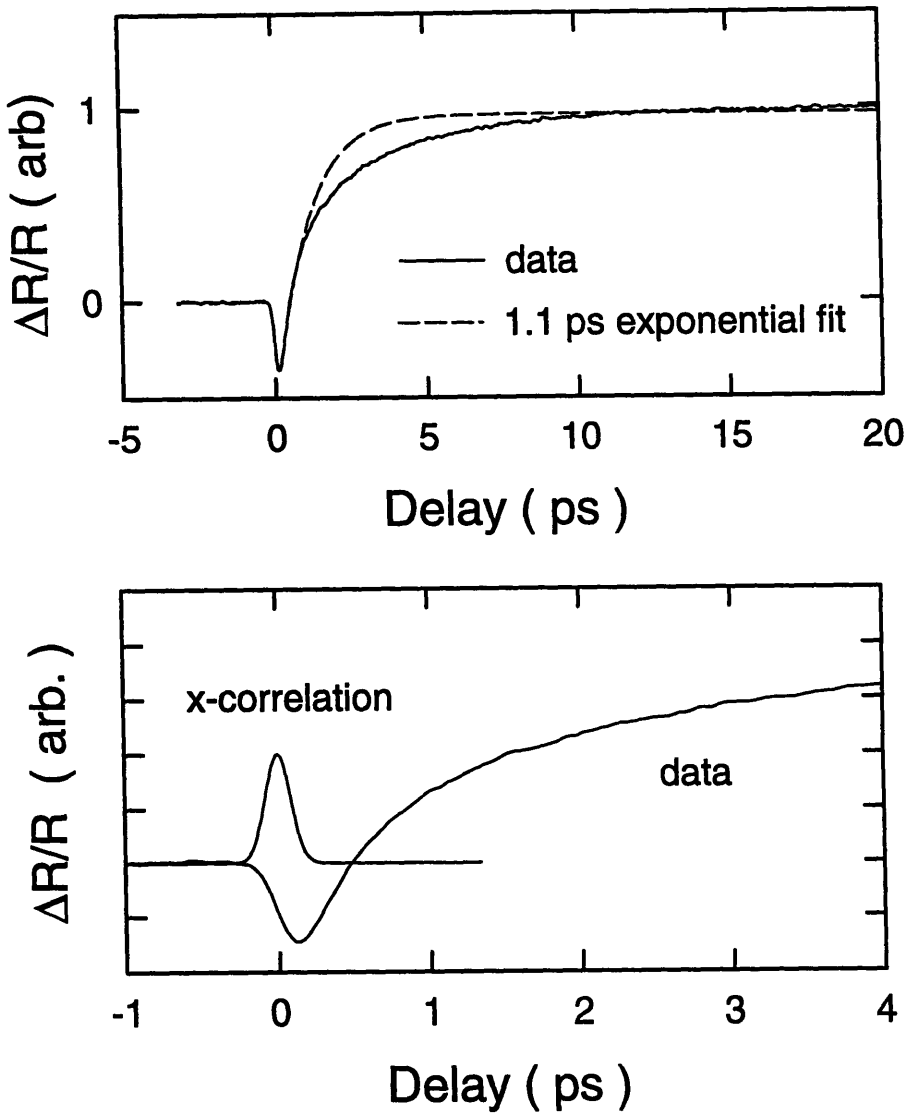

Figure 6-3: Top: Pump-probe trace at 425 nm with 1.1 ps timeconstant fit to demonstrate non-exponential nature of the response. Bottom: Close-up view at short times with the measured system cross-correlation. The response is composed of two competing step functions, one of which has a slow turn-on time.

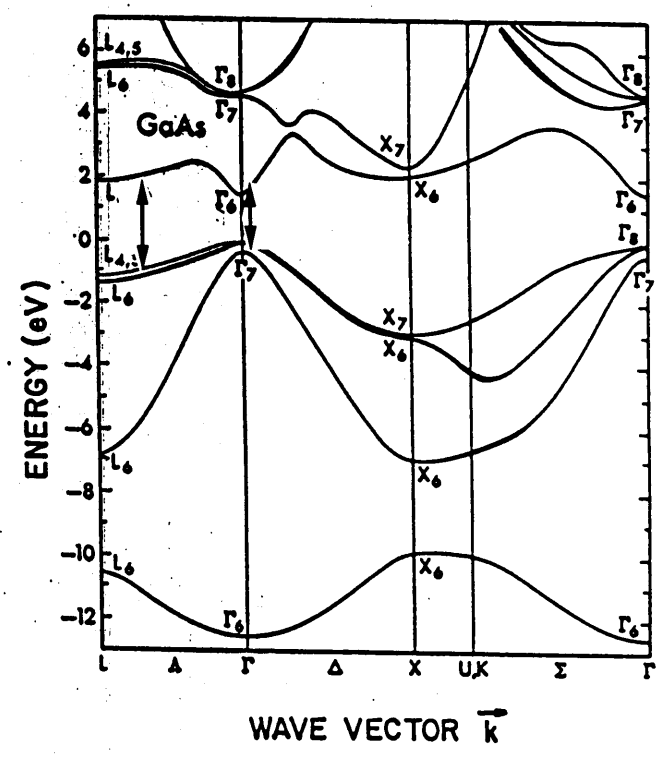

Figure 6-4: Band structure of GaAs. The arrows mark the pump and probe transitions.

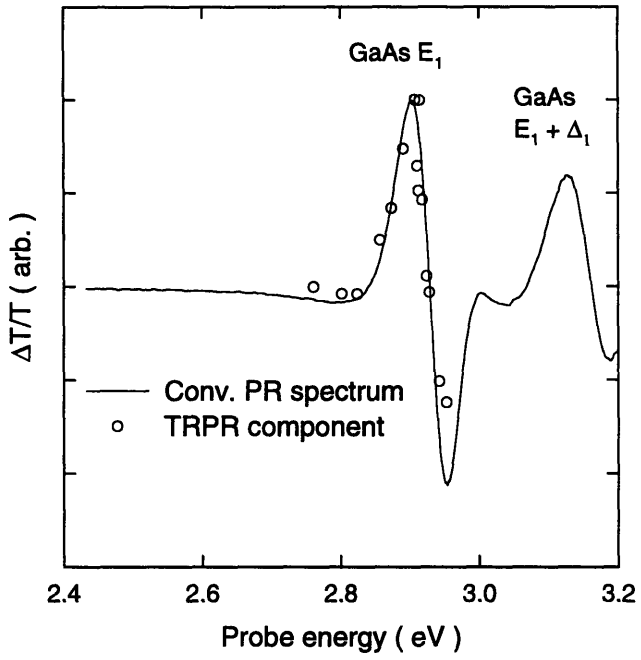

Figure 6-5: Solid curve: Conventional PR spectrum of the E_1 GaAs transition. Circles: Magnitude of the slowly rising component in the reflectivity response.

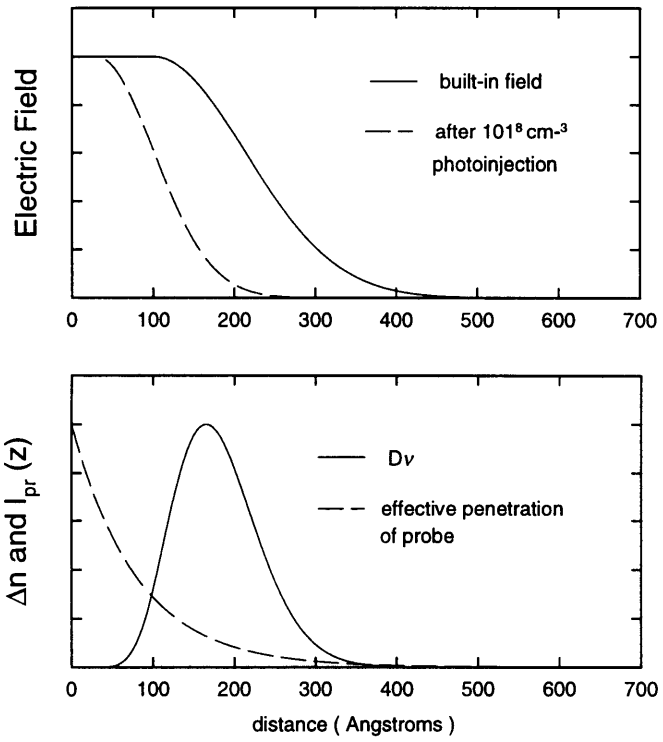

Figure 6-6: Top: Plot of the spatial dependence of the surface electric field before and after 10^{18} cm^{-3} photoinjection. Bottom: Index changes due to the free carrier field screening (solid line), and penetration of the 2.9 eV probe.

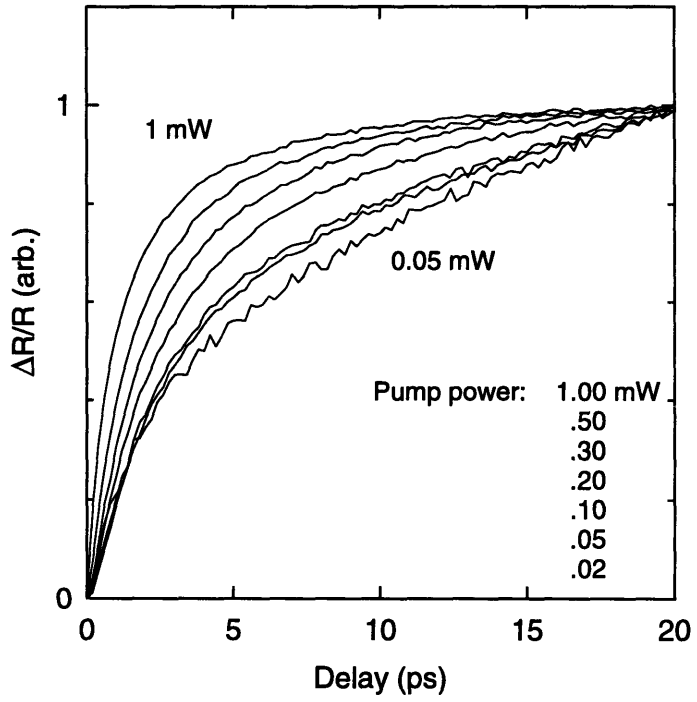

Figure 6-7: Dynamics of PR component as a function of pump power. Traces are scaled to compare the shape of the temporal response.

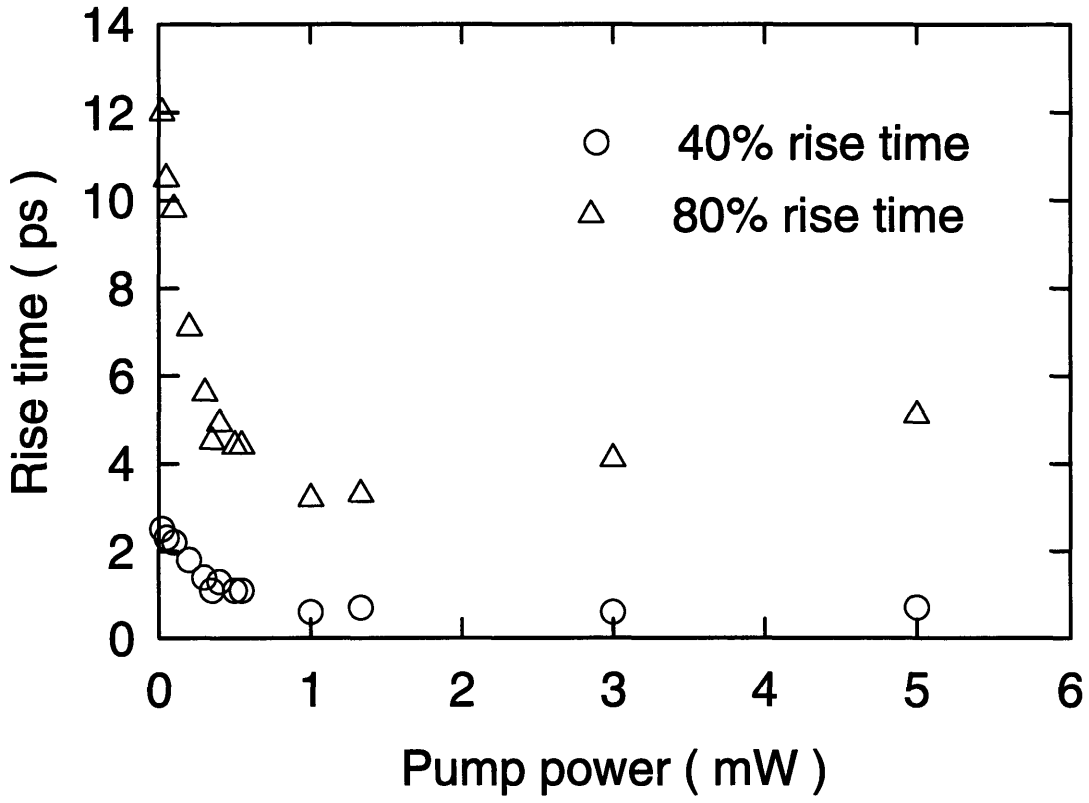

Figure 6-8: 40% rise time (circles) and 80% rise time (triangles) of the non-exponential dynamics in Fig. 6-7. With more free holes available to be trapped, the screening of the surface electrons gets faster.

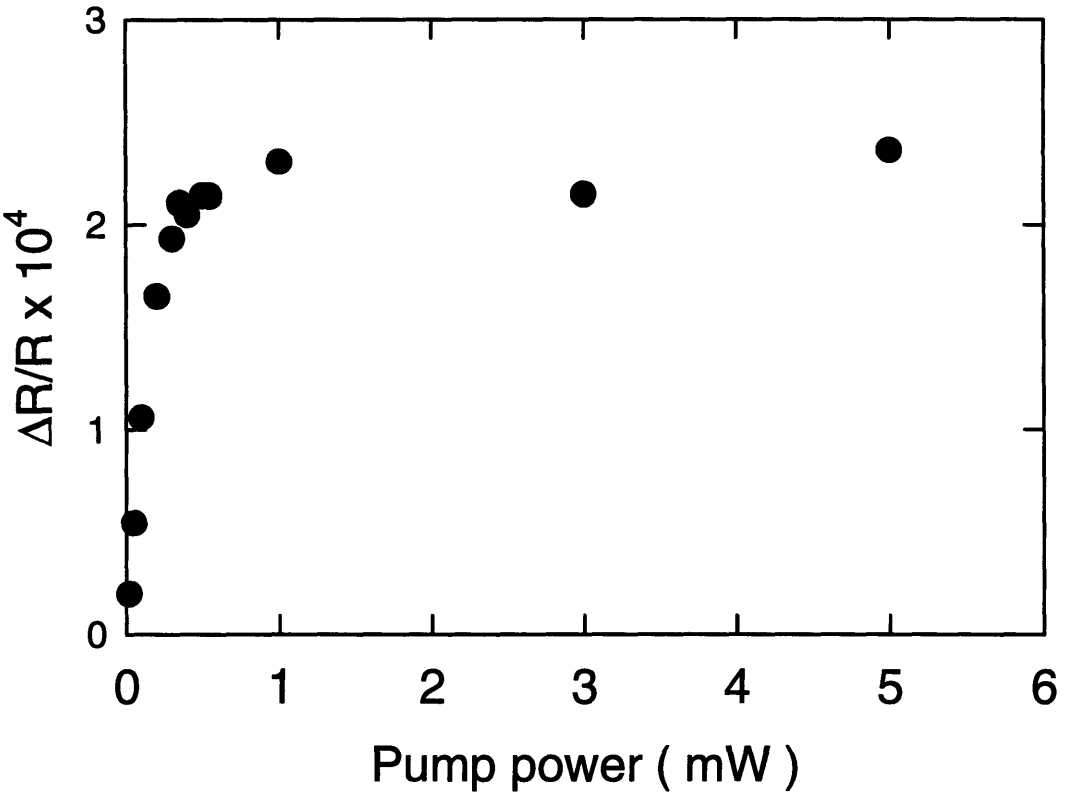

Figure 6-9: Saturation of the PR signal size with pump intensity occurs at the same point as the saturation of the response time.

Part III

Ultrafast optical nonlinearities in ZnSe

Chapter 7

Introduction

The optical and electronic properties of semiconductors are governed by fundamental scattering processes between elementary material excitations [71, 72, 73]. Mobile electrons and holes scatter among the various Bloch states of the ideal, single-particle Hamiltonian, used to determine the bandstructure, due to interactions among themselves, vibrations of the lattice, collective plasma oscillations, and impurities. The processes result in redistribution of momentum and energy and determine macroscopic quantities such as the electrical and thermal conductivity and the optical absorption and luminescence spectra.

Often, these interactions are calculated using time-dependent perturbation theory (Fermi's golden rule) to obtain the rates at which certain processes occur [72, 74]. Sorting the many possible scattering mechanisms according to timescale serves to establish the basic physical environment in which further analysis of a specific experiment or devices should proceed. For instance, for short enough time or distance scales, and at low densities, the motion of carriers can be treated ballistically using semi-classical equations of motion. In another situation, fast scattering may necessitate calculating averaged velocities and energies of a distribution of particles using the Boltzmann equation [75]. Sophisticated numerical methods such as Monte Carlo calculations attempt to track the individual paths of test particles in devices such as high speed transistors. The rates of many simultaneously occurring processes are needed as input to calculate the probability that a given particle will continue on its current trajectory or be scattered at each time step.

Since many of these interactions happen on sub-picosecond (10^{-12} sec) timescales, direct

experimental observation of scattering times has had to await the development of ultrashort pulse lasers. As discussed, briefly, in the last chapter, ultrashort pulses can be used to excite a material and then gate or sample the transient changes in the absorption or reflectivity with a time resolution far beyond the capability of electronics. The explosion of interest in Ultrafast Optics in the past 10 years has stemmed, to a large degree, from the fervent hope that spectroscopic determination of the properties of semiconductors on ever shorter timescales can lead to faster electronic (and optical) devices for communications, computing, and instrumentation. Pulses of 100 fs (10^{-13} sec) duration are routinely produced by modelocked dye [76], color-center crystal [77], solid state [78], and fiber lasers [79] . The current record for pulse duration is 4.5 fs obtained by compression of 10 fs pulses from a cavity-dumped modelocked Ti:sapphire laser operating at 800 nm [80].

These femtosecond sources have been used to study a wide variety of physical processes in the near-IR III-V semiconductors such as GaAs and the important InGaAsP family of compounds. This work has resulted in the identification of four timescales relevant for non-equilibrium carrier dynamics in semiconductors [81]. The four regimes are the *coherent regime*, the *non-thermal regime*, the *hot-carrier regime*, and the *isothermal regime*. These time scales serve only as a general guide and some overlap may exist depending on the specific situation.

The *coherent regime* ($<$ 100 fs) deals with the fastest fundamental processes. Here, the oscillators, comprised of the electronic states of the medium, have not yet dephased by collisions and are able to coherently follow the pump field excitation. Many of the ideas of atomic physics, on much slower nano-second to microsecond timescales, have analogs in semiconductors in this regime. Photon echoes, quantum beats, and free induction decay have all been observed for quantum well states [82](wave packet dynamics), excitons [83], and even free carrier transitions (heavy hole -light hole beats) [84, 85]. Most of these experiments must be carried out at low temperatures and low densities to avoid rapid thermal dephasing.

In the *non-thermal regime* from 50fs to 500fs, with the material coherence destroyed, the excitations of the medium are described as electrons and (or) holes occupying bandstructure states. The distribution functions of the electrons and holes are not Fermi-Dirac, and still retain the characteristics of the excitation process (e.g., the pump laser spectrum)[86, 87]. This situation is called spectral-hole burning [88]. At high densities, carrier-carrier scattering

events act to redistribute energy [89, 90, 91, 92] and momentum [93]in the population and bring the distribution to equilibrium. At lower densities, equilibrium must arise from slower carrier-phonon scattering events. Thus, the time scale of this regime is somewhat blurred. The transfer of electrons from the central conduction band valley to the satellite valleys also occurs on this time scale [94, 95].

Having reached an equilibrium distribution among themselves, the electrons and holes can each be described by a temperature. These temperatures may be well above the lattice temperature, and so this is the *hot-carrier regime.* The important processes here are carrier-phonon scattering and electron-hole scattering to establish a common temperature between the electron, holes, and the lattice. This time scale (200fs - 5ps) is very important for small, high speed electronic devices [96, 97]such as HEMTs (hot electron mobility transistors) and Gunn diodes as well as optical devices such semiconductor laser diodes and amplifiers .

The slowest regime is the *isothermal regime* where the cold electron and hole distributions recombine to establish over-all equilibrium in the system (i.e., a single Fermi level). In good quality direct bandgap material, recombination times are on the order of 1 - 10 ns. Laser diode require long carrier lifetimes in order to achieve population inversion, but currently there has been much interest in the ultrafast optics community on materials with very short carrier lifetimes on the order of 100 fs. Materials such as low temperature grown GaAs [98, ?]are useful as fast saturable absorbers for modelocking lasers to produce short pulses and as photoconductive antennas in THz radiation experiments. Recombination physics, therefore, can also be important in the other, faster regimes.

The work presented in this thesis is mostly concerned with the non-thermal and hot-carrier regimes described above. The physics on these time scales is most directly applicable to useful devices. Figure 7-1 shows a situation that can occur in a high field region of a semiconductor transistor [97, 99]. Electrons diffusing into a space charge region are accelerated by the electric field. This would result in the translation of the electron distribution function up in energy as the electrons move. Fast carrier-carrier interactions prevent this from happening and the distribution evolves to a smeared out high temperature Fermi distribution. This hot electron distribution then cools via phonon emission which transfers energy to the lattice. Since the mobility of the electrons may be a function of their energy above the conduction band [100],

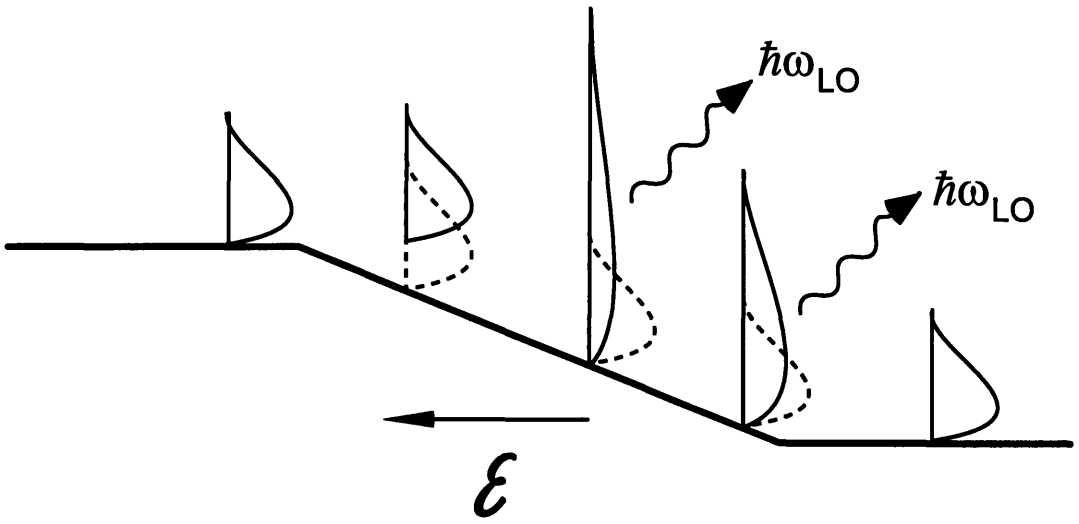

Figure 7-1: Schematic diagram of an electron distribution injected into a region of high electric field. Electrons are initiallly ballistically accelerated, but fast carrier-carrier scattering results in a hot Fermi distribution which subsequently cools to the lattice temperature by emmitting phonons.

the speed of the device depends on the rate of energy increase due to the electric field and energy loss due scattering with the lattice.

Carrier-phonon interactions with sub-picosecond time constants are important on much slower times scales as well. Figure 7-2 shows a quantum well being pumped by current injection from the barrier materials. The well provides good spatial confinement of the electron and hole populations which is necessary for population inversion. However, it also means that each electron and hole brings ΔE_c or ΔE_v of energy with it which heats up the distributions. The lasing optical fields acts to remove cold carriers by stimulated emission, further heating the distributions. Temperature changes of a few degrees K can affect the total gain available in the device and may lead to shifting of the lasing wavelength. In addition, phonons can directly take part in the stimulated emission process. Knowledge of the carrier phonon coupling coefficient obtained from ultrafast measurements can be useful in modelling these processes [101].

Understanding fast carrier dynamics is therefore important in laser modelling. The best example of this is the quantum cascade laser, in which the phonon scattering rates between quantum well subbands are engineered to achieve population inversion [102]. As new materials,

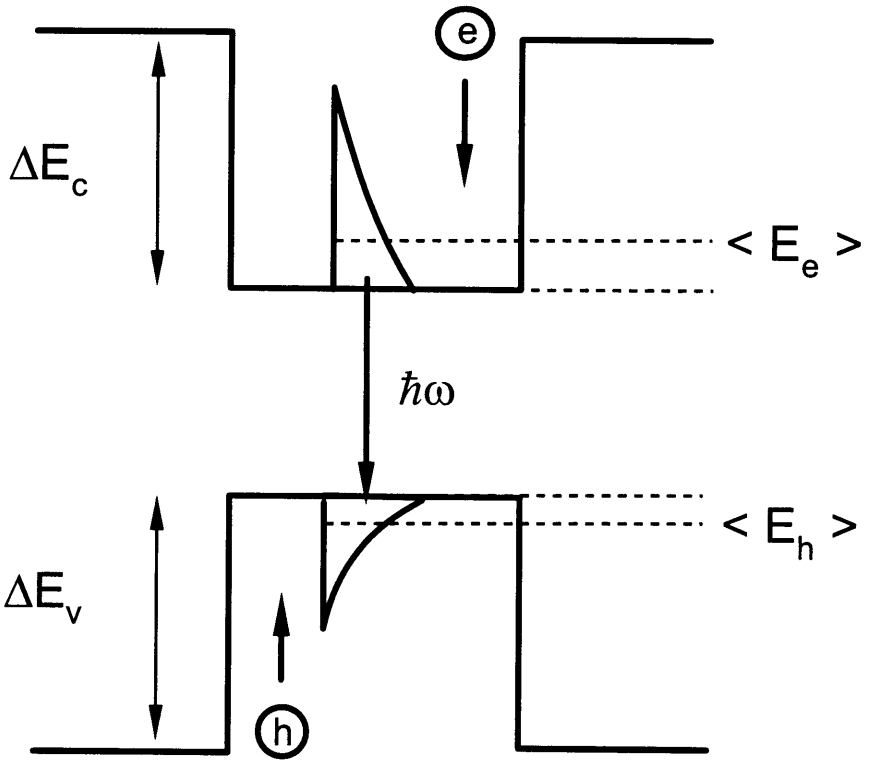

Figure 7-2: Carriers injected into a quantum well laser from the barriers heat up the distributions in the well. Equilibrium is determined by the carrier-phonon couplings.

such as ZnSe and GaN, are developed for use as lasers, efforts are being made into understanding how stimulated emission is influenced by strong excitonic effects which are not present in the near-IR III-V materials [103, 104]. Since the free carrier -phonon and exciton-phonon scattering rates are expected to be much larger in these wide band gap semiconductors, their effects are important as well .

Before moving on to calculation of carrier-phonon scattering and presentation of experimental results in Chapters 8, 9, and 10, it is helpful to discuss optical absorption at a semiconductor bandedge in order to understand how optical probes can measure carrier temperature and dynamics. The absorption spectrum near the band edge (in 3 dimensions) is given by

$$\alpha(\hbar\omega) = \alpha_0\sqrt{\hbar\omega - E_g}\,[1 - f_c(E_c) - f_v(E_v)]\,U(\hbar\omega - E_g) \tag{7.1}$$

where the conduction and valence band energies, E_c and E_v are determined by $\vec{k}$ conservation to be

$$\begin{aligned} E_c &= \frac{\hbar\omega - E_g}{1 + \frac{m_e}{m_h}} \\ E_v &= \frac{\hbar\omega - E_g}{1 + \frac{m_h}{m_e}}. \end{aligned} \tag{7.2}$$

Here, α_0 is assumed to be constant in energy, depending only on the energy-independent momentum matrix element between the conduction and valence bands. This is the free carrier model of optical absorption. The square root factor along with the step function, U, describe the density of states above the bandgap, E_g. The last factor, involving the Fermi functions, gives the occupation of the conduction and valence band states connected at photon energy $\hbar\omega$. The Fermi functions in 7.1 refer to the occupation of electrons in the conduction band and holes in the valence band each with their own density and, therefore, (quasi-) Fermi level. For absorption to take place at $\hbar\omega$, there must be an electron (no hole) at energy E_v in the valence band and a hole (no electron) at energy E_c in the conduction band. For the case of undoped, unexcited material, there are no electrons in the conduction band and no holes in the valence band. Thus $f_c = f_v = 0$ and the absorption simply follows the density of states. For non-zero electron and hole densities, the Fermi functions act to reduce the absorption. Since the Fermi

function range between zero and one, the absorption, and certain energies, can be made zero or negative indicating transparency and optical gain.

Figure 7-3 shows the absorption spectrum calculated with Eq. 2.37 and parameters for ZnSe. The dashed line is the empty band case and the solid line is the case for N-type doping at 3×10^{18} cm^{-3} and at 300K. Note how the absorption edge has been blue-shifted from the bandedge energy ($\hbar\omega - E_g = 0$) by the presence of the electrons. Changing the absorption in this manner is known as bandfilling or the Burstein-Moss shift, and results from the Pauli-exclusion principle. When the carriers are optically injected, the absorption changes are said to be due to bandfilling nonlinearities [105].

Bandfilling depends on the density and the temperature of the carriers through the Fermi functions. Changes to these parameters perturb the absorption spectrum in different ways. The middle plot of Fig. 7-3 shows the change in absorption due to an increase in the carrier density. The absorption edge is simply further blue-shifted, and the absorption is decreased at all energies near the bandedge. The bottom plot, in contrast, shows the effect of a temperature increase. A higher temperature means a higher average energy. Thus, high energy states have their population increased at the expense of the lower states. The absorption is thus decreased above the Fermi energy, and increased below it. This spectral signature for carrier heating will be important for identifying dynamics observed in the time domain. The experiments of the last chapter show how spectral information can be crucial in discriminating among various possible physical processes.

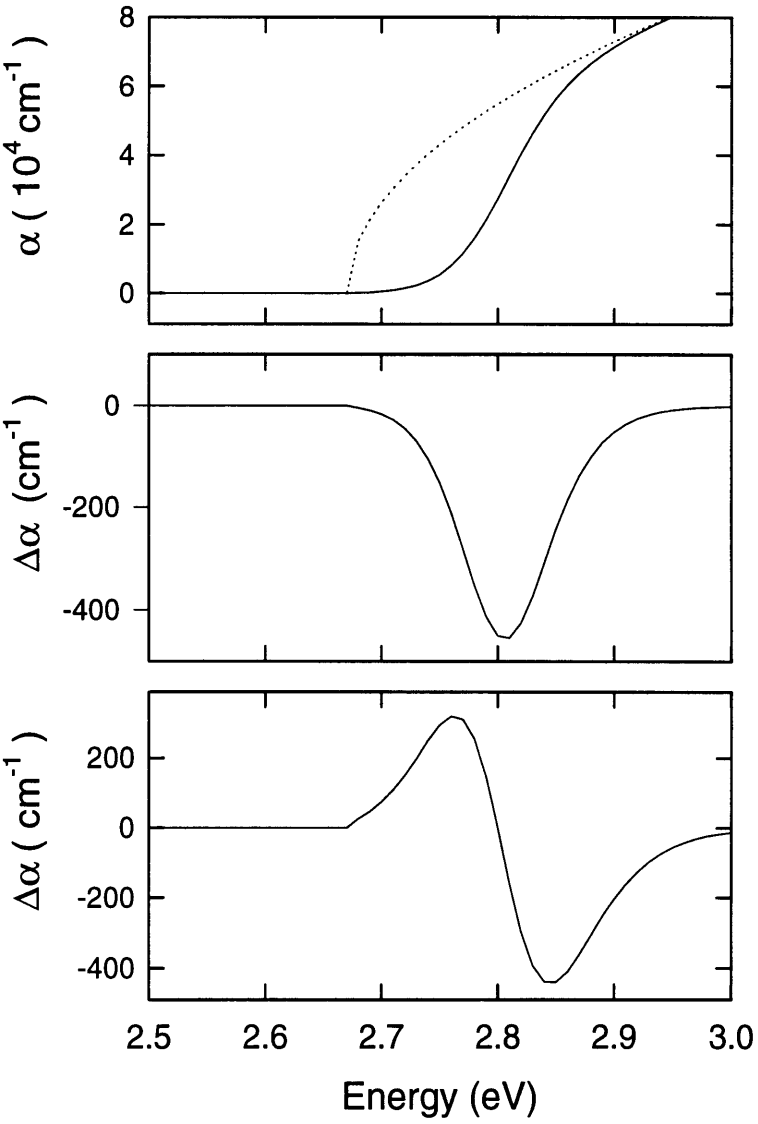

Figure 7-3: Top:Free electron calculation of the ZnSe absorption spectrum at room temperature for an empty band (dotted curve) and with $1.3\text{x}10^{19}\text{cm}^{-3}$ electrons present ($\mu = 5kT$) (solid curve). Middle: Effect on absorption of changing the carrier density by 10% ($+1.3\times10^{18}$ cm^{-3}). Bottom: Effect of changing the carrier temperature by 10% (+30K).

Chapter 8

Electron-phonon interactions and carrier dynamics

8.1 Introduction

This chapter will present a calculation of the energy loss rate of an electron gas to the lattice via optical phonon emission. The fundamental reason for the coupling is that, to an electron with wavevector $\vec{k}$ in a Bloch eigenstate of the ideal crystal lattice, a phonon appears as a disruption of the crystal's periodic potential. Electrons will therefore scatter from this potential into new Bloch states with new wavevectors [72]. Likewise, an electron's charge pulls on the ions of the lattice and can set up vibrations as it moves. Many type of electron-phonon scattering mechanisms exist. Strain of the lattice as it vibrates can be viewed as a local change in the lattice constant, especially when the wavevector is small. The resulting change in the bandgap is a scattering potential for the electrons. This mechanism is known as deformation potential phonon scattering and occurs for both acoustic and optical phonons [72, 74]. Deformation potential optical phonon scattering within the central conduction band (Γ-valley) is not allowed for symmetry reasons. In solids with some degree of ionic bonding and no inversion symmetry, displacement of the ions also sets up internal electric fields. Scattering from these potentials are known as piezo-electric scattering for acoustic phonons, and polar optical phonon (POP) scattering for optical phonons [72, 74, 75].

Other scattering mechanisms exist as well. Electrons can exchange energy with collective

oscillations of the entire electron gas by emitting and absorbing plasmons. When the plasma frequency approaches the phonon frequencies, scattering occurs between the coupled plasmon-phonon modes. Carrier-carrier scattering and scattering from charged and neutral impurities are important for transport effects. Since they are elastic, these mechanisms do not represent energy loss channels for the electron gas and will not be considered.

Of the phonon scattering mechanisms, polar optical phonon scattering gives the largest energy loss rate for carriers in alloyed zinc-blende semiconductors such as GaAs and ZnSe. The main reason is that carrier distributions residing at the Brillouin zone center ($\vec{k} = 0$) only couple to small wavevector phonons. The energy in an acoustic wave is proportional to the wavevector and is therefore small compared to the optical phonon energies. Each scattering event with acoustic phonons removes only a small amount of energy from the electrons.

Even considering only POP scattering, the calculation presented in the literature are quite complex, and often only numerical results are presented for the energy loss rates. This results primarily because of the nature of the experiments they attempt to describe. Hot carrier distributions in semiconductors are most easily generated by tuning a short pulse laser sufficiently far above the absorption edge [87, 106, 91]. The initial temperature can be several thousand degrees. However the initial distribution is determined by the laser pulse spectrum and is not Fermi-Dirac. Thermalization thus occurs simultaneously with energy loss to the lattice. At high injected densities, the plasma will screen the polar interaction with the phonons [107]. The screening will, however, depend on the detailed form of the carrier distribution and requires a calculation of the energy and wavevector-dependent dielectric constant, $\epsilon(q, \omega)$. This is known as 'dynamical screening' [108]. A most important concept is that of the 'phonon bottleneck'. If large numbers of optical phonons are launched by the plasma, the temperature of the phonons, defined by the occupation number, will increase until the rates of phonon absorption and emission are identical. At this point the phonons are no longer an energy loss channel for the electrons and the system must wait for the optical phonons to decay into acoustic phonons. The phonon lifetime in GaAs is about 6 ps. These hot phonon effects were first pointed out by Shah [109] and are the dominant factor in carrier cooling in direct absorption experiments [110, 111]. All of these complications are in addition to the existence of both electrons and holes, each with their own couplings and temperatures.

Although Monte-Carlo simulations agree well with observations [112], little information on the fundamental electron- and hole-phonon coupling strength can be obtained from direct injection experiments. Pump-probe experiments on diode lasers can be performed in a more perturbative regime [113, 114]. Forward biased diode lasers have a large electrically injected electron-hole plasma in their active regions. Pulses propagating at the wavelength where the gain just balances the loss (transparency point) do not cause any carrier density changes by stimulated emission to first order. Weaker absorption processes, such as free carrier absorption (FCA) and two-photon absorption (TPA) excite carriers to high energy states within their own bands. Thermalization with the background carrier density causes a slight warming of the electron and hole distributions. Typical temperature changes are below 10 K. The fact that the carrier plasma is already present and the temperature changes are small eliminates the dynamical screening and hot phonon effects, making the analysis much simpler.

The experiments presented in chapter 11 are, in principle, even cleaner. A below band pump pulse was used to heat carriers in doped thin film samples of ZnSe. The induced temperature changes were only 0.05K. This represents a totally unique experimental environment for studying carrier dynamics. The calculation of the cooling time constant presented in the next section is adapted from one by J. Shah of Bell Laboratories [115]. It was intended as a starting point for more complex calculations involving the effects described above. In the small ΔT limit, however, it should provide a complete description of the dynamics observed in this thesis work. The only modification is the addition of screening effects at high carrier densities. The main purpose of this analysis is to show that the rate of temperature change, for small ΔT, is linear in ΔT implying a single exponential time response, and to quantify the effects of bandfilling and screening at high carrier densities. With these features understood, it should be possible to draw conclusions about the electron- and hole-phonon coupling from the measured cooling time constants.

8.2 LO phonon emission rate for a single electron

An electron propagating through the lattice couples to longitudinal optical (LO) phonons with wavevector $\vec{q}$ via the Frölich matrix element [72], $|M_q|^2$, given by

$$|M_q|^2 = V_q \frac{\hbar\omega_{LO}}{2}\left(1 - \frac{\epsilon_\infty}{\epsilon_0}\right)\frac{1}{\Omega}, \tag{8.1}$$

where

$$V_q = \frac{e^2}{\epsilon_\infty \varepsilon_0 q^2}. \tag{8.2}$$

Here, $\hbar\omega_{LO}$ is the phonon energy, which is about 30 meV for both GaAs and ZnSe. The low and high frequency dielectic constants are $\epsilon_0\varepsilon_0$ and $\epsilon_\infty\varepsilon_0$ with ε_0 being the permittivity of free space (MKS units are used throughout). Ω is a normalization factor equal to the volume of the crystal.

This coupling factor leads to emission and absorption of LO phonons which occur at a rate given by Fermi's golden rule

$$\frac{dN_q}{dt} = \frac{2\pi}{\hbar}\left[\left|\left\langle \vec{k}-\vec{q}, N_q+1\left|H'\right|\vec{k}, N_q\right\rangle\right|^2 \delta\left(E_k - E_{k-q} - \hbar\omega\right)\right. \tag{8.3}$$

$$\tag{8.4}$$

$$\left. - \left|\left\langle \vec{k}+\vec{q}, N_q-1\left|H'\right|\vec{k}, N_q\right\rangle\right|^2 \delta\left(E_k - E_{k+q} + \hbar\omega\right)\right], \tag{8.5}$$

where $\vec{k}$ is the electron wavevector and H' is the Frölich Hamiltonian. The first term is for emission and the second for absorption. Both processes must conserve momentum and energy. Figure 8-1 shows vector diagrams for both processes with initial electron wavevector $\vec{k}$ and phonon wavevector $\vec{q}$. From the geometry, one immediate conclusion is that phonons can only be emitted in the forward direction with θ, the angle between $\vec{k}$ and $\vec{q}$, $< \pi/2$. No restriction applies to phonon absorption.

These transitions lead to a lifetime for the electron state $\vec{k}$

$$\frac{1}{\tau\left(\vec{k}\right)} = \sum_q \frac{dN_q}{dt}. \tag{8.6}$$

The lifetime due to the emission process by itself is related to the energy relaxation time and

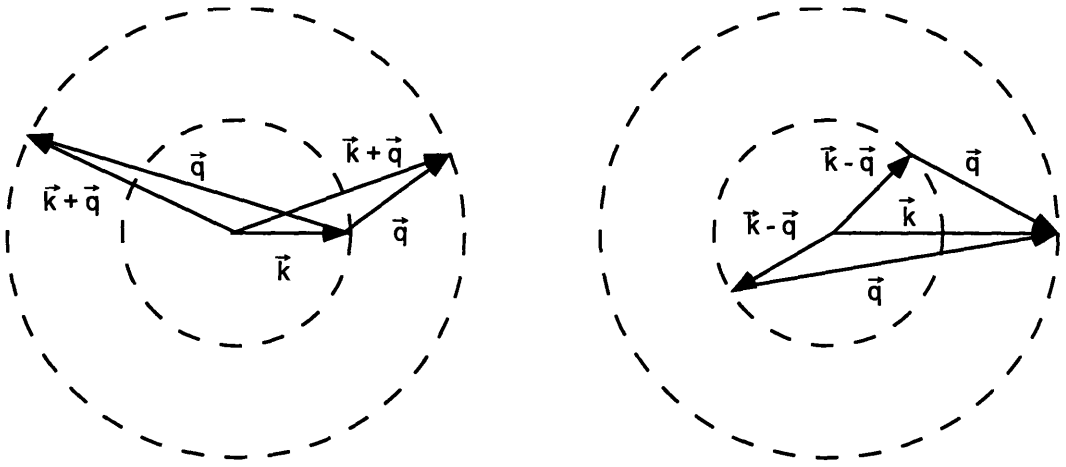

Figure 8-1: Vector diagrams of the optical phonon absorption and emission processes.

will be calculated next. Starting from Eq. 8.6, using only the emission rate in Eq. 8.3 and converting the sum over q to an integral we obtain

$$\frac{1}{\tau(\vec{k})}\bigg|_e = \frac{\Omega}{\pi\hbar}\int_0^\infty q^2 dq M_q^2 \left(N_q + 1\right)\int_{-1}^{1} d(\cos\theta)\delta\left(E_{\vec{k}} - E_{\vec{k}-\vec{q}} - \hbar\omega\right). \tag{8.7}$$

The argument of the delta function is

$$-\frac{\hbar^2}{2m}\left(q^2 - 2kq\cos\theta - \frac{2m\omega}{\hbar}\right). \tag{8.8}$$

For a given angle of emission, q must be

$$q = k\cos\theta \pm \sqrt{k^2\cos^2\theta - q_0^2} \tag{8.9}$$

where $q_0^2 = 2m\omega/\hbar$. Since q must be real and positive, the minimum value of $\cos\theta$ is k/q_0 which is also positive. This just agrees with the conclusion of Fig. 8-1 that phonons are emitted in

the forward direction. As $\cos\theta$ ranges from k/q_0 to 1, q will be bounded by the values

$$\begin{aligned} q_{\min} &= k - \sqrt{k^2 - q_0^2} \\ q_{\max} &= k + \sqrt{k^2 - q_0^2}. \quad (emission) \end{aligned} \tag{8.10}$$

For reference, the absorption is treated in a similar manner. The argument of the delta function in the second term of Eq. 8.3 will equal zero when

$$q = \sqrt{k^2 \cos^2\theta + q_0^2} - k\cos\theta. \tag{8.11}$$

This will limit q to

$$\begin{aligned} q_{\min} &= \sqrt{k^2 + q_0^2} - k \\ q_{\max} &= \sqrt{k^2 + q_0^2} + k. \quad (absorption). \end{aligned} \tag{8.12}$$

Note that $\cos\theta$ is not restricted in this case.

Returning to the emission rate calculation, the integral over $\cos\theta$ acts to limit the bounds on the integral over q

$$\left.\frac{1}{\tau(\vec{k})}\right|_e = \frac{\Omega}{\pi\hbar}(N_0+1)\int_{q_{\min}}^{q_{\max}} q^2 dq M_q^2 \frac{m}{\hbar^2 kq}.$$

Using Eq. 8.1, and the fact that

$$\sinh^{-1}(x) = \ln\left[x + \sqrt{1+x^2}\right],$$

the final result for the inverse lifetime for emission is

$$\left.\frac{1}{\tau(\vec{k})}\right|_e = \frac{e^2\hbar\omega\left(\frac{\epsilon_0}{\epsilon_\infty}-1\right)}{2\pi\epsilon_0\varepsilon_0\hbar^2}\sqrt{\frac{2m}{E(k)}}(N_0+1)\sinh^{-1}\left(\sqrt{\frac{E(k)}{\hbar\omega}}\right) \tag{8.13}$$

where N_0 is the Bose-Einstein occupation of the LO phonon. Since the energy of optical phonons is essentially independent of wavevector, this factor could be pulled from the integral in Eq. 8.7. This lifetime is plotted in Fig. 8-2 versus energy above the bandedge for GaAs and ZnSe. The relevant material parameters for the calculation are shown in Table 8.14 and were obtained

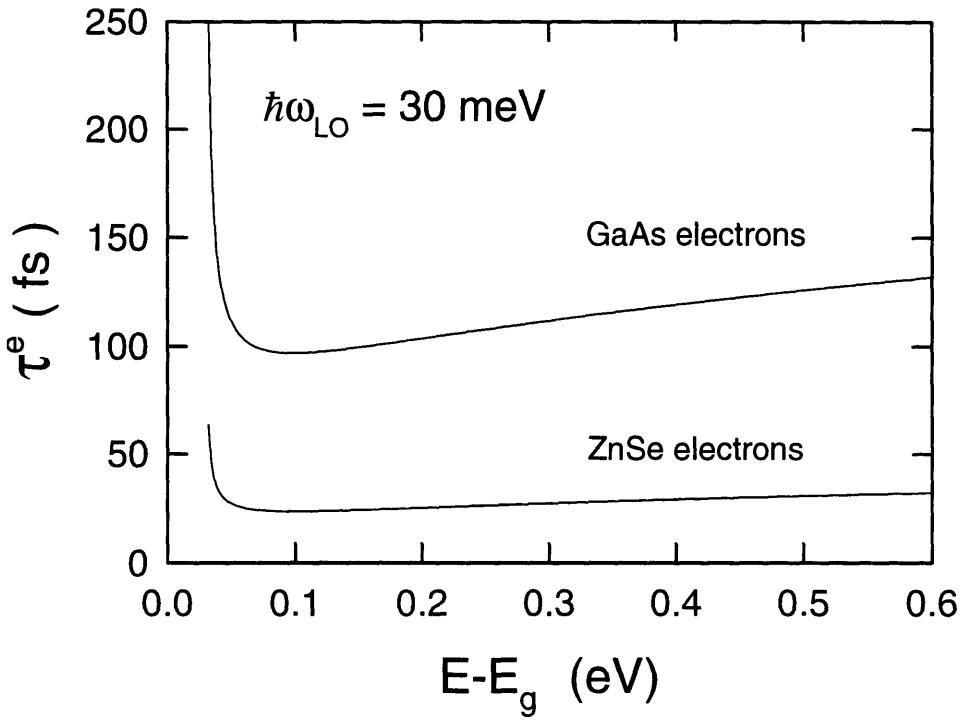

Figure 8-2: Phonon emission lifetime as a function of energy for a single electron in ZnSe and GaAs. When $E < \hbar\omega_{LO}$ phonon emission is impossible.

from Ref [2].

	ZnSe	GaAs
E_g	2.67eV	1.42eV
m_e^*	0.15 m_0	0.067 m_0
m_{hh}^*	0.8 m_0	0.5 m_0
ε_0	9.2	13.2
ε_∞	6.2	10.7
$\frac{1}{\varepsilon_\infty} - \frac{1}{\varepsilon_0}$	0.053	0.018
$\hbar\omega_{LO}$	31 meV	36 meV

(8.14)

The larger electron effective mass and the more polar nature of the ZnSe bonding, reflected in the large relative difference in the high and low frequency dielectric constants, both act to reduce the ZnSe lifetime with respect to GaAs. The large increase in the lifetime as the electron energy approaches the bandedge is due to the fact that an electron must have at least $\hbar\omega_{LO}$ of energy to emit an optical phonon.

These lifetimes indicate that phonon scattering is a relatively fast process. The effects of non-zero occupation of the final scattering states (i.e. bandfilling), and screening of the Frölich interaction both act to slow things down and these effects will be dealt with in the next section.

8.3 Carrier distribution cooling by LO phonons

The calculation presented in this section is based on a review article by J. Shah [115]. A few changes have been made in the definitions of the electron and phonon wavevectors in order to conform to the analysis of the previous section. For a distribution of electrons, an energy loss rate, rather than a lifetime is calculated. It is assumed that an amount of energy ΔE per particle has been added to the electron gas with energy per particle $E_0 = E_T/n\Omega$,where E_T is the total energy of the gas, n is the electron density, and Ω the volume. We are interested in calculating the time dependence of $E(t) = E_0 + \Delta E(t)$. The rate of excess energy loss is obtained, similarly to Eq. 8.6, by summing the rate of production of optical phonons in all modes q. To make this an intensive quantity, we divide by the total number of electrons to get

the rate of excess energy loss per electron

$$\frac{d\Delta E}{dt} = -\frac{1}{n\Omega}\sum_q \hbar\omega_{LO}\frac{dN_q}{dt}. \tag{8.15}$$

The rate of phonon production for each mode $\vec{q}$ will be calculated first. The expression is similar to the one used before (Eq. 8.3), but now we must sum over all of the electrons which can emit and absorb phonons and take into account the occupation of the initial and final scattering states. The starting point is therefore,

$$\frac{dN_q}{dt} = \frac{2\pi}{\hbar}\sum_k \left[\begin{array}{l} \left|\left\langle \vec{k}-\vec{q}, N_q+1 \left| H' \right| \vec{k}, N_q \right\rangle\right|^2 \delta\left(E_k - E_{k-q} - \hbar\omega\right) f(\vec{k})(1-f(\vec{k}-\vec{q})) \\ -\left|\left\langle \vec{k}+\vec{q}, N_q-1 \left| H' \right| \vec{k}, N_q \right\rangle\right|^2 \delta\left(E_k - E_{k+q} + \hbar\omega\right) f(\vec{k})(1-f(\vec{k}+\vec{q})) \end{array} \right]. \tag{8.16}$$

Here, N_q is the Bose-Einstein occupation factor for the phonons with the temperature equal to the *lattice* temperature, T_L. The emission and absorption terms will be treated separately. Converting the sum over electron wavevectors, $\vec{k}$, to an integral in the standard way, the emission rate becomes

$$\frac{dN_q}{dt}\Big|_e = \frac{\Omega}{\pi\hbar}\int_0^\infty k^2 dk M_q^2 \left(N_q+1\right) f(\vec{k}) \int_{-1}^{1} d(\cos\theta)\delta\left(E_{\vec{k}} - E_{\vec{k}-\vec{q}} - \hbar\omega\right)(1-f(\vec{k}-\vec{q})). \tag{8.17}$$

The argument of the delta function must be evaluated

$$E_{\vec{k}} - E_{\vec{k}-\vec{q}} - \hbar\omega = -\frac{\hbar^2}{2m}\left(q^2 - 2kq\cos\theta - \frac{2m\omega}{\hbar}\right) = 0 \tag{8.18}$$

in order to determine when it is zero. Since, the integral is over $\vec{k}$, Eq. 8.18 will be recast in the form

$$\cos\theta = \frac{q^2+q_0^2}{2kq}$$

using the definition of q_0 given in the last section. Since $\cos\theta < 1$, is a minimum value for k for which the delta function will give a non-zero contribution to the total integral,

$$k^e_{\min} = \frac{q^2 + q_0^2}{2q} = \frac{m}{\hbar^2 q}\left(\frac{\hbar^2 q^2}{2m} + \hbar\omega\right). \tag{8.19}$$

Changing variables to

$$\epsilon = \frac{\hbar^2 k^2}{2mk_B T_e} - \frac{\hbar\omega}{kT_e},$$

the integration over k becomes

$$\frac{dN_q}{dt}|_e = \frac{m^2 k_B T_e \Omega}{\pi\hbar^5 q} M_q^2 (N_q + 1) \int_{\epsilon_{\min}}^{\infty} d\epsilon f(\epsilon + \tfrac{\hbar\omega}{k_B T_e})(1 - f(\epsilon)). \tag{8.20}$$

The value of $\epsilon_{\min}$ is given by

$$\epsilon_{\min} = \frac{\hbar^2}{8mk_B T_e}\left(q - \frac{q_0^2}{q}\right). \tag{8.21}$$

This change of variables differs from the expressions used by Shah, but is necessary given the more intuitive definition of the initial and final state wavevectors in Eq.8.16. The end result will be identical, however.

Going back to Eq. 8.16 , the absorption term is treated in an analogous way. The minimum electron k value for absorbing a phonon at wavenumber q is

$$k^e_{\min} = \frac{q^2 + q_0^2}{2q} = \frac{m}{\hbar^2 q}\left(\frac{\hbar^2 q^2}{2m} - \hbar\omega\right). \tag{8.22}$$

Variable are changed from k to ϵ by

$$\epsilon = \frac{\hbar^2 k^2}{2mk_B T_e},$$

which results in the same value for $\epsilon_{\min}$ as found for the case of emission. Thus, the rate of phonon absorption at wavevector $\vec{q}$ is

$$\frac{dN_q}{dt}|_a = -\frac{m^2 k_B T_e \Omega}{\pi\hbar^5 q} M_q^2 (N_q) \int_{\epsilon_{\min}}^{\infty} d\epsilon f(\epsilon)(1 - f(\epsilon + \tfrac{\hbar\omega}{k_B T_e})). \tag{8.23}$$

Putting these expression together, the net generation rate of phonons of wavevector $\vec{q}$ is

$$\frac{dN_q}{dt} = \frac{dN_q}{dt}|_e + \frac{dN_q}{dt}|_a \tag{8.24}$$

$$= \frac{m^2 k_B T \Omega}{\pi \hbar^5 q} M_q^2 \int_{\epsilon_{\min}}^{\infty} d\epsilon \left[(N_q+1) f(\epsilon + \tfrac{\hbar\omega}{k_B T_e})(1-f(\epsilon)) - N_q f(\epsilon)(1-f(\epsilon+\tfrac{\hbar\omega}{k_B T_e})) \right] \tag{8.25}$$

Using the definition of the Fermi and Bose functions, it can be shown that

$$\begin{aligned} f(\epsilon+x)(1-f(\epsilon)) &= (f(\epsilon)-f(\epsilon+x))N(x) \\ f(\epsilon)(1-f(\epsilon+x)) &= (f(\epsilon)-f(\epsilon+x))(N(x)+1). \end{aligned} \tag{8.26}$$

With this trick, Eq. 8.24 simplifies to

$$\frac{dN_q}{dt} = \frac{m^2 k_B T \Omega}{\pi \hbar^5 q} M_q^2 [N(T_e) - N(T_L)] \int_{\epsilon_{\min}}^{\infty} d\epsilon (f(\epsilon) - f(\epsilon + \tfrac{\hbar\omega}{k_B T_e})). \tag{8.27}$$

These integrals can be directly evaluated since

$$\int_{\epsilon_{\min}}^{\infty} d\epsilon f(\epsilon) = \ln\left[1 + \exp(\eta - \epsilon_{\min})\right] \tag{8.28}$$

where η is the chemical potential,μ, normalized to $k_B T_e$. The final result for the phonon generation rate is

$$\frac{dN_q}{dt} = \frac{m^2 k_B T \Omega}{\pi \hbar^5 q} M_q^2 [N(T_e) - N(T_L)] \ln \left[\frac{1 + \exp\left(\eta - \frac{\hbar^2}{8 m k_B T_e}\left(q - \frac{q_0}{q}\right)^2\right)}{1 + \exp\left(\eta - \frac{\hbar^2}{8 m k_B T_e}\left(q + \frac{q_0}{q}\right)^2\right)} \right] \tag{8.29}$$

The energy loss rate from Eq.8.15 can now be calculated. Using the result Eq. 8.29 and converting the discrete sum over $\vec{q}$ to an integral,

$$\frac{d\Delta E}{dt} = -\frac{1}{2\pi^2 n} \int_0^{\infty} dq \hbar\omega q^2 \frac{dN_q}{dt} \tag{8.30}$$

$$= -\frac{e^2 m^2 k_B T_e (\hbar\omega_{LO})^2}{4\pi^3 \hbar^5 n \varepsilon_0} \left(\frac{1}{\epsilon_\infty} - \frac{1}{\epsilon_0}\right) [N(T_e) - N(T_L)]$$

$$\int_0^\infty q dq \frac{1}{q^2} \ln \left[\frac{1+\exp\left(\eta - \frac{\hbar^2}{8mk_BT_e}\left(q-\frac{q_0}{q}\right)^2\right)}{1+\exp\left(\eta - \frac{\hbar^2}{8mk_BT_e}\left(q+\frac{q_0}{q}\right)^2\right)} \right] . \quad (8.31)$$

Eq. 8.30 is valid at all temperatures and densities. The calculation of the phonon generation rate allows construction of coupled rate equations for the phonon occupation numbers and the electron gas excess energy. This approach can be used to investigate hot-phonon effects which occur when $T_e \gg T_L$.

Rather than proceed in this direction, it is useful to examine Eq. 8.30 in the limit where $T_e \approx T_L$. A key feature of the pump-probe results in Chapter 11 is the ability to measure the dynamics in the perturbative regime. The electron temperature appears in several places in Eq. 8.30: in the prefactor, in the Bose-Einstein factors, and inside the integral explicitly and implicitly through η. The entire expression must be Taylor expanded in T_e. However, using $T_e = T_L + \Delta T$, the Bose factors give the result

$$N(T_L + \Delta T) - N(T_L) \;=\; N(T_L)^2 \frac{\hbar\omega}{kT_L} \exp(\frac{\hbar\omega}{kT_L}) \frac{\Delta T}{T_L} \quad (8.32)$$

which is already first order in ΔT. The T_e in the other factors can be simply substituted with T_L. For small changes in the electron temperature, the excess energy loss rate is, therefore linearly proportional to ΔT.

The excess energy per electron can be expressed in terms of the change in the electron temperature. The specific heat is defined as

$$C_V = \frac{1}{Nk} \frac{dE}{dT} |_V \,, \quad (8.33)$$

where E and N are the total energy and number of particles in the gas. C_V for a Fermi gas [116] is plotted in Fig. 8-3 as a function of the dimensionless degeneracy parameter $\eta = \mu/kT$. At low densities ($\eta < 0$) the classical result of $\frac{3}{2}$ holds. At high densities the specific heat

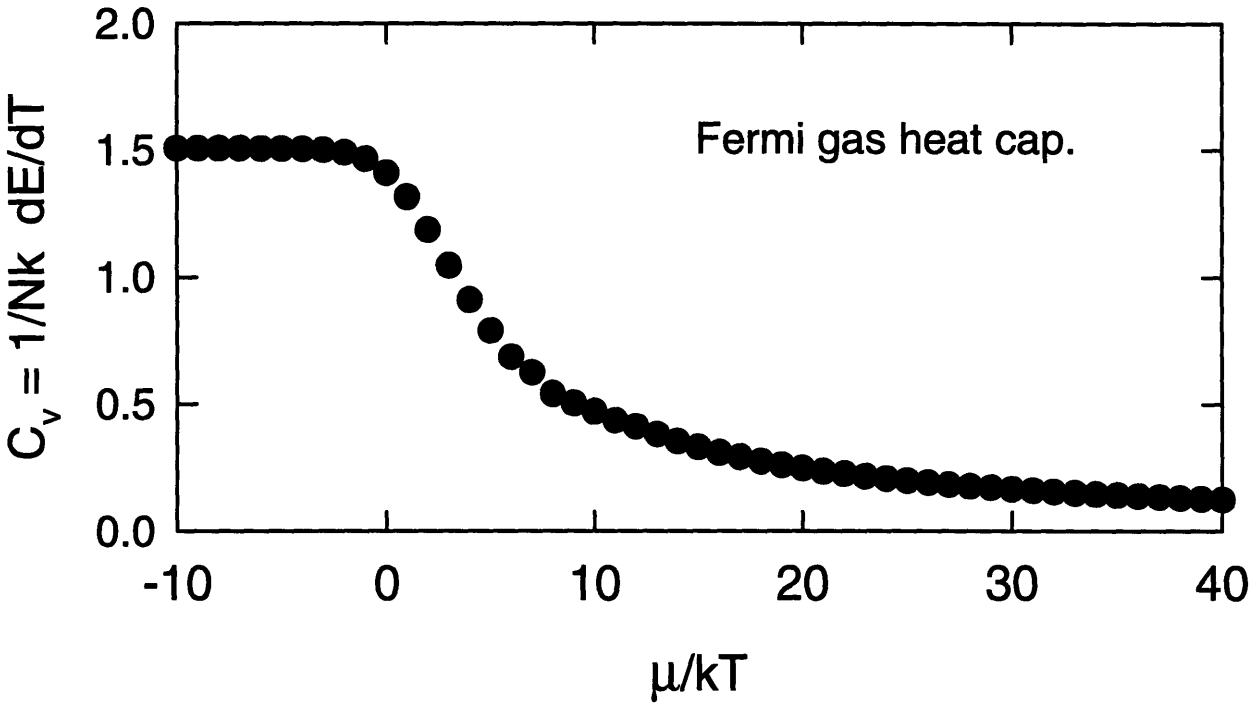

Figure 8-3: Specific heat of a Fermi gas as a function of μ/kT.

decreases to zero as the standard Fermi gas result

$$C_V = \frac{\pi^2}{2}\frac{kT}{\mu}.$$

Therefore,

$$\frac{d\Delta E}{dt} = C_V \frac{d\Delta\left(kT\right)}{dt} \tag{8.34}$$

and Eq. 8.30 can be expressed as a simple first order differential equation in ΔT

$$\frac{d\Delta\left(kT\right)}{dt} = -\frac{\Delta\left(kT\right)}{\tau_e}. \tag{8.35}$$

This is one of the major result of this chapter. It predicts that for $\Delta T/T_L \ll 1$, changes in the carrier temperature should relax as a single exponential with a time constant calculated with Eqns. 8.30, 8.32, and 8.34 which are valid for optical phonon coupling at all temperatures and degenerate statistics.

Before numerical evaluations of the cooling timeconstants are presented, modifications due to screening of the Frölich interaction at high densities will be discussed. When the density is high enough, the carriers begin to contribute significantly to the dielectric constant, $\epsilon\left(q,\omega\right)$ of the material. Screening of the electric fields caused by the vibration of the polar bond occurs, and this reduces the electron-phonon coupling. The dielectric constant due to mobile charge carriers is given by the Lindhard [72]dielectric formula

$$\epsilon\left(q,\omega\right) = 1 + 2V_q \sum_{\vec{p}} \frac{f(\vec{p}+\vec{q}) - f(\vec{p})}{\omega + i\delta - E_{\vec{p}+\vec{q}} + E_{\vec{q}}}. \tag{8.36}$$

Calculations of dynamic screening make use of this formula when the carrier distributions, f, are far from equilibrium. Das Sarma et. al. in Ref. [107] show that an upper limit to the effect of screening can be obtained by using $\epsilon(q,0)$, the static dielectric constant . It can be shown that

$$\epsilon\left(q,0\right) = 1 + \frac{\kappa^2}{q^2}, \tag{8.37}$$

where

$$\kappa = \sqrt{\frac{e^2}{\epsilon_\infty \varepsilon_0}\frac{\partial n}{\partial \mu}} \tag{8.38}$$

is the general expression for the screening wavevector for a Fermi gas.

To include the effects of screening in the previous analysis, the substitution

$$V_q \rightarrow \frac{V_q}{\epsilon(q,0)} = \frac{e^2}{\epsilon_{\infty\varepsilon_0}}\frac{1}{q^2+\kappa^2} \tag{8.39}$$

is made. Changing the scaling of q by the factor

$$\frac{1}{\lambda_T} = \sqrt{\frac{mk_BT}{2\pi\hbar^2}}, \tag{8.40}$$

will help in predicting when screening will be important. Using these substitutions, the temperature dynamics can be expressed as

$$\frac{d\Delta T}{dt} = -\frac{1}{\tau_0}\Delta T \int_0^\infty dx \frac{x}{x^2+\left(\frac{\lambda\kappa}{4\pi}\right)^2} \ln\left[\frac{1+\exp\left(\eta-\pi\left(x-\frac{1}{4\pi x}\frac{\hbar\omega}{k_BT}\right)^2\right)}{1+\exp\left(\eta-\pi\left(x+\frac{1}{4\pi x}\frac{\hbar\omega}{k_BT}\right)^2\right)}\right]. \tag{8.41}$$

With this variable change, it is evident that the logarithm term is controlled only by the ratio of the phonon energy to kT.

Figure 8-7 shows the integrand of Eq. 8.41 calculated for ZnSe electrons at three different carrier densities with, and without the screening correction. The function is small for $\eta < 0$ (low densities) but rapidly increases as η moves into the conduction band. Note how the integrand is zero for small x and then turns sharply upward. This occurs at about $x_c = \sqrt{\hbar\omega/4\pi k_BT}$ where the terms in the numerator and denominator exponential functions start to become appreciably different. This is independent of density and effective mass and represents the fact that the phonon wavevector must have a minimum value due to the curvature of the bands. The dashed curves in the three plots have screening included. The screening effectively limits the growth of the logarithm term at small x. The vertical dotted lines show the value of $x_s = \lambda\kappa/4\pi$ for each case. Screening is seen to become important when $x_s > x_c$. For densities where κ is in the Debye screening regime, $x_s = \frac{1}{\sqrt{8\pi}}\hbar\omega_p/k_BT$ where ω_p is the plasma frequency. Thus screening

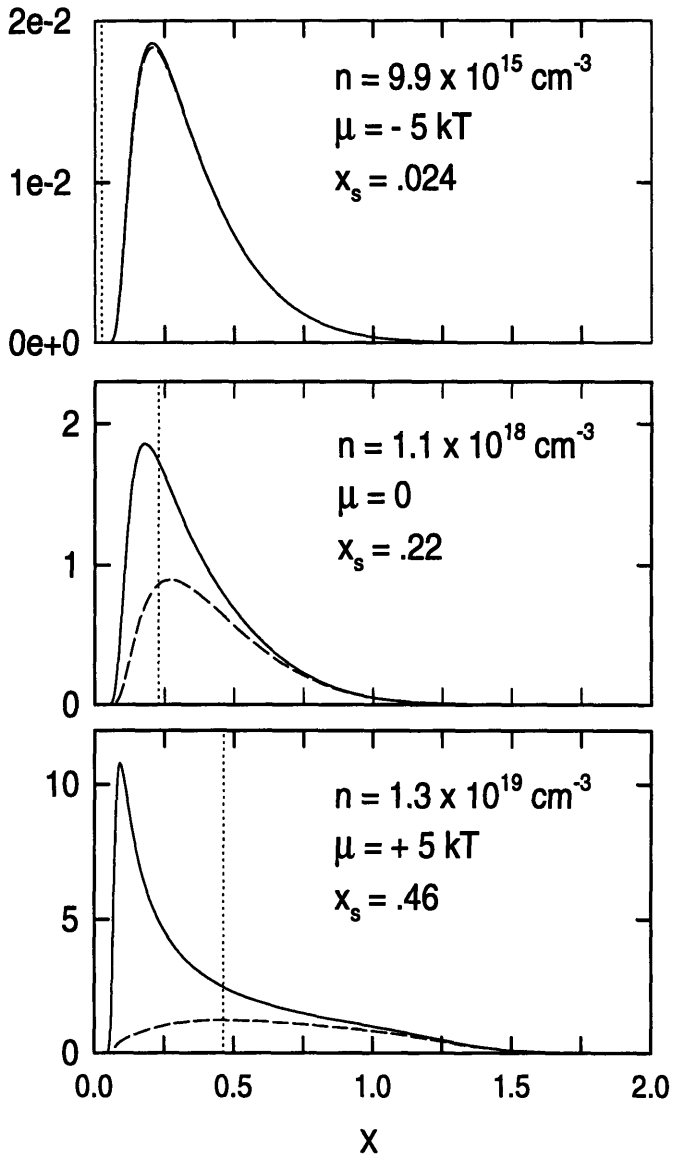

Figure 8-4: Plots of the integrand of Eq. 8.41 for increasing carrier density (top to bottom). The parameter x is a normalized phonon wavevector. Note the change in the vertical scales with density. The solid curves neglect screening and peak just above the value of the minimum possible phonon momentum. The dashed curves show the effect of screening in reducing the energy loss contribution from the low wavector phonons. x_s, defined in the text, is a measure of the extent of the screening to larger wavevectors.

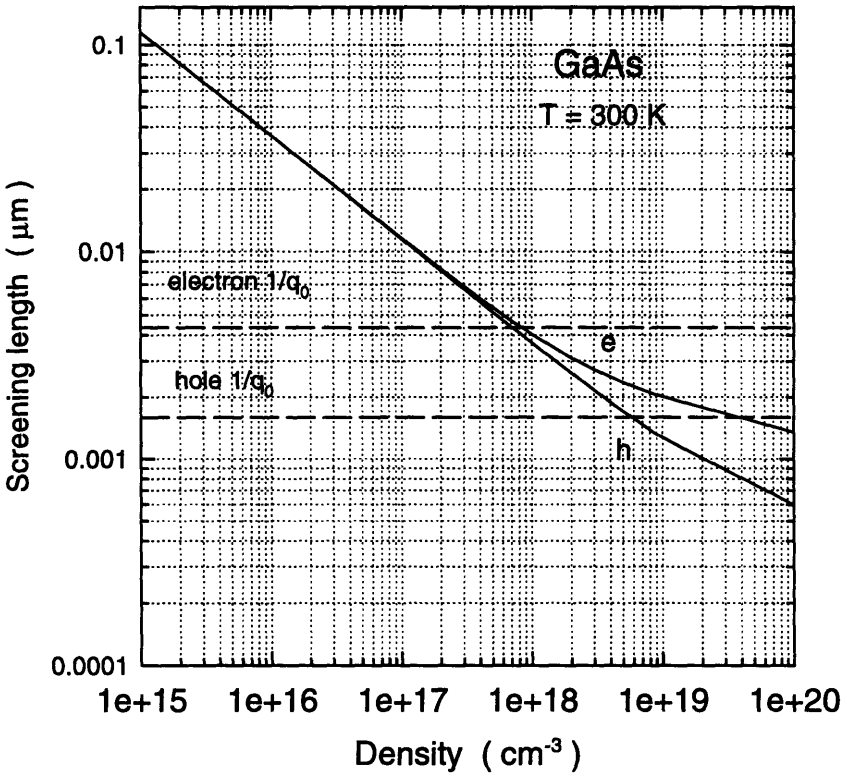

Figure 8-5: Screening lengths, $1/\kappa$, for electrons and holes in GaAs. When $\kappa \sim q_0$, screening is important in the carrier-phonon coupling coefficient.

is important when $\omega_p \approx \omega_{LO}$. Figures 8-6 and 8-5 show the screening lengths, $1/\kappa$, as a function of carrier density for ZnSe and GaAs electrons and holes. The flattening of the curves as high densities indicates the switch from Debye to Thomas-Fermi screening. The horizontal lines represent the values of $q_0/4\pi$,another measure of when screening of the phonon interaction is important.

Figure ?? shows the results of numerically evaluating the integral in Eq. 8.41. Screening results in smaller values at high densities which increases the cooling time constant. The drop off at low densities is balanced by the density factor in the denominator of Eq. 8.30. Figures 8-8 and 8-9 show the calculated time constants for electrons and holes. At low densities the time constant becomes independent of density as the occupation of the initial an final states are no longer important. As the bandfilling increases and the Fermi level move up into the band, some slowing of the cooling process is observed. At the densities of interest for devices and for

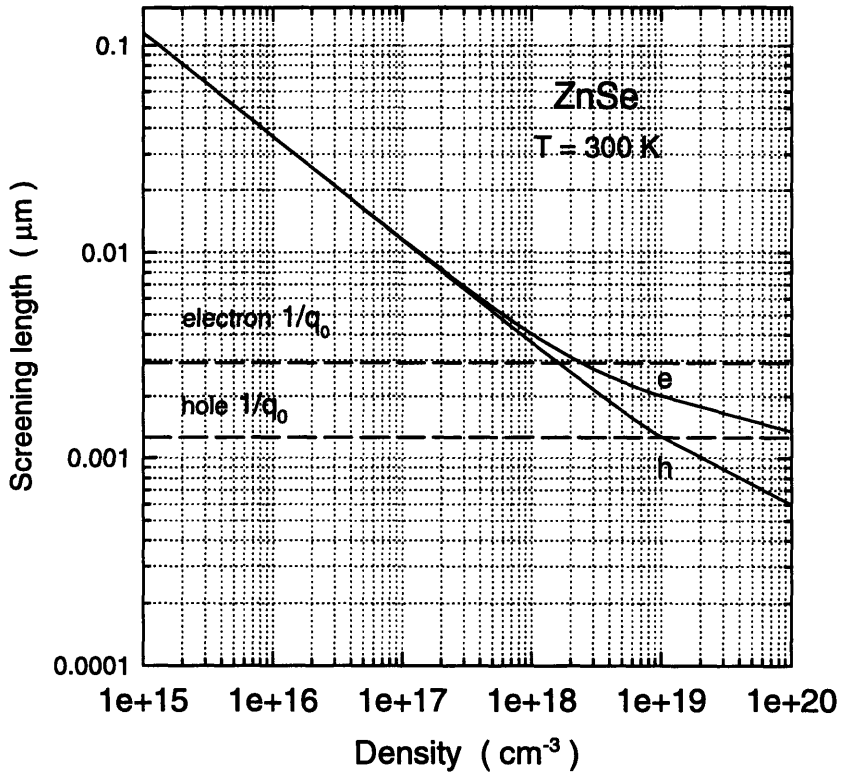

Figure 8-6: Screening lengths, $1/\kappa$, for electrons and holes in ZnSe as a function of carrier density.

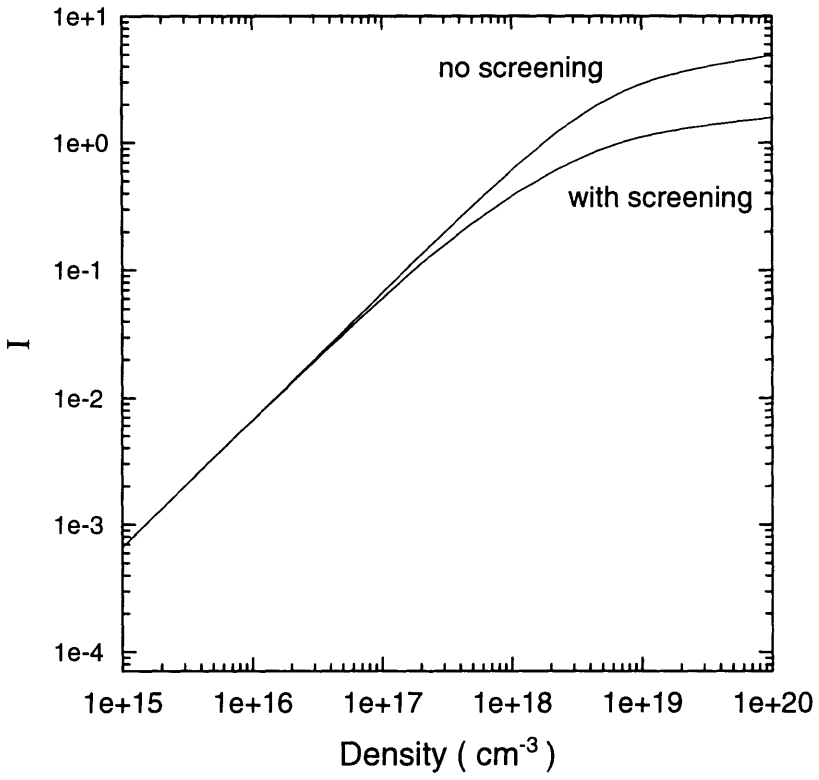

Figure 8-7: Numerical evaluation of the integral of Eq. 8.41.

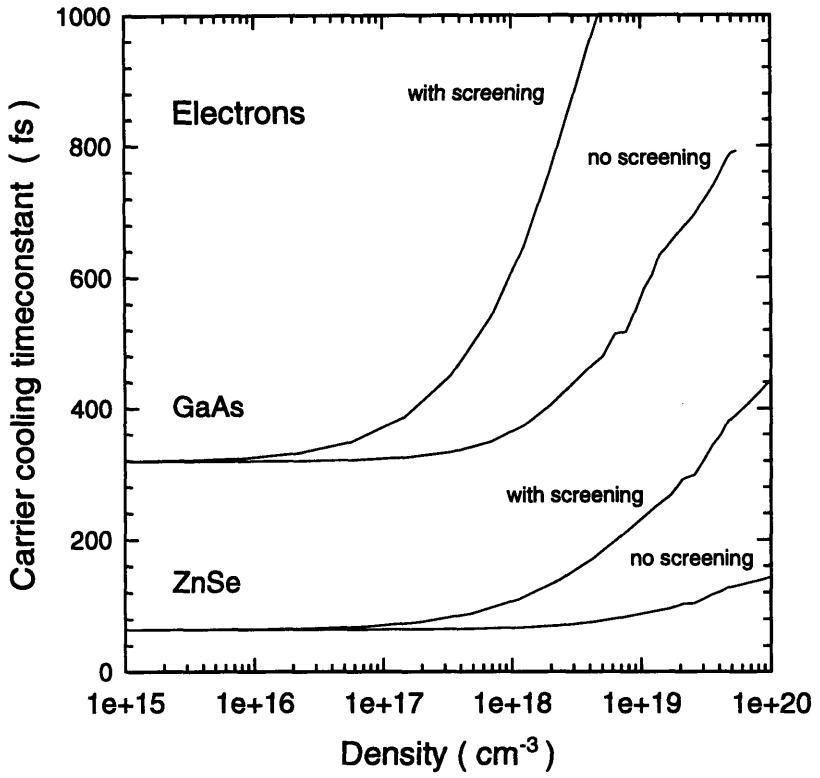

Figure 8-8: Calculated cooling time constants for electrons in ZnSe and GaAs as a function of carrier density.

the pump probe experiments, 10^{17}–10^{19} cm^{-3}, this is seen to be a rather small effect, however. The screening caused by high carrier densities is a much more important factor.

In conclusion, the cooling rates for carrier distributions have been calculated for arbitrary temperatures and degeneracy factors. The most important result is that for small deviations from the lattice temperature, the carrier temperature will relax exponentially with a single time constant. Bandfilling effects have a small effect on the time constant. Screening effects are very important, however. From the time constant plots, Figs. 8-8, 8-9, and 8-2, ZnSe is seen to have much faster time constants compare to GaAs due to its more polar bonding. In both GaAs and ZnSe, the holes are predicted by this Frölich coupling theory to be faster than the electrons. These predictions will be compared to experimental results in Chapter 11.

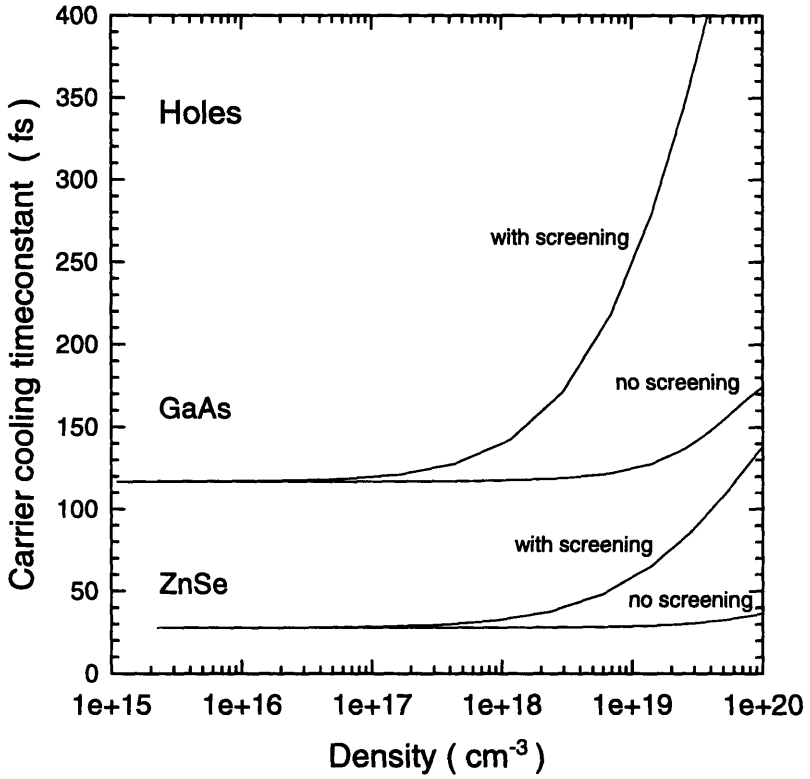

Figure 8-9: Calculated cooling time constants for holes in ZnSe and GaAs as a function of carrier density.

Chapter 9

Sample preparation and characterization

The ZnSe films studied in these experiments were grown in Prof. Leslie Kolodziejski's MBE lab at MIT. Both gas-source and solid-source samples were used. The gas-source technique uses metal-organic compounds as the Zn and Se source materials. Using these gas sources allows much better control of the beam fluxes hitting the substrate, but results in incorporation of atomic hydrogen into the lattice [117]. No difference was seen in the dynamics or optical properties between the gas and solid-source samples which could be attributed to this interstitial hydrogen. The IR pumping technique of Chapter 11 is extremely sensitive to mid-gap impurities [118], and none were found in densities high enough to interfere with the experiments.

Both N and P-type ZnSe samples were fabricated in order to look at the carrier dynamics of electrons and holes separately. Chlorine was used for N doping and nitrogen for P doping. All doping concentrations were measured by SIMS (Secondary Ion Mass Spectroscopy) by Charles Evans & Associates. Unintentionally doped samples were grown as well. These samples typically have a [Cl] concentration of about 10^{16} cm^{-3} and are therefore N-type. This concentration is negligible compared to the densities needed to cause significant bandfilling for observation of the carrier dynamics ($\sim 10^{18}$ cm^{-3}).

9.1 GaAs substrate removal

Once the samples were obtained, the GaAs substrates had to be removed to allow transmission measurements. This was accomplished by polishing and etching. The wafers were first cleaved into small chips about 5mm on a side. These were then glued epi-side down on fused silica glass flats (S1UV) obtained from Esco Products Incorporated. UVAX 600 ultraviolet transparent epoxy from Zymet Incorporated was used with an extruder gun. The extruder nozzle mixes the epoxy without creation of air bubbles that scatter light. Only a tiny amount of glue is necessary to hold the sample in place for the mechanical polishing. The crucial step is to press the sample against the glass disk while it dries overnight. The key to exposing large areas of the ZnSe film without much surface damage is flatness. Tilt of the sample results in a non-uniform thickness of the substrate after the polishing step. The etch will then uncover only a narrow strip of the ZnSe on one side of the sample when it breaks through.

With the sample firmly glued in place, the glass disk was bonded to the polishing block of a South Bay Technology model 145 polishing fixture. This hand-held jig has a threaded screw on which the polishing block and sample are attached allowing the sample to be extended as the polishing proceeds. 'Crystal bond' adhesive was used for the temporary bonding of the glass disk to the polishing block. Crystal bond is useful since it can be applied by heating the block and removed with acetone. The flatness of the bond to the polishing block was checked with a tool gauge (Starret Machine Co.) which is accurate to 10 μm. If the height of the block with the bonded glass disk was not uniform to within 10 μm, the disk was melted off and remounted. Polishing was done with $9\mu m$ grit polishing film also obtained from South Bay Technology, and plenty of water. The sample was extended with the threaded insert in 25 μm steps. The thickness of the sample substrate was periodically checked as the polishing proceeded with the tool gauge until about 30 μm was reached. Flat mounting enables controlled polishing to this thickness. The sample and disk were then removed for etching.

A solution of 500 ml 30% H_2O_2 with 10-20 ml of concentrated Ammonium Hydroxide (NH_4OH) added was used for the etch. This etch is not very selective, long exposure (>1 or 2 min) to the etch will result in a poor surface and reddening due to formation of Se rich surface layers. The care taken to keep the substrate thickness uniform, and to polish close to the epi-layer results in uncovering of a large region (even the whole substrate) all at once with

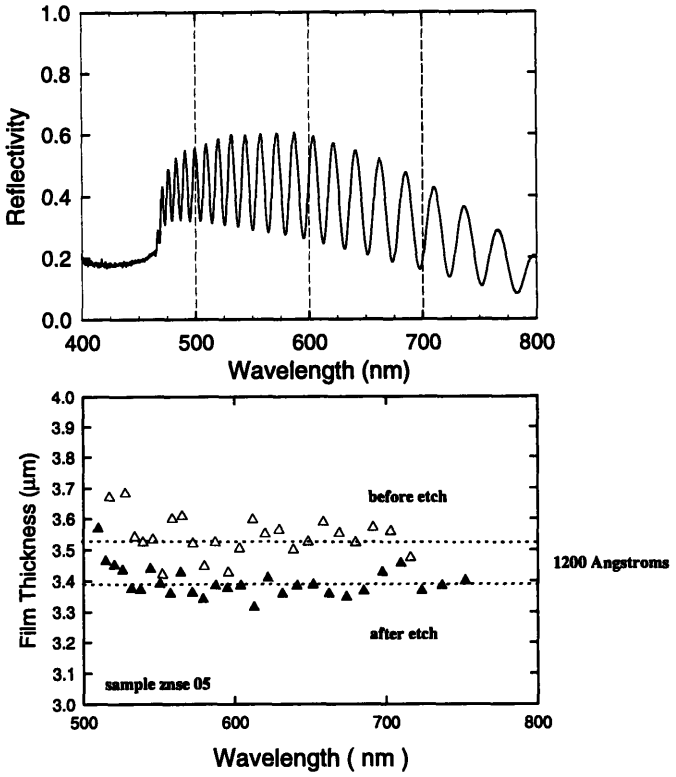

Figure 9-1: Top: Reflectivity spectrum of a 3.4 μm thick ZnSe film before substrate removal. Bottom: Thickness estimated for each Fabry-Perot oscillation before and after etching showing about 1200 Å of material removed.

minimal exposure of the ZnSe to the etch. Sometimes black wax dissolved in tri-chloroethylene was used to paint the sides and define one or more etch regions allowing multiple attempts. Generally, the etch proceeded at 2 to 5 μm / min. and the sample was held in plastic forceps and vigorously shaken in the solution until light was observed indicating the yellow ZnSe film was uncovered. The sample was then washed in water and dried with a nitrogen gun. The etch solution could be used for four or five different samples before being changed.

The etching procedure, even with the above precautions inevitably removed some material. The surface, however, would still show good specular reflection properties. The top plot of Fig. 9-1 shows the measured reflectivity spectrum of a 3.4 μm thick ZnSe film before etching. The bottom plot shows estimations of the film thickness obtained for every Fabry-Perot fringe from the sample before, and after etching showing that about 1200 Å of material had been removed.

Use of a more selective photoetching procedure, such as described in Ref [119], may give better results, but at the expense of increased complexity and inability to open large windows in the substrate.

9.2 Absorption measurements

Knowledge of the film thickness and the material absorption are important for fabricating a sample of about 1 absorption depth thickness for transmission measurements and to calculate the carrier densities generated by the pump and probe beams. There was a slight problem with this as the established value for the ZnSe absorption length was reported to be 1000Å. If this were true then the roughly 1200 Å of material removed in the etch process would make it very hard to make a suitable film.

Fortunately, absorption measurements resulted in an absorption length of about 2200 Å. Starting film thicknesses were thus chosen to be 5000Å to allow for material removed by the etch as well as thickness variations across the wafer. The absorption and sample thicknesses were measured by white-light reflection and transmission using a tungsten lamp filtered by a monochromator. Three detectors were used to measure the incident spectrum as well as the reflected and transmitted spectra through the film. The beam from the monochromator was stopped down to form a narrow beam with as little divergence as possible. The reflection was taken off the sample at about 10° angle of incidence. Recording all three power levels simultaneously with three lock-in amplifiers avoided drift of the lamp spectra and power. The sample thicknesses were determined by fitting the reflection spectra in the below-band region where the dispersion of the index is minimal. Even when precautions were taken to collect all of the incident light, losses from scattering and reflections of the lenses prevented determination of absolute reflectivities and transmission to better than 10%. Therefore, the measured reflection and transmission traces were scaled using a least squares fit to R+T=1 in the range 600 to 900 nm. Figure 9-2 shows the scaled reflectivity and transmission spectra with their sum. This is a valid procedure since the absorption in this region is negligible, and any loss due to clipping or scattering should be wavelength independent. Then absorption above the ZnSe bandedge

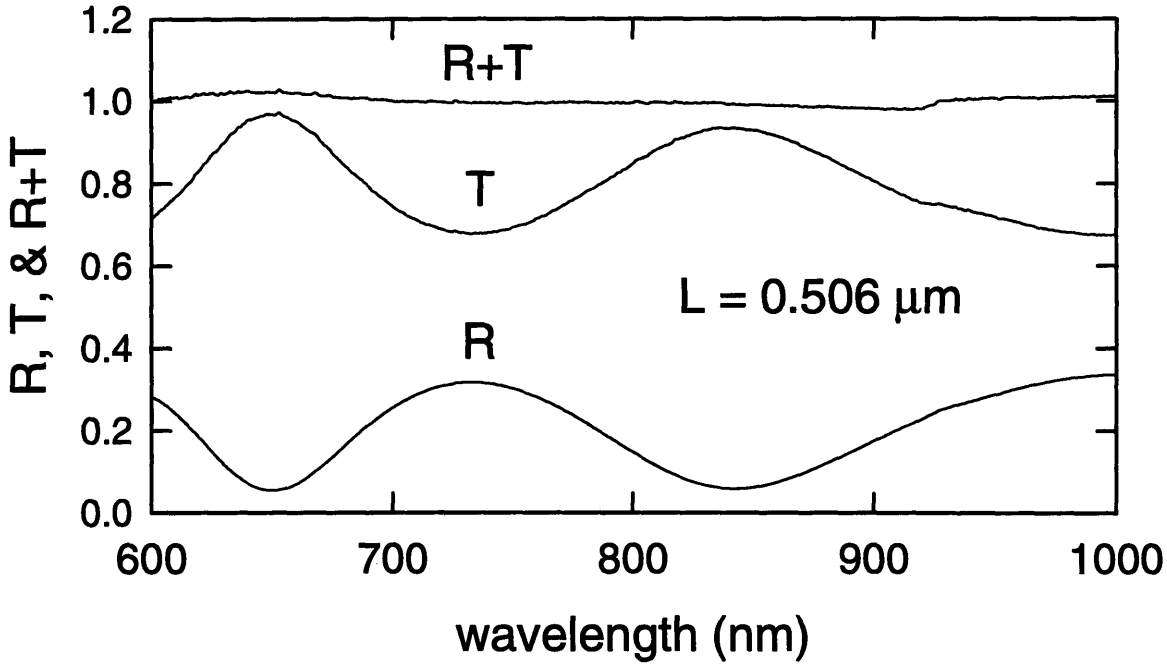

Figure 9-2: Reflectivity and transmission spectra of a P-type ZnSe film.

could then be calculated from

$$\alpha = \frac{-1}{L} \ln \frac{T}{1-R} \tag{9.1}$$

which is accurate if the optical density is high enough. Absorption spectra determined from this procedure are shown in Fig. 9-3 for four samples with dopings as shown. The unintentionally doped sample has an absorption just above the bandedge of 4.0×10^4 cm^{-1}. The P-type sample doping is low enough so that the Coulomb enhancement, which results in the step like structure, is not yet screened. It shows an absorption of 4.5×10^4 cm^{-1} which is in good agreement with the first sample. Several other unintentionally doped sample gave similar results. The N-type samples show the effects of bandfilling due to the large electron populations present (see Fig. 7-3). The fact that all four of the measured absorption values agree at high energies (beyond the effects of bandfilling) provides added confirmation of the validity of the method used. Thus, a value of 4.2×10^4 cm^{-1} was used in calculating injected carrier densities and other parameters in this thesis work. A last point to notice in Fig. 9-3 is how the absorption edges for the N-type samples do not appear to be moving to higher energies with doping. This is attributed

to bandgap renormalization effects [73].

9.3 Carrier lifetime and optical damage effects

The last area for sample characterization is the measurement of the carrier lifetime. Good quality material, with the potential to be used in lasers or other devices should have lifetimes in excess of several hundred picoseconds, at least. Figure 9-4 shows a pump probe transmission trace for an unintentionally doped film taken out beyond 350 ps. The warping and curvature of the trace is due to incorrect alignment of the stepping motor stage resulting in the pump beam walking slightly as the stage is scanned. The dotted traces are the actual data taken when the signal was peaked up at either end of the scan. The average should remove some of the effects of the pump walking, but evidently not all. Careful alignment is necessary for long scans. In any event, this typical result shows that the carrier lifetimes were at least 400ps and the films were of good quality compared to results [120, 121] presented in the literature.

After exposure to the lasers, this did not remain the case. Figure 9-5 shows the effects of photodegradation on the carrier lifetime. The trace labelled t=0, actually has been degraded in the alignment procedure. Figure 9-6 show the effect on the measured pump-probe dynamics at the onset of damage.

The damage was observed to depend solely on the average above-band light intensity on the sample. The only way found to get around this problem was to reduce the repetition rate of the source. This enables the use of pulse energies adequate to inject the desired carrier densities while, at the same time, using average powers low enough so that the measurements could be completed before damage set in. This works because the noise on the probe beams was dominated by classical noise (due to vibrations etc.) which is proportional to the average power. Thus, the detected probe power could be lowered without affecting the S/N ratio. This would not be the case for detection at the shot-noise limit where the S/N ratio depends on the collected power and the integration time.

This damage is believed to be related to the formation of 'dark-line defects' that currently limit the operating lifetime of ZnSe-based laser diodes [10]. These defects are believed to result from threading dislocations originating at the ZnSe/GaAs interface. No systematic study

of the damage was undertaken in this work. However, it is interesting to note that similar damage effects were seen for a bulk ZnSe substrate wafer obtained from Sumitomo for use as an alternative to GaAs (Fig. 9-7). Reducing the rep-rate slows the damage process by allowing lower average powers. The data in Fig. 9-7 shows that the damage is not thermal, since the thickness here is 500μm. It also indicates that other damage mechanisms may also be working, since no GaAs interface was present.

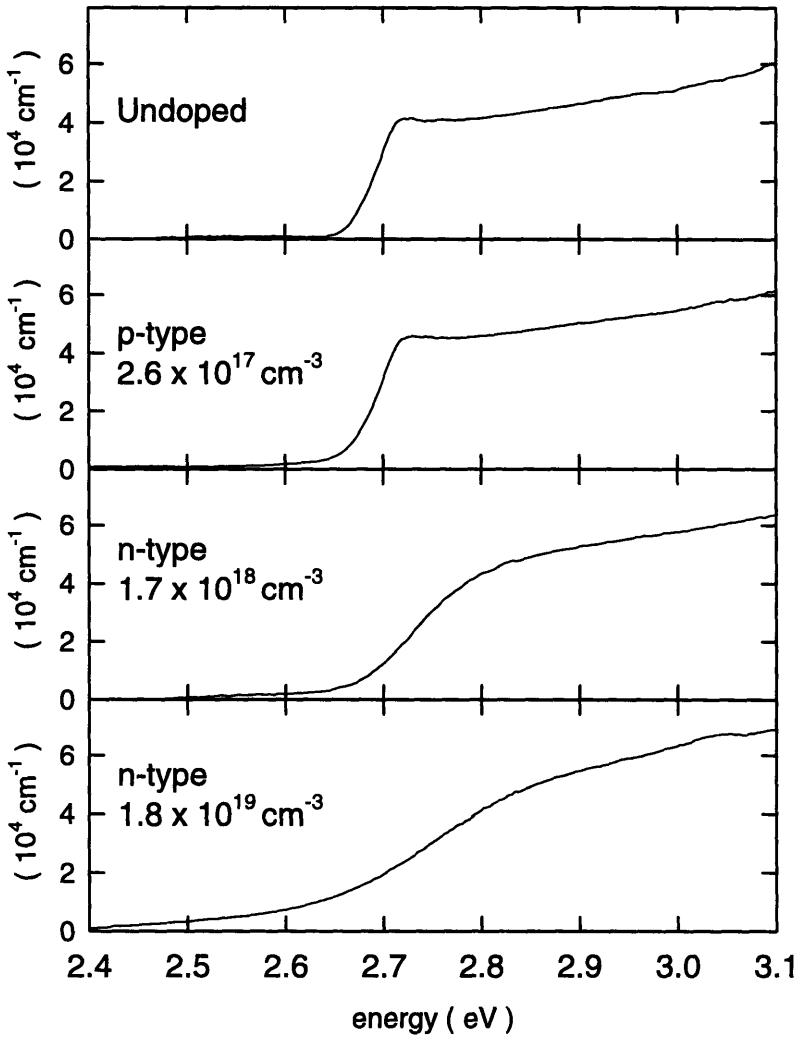

Figure 9-3: Absorption spectra for four ZnSe samples doped (Top) unintentionally (Second from top) p-type $2.6 \times 10^{17} cm^{-3}$, (Second from bottom) n-type $1.7 \times 10^{18} cm^{-3}$, and (Bottom) n-type 1.8×10^{19} cm^{-3}.

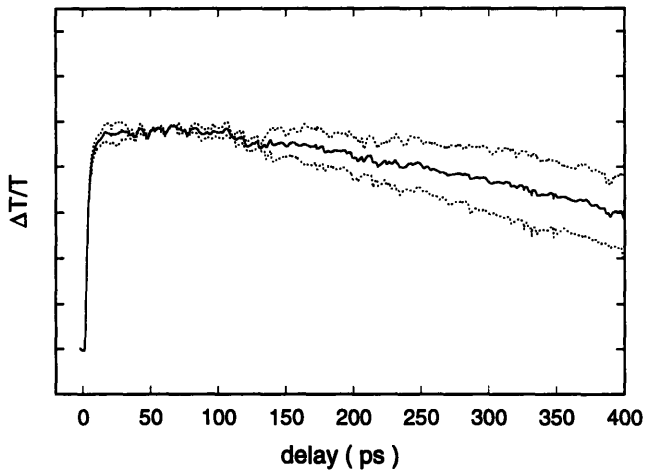

Figure 9-4: Long pump-probe scans to verify long carrier lifetime. Dotted curves are scans with alignment peaked at the beginning and end of the stage travel. Solid line is the average. The Curvature is due to the stage motion not being exactly parallel to the pump beam. The lifetime is greater than 400 ps indicating excellent quality films.

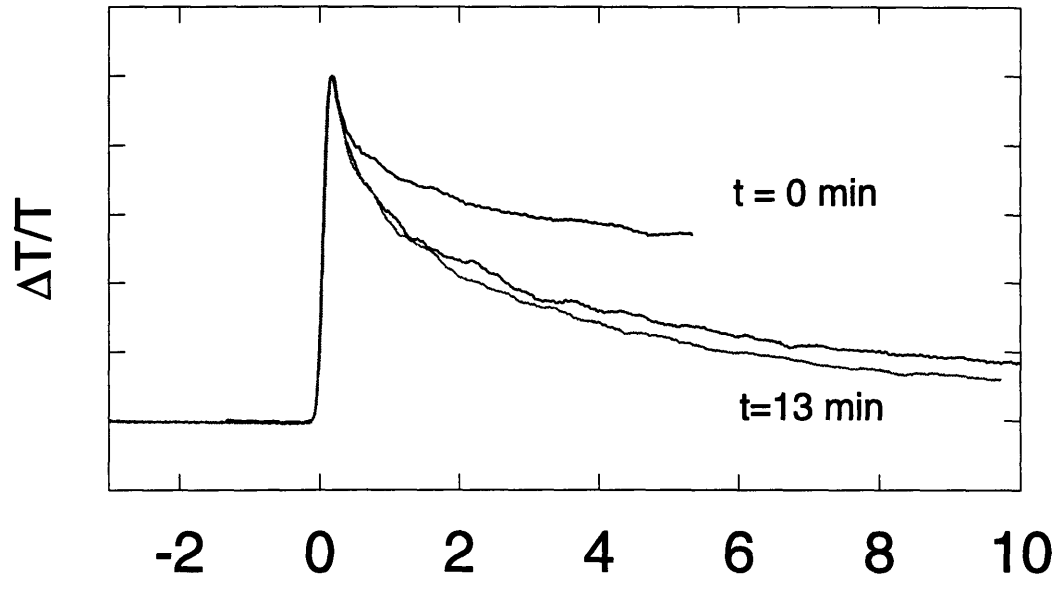

Figure 9-5: Optical degradation of the ZnSe films resulting in reduced carrier lifetime due to trap formation.

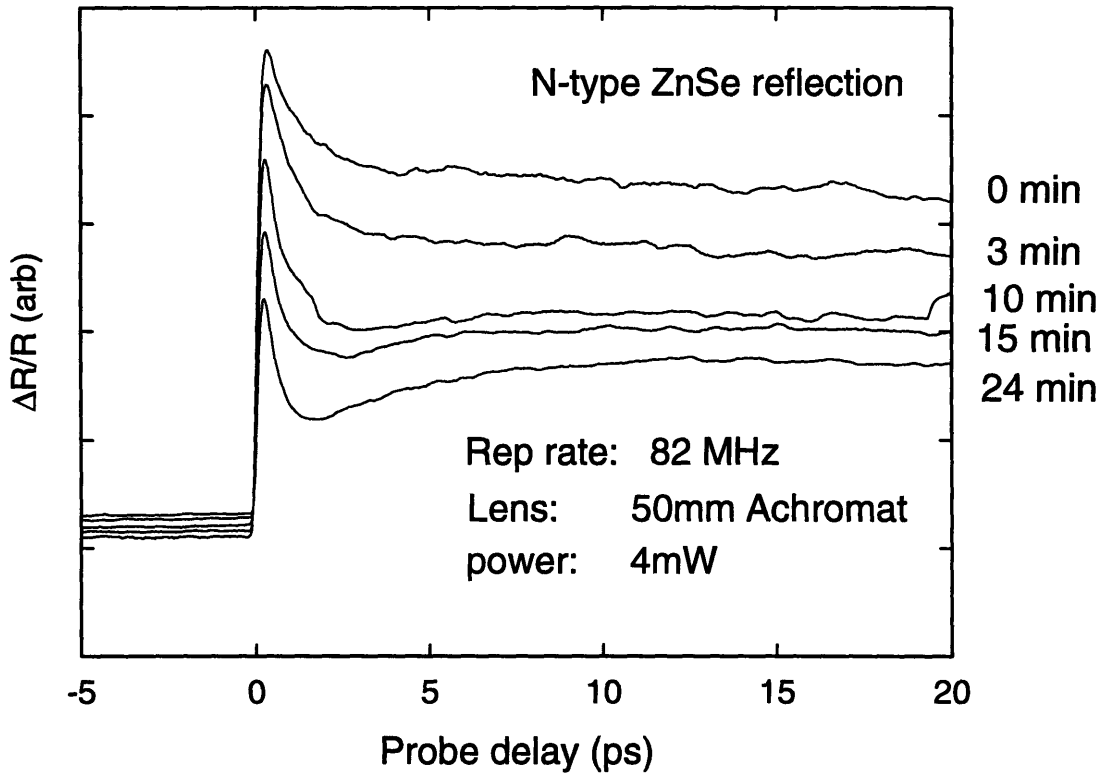

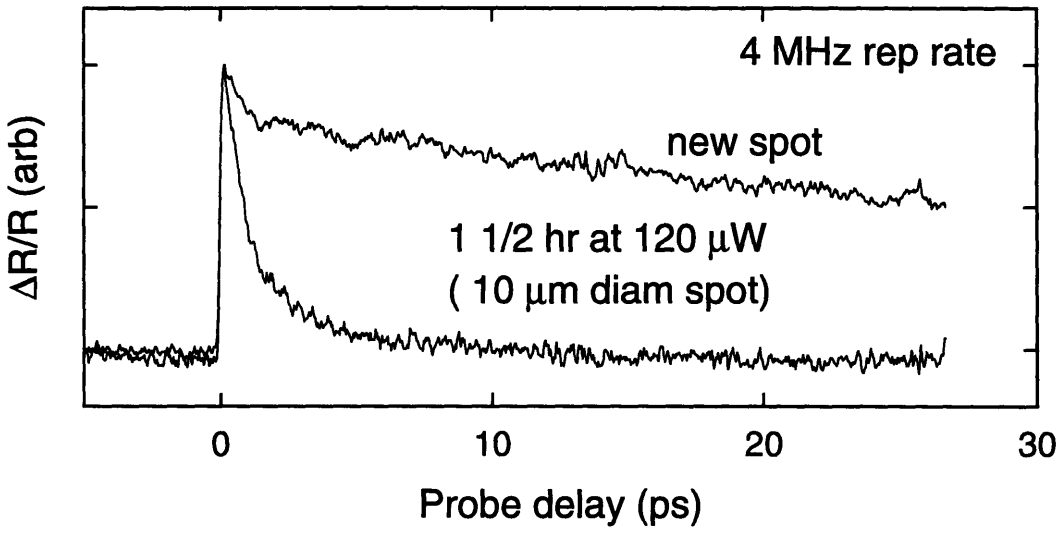

Figure 9-7: Damage induced in a ZnSe bulk crystal after 1 1/2 hours exposure to the pump at a reduced rep-rate. Pulse energies are same as before.

Chapter 10

Above band pumping and Coulomb screening effects

The most convenient way to create a hot carrier distribution in a semiconductor is to simply tune the pump laser above the bandedge. The initial distributions will then have an average kinetic energy equal to the difference in energy between the laser energy and the bandgap. The corresponding temperatures, after thermalization takes place can be on the order of 1000K, much hotter than the lattice. Figure 10-1 shows the evolution from the initial non-thermal electron and hole populations, which are determined by the laser spectrum, to a hot Fermi distribution which cools to the lattice temperature via LO phonon emission. For the experiments in this chapter, the pump and probe have the same wavelength.

Some of the complications arising from above band pumping were described in chapters 7 and 8. One immediate observation is that both electrons and holes are created. The cooling dynamics may be affected by the energy transfer rate between these separate populations. The very high initial temperatures also may lead to hot-phonon [109, 110], and dynamical screening [108] effects which would necessitate modification of the theory of Chapter 8. The big advantage of directly generating the distributions is that large changes in the probe transmission can be created because the near bandedge density of states is small and can be easily saturated. Probe modulations of 10% or more are possible.

All of these considerations will be seen to be irrelevant, however, because a different phys-

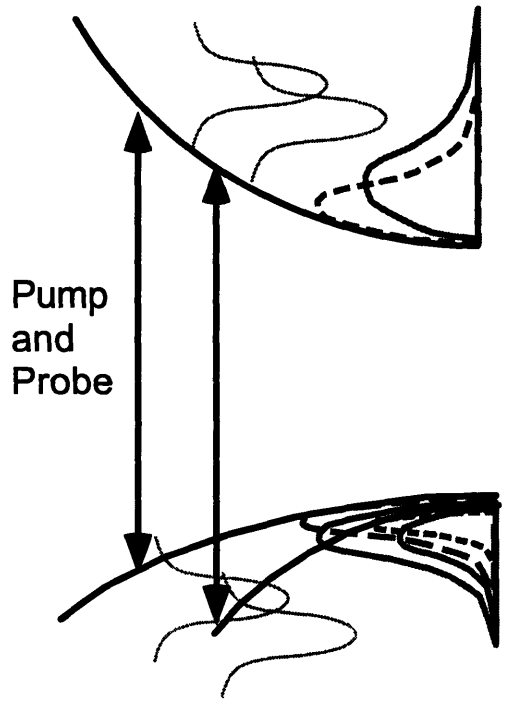

Figure 10-1: Above band pump pulse creates non-thermal electron and hole distributions that quickly thermalize to a hot Fermi distribution which cools to the lattice temperature by emitting LO phonons.

ical effect dominates the absorption changes. The simple picture of semiconductor absorption presented at the end of chapter 8 is not valid for ZnSe because of excitonic effects. The results of this chapter will show that screening of the electron-hole Coulomb attraction is the dominant absorption saturation mechanism for injected densities up to 10^{18} cm^{-3}.

10.1 Single wavelength pump-probe set-up

The experimental set-up is shown in Fig. 10-2 . 100 fs pulses from a modelocked Ti:sapphire laser are focused onto a 0.5mm beta-barium-borate (BBO) crystal, obtained from Inrad corp.,with a 50 mm lens to generate blue pulses. With 600 mW incident power at 900 nm about 30 mW of SHG could be produced.

The repetition rate of the blue pulse train was then reduced from the 82 MHz rep rate of the Ti:sapphire oscillator to 4 MHz using a fused silica acousto-optic cavity dumper in a single pass mode. The beam was focussed onto the dumper crystal at Brewster's angle with a 120 mm lens. Care must be taken to ensure that the beam travels parallel to the transducer pad for maximum diffraction efficiency. The efficiency of the dumper was typically 50% as measured on the undiffracted beam using a fast detector. The cavity dumper provided a convenient method for controlling the power in the beams without misaligning them or changing zero-delay.

Reducing the rep rate was necessary to avoid the effects of optical damage seen in the last chapter. The signal size, $\Delta T/T$, is determined by the pump pulse energy. Since low frequency mechanical chopping was used, the dominant noise on the probe beam was due to classical sources such as vibrations and fluctuations of the Argon laser pumping the Ti:sapphire laser. These fluctuations scale with the probe power, so reducing the probe average power resulted in the same signal to noise ratio. This holds until so little probe light is used that electronic noise in the detector amplifier becomes important.

Because the glass optics used in the set-up are quite dispersive in the blue, a pair of fused silica Brewster prisms were used for dispersion compensation. Auto-correlations as short as 77 fs could be obtained as shown in Fig. 10-3, indicating 50 fs pulses assuming a $\mathrm{sech}^2(t)$ pulse waveform. Typical pulsewidths were 60 fs.

The pulses emerging from the prism sequence were then sent to the pump-probe experiment.

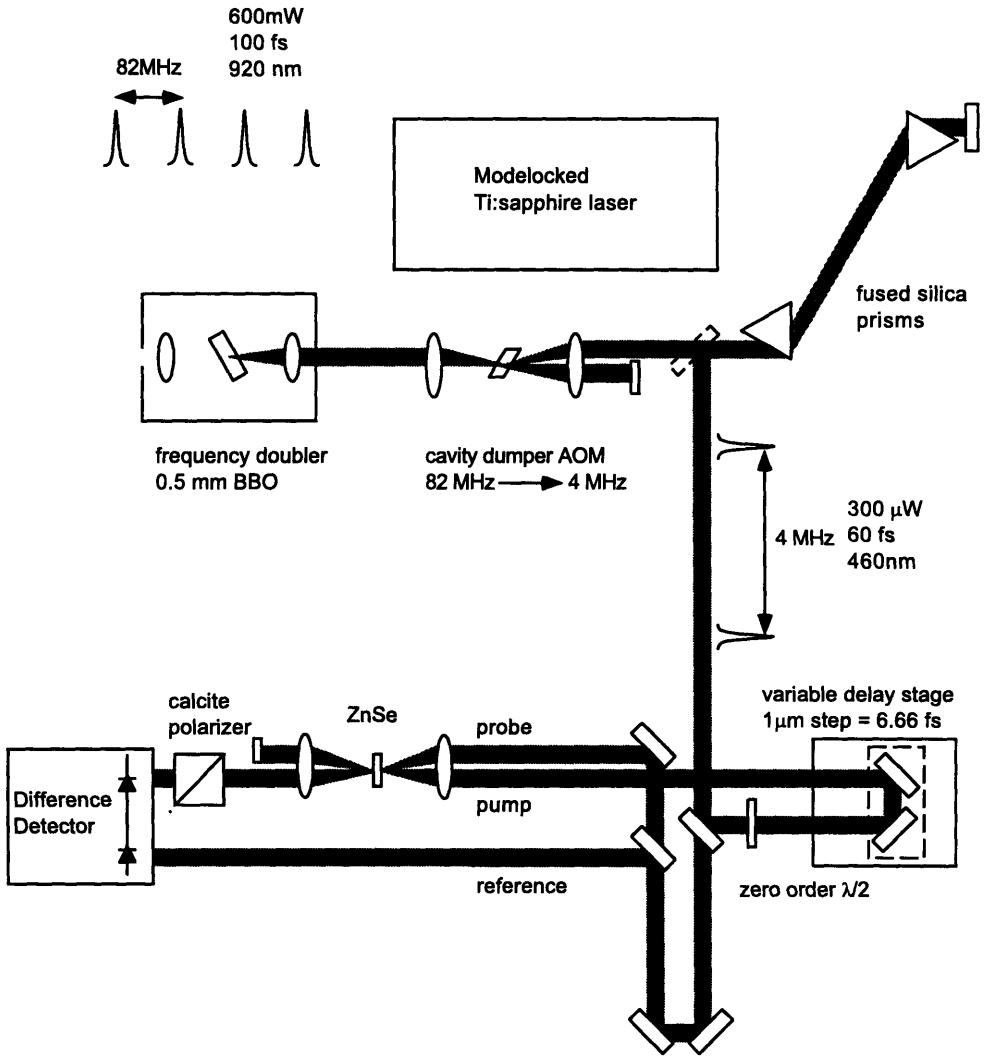

Figure 10-2: Single wavelength blue-pump blue-probe experimental set-up. AOM reduces the rep rate to avoid damage effects. PRisms are use to obtain 60 fs pulses.

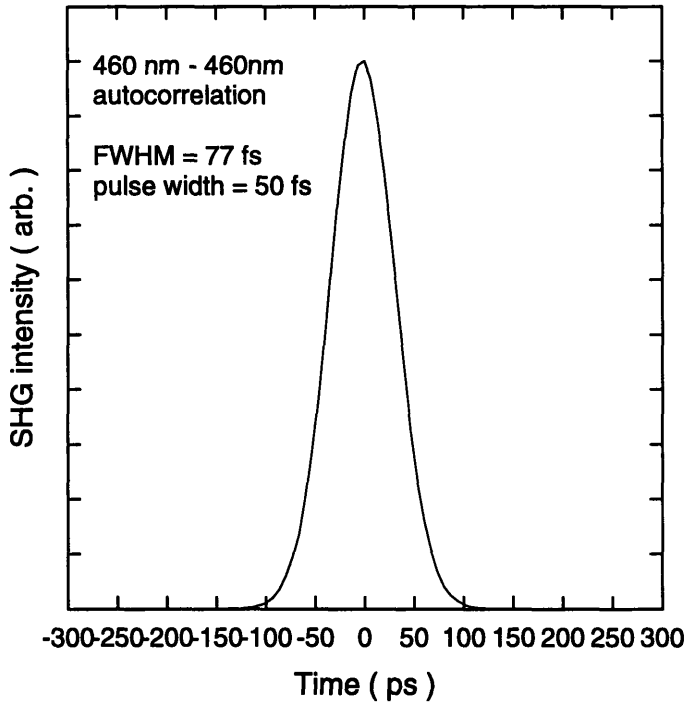

Figure 10-3: Measured auto-correlation of 460 nm pulses used in the single wavelength pump-probe experiments. A 100μm BBO crystal was used to produce SHG at 230nm. At FWHM is 77fs indicating a pulsewidth of 50fs assuming a 1.55 deconvolution factor for sech^2 pulses.

A beam splitter was used to create a pump probe beams. The pump arm had a retro-reflector mounted on a 1 μm resolution stepping motor stage. Thus the optical path length of the pump could be adjusted in 6.6 fs steps.

The beams were then brought together, side by side and made parallel. A 50 mm fused silica lens was used for focusing onto the sample in a non-colinear geometry. Measurements of the beam waist size using a razor blade mounted on a 0.1 μm resolution stepping motor stage determined the spot size to be about 13 μm in diameter. Careful alignment is necessary to ensure that the beams cross with their minimum waist size. This happens only if the beams are parallel, and hit the lens in symmetrical positions about the center. A 10μm diameter pinhole was used to achieve spatial overlap of the beams at their waist.

Temporal overlap was achieved by auto-correlation of the blue pulses. A 100μm BBO crystal (actually cut for the third harmonic of Ti:sapphire) was used to generate 225 nm radiation when the pulses arrived simultaneously. Use of a solar blind PMT was crucial for finding the small amount of UV light generated in the presence of large amounts of scattered blue light. Usually, when aligning the system from scratch, the undiffracted beam was aligned through the system first since more peak power was available for finding zero-delay.

With the system aligned the sample was placed in the focus. The transmitted probe beam was then sent to one Si photo-diode of a balanced difference detector circuit. A reference beam, split off from the probe before the sample was used on the other photo-diode. By electronically subtracting the signals generated by the probe before and after the sample, the pump induced modulations could be enhanced versus the laser noise which was common to both the probe and reference. A factor of 30 reduction in the probe fluctuations could be achieved this way.

10.2 Experimental results

Pump-probe results taken in transmission are shown in Fig. 10-4. The traces are for different probe wavelengths tuning across the ZnSe absorption edge at 462 nm. A pump power of 120 μW was used, resulting in an injected density of 2.4×10^{18} cm^{-3} electron-hole pairs. Near the bottom of the band, large bleaching of the absorption is seen. Tuning to lower energies, the signal size decreases as the pump and probe overlap the absorption spectrum less. At higher

energies, the signal also decreases, since the optically injected carriers thermalize to the bottom of the band and have their greatest effect on those states. The transmission signal eventually goes negative at high energies. This is due to index effects. The index changes, which go along with the absorption saturation, extend to a wider wavelength region due to the Kramers-Kronig relations. At these wavelengths the absorption saturation of the low energy states results in an increase of the index of refraction. This increases the reflected power and decreases the amount transmitted. The induced transmission changes persist for several hundred picosecond until recombination occurs to remove the carrier populations.

The dynamics exhibit two components; a step response due to the injected carriers and a delta function response. The magnitude of these components is plotted against probe energy in Fig. 10-5. Both signals are localized to the near bandedge states as expected for band filling processes. The delta function response is attributed to the optical Stark effect because it occurs only at the bandedge. A coherent artifact can also cause spurious delta function responses when only slow dynamics are present [122]. These effects are ruled out since the effect is not seen at all wavelengths, and the pump and probe are orthogonally polarized. The optical Stark effect is discussed in Chapter 11.

A closer look at the temporal dynamics is shown in Fig. 10-6 for probe wavelengths of 454 and 461 nm. The striking feature of these traces is the lack of any dynamics on a several hundred femtosecond timescale. For the 454 nm trace, the initial electron temperature was about 600 K. Thus, large changes in the state filling should be observed as the carrier distribution cools. Instead, a flat step response is seen. With 100fs cross-correlation resolution, some effects due to spectral hole burning [91, 123] are also expected, even if the dynamics could not be time-resolved. No changes in the spectrum or the dynamics were observed when reducing the pump power to as low as 16 μW. The conclusion can only be that some other physical process is involved in the absorption saturation besides bandfilling.

10.3 Coulomb enhancement and excitonic effects

In simple treatments of optical absorption in semiconductors, the electron and hole band states are assumed to be free carrier plane wave states. This results in the coupling between the

states being solely determined by the interband momentum matrix element, p_{cv}. In the Kane model [72], p_{cv} can be shown to essentially independent of wavevector $\vec{k}$ for the near bandedge states. Thus, the absorption spectrum is determined only by states filling effects as discussed at the end of chapter 7. This treatment neglects the Coulomb attraction between the excited electron-hole pair.

A more correct theory of semiconductor absorption is the Elliot formalism introduced in chapter 2. The Elliot formula for the imaginary part of the dielectric constant (absorption) due to interband transitions is

$$\mathrm{Im}\,\varepsilon\left(\hbar\omega\right) = \frac{4\pi^2 e^2}{m^* \omega^2} \left|\hat{\epsilon} \cdot \mathbf{P}_{cv}\right|^2 \sum \left|\Phi_i\left(r=0\right)\right|^2 \delta\left(E_i - \hbar\omega\right) \tag{10.1}$$

where the envelope function Φ is found by solving the relative coordinate Schrödinger equation with the electron-hole Coulomb attraction included

$$\left[\frac{\hbar^2}{2\mu_r^*}\left(\frac{\partial^2}{\partial x^2} + \frac{\partial^2}{\partial y^2} + \frac{\partial^2}{\partial z^2}\right) + \frac{e^2}{4\pi\epsilon r} - E_i\right] \Phi_i(\vec{r}) = 0. \tag{10.2}$$

Eq. 10.2 is the equation for the hydrogen atom, and the solutions will be the hydrogenic wavefunctions. The bound states with negative energy are known as excitons and result in absorption peaks below the bandedge at low temperatures. The exciton binding energy, E_{ex}, is about 20 meV in ZnSe. This is much bigger than the 4 meV for GaAs. At room temperature the exciton is almost completely ionized, however. The states with $E_i > 0$ are the continuum of hydrogen scattering states. These states correspond to the free particle conduction and valence band states when the Coulomb attraction is small. For ZnSe the effects of electron-hole attraction are quite large for the band states even at room temperature.

When Eq. 10.1 is evaluated, the absorption spectrum for an undoped semiconductor can be written as [73]

$$\alpha(\Delta) = \alpha_0 \left[4\pi\delta(\Delta+1) + C(\Delta)\sqrt{\Delta}U(\Delta)\right], \text{with} \tag{10.3}$$

$$\Delta = \frac{\hbar\omega - E_g}{E_{ex}}.$$

The delta function term in the brackets represents the exciton absorption. The second term with the unit step function, U, represents the above band continuum absorption. The square root factor is the density of states. The effect of including the Coulomb attraction is the factor, C, known as the Coulomb enhancement factor. It appears as an energy-dependent matrix element and is given by

$$C(\Delta) = \frac{\frac{\pi}{\sqrt{\Delta}} e^{\frac{\pi}{\sqrt{\Delta}}}}{\sinh \frac{\pi}{\sqrt{\Delta}}}. \tag{10.4}$$

As $\Delta \rightarrow 0$, C blows up as $\Delta^{-\frac{1}{2}}$ indicating that the absorption is constant above the bandedge rather than given by the square-root density of states as in the free particle case. Figure 10-7 shows the continuum absorption spectrum as well as the Coulomb enhancement and density of states factors.

The reason these modifications are important is because this excitonic contribution to the above band absorption is susceptible to screening by free carriers. The enhanced absorption predicted out to arbitrarily high energies in Fig. 10-7 is an artifact of the $1/r$ Coulomb potential. In the presence of a background free carrier density, the Coulomb attraction is screened and the potential is given by a Yukawa potential

$$V(r) = \frac{e^2}{4\pi\epsilon r} e^{-\kappa r} \tag{10.5}$$

where κ is the screening wavevector. The Schrödinger Eq. cannot be evaluated for this potential. Banyai and Koch [124] solved it for a close approximation given by

$$V(r) = \frac{2e^2\kappa}{\epsilon} \frac{1}{e^{2\kappa r} - 1}. \tag{10.6}$$

The absorption spectra found by Banyai and Koch is

$$\begin{aligned} \alpha(\hbar\omega) &= \alpha_0(1 - f_c - f_v) \left[\left(1 - \tfrac{1}{g^2}\right) \delta_\Gamma(\Delta + 1) \right. \\ &\left. + \int_0^\infty dx \frac{\sinh(\pi g\sqrt{x})}{\cosh(\pi g\sqrt{x}) - \cos(\pi\sqrt{4g - xg^2}} \delta_\Gamma(\Delta - x) \right] \end{aligned} \tag{10.7}$$

where $g = 1/a_0\kappa$ with a_0 the Bohr radius of an exciton and Δ is the normalized energy as

defined above. The factor δ_Γ is a phenomenological broadening parameter given by

$$\delta_\Gamma(x) = \frac{2}{\pi\Gamma\cosh(x/\Gamma)} \tag{10.8}$$

where Γ is chosen to fit measured absorption spectra ($\Gamma \tilde{} kT$). The absorption in now dependent on the carrier density through the Fermi occupation factors as well as the parameter g which resulted from the density dependence of the electron-hole potential. The exciton term in Eq. 10.7 is ionized for $g \rightarrow 1$, or when the screening length becomes equal to the exciton Bohr radius. The density at which this occurs is known as the Mott density and it serves as a dividing line between densities where exciton effects are important and where they can be neglected.

Figure 10-8 shows calculated absorption spectra for ZnSe and GaAs at 300K using the Banyai-Koch formula. The solid curves are for a carrier density of 10^{15}cm^{-3} which is negligible for both screening and bandfilling effects. The ZnSe curve appears to resemble the measured absorption spectra in the last chapter quite well. The energy scale for Coulomb effects is the exciton binding energy. Thus, these effect are more pronounced at energies far from the band-edge in ZnSe. Because the GaAs exciton binding energy is so small, the Coulomb enhancement effect is washed out by the thermal broadening and only affects states close to the bandedge. The GaAs spectrum is close to being described by the free carrier square-root density of states model.

The dashed lines are for the case of the carrier density equal to the Mott density for each material. The change in the GaAs absorption is small since the Coulomb enhancement was small to begin with. The effect of the ZnSe, however, is drastic with a large reduction in the absorption over the same spectral region where bandfilling effects are expected. These changes are due almost solely to screening. The Mott density is 4.4×10^{17} cm^{-3} for ZnSe and 6×10^{16} cm^{-3} for GaAs. Bandfilling effects only start become significant when the Fermi level reaches the conduction band edge. This occurs at 1.1×10^{18} cm^{-3} for ZnSe and 3.3×10^{17} cm^{-3} for GaAs, well above the Mott density in each case.

10.4 Discussion

The reason no carrier dynamics were evident in the pump-probe traces is now evident. Creation of an electron-hole plasma by the pump screens the Coulomb enhancement and saturates the plasma. Any bandfilling dynamics present only cause small changes that ride on the back of this large signal and are thus very hard to discern. The spectrum of the step component appears to follow the shape of the changes in absorption calculated in Fig. 10-8. It is interesting that the high initial temperatures, and potentially non-thermal distributions due to spectral hole-burning, do not seem to affect the screening. The screening wavevector, as seen in Chapter 7, is related to the dielectric function of the electron-hole plasma, $\epsilon(q,\omega)$, which in turn is a function of the carrier distributions and temperatures. Since dynamical screening has been shown to be important for the electron-phonon interaction in previous carrier dynamics studies, it might be expected to play a role in these electron-exciton effects. This appears not to be the case, however, since the screening just seems to be turned on by the pump and to remain on for the carrier lifetime. It could be the case that at 2.4×10^{18} cm^{-3}, the screening could be saturated and thus independent of the carrier temperature. Result taken for injected densities as low as $3\times10^{17}cm^{-3}$ do not show any temporal dynamics either, however.

To measure the carrier-phonon coupling and dynamics in ZnSe, it appears that it is necessary to avoid large carrier density changes. An experimental technique to accomplish this is described in the next chapter.

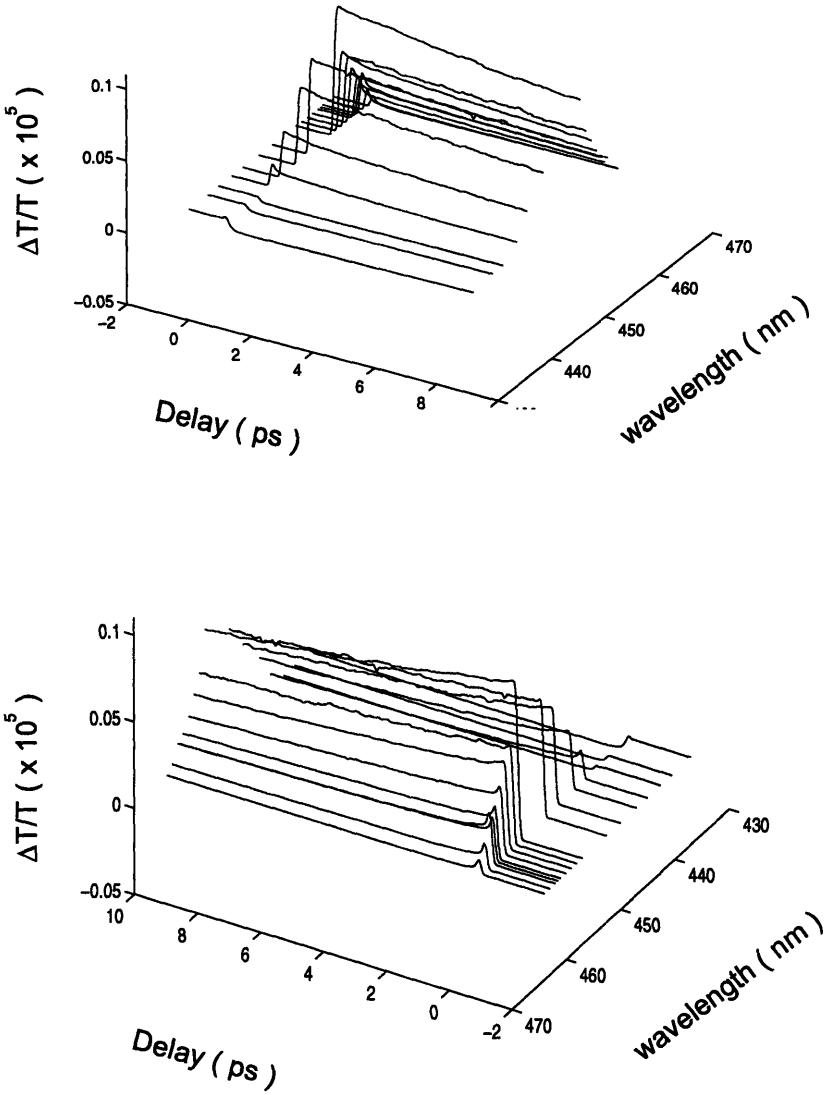

Figure 10-4: Blue Pump- Blue probe transmission traces for undoped ZnSe tuning across the bandedge at 462 nm (2.67eV).

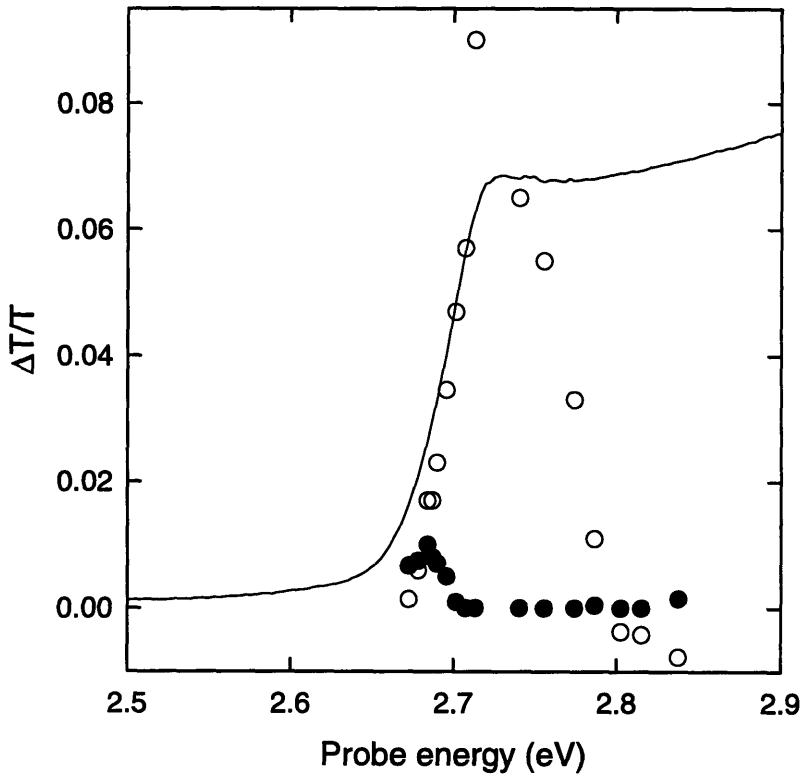

Figure 10-5: Magnitudes of the step component (white circles) and the instantaneous componet (dark circles) as a function of probe energy. The solid curve is the measured absorption spectrum.

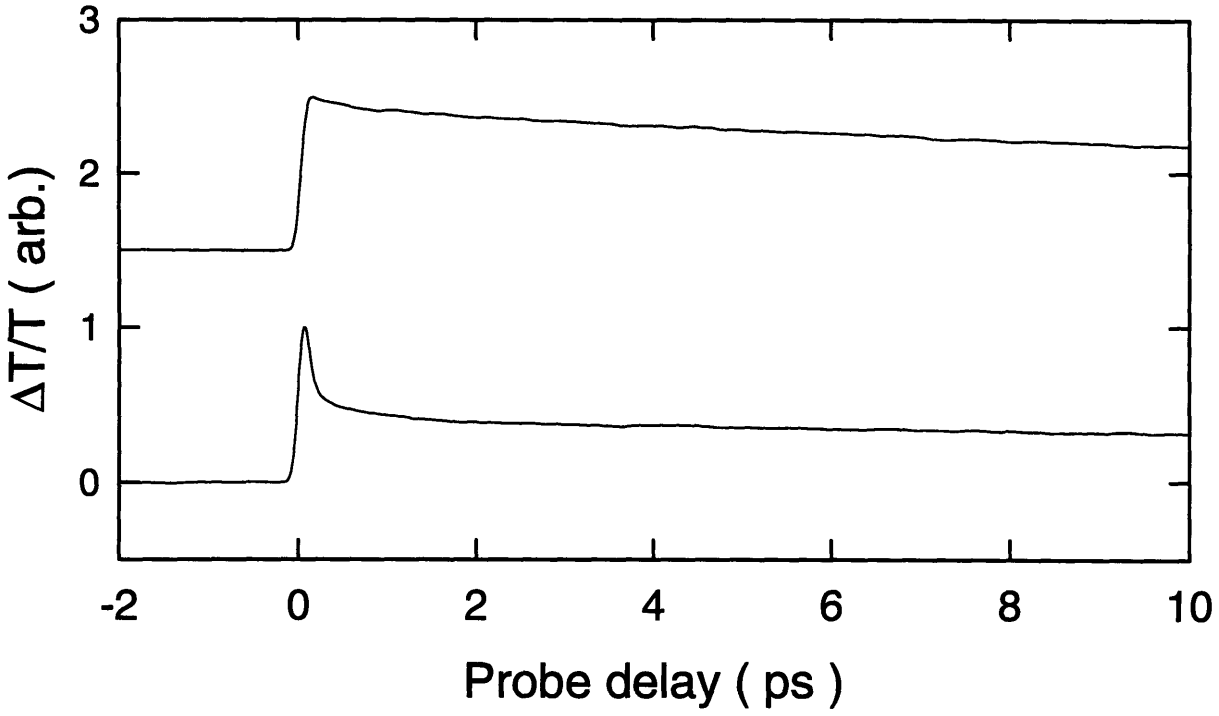

Figure 10-6: Pump probe traces at 454 nm (top) and 461 nm (bottom). No evidence for carrier dynamics is seen. The instantaneous component in the lower trace is due to the optical Stark effect.

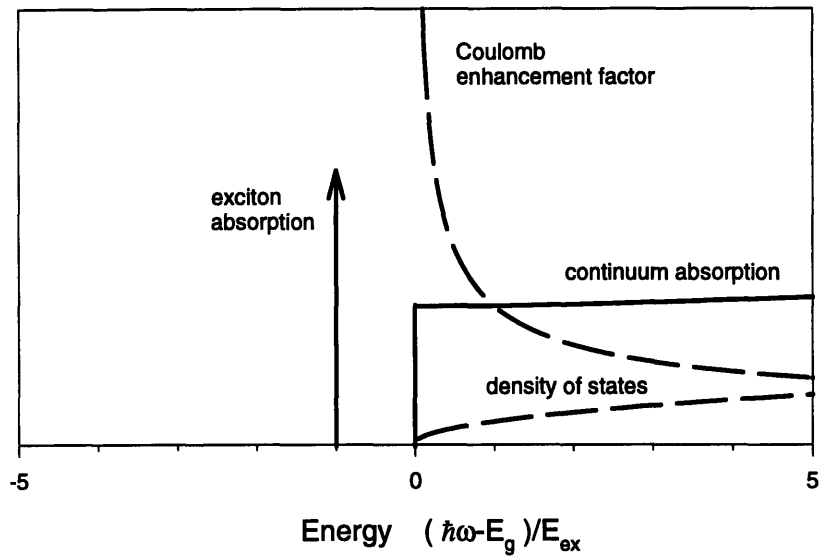

Figure 10-7: Schematic diagram of the effects of Coulomb enhancement on semiconductor absorption spectra. The energy scale is normalized to the exciton binding energy. The above-band, continuum absorption (solid line) is given by the product of the 3-D density of states and the Coulomb enhancement factor (CEF) (dashed lines). The divergence of the CEF exactly balances the square root energy dependence of the density of states leading to a step like absoprtion spectrum. Coulomb attraction also leads to a bound state (the exciton) which contribute and absorption peak below the bandedge.

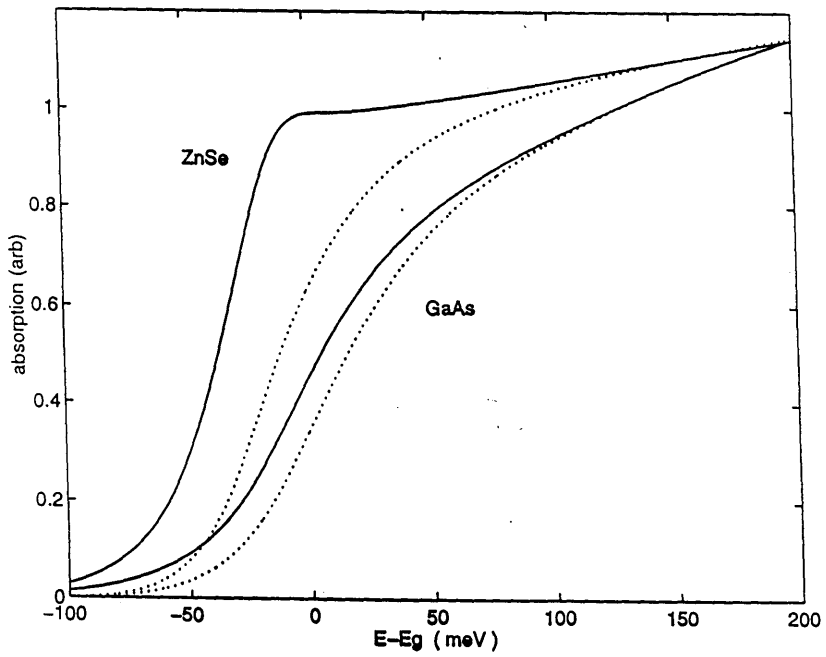

Figure 10-8: Comparison of the calculated ZnSe and GaAs absorption spectra at very low carrier densities (solid line) and at the Mott densities (dashed line). The large reduction in the ZnSe absorption is due to screening of the Coulomb enhancement.

Chapter 11

Below band pumping and intervalley scattering

In the above band pumping experiments of the last chapter, the carrier temperature dynamics were completely masked by Coulomb screening effects despite the fact that the initial temperatures were on the order of 1000 K. Since the cooling time constants are the quantities of interest for comparison to the electron-phonon coupling theory of Chapter 8, a method for inducing a pure temperature change in the carrier distributions, without any density changes, would be desirable. Measurements in semiconductor diode laser amplifiers [113, 114] have shown that free carrier absorption (FCA) can be used to heat carrier distributions without changing the total carrier density.

Free carrier absorption is a process where electrons or holes are promoted to high energy states within their own band [125, 126]. Emission or absorption of an optical phonon is required to conserve momentum. Thus, FCA is a two step process. In the interpretation of second order perturbation theory, carriers are excited to a virtual state by a photon. If absorption or emission of a phonon occurs while the carrier is in the virtual state, a real carrier can be created high in the conduction or valence bands. This process is depicted in Fig. 11-1. Through carrier-carrier scattering collisions, the promoted carrier will transfer its excess energy to the cold distribution at the bottom of the band and cause a temperature increase. An interband resonant probe can monitor this temperature change through the occupation of the near bandedge states as

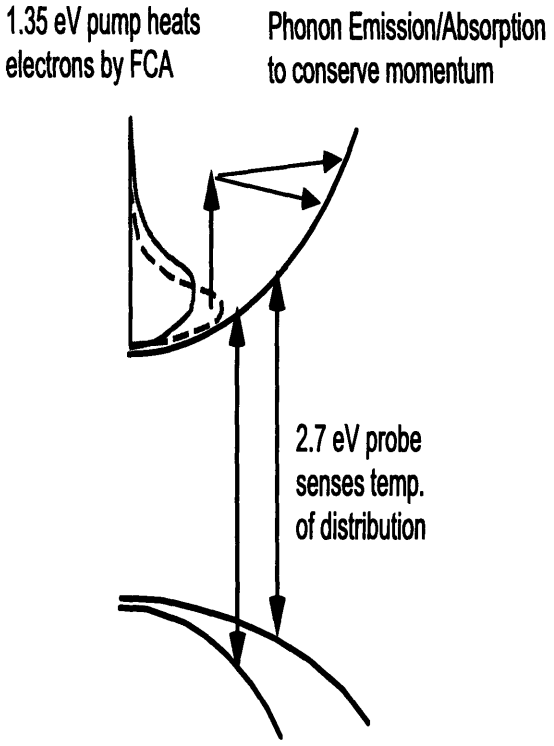

Figure 11-1: The free carrier absorption (FCA) process in semicondcutors involves a transition to virtual state by an photon and subsequent scattering by phonon emission or absorption to a high energy state in the same band.

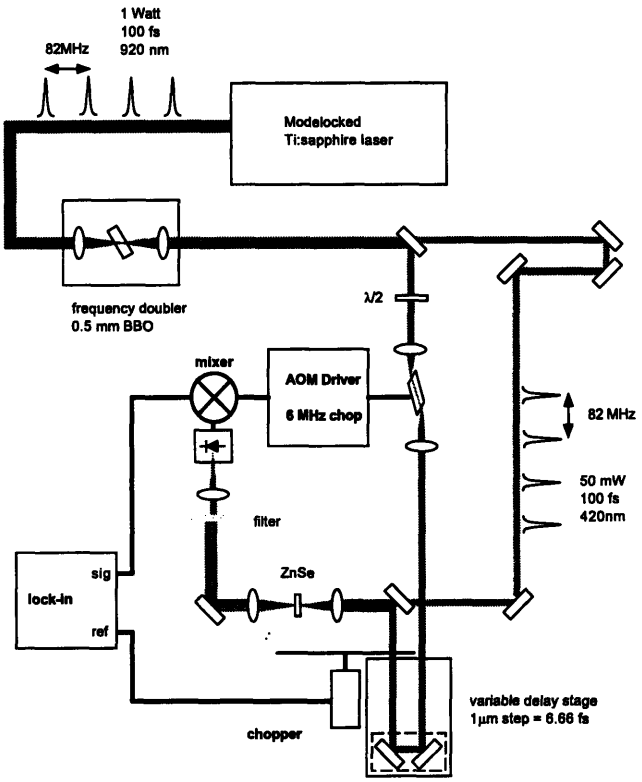

Figure 11-2: Two-wavelength pump-probe set-up for balow band pumping by FCA. An acousto-optic modulator is used for RF chopping to achieve shot-noise limited detection.

discussed at the end of Chapter 7. Because FCA is an intraband process, no extra carriers are created and the density is unaffected.

11.1 Two-wavelength Pump-probe Experimental set-up

A two-wavelength pump-probe experiment designed to implement this FCA pumping scheme is shown in Fig. 11-2. The modelocked Ti:sapphire laser was used again, as with the above-band pumping experiments, to provide 100 fs optical pulses. The probe pulse was obtained by SHG in a 0.5mm BBO crystal. Tuning the Ti:sapphire output from 860nm to 960nm enabled the probe pulses to be tuned around the ZnSe bandedge in the range 430nm to 480nm. The fundamental Ti:sapphire pulses were used for the pump. The blue and near IR beams emerging from the nonlinear BBO crystal were separated with a dichroic dielectric mirror into to the two arms

of the pump-probe set-up. The pump pulse was retro-reflected off a mirror mounted on a 1 μm stepper motor stage to provide the delay scanning. The beams were then recombined with another dielctric mirror in a co-linear geometry. A 50 mm fused silica lens was used to focus the beams on the sample. Because of the wavelength dependence of the index of refraction of the lens, the pump and probe beams did not focus at the same distance from the lens. Thus the spot sizes at the sample were not known with precision. The size of the IR beam on the lens was set to be roughly twice the size of the probe beam to account for the wavelength dependence of the diffraction limited Gaussian beam waist sizes. The position of the sample film in the focus was simply adjusted to maximize the probe signal. No dispersion compensation was used in these experiments because separate prism pairs would have to be used in the pump and probe arms. This would lead to variation in the zero-delay position of the stepper motor as the wavelengths were tuned. The measured cross correlation between the pump and probe was 180 fs. The use of fused silica lenses instead of achromats, which would have helped the chromatic aberration problems, was necessary to minimize dispersion and pulse broadening in the set-up.

Because it is a two-step, phonon assisted process, FCA is very weak. Typical absorption strengths are about 10 cm^{-1} in GaAs at wavelengths around 850 nm and at carrier densities in the 10^{18} cm^{-3} range. The diode laser pump-probe experiments were able to use such a weak excitation method because of the long interaction lengths possible in waveguide geometries. For a thin film on the order of 5000Å, FCA will result in about only 5×10^{-4} of the pump pulse photons being absorbed. A 30 pJ pump pulse, focussed on a 10 μm spot will therefore induce a temperature rise of 0.04 K in the carrier distribution.

To measure the small changes in probe absorption that result from these tiny temperature increases, high frequency RF detection methods are required. At low frequencies, the output power of the Ti:sapphire laser fluctuates due to acoustic vibrations in the laser cavity as well as variations in the power of the argon ion pump laser. Above a few MHz, acoustic vibrations are absent and the Ti:sapphire gain medium can no longer follow fluctuations in the argon pump. The output power is then limited only by shot-noise. To move the probe signal beyond the low frequency laser noise, a fused silica acousto-optic modulator (AOM) obtained from Brimrose Corp. was used to chop the pump beam at 6 MHz. A second, mechanical chopper was also used to put kHz sidebands on the 6 MHz carrier. After the sample, the pump beam was eliminated

with a Schott BG-39 colored glass filter. The detected probe signal was mixed with the carrier frequency to move the sidebands within the detection range of a simple low frequency lock-in amplifier. A two-phase RF signal generator was used to generate the 6 MHz AOM drive and mixing signals. Adjustment of the phase between the mixing and AOM drive signals is necessary to account for the phase shifts due to the detector circuit, the AOM drive amplifier, and the propagation delay of the acoustic wave in the AOM crystal. Probe modulations as small as 10^{-6} can be routinely found with this system using probe photo-currents as low as a few μA. This detection system was developed by S. B. Fleischer and more details of the detection circuit can be found in his Ph. D. thesis (EECS Dept., MIT, Jan. 1997).

11.2 Spectral response

Using the set-up of Fig. 11-2, pump-probe measurements were made on of n- and p-type ZnSe films. Because the carriers are not generated optically, the distributions must be created in the material by doping. Pump powers between 2 and 5mW were used which resulted in probe transmission changes of about 10^{-5}. The probe power was kept below 300 μW to avoid onset of optical damage as observed in the above band experiments (Chapter 9). High pump powers are not a problem since the pump is far below band at about half the bandgap. No changes in the pump-probe traces indicating damage were observed, however this may be due to the fact that this experiment is not sensitive to reductions in the carrier lifetime.

Experimental results for n-type ZnSe are shown in Figs. 11-3 through 11-5. Figure 11-3 shows traces obtained from a $1.7\times10^{18}\text{cm}^{-3}$ sample for probe wavelengths tuning across the ZnSe bandgap at 462 nm. Fast, pico-second timescale dynamics are immediately evident, in contrast to the above-band pumping experiments (Fig. 10-4). The response is composed of an instantaneous delta function component, and an exponential relaxation. Both components show an interesting spectral dependence. The instantaneous component is negative at long wavelengths where the probe is below the absorption edge. This is consistent with two-photon absorption. When the pump and probe are overlapped in time, a pump and a probe photon can be simultaneously absorbed on a high energy transition in the bandstructure. The presence of the pump thus acts as a loss mechanism that disappears when the pump pulse is

not temporally overlapped with the probe. At shorter wavelengths, tuning into the band, the instantaneous component flips sign, representing a bleaching of the probe absorption. This response is attributed to the optical Stark effect which will be discussed in the next chapter.

The exponential component is due to the electron dynamics. From the observed size of the transmission changes, about 10^{-5} $\Delta T/T$, temperature changes of 0.05K are inferred. The signal is negative at long wavelengths and flips sign at shorter wavelengths. The bottom plot is of the same data, only inverted to better show the response at low energies. This is exactly the signature of a temperature change in the distribution which lowers the occupation of low energy states, causing more absorption, and increases the occupation of high energy states, resulting in bleaching. The response also recovers to zero within several picoseconds indicating that the response is not due to density changes. Even though the pump is below the bandedge, mid-gap defect states could be ionized by the pump resulting in additional electrons being promoted to the conduction band. These carriers would be expected to remain in the band for several hundred picoseconds, however. The short recovery time, combined with the observed spectral dependence, confirm that the dynamics are due to cooling of the electron distribution. Figures 11-4 and 11-5 show the response of films doped n-type to $1.8\times10^{19}cm^{-3}$ and $1\times10^{20}cm^{-3}$, respectively. The dynamics are very similar.

Figure 11-6 shows the response of a p-type sample doped with nitrogen at 8×10^{17} cm^{-3}. Because of the 110 meV acceptor ionization energy, this results in a free hole density of only about 2.6×10^{17} cm^{-3}. Obtaining high p-type doping is an outstanding problem in ZnSe growth research. The small hole density results in a much smaller heating signal which is not readily apparent in the data of Fig. 11-6. The dominant responses are the instantaneous optical Stark effect and TPA which is seen at the low and high energy sides of the plot, away from the vicinity of the sharp absorption edge. The reduction in the cooling response at low densities is another reassuring verification that the experiment is measuring intraband processes.

The power dependences of the cooling dynamics for the $1.8\times10^{19}cm^{-3}$ n-type and the p-type sample are shown in Figs. 11-7 and 11-8. The signals are linear in both pump and probe power as expected for FCA heating of the distributions.

To get a clearer picture of the spectral response of the instantaneous component and the cooling dynamics, Fig. 11-9 plots the magnitude of the signals against probe wavelength along

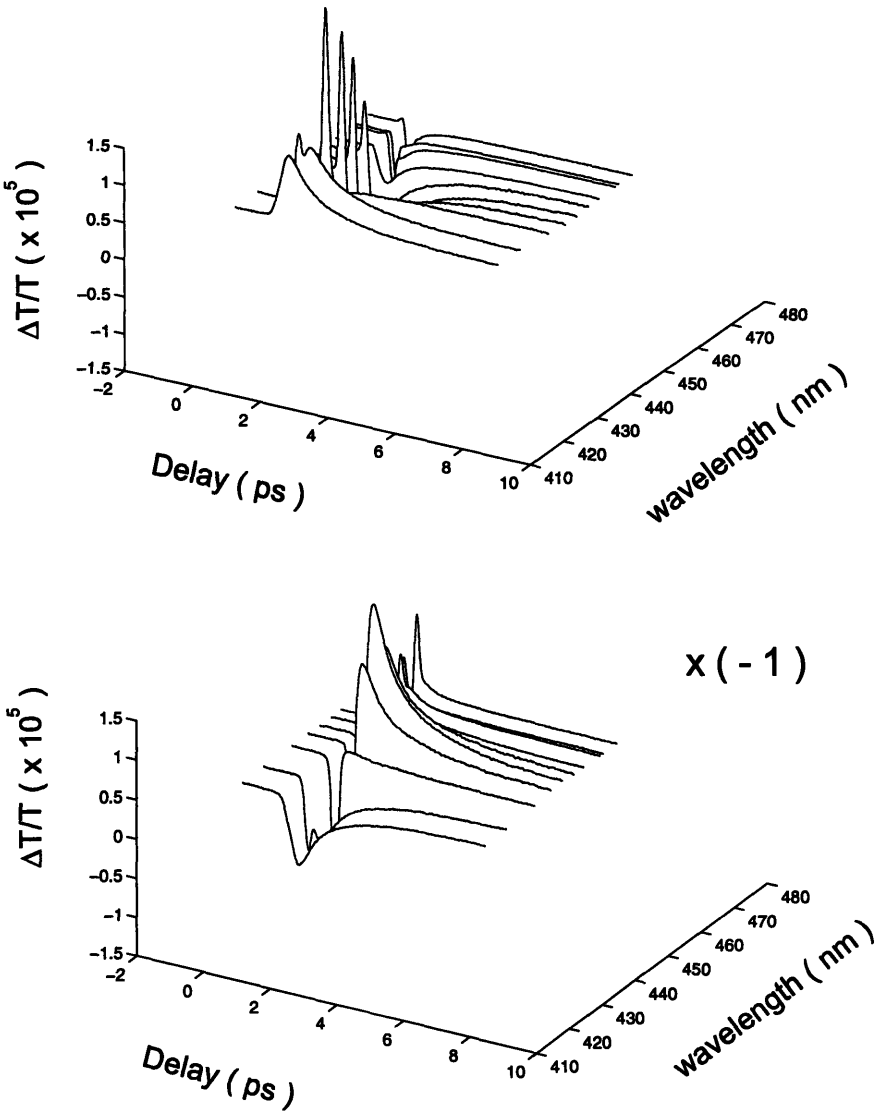

Figure 11-3: Pump-probe traces for a $1.7\times10^{18}\text{cm}^{-3}$ n-type ZnSe sample for probe wavelengths tuning across the absorption edge at 462 nm. The exponential electron cooling response is clearly evident along with instantaneous dynamics due to two-photon absorption and the optical Stark effect.

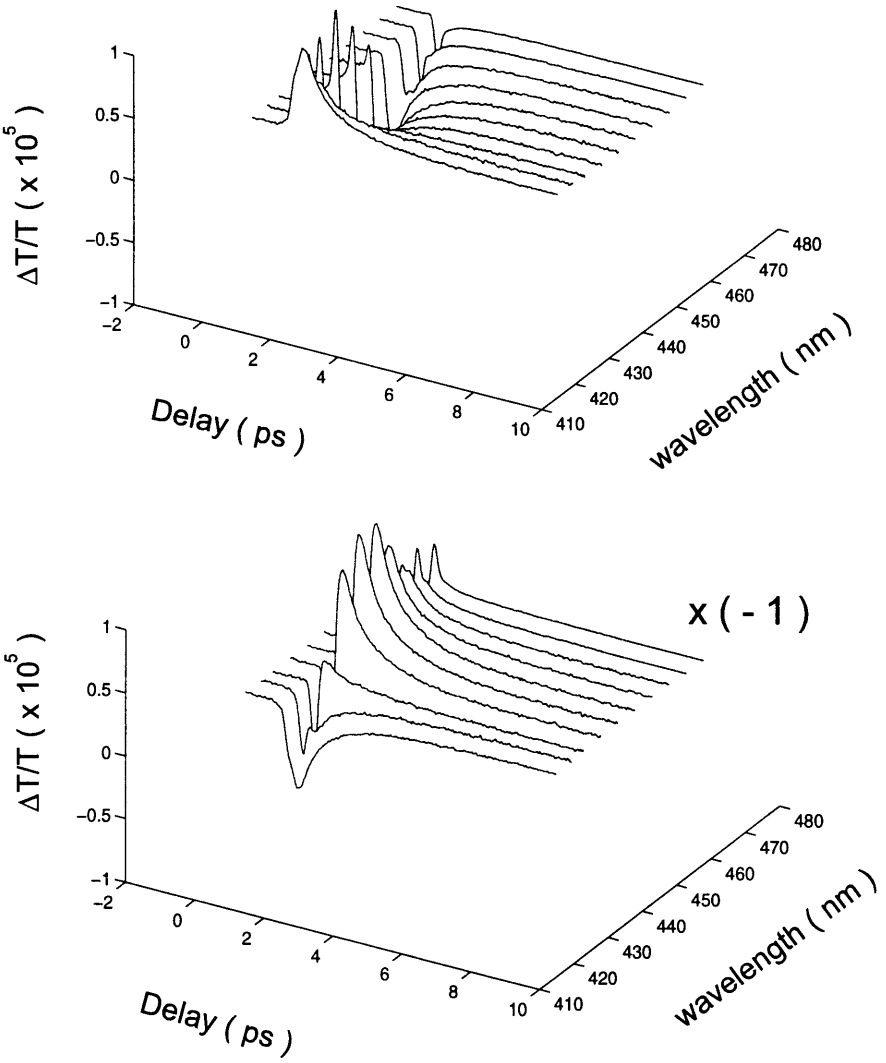

Figure 11-4: Below band pumping results for a $1.8\times10^{18}\text{cm}^{-3}$ n-type ZnSe sample.

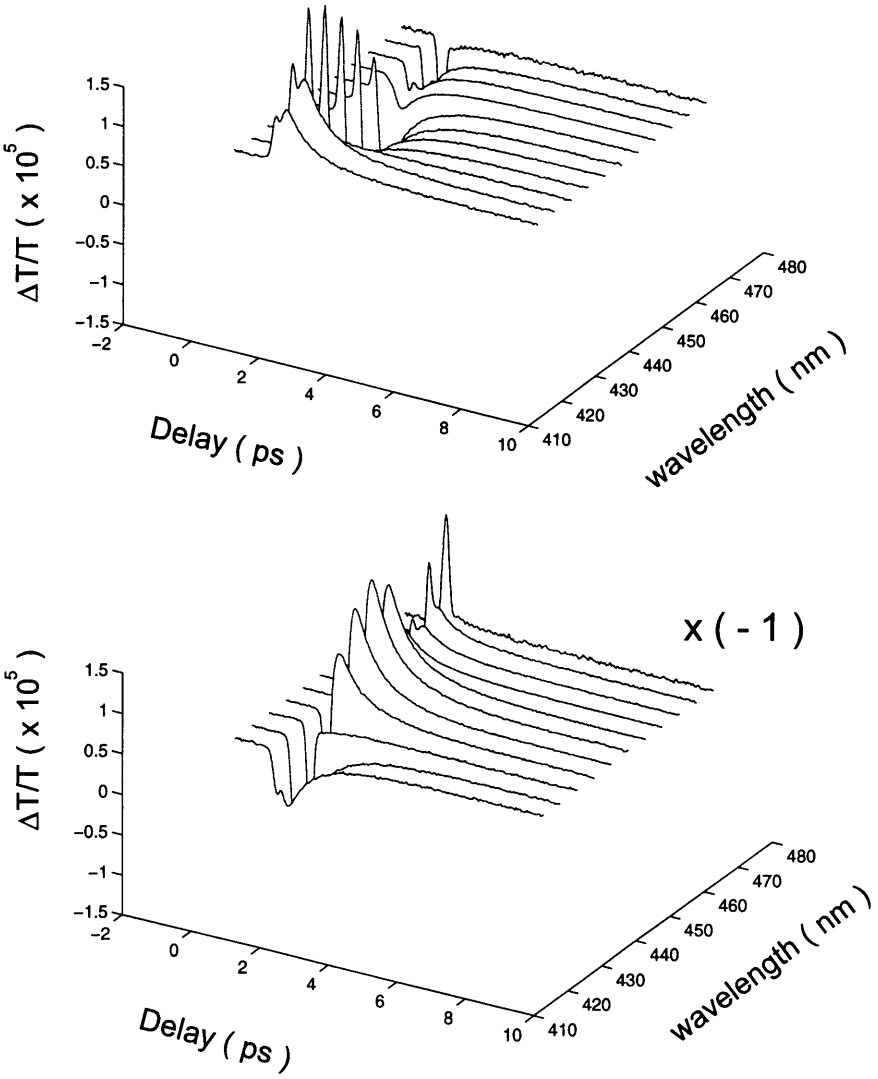

Figure 11-5: Below band pumping traces obtained for a 1×10^{20}cm^{-3}n-type ZnSe sample.

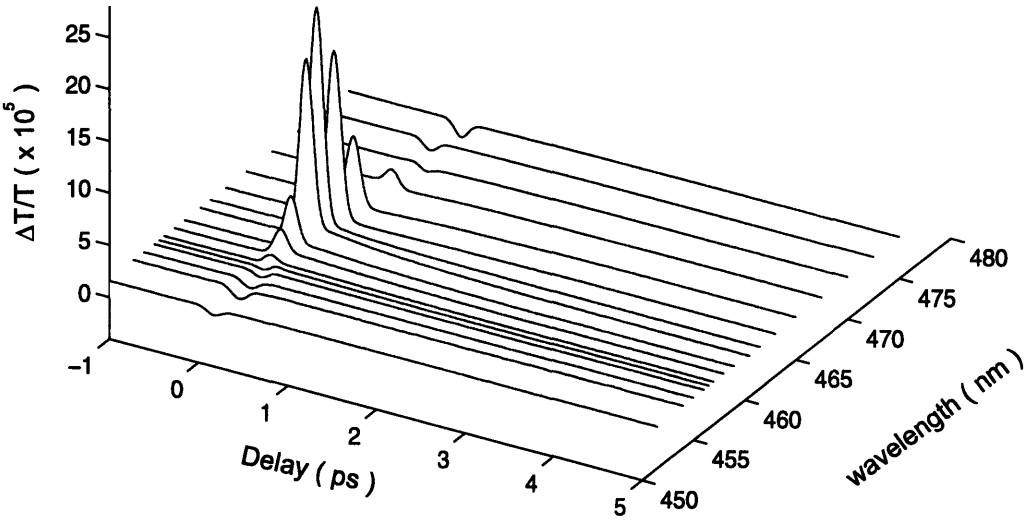

Figure 11-6: Below band pumping results for p-type ZnSe with a hole density of $2.6\times10^{17}\text{cm}^{-3}$. The response is dominated by the optical Stark effect, but a small carrier heating is still present despite the low doping.

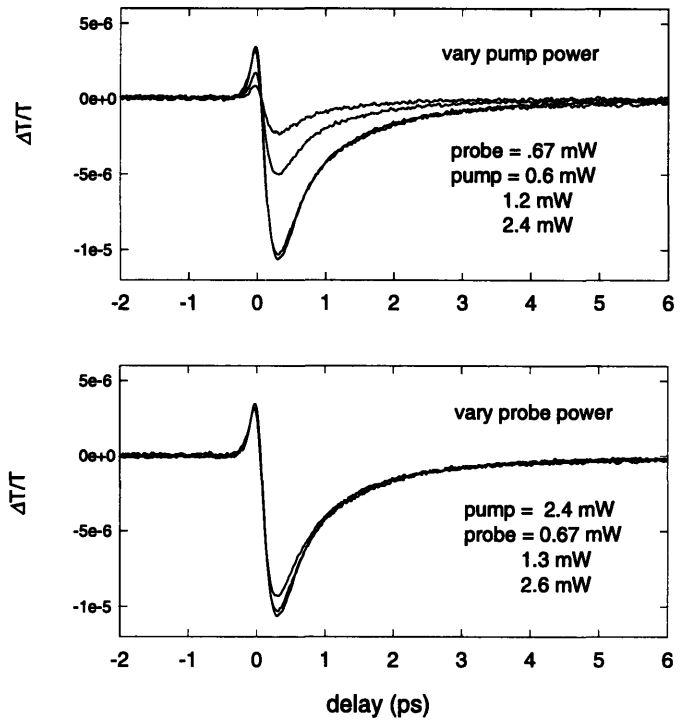

Figure 11-7: Intensity dependence of the carrier heating component of the response for the 1.7×10^{18} cm^{-3} n-type sample.

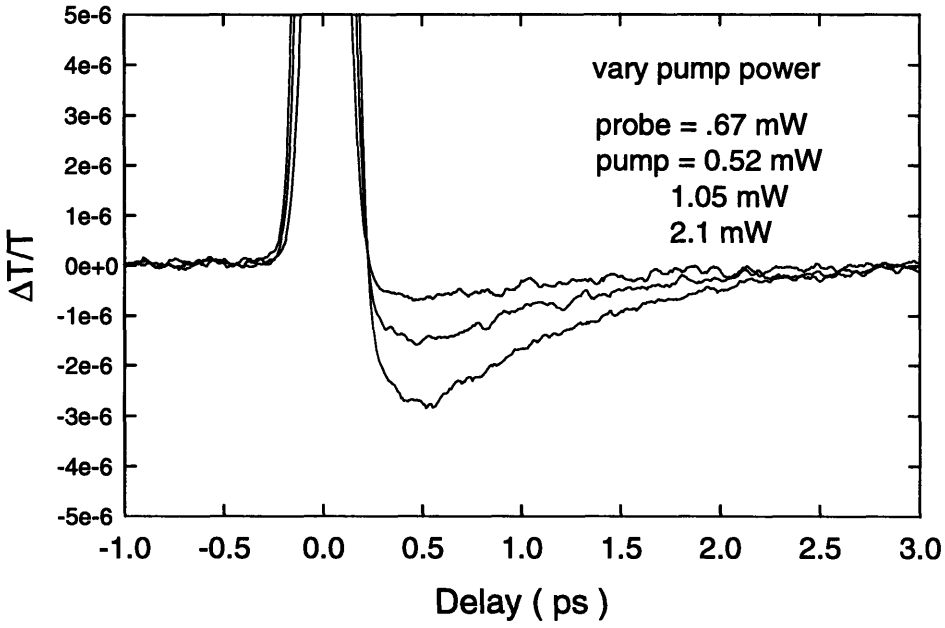

Figure 11-8: Intensity dependence of the carrier heating component of the response for the 2.6×10^{17} cm^{-3} p-type sample.

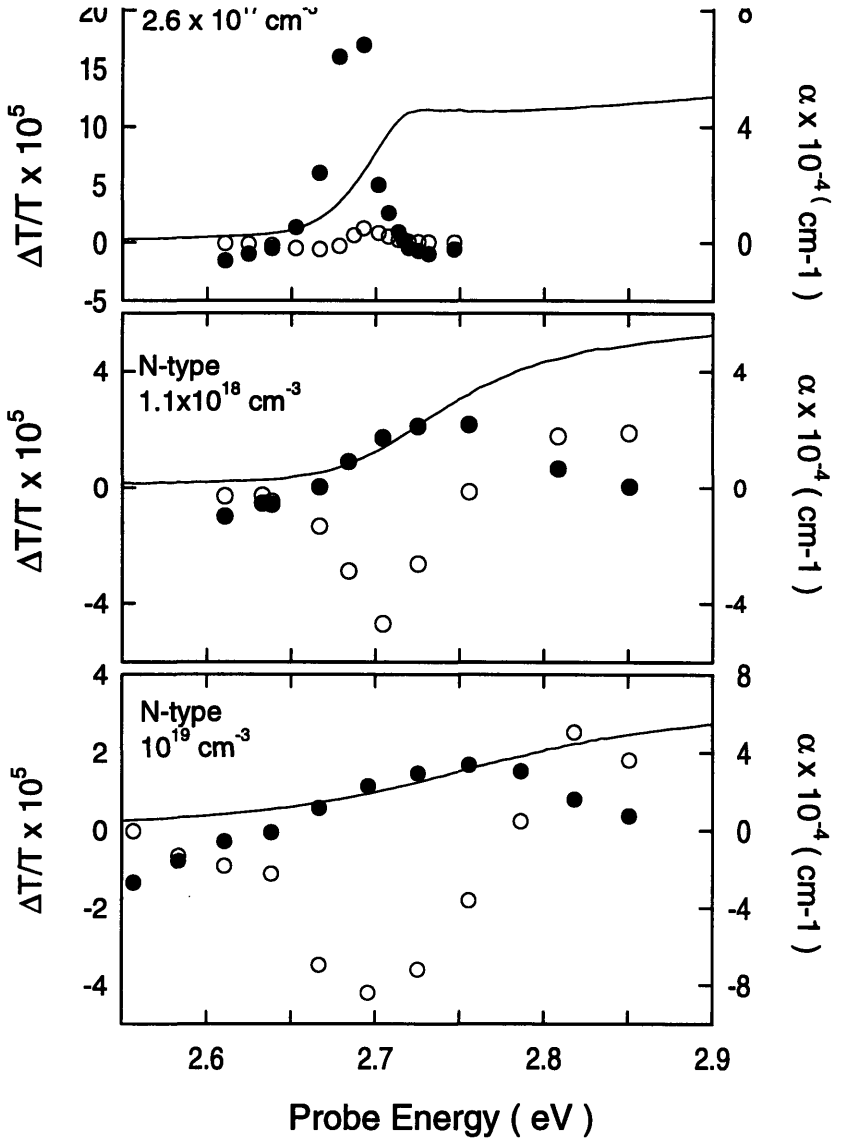

Figure 11-9: Magnitude of the instantaneous (filled circles)and carrier heating (open circles) reponse components plotted against probe energy with the measured linear absorption spectrum for ZnSe films with different doping densities. Top: p-type 2.6×10^{17} cm^{-3}. Middle: n-type 1.7×10^{18} cm^{-3}. Bottom: n-type 1.8×10^{19} cm^{-3}.

with the measured linear absorption spectra. The top plot is for the p-type sample. The absorption still maintains a step-like spectrum due to Coulomb enhancement because the hole density is below the Mott density. The sign flip in the heating signal is a measure of the average energy of the distribution. It lies close to the bandgap energy because the low carrier concentration results in the distribution being crowded toward low energies. The next plot down is for the 1.7×10^{18} cm^{-3} n-type sample. Here, the Fermi energy has moved up into the band and the sign change in the thermal component occurs at higher energies. The bottom plot for the 1.8×10^{19} sample agrees with this behavior. The spectral responses of both n-type samples seem to be weighted more towards induced absorption rather than being symmetric, with equal size positive and negative transmission changes at high and low energies as predicted in Fig. 7-3. As the photon energy is increased, the probe connects higher energy conduction band states with the heavy hole valence band. These transitions yield a postive contribution to the probe transmission change. At the same time, however, transitions from the light hole valence band to lower energy conduction band states become important. These transitions give a negative contribution to the transmission and cause the spectral response to go more negative than positive as the probe is tuned.

The instantaneous response for all three samples is negative, consistent with TPA, for energies away from the absorption edge [127, 128, 129]. Since TPA connects states high in the conduction and valence bands, it has nothing to do with the bandedge transitions and can be assumed to be constant over the narrow energy range of interest here. On top of the TPA signal, a bleaching component appears at wavelengths where the linear absorption in changing rapidly. This is the behavior predicted for the optical Stark effect and it will be discussed further in Chapter 12.

11.3 Temporal response

While the spectrum of the dynamics proves that the measurements are due to carrier heating, the time response of the traces gives information on the carrier-lattice coupling. The hole dynamics for the p-type sample are plotted in Fig. 11-11 for a probe energy of 2.70 eV. The data can be fit with a delta function and a single 900 fs exponential. The same time constant

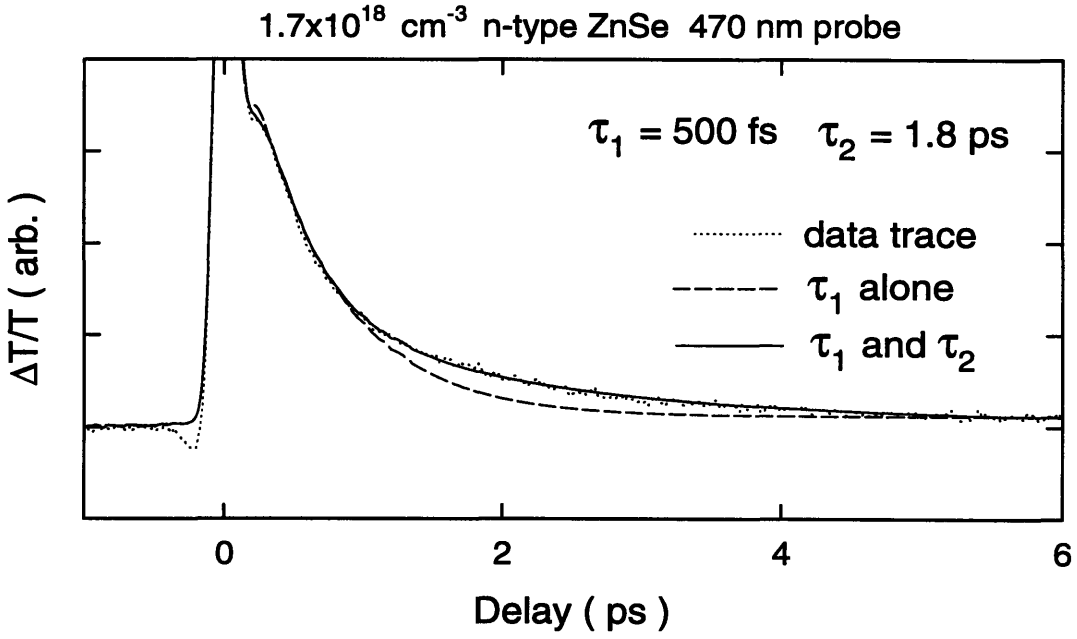

Figure 11-10: Electron dynamics measured at 2.63 eV for the low-doped n-type sample ($1.7\times10^{18}cm^{-3}$). The dotted trace is the experimental data. The dashed curve is a fit to a single 500 fs exponential to demonstrate the presence of a second 1.8 ps timeconstant. The solid curve is the two exponential fit using 500fs an 1.8ps.

can be used to fit the traces across the whole distribution.

The situation for the electron dynamics is more complicated. Figure 11-10 plots the trace for the 1.7 $\times10^{18}$ cm^{-3} sample (hereafter referred to as the low doped sample) at a probe energy of 2.63 eV. The trace is actually negative, but has had its sign flipped for plotting. The solid line is an attempted fit with a single 500 fs exponential. The fit is good for the initial relaxation, but fails to account for the long tail in the response. A better fit is obtained by adding a second exponential with a 1.8 ps timeconstant. A single exponential is unable to describe both the initial slope and the tail at several picoseconds delay. Thus use of a second time constant is warranted. The same 500fs and 1.8 ps time constants can be used to fit the data at all probe wavelengths across the electron distribution. However, the relative sizes of the two exponentials change. Figure 11-12 shows traces taken at probe energies of 2.63 eV (fastest inner trace),

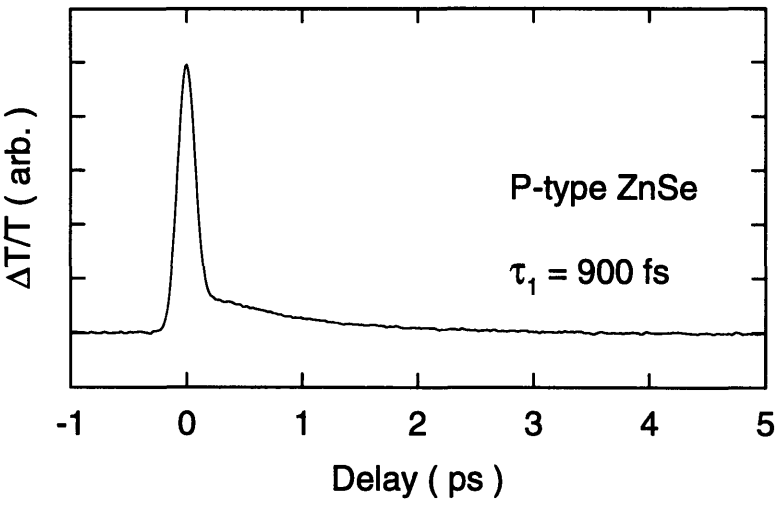

Figure 11-11: Hole cooling dynamics for the 2.6×10^{17} cm^{-3} p-type sample are well fit by a single 900fs time constant.

2.67 eV, 2.72 eV, and 2.75 eV (slowest outer trace). The traces have been normalized so that the sum of exponential components evaluated at zero delay are the same in order to compare the dynamics. The higher energy traces are still not well fit by a single exponential. They appear slower because the 1.8 ps component is larger. This energy dependent response is only seen for the low doped n-type sample. The two higher doped samples both require two time constants, but the relative magnitudes, and therefore the shapes of the traces, stay the same at all probe wavelengths.

The need for two time constants and the energy dependent time response are both inconsistent with the theory of Chapter 8. The induced temperature changes are probably the smallest that have ever been measured in a carrier dynamics experiment, and the linearized theory of Eqns. 8.32 and 8.41 certainly applies. In this case, however, only a single exponential is predicted. In addition, for a small temperature rise and fast thermalization times, the excited distribution must be at all times Fermi-Dirac. The time dependence enters only through the time dependent temperature. It is a simple matter to show that the occupations of all states in the distribution must, therefore, have the same time response.

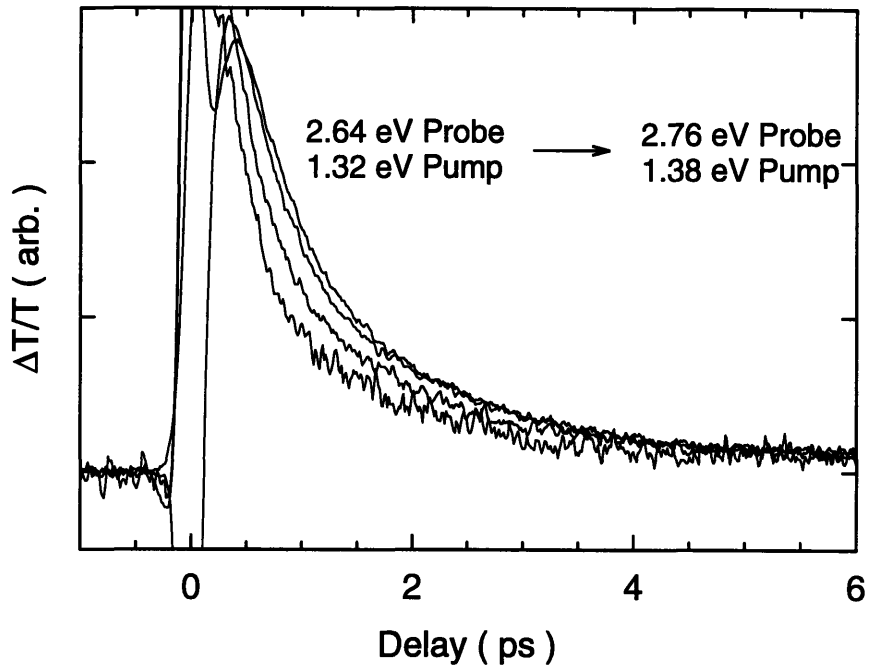

Figure 11-12: Normalized pump-pribe traces for the low doped n-type sample to compare the shape of the time response measured at different probe energies. From the inner, fat trace to the outer, slowest trace the probe energies are 2.63 eV, 2.67eV, 2.72eV, and 2.75 eV.

Pump probe experiments in GaAs have shown that the fundamental carrier-carrier scattering times in a degenerate electron gas are on the order of 10 fs [85, 93, 92]. The energy redistribution and electron thermalization times have also been shown to be at most 100 fs at these densities [86, 106, 130, 131]. The sub 100fs spectral hole burning time constant measured in CdSe [123]demonstrates that II-VI an III-V material can be expected to behave similarly for these processes. Attributing the observed dynamics to a non-thermalized electron distribution would thus be a major departure from established results.

11.4 Intervalley scattering

A simple explanation of this inconsistency is that intervalley scattering accounts for the 1.8 ps time constant [95, 131, 132, 133, 134, 135, ?]. As stated previously, free carrier absorption involves emission of an optical phonon in order to conserve energy and momentum. Figure 11-13 shows a schematic diagram of the ZnSe conduction band structure. The cold electron distribution due to the doping resides at the central Γ-valley minimum. Electrons from this distribution which are kicked up in energy by the pump photons can scatter either to high energy states within the Γ-valley or to states near the Brillouin zone boundary at the L symmetry point. The fifty percent branching ratio labelled in the figure will become clear shortly. Those electrons which scatter to the Γ-valley quickly thermalize and transfer their energy to the cold distribution which subsequently cools with the observed 500fs timeconstant. The electrons which scatter to the L-valley cannot interact with the Γ-valley distribution because no intermediate states are available to satisfy conservation of energy and momentum. Eventually, they emit optical phonons and return to the Γ-valley where they provide additional heating of the distribution.

Delayed cooling behavior due to intervalley scattering has been observed in time-resolved luminescence experiments of GaAs where a 3 ps timeconstant was measured [134, 135]. $L-\Gamma$ return times in the 0.7 to 2 ps range have also been measured in GaAs pump-probe studies [95, 131, 136]. A 1.8ps $L-\Gamma$ return time for ZnSe is reasonable despite its increased electron-LO phonon coupling since these long effective scattering times result mainly from the relative densities of states between the L and Γ-valleys. The large L-valley density of states make it less probable that an individual phonon scattering event takes the electron back to the Γ-valley

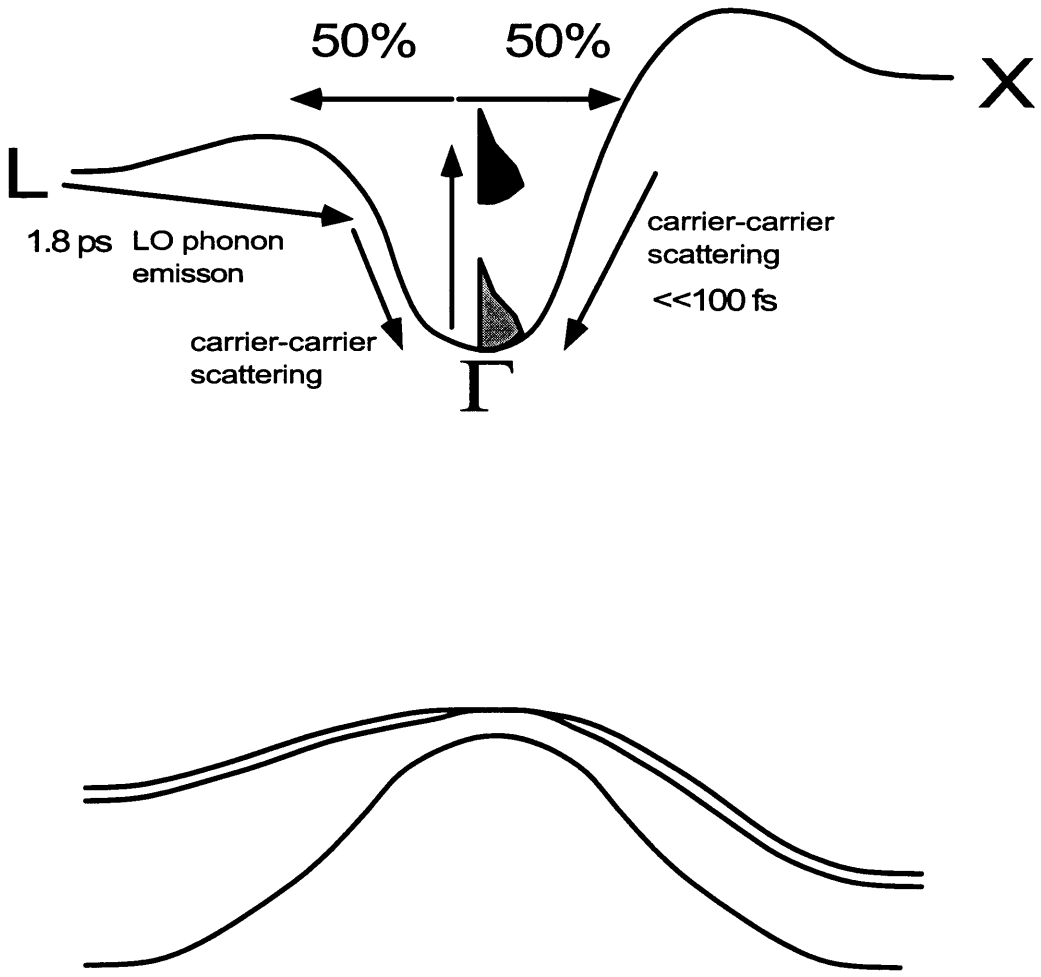

Figure 11-13: Schematic diagram of the FCA carrier heating processes. Electrons scattering within the Γ-valley quickly thermalize with and heat the cold distribution which cools in 500fs. Electrons scattered to the L-valley remain there for 1.8 ps before returning to the Γ-valley and causing additonal heating.

rather than to an equivalent L-valley pocket on another face of the Brillouin zone.

This model explains the bi-exponential electron response, but does not account for the energy dependence found in the low doped sample. An answer can be obtained by analyzing the data according to the following phenomenological fitting procedure. The action of the pump on the cold electron distribution with the inclusion of the delayed L-valley electrons can be described by a 'heating function', $Q(t)$, given by a delta function and an exponential term as

$$Q(t) = a_1\delta(t) + \frac{a_2}{\tau_2}\exp(-t/\tau_2)U(t) \tag{11.1}$$

where U is, as usual, a unit step function. The electron relaxation, $R(t)$, is described by a single 500 fs exponential as

$$R(t) = \frac{1}{\tau_1}\exp(-t/\tau_1)U(t). \tag{11.2}$$

The measured pump-probe trace, $h(t)$, is the convolution of the heating and response functions and is given by

$$h(t) = \frac{a_1}{\tau_1}\exp(-t/\tau_1)U(t) + \frac{a_2}{\tau_2-\tau_1}\exp(-t/\tau_2)\{1-\exp(-t[\tfrac{1}{\tau_1}-\tfrac{1}{\tau_2}])\}U(t). \tag{11.3}$$

The first term described the initial cooling response due to the Γ-valley electrons, and the second term is the delayed response. If the second term is multiplied out, it is apparent that the response can be written as the sum of two exponentials. The form in Eq. 11.3 is useful, however, because from Eq. 11.1 the fraction of the electrons scattered to the L-valley, L_f, is given by

$$L_f = \frac{a_2}{a_2+a_1}. \tag{11.4}$$

By fitting the observed response with Eq. 11.3 (and including a delta function due to TPA and optical Stark effect) , the coefficients a_1 and a_2 can be determined and used to find the L-valley fraction. Figure 11-14 gives a graphic picture of the heating and cooling responses.

The wavelength dependence of fraction of the electrons scattered to the L-valley holds the key to the energy dependence. The black circles in Fig. 11-15 plot L_f against the *pump* photon energy minus one LO phonon energy of 31 meV. Remember that the pump energy must tune with the probe since the probe is obtained by SHG. The lower plot is for the low doped sample.

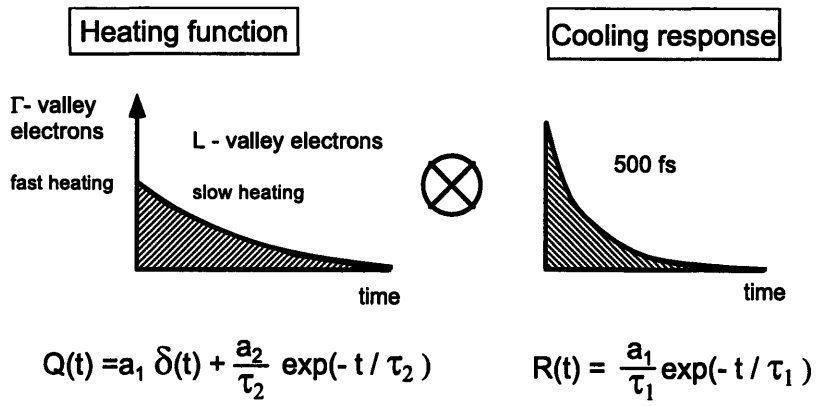

Figure 11-14: The fundamental electron cooling response shown on the right side is an exponential cooling response with a 500 fs timeconstant. Because of the delayed heating effects of intervalley scattering, the electron response is driven by the heating function shown on the left. The observed pump probe response is the convolution of these functions.

The decrease of L_f at low pump energies accounts for the faster response seen for the low energy states. This decrease can be explained by the pump being tuned across the threshold energy for scattering to the L-valley, $E_L - \hbar\omega_{LO}$, where E_L is the energy of the L-valley minimum above the bottom of the Γ-valley. The dotted curves in Fig. 11-15 represent the distribution of electrons excited by FCA which is simply the Γ-valley distribution raised by the pump photon energy. As the pump is tuned, this distribution slides across the L-valley density of states (LDOS) which is shown by the dashed line. The number of electrons scattering to the L-valley is proportional to the overlap of the excited distribution and the LDOS as is plotted with the solid line. This assumes that the matrix element for scattering is independent of final energy in the L-valley, which should be a good approximation for energies near the minimum, E_L.

To fit the observed L_f from the pump-probe responses, the L-valley is determined to lie 1.30 eV above the Γ-valley. The exact energy of the L-valley is not known with precision. Chelikowski and Cohen [137] place it at 1.2 eV above the Γ minimum while a more recent publication by Markowski et. al. [138] reports a theoretical value of 1.25 eV and an experimental value of

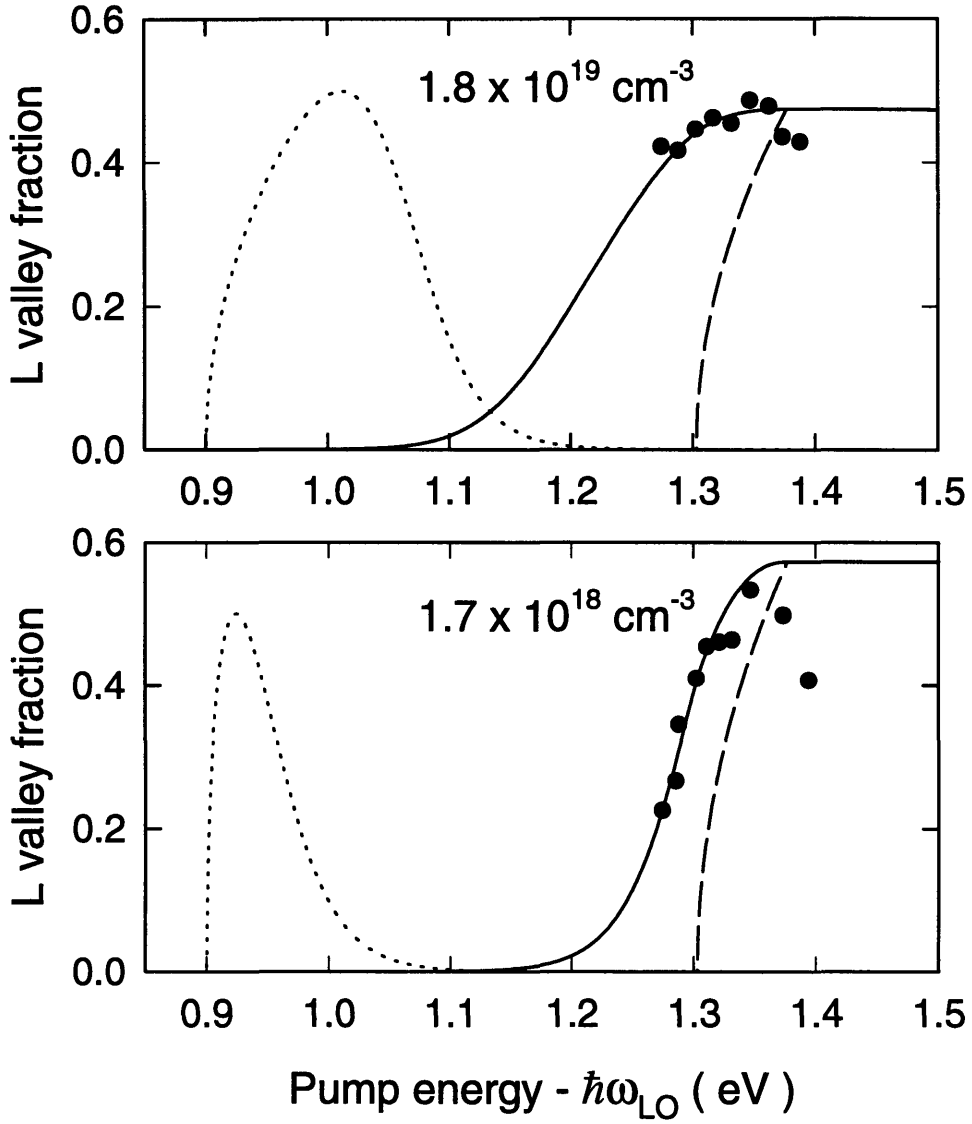

Figure 11-15: Black circles: The measured fraction of excited electrons scattered to the L-valley by FCA as extracted from the pump-probe dynamics. Dotted curves: The electron distribution raised by a pump photon energy. Dashed curve: The L-valley density of states. As the pump is tuned the excited distribution slides across the L-valley DOS. Solid line: The fraction L-valley electrons created for a given pump photon energy, determined by the overlap of the excited distribution and the LDOS.

1.4 eV. Both of these calculations and the experimental result determine the L-valley energy by subtracting the measured bandgap and valence band width from the ZnSe E_1 transition. The bandgap is, of course, well known, and the E_1 energy is accurately found from modulation spectroscopy methods. The valence band width, however, must be determined by photoemission measurements [139, 140] which have an uncertainty of about 600 meV.

The dashed curves in Fig. 11-15 are an estimation of the shape of the LDOS based on published bandstructures [137, 138]. Initially, the density of states rises as $(E - E_L)^{1/2}$ due to the ellipsoidal energy surfaces centered on the L-point [100, 132]. Moving from L to Γ, an inflection point in $E(\vec{k})$ is found which indicates a transition from closed ellipsoids to open energy surfaces. This results in a slope change in the LDOS. Assuming the L-valley mass is the same as the valence band mass at the L-point (i. e. the conduction and valence bands track each other near the L-point), and using values between 0.7 and 1.3 eV [139, 140] results in a value of 40 to 90 meV above E_L for the position of the slope change. A value of 75 meV was used for the fit in Fig. 11-15.

The threshold energy is well supported by the data for the low-doped sample; however, the larger width of the electron distribution in the 1.8×10^{19} cm^{-3} sample lowers the resolution for probing the LDOS in this manner, and the energy dependence is flattened out as shown in the top plot of Fig. 11-15. This explains why only the low doped sample showed change in the shape of the time response. Electrons scattered to the L-valley with sufficient excess energy can rapidly scatter via phonon emission or impurity scattering to regions of the Brillouin zone (such as near the Λ-point) which still have a large density of states, but are close enough to $\vec{k} = 0$ for electron-electron scattering to take place. This accounts for the decrease in the $L-$valley scattering ratio at high pump energies for the low doped sample, and for the smaller fraction observed for the high doped sample where the large width of the distribution results in more electrons arriving in the L-valley with large excess energies. Since the exact energy dependence of this process is not known, the slope of the effective LDOS is set equal to zero above the inflection point in order to obtain a reasonable fit to the data on the low energy side. This uncertainty does not affect the placement of the L-valley threshold which is the primary goal. It is very interesting that similar decreases in observed L-valley scattering at high energies have been reported very recently in experiments on InAlGaP/InGaP quantum wells [141].

11.5 Conclusions

This interpretation for the apparent energy dependent electron relaxation is the most plausible explanation consistent with the requirement that the electrons establish a quasi-equilibrium Fermi distribution on a time scale of < 100 fs. The value of E_L is in reasonable agreement with previous experimental and theoretical investigations. Electron dynamics have been used before to determine the value x_c of the direct/indirect cross-over point versus Al concentration in $Al_xGa_{1-x}As$ [142]. these results show that intraband processes can be a valuable tool for measuring bandstructure parameters not accessible by direct optical transitions.

The temporal dynamics yielded several interesting timeconstants for electron-lattice scattering. The $L-\Gamma$ return time by optical phonon emission and absorption was found to be 1.8 ps which is similar to GaAs. The electron distribution cooling time constant was measured to be 500fs, while the holes were found to cool more slowly with a 900 fs time constant. These results are surprising in comparison to the theoretical values of around 120 fs for electrons and 40 fs for holes (see Figs. 8-8 and 8-9). The unprecedentedly low temperature changes used in these carrier dynamics studies eliminated many complicated effects such as hot phonon bottle-necks and dynamical screening which are present in above band pumping experiments. Coupling of the LO-phonons to the plasma mode results in a renormalization of the phonon frequencies, and, from the literature [72, 107, 74], this effect seems to be the only physics not included in the calculations in Chapter 8. This effect was left out because the energy shifts at the carrier densities used in these experiments are small and have been shown to be unimportant by Das Sarma [107] in GaAs calculations. It is not believed that this effect could account for a factor of five slowing of the cooling rate. The large disagreement between experiment and theory must be traced to the Frölich coupling matrix element (Eq. 8.1) since the small temperatures result in such a clean experimental situation. In studies of metals and superconductors, the electron-phonon coupling is treated as a parameter to be experimentally determined [143, 144]. No previous semiconductor pump-probe experiments have had the potential to accurately determine the electron-phonon coupling strength. This below band pumping technique, and the ability to measure very small transmission, and therefore temperature changes, may lead to

improved understanding of carrier-lattice interactions in semiconductors.

Chapter 12

Optical Stark effect

The large bleaching signals observed at zero delay in the last section are due to the optical Stark effect. The optical, or AC Stark effect, is a light induced level shift which follows the intensity of a non-resonant pump essentially instantaneously. The idea is borrowed from atomic physics where it has been known for a long time and is tied to such phenomena as Mollow triplets in luminescence spectra. At large pump detunings, semiconductor interband transitions can be modelled as a collection of simple quantum mechanical two-level systems [145] and treated exactly like discrete atomic energy levels. When the pump laser is tuned close to resonance with the exciton and bandedge continuum, the situation is more complicated, requiring treatment of many-body interactions in the virtual electron-hole pair plasma [146, 147]. Many investigations have been performed in this regime on III-V semiconductor such as GaAs [148, 149, 150], as well as wider bandgap materials such as CdS [151]. The instantaneous index changes associated with the optical Stark effect have been the subject of intense interest for applications in ultrafast optical switching [152, 153, 114]. In the IR pump-blue probe experiments in this work, the pump is at much larger detuning than is normally used. This results in a particularly clean observation of the shift in the bandedge and allows a comparison of doped and undoped samples; a test which has not been performed before.

Figure 12-1 shows the shift induced in a two-level system due to an off-resonant pump. The reason for the shift can be explained using the fundamental concepts of the uncertainty

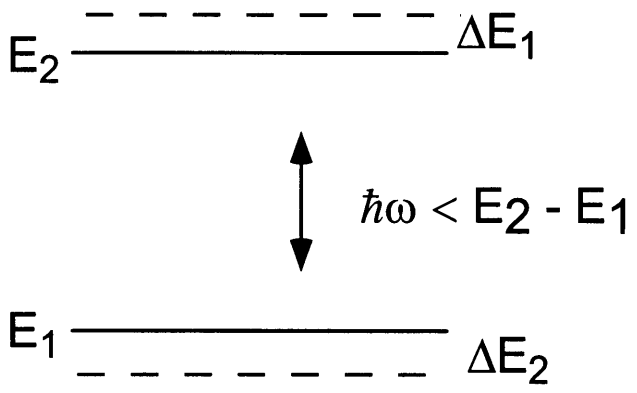

Figure 12-1: Schematic of the level repulsion induced by an intense optical field detuned below resonance.

principle and energy conservation. The time-energy uncertainty relation,

$$\Delta E \Delta t_{obs} \geq \hbar, \tag{12.1}$$

states that the uncertainty in a measurement of the energy of a system is related to the amount of time in which the observation occurs. For an observation time, $\Delta t \tilde{} 1/\Delta\omega_p$, the uncertainty in the energy is on the order of that necessary to excite an electron to the upper state. This excited electron is called a 'virtual' electron because it exists only for a time less than $1/\Delta\omega_p$.The small amount of time the electron spends in the upper state is not observed directly, but it has consequences for the light-atom system as a whole since energy must be conserved on long timescales. The expectation values for the energies of the atom and radiation field, with the atom initially in the ground state (E=0), are

$$\begin{aligned} < \ E >_{atom} &= (0 - \Delta\epsilon)(1-p) + (E + \Delta\epsilon)p \\ < \ E >_{light} &= N\hbar\omega_p(1-p) + (N-1)\hbar\omega_p p \end{aligned} \tag{12.2}$$

where a shift, $\Delta\epsilon$, has been postulated in the upper and lower state energies, and $p << 1$ is the

probability of finding the atom in the upper state. The total energy is constant and is given by

$$< E >_{Total} = N\hbar\omega_p = < E >_{atom} + < E >_{light} . \tag{12.3}$$

Plugging in Eq.12.2, the result is

$$0 = (E - \hbar\omega_p)p - \Delta\epsilon + 2\Delta\epsilon p. \tag{12.4}$$

Since the last term is of second order in p, it follows that is indeed a shift of the levels given by

$$\Delta\epsilon = (E - \hbar\omega_p)p. \tag{12.5}$$

Because p>0, this result states that for $E > \hbar\omega_p$ the transition is red-shifted, and for $E < \hbar\omega_p$ it is blueshifted. The atom is always pushed out of resonance by the light. This conclusion remains if the atom is initially considered to be in the upper state. Thus an inverted (gain) medium exhibits the Stark shifts of the same magnitude and sign. This simple reasoning can be pushed a little further by estimating the probability, p, as the rate of excitation, W, times the lifetime, τ, and using Fermi's golden rule,

$$\begin{aligned} p &= W \times \tau \\ &= \frac{2\pi}{\hbar} |ed \cdot \mathcal{E}|^2 \frac{1}{\hbar\Delta\omega_p} \times \frac{1}{\Delta\omega_p}. \end{aligned} \tag{12.6}$$

Here, because of the short lifetime of the electron, the density of final states appears smeared out to $1/\hbar\Delta\omega_p$. The total shift in the transition energy is

$$\hbar\Delta\Omega = 2\Delta\epsilon = \frac{4\pi}{\hbar} \frac{|ed \cdot \mathcal{E}|^2}{\hbar\Delta\omega_p}. \tag{12.7}$$

This simple calculation actually overestimates the shift, but it does correctly predict that the shift is proportional to square of the dipole moment (i.e. proportional to the absorption), is linear in the pump intensity, and falls off as the inverse of the pump detuning.

This problem may be solved exactly, of course. A neat solution presented by Joffre will be

briefly discussed here. The Hamiltonian of the atom in the presence of the pump field is

$$\begin{aligned} \mathbb{H} &= \mathbb{H}_0 - \boldsymbol{\mu} \cdot \mathcal{E}_p(t) \qquad (12.8) \\ &= \begin{bmatrix} 0 & 0 \\ 0 & E \end{bmatrix} - \begin{bmatrix} 0 & \mu \\ \mu^* & 0 \end{bmatrix} \mathcal{E}_p \exp(-i\omega_p t). \end{aligned}$$

By making a unitary transformation with the matrix

$$\mathbb{U} = \exp(-i\mathbb{W}_p t) \text{ , where} \qquad (12.9)$$

$$\mathbb{W}_p = \begin{bmatrix} 0 & 0 \\ 0 & \omega_p \end{bmatrix},$$

an equivalent Hamiltonian, H', is formed

$$\mathbb{H}' = \mathbb{U}\mathbb{H}\mathbb{U}^\dagger + i\hbar \frac{d\mathbb{U}}{dt}\mathbb{U}^\dagger. \qquad (12.10)$$

$\mathbb{H}'$ is then independent of time and is given by

$$\mathbb{H}' = \begin{bmatrix} 0 & -\mu\mathcal{E}_p \\ -\mu^*\mathcal{E}_p & E - \hbar\omega_p \end{bmatrix}. \qquad (12.11)$$

The new eigenvalues of the two-level system in the presence of the pump are then

$$E' = \frac{\hbar\omega_p}{2} \pm \frac{\hbar\omega_p}{2}\left(1 + \frac{2|\mu|^2 \mathcal{E}_p^2}{\hbar^2 \Delta\omega_p^2}\right)^{\frac{1}{2}}. \qquad (12.12)$$

For low enough pump intensity, the total shift in the transition energy is therefore

$$\hbar\Delta\Omega = \frac{2|\mu|^2 \mathcal{E}_p^2}{\hbar^2 \Delta\omega_p^2} \qquad (12.13)$$

which agrees with the previous estimation in Eq.12.7 within a factor of 2π.

At large detunings, the interband absorption spectrum of a semiconductor can be modelled

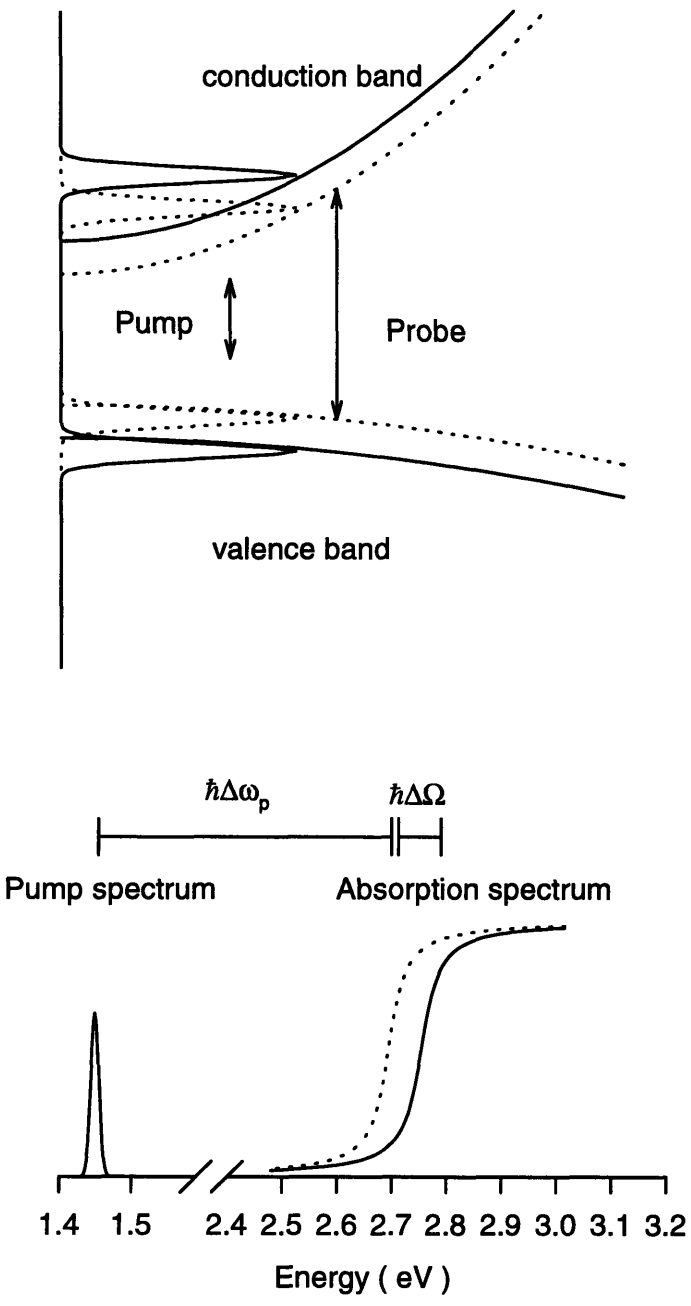

Figure 12-2: Top: The conduction and valence bands can be viewed as an array of two-level systems, one for each $\vec{k}$. Bottom: A below band pump beam shifts the transition energies of all of the two-level systems and causes the absorption edge to undergo a rigid blueshift.

as an array of two-level systems as shown schematically in Fig. 12-2. Optical transitions between valence and conduction band free carrier Bloch states are usually expressed in terms of the interband momentum matrix element p_{cv}. An equivalent dipole length can be defined using the results of the Thomas-Reiche-Kuhn sum rule

$$p_{cv} = m_0 \omega_{cv} x_{cv}, \tag{12.14}$$

and the Kane expression for evaluating the momentum matrix element

$$\frac{p_{cv}^2}{m_0} = \frac{E_g m_0}{2m_c^*}. \tag{12.15}$$

For GaAs and ZnSe, x_{cv} is 6.3Å and 3.0Å, respectively. In any event, Eq. 12.13 states that the Stark shift is proportional to the same material-light coupling that gives rise to linear absorption. This coupling, $\mu, x_{cv},$or p_{cv}, will be referred to as the optical matrix element from here on.

In fact, for a semiconductor the change in absorption seen by a resonant test beam due to the strong, detuned pump is just

$$\Delta\alpha(\omega, I_p) = \alpha_0(\omega - \Delta\Omega) - \alpha_0(\omega). \tag{12.16}$$

This is shown in the bottom drawing in Fig. 12-2. The relative change in transmission is simply

$$\frac{\Delta T}{T} = \Delta\Omega \times \frac{\partial \alpha}{\partial \omega} L. \tag{12.17}$$

Figure 12-3, shows the magnitude of the instantaneous bleaching component of the response for three of the samples discussed in the last Chapter. The solid lines represent the measured linear absorption spectra. The peak of the bleaching response occurs near the photon energy where the absorption has the largest slope, just as Eq. 12.17 suggests. In addition, the size of the signal seems to follow the sharpness of the absorption edge for all of the sample studied.

Before these dynamics can be associated with the Stark effect, other possible mechanisms such as a 'two-photon' Stark effect or other two-photon resonant effects [154, 155]. These mechanisms must be explored since the pump is at exactly half the bandgap when the probe

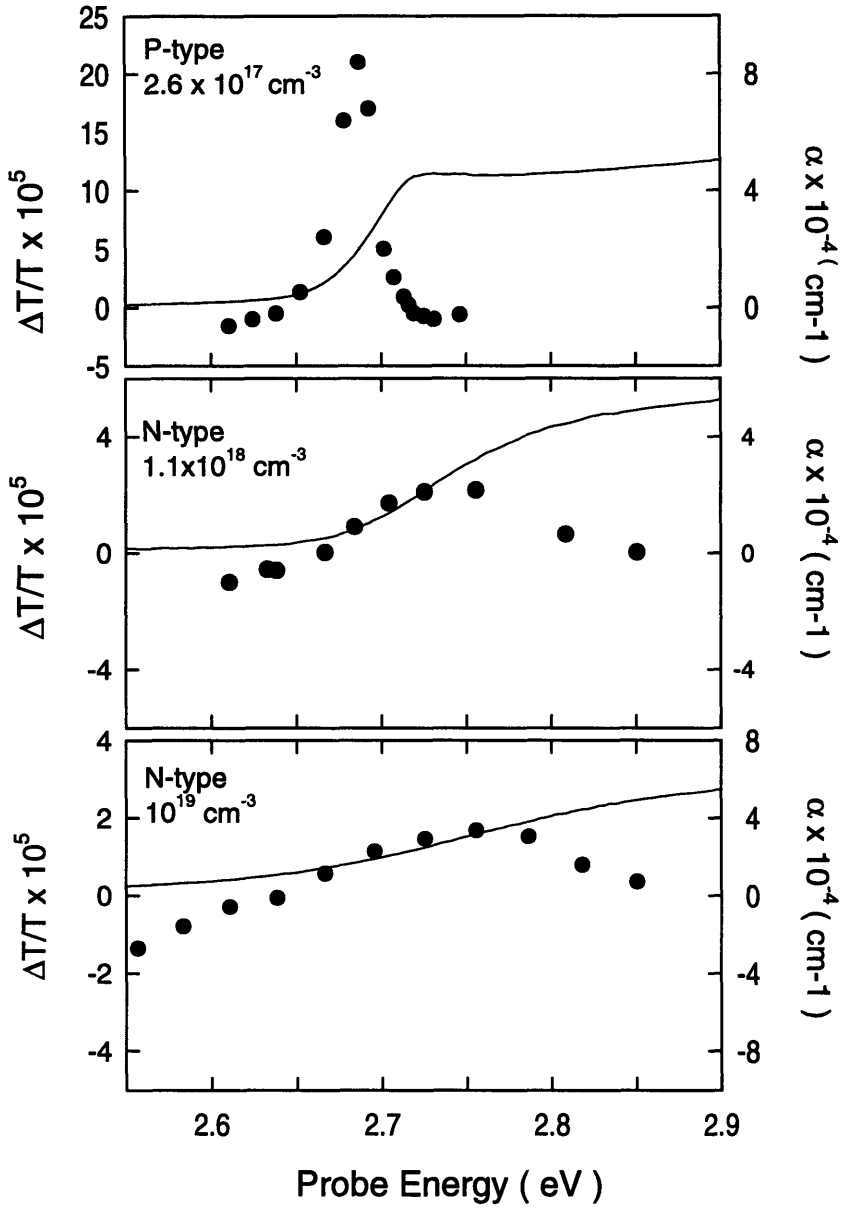

Figure 12-3: Magnitude of the instantaneous bleaching component as a function of the probe energy. Spectrum follows the derivative of the linear absorption (solid line) indicative of a shift of the bandedge.

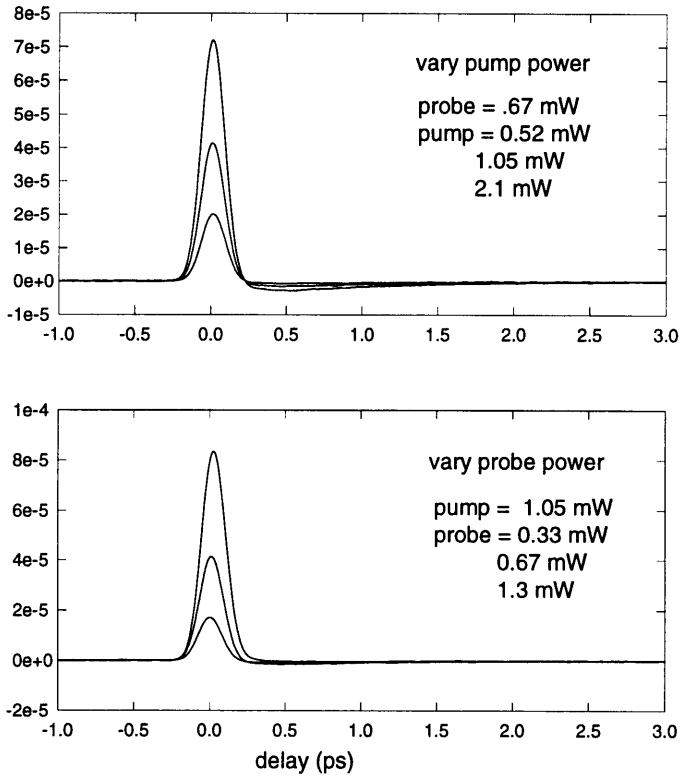

Figure 12-4: Pump and probe power dependence of the Stark signal for the P-type (2.6×10^{17} cm^{-3}) sample.

tunes across the bandedge. Thus, although they would be of higher order in the pump intensity ($\tilde{}I_p^2$), resonance enhancement may make up for the difference. Figure 12-4 shows pump probe traces on the P-type sample (corresponding to the top plot in Fig. 12-3) as a function of pump and probe power. The observed linear dependence on pump and probe intensity agrees with the simple, one-photon, Stark effect described above. Two-photon effects due to the pump would also be expected to create some real electron-hole pairs and give rise to a long lived response which is not observed. A final check performed was to vary the pump polarization. No change in the signal size was observed in accord with the isotropic symmetry of the optical Stark effect [156].

With the Stark effect established as the mechanism of the bleaching dynamics, an interesting test of the light-matter coupling in these ZnSe samples was performed. The ability to observe the Stark shift at such large pump detunings (1.33 eV = $60 \times E_{ex}$) is a nice feature of this

experiment. At smaller detunings, part of the pump spectrum usually overlaps the absorption spectrum resulting in saturation of the absorption due to the generation of real carriers. In addition, coherent polarization effects are often observed in experiments using a white-light continuum probe pulse. These features distort the absorption spectra from a pure, rigid shift of the bandedge. Extracting the energy shift is interesting because it contains the material dipole moment which it turn holds information on the nature of the electron-hole pair states. In Chapter 10, Coulomb attraction between the excited electron and hole was seen to cause an increase in the absorption near the bandedge. This increased coupling can be screened out by a background plasma. Thus, one might expect to see the effects of Coulomb enhancement in the Stark effect by comparing samples doped above and below the Mott density.

The magnitude of the transmission change due to the Stark shift is obtained from the plots in Fig. 12-3 by taking the peak value and subtracting off the two-photon absorption contribution observed at the high and low ends of the spectrum away from the absorption edge. This value is then divided by the measured slope in the linear optical density (αL) and normalized to the pump power used. The pump power was corrected by the measured surface reflectivity at the pump wavelength. Using the sample thicknesses as determined from the Fabry-Perot fringes, the average intensity inside the film was also calculated, but this led to only a very small correction. Note that the sample thickness and absorption are not needed independently for the slope in the optical density.

The results of these calculations are relative measures of the magnitude squared of the material optical matrix elements. Determination of the absolute value of the matrix elements or dipole moments requires detailed knowledge of the spots sizes of the pump and probe on the sample. As discussed previously, due to the dispersion of the fused silica lens used, the pump and probe waist sizes are not the same. This uncertainty is not relevant for the relative comparisons of interest here. These normalized matrix elements are plotted in Fig. 12-5 for five samples with different doping levels. For samples doped above the Mott density, a factor of 2 decrease is seen, corresponding to a $\sqrt{2}$ decrease in the optical matrix element. The error bars on the data points refer to the maximum and minimum values obtained using several measurements of the various parameters. The absorption (optical density actually) spectra were measured twice for each sample and both values were used in the calculation. Likewise,

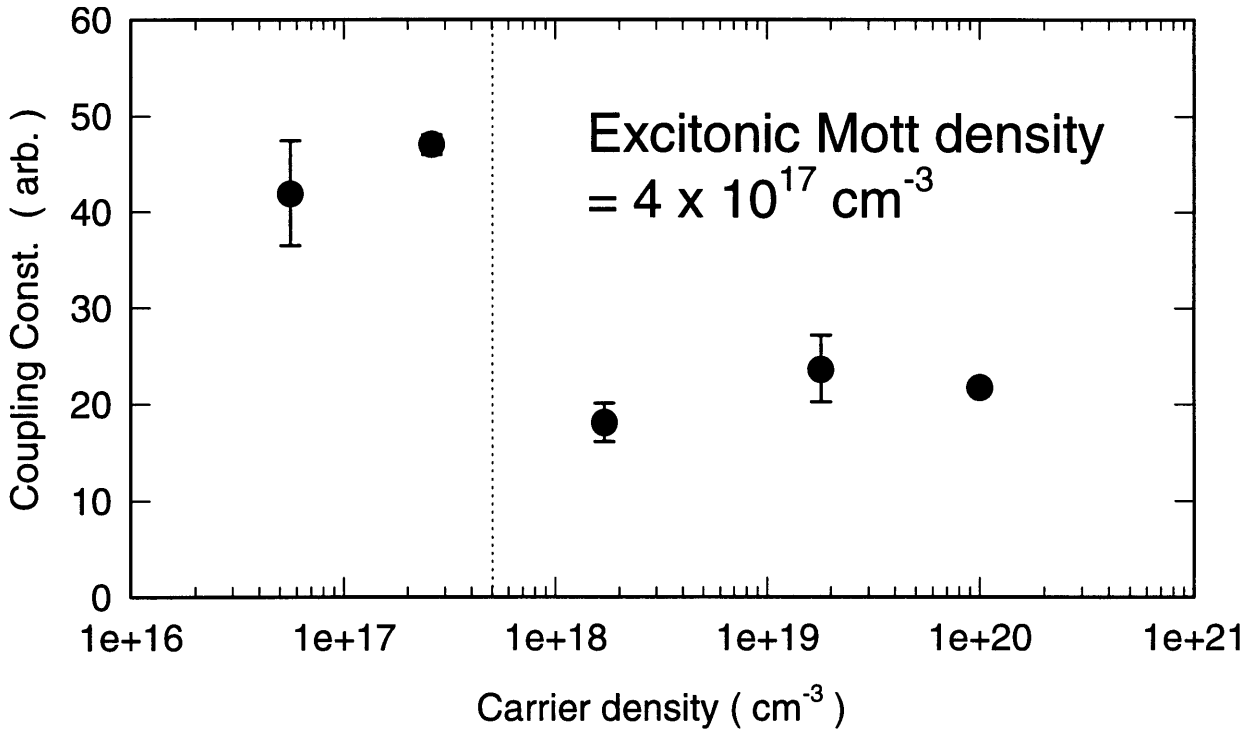

Figure 12-5: Measure of the interband optical matrix element deduced from the Stark shifts for five samples at different doping densities.

upper and lower bounds on the size of the two-photon absorption (as seen in Fig. 12-3) were taken into account for the high doped samples.

The data seem to agree with the idea of screening of the Coulomb enhancement of the matrix elements when the carrier density is large. Above the Mott density, the coupling has essentially the same value as would be the case for the bare interband momentum matrix element. When excitonic effects are present, the coupling to the pump, and therefore the Stark shift, is increased. However, the many-body theory of the optical Stark effect due to M. Combescot [157] actually does not predict such behavior. At large detunings, this theory states that the Stark shift is independent of the Coulomb attraction between electron-hole pairs and is given by the bare free-carrier Kane momentum matrix element, p_{cv}. Arguments can be made however, that the proof used to deduce this dependence rely on evaluating sums whose rates of convergence may be very slow. Thus, even 60 exciton binding energies detuning may not be in the large detuning limit of the theory.

Doping the semiconductor with a large carrier density does effectively turn off the electron hole Coulomb attraction. It may, however introduce other effects as well. Theories of the Stark effect treat each of the pairs of conduction and valence band states as independent two-level systems. This follows from the assumption of momentum conservation in photon absorption. The perturbation Hamiltonian introduced by the pump does not connect states from different pairs together and their shifts can be calculated independently. Fast intraband scattering processes, such as carrier-carrier scattering of impurity scattering at high doping levels, may change this picture, however. Four-wave mixing experiments with the shortest pulses available [85] indicate that dephasing times can be well under 10fs in highly excited bulk GaAs. This is not far off from the 3.2fs lifetime of the virtual carriers created by the half-bandgap pump in these experiments. Other effects such as bandgap renormalization due to the virtual carrier population could cause a competing red-shift that would be larger for the high doped samples, using the phenomenological bandgap renormalization expression in Ref. [73]. One last idea to consider is that Stark shifts between the conduction band and the next higher band at $k = 0$ are not negligible. The transition energy is 7.33eV-2.67eV=4.66eV. Thus, the 1.35 eV pump would only be 3.31 eV off resonance and would make a contribution of about 40% of the size of the valence-conduction transition (assuming the matrix elements are the same).

Chapter 13

Conclusions and Future Work

The time resolved measurements performed in this work have pointed to both differences and similarities between ZnSe and III-V semiconductors such as GaAs. The larger excitonic binding energy in ZnSe leads to pronounced enhancement of the above-band continuum absorption. For above-band pumping experiments with large photo-injected carrier densities, screening of this enhancement was found to be the dominant optical nonlinearity even at densities up to 2×10^{18} cm^{-3}. Although this effect was shown in CW saturation experiments [158], the complete lack of any fast dynamics in the pump-probe traces of Chapter 10 does yield further insights. First, no sign of spectral hole burning was evident in spite of the reasonably short, 50 fs, pulses used. A spectral hole is the localized absorption saturation which would occur through bandfilling if the injected carrier distribution initially resembled the laser pulse spectrum. A single wavelength experiment does not monitor the spectrum of the absorption changes induced by the pump, but dynamics associated with the redistribution of the carriers in energy should be observed in the time domain. Even if screening, rather than bandfilling, dominates the absorption changes, changes in the Coulomb screening as the carrier distribution evolves to a Fermi distribution should affect the carrier contribution to the dielectric constant, and thus give rise to a time dependent component in the pump-probe traces. The same argument should hold for the carrier cooling, but no dynamics were observed.

Quantum wells enhance the exciton binding energy by a factor of 4. Coulomb enhancement of the above band absorption also is present, but the screening capability of a 2-D electron gas is considerably reduced from the 3-D case. This is because, in quantum wells, the carriers are

confined to the well plane, but the fields due to the charges can extend into the barrier material and are therefore still 3 dimensional. Phase-space filling, rather than screening, has been found to be most important for exciton ionization and absorption saturation in GaAs quantum wells. Repeating the above band pumping experiments for ZnCdSe/ZnSe or ZnSe/ZnSSe quantum well material would be an interesting comparison and may also give important information on the gain mechanism in ZnSe base laser diodes. Several theories of stimulated emission in II-VI quantum wells have indicated that excitonic and Coulomb effects are important [103, 104].

Once the screening effects were circumvented by going to below-band pumping, the carrier dynamics observed for ZnSe appeared quite similar to that seen in GaAs and other III-V materials. More work is necessary for a true comparison, however, since the vast majority of GaAs pump probe studies of carrier dynamics have used above band optical pumping to created excited plasmas. The only perturbational studies of carrier cooling dynamics in GaAs, in fact, have been pump-probe experiments on GaAs semiconductor laser amplifiers [113, 114]. These experiments were complicated by the presence of a two-component plasma, but dynamical screening and hot-phonon effects can be neglected since the induced temperature changes were only about 10K. The measured cooling timeconstant of 900 fs [114] seen in the GaAs experiments is close to the 500fs and 900fs timeconstants found for ZnSe in this work. Given the predictions of the Frölich matrix element based on the high and low frequency dielectric constants, energy exchange with the lattice should be almost an order of magnitude faster in ZnSe at densities of 10^{18} cm^{-3}.

The unprecedentedly low value of the induced carrier temperature changes in these FCA pumping experiments ($\Delta T \tilde{} 0.05K$), should allow a straight forward calculation of the carrier-LO phonon coupling constant, as carried out in Chapter 8. The dramatic failure of this theory bears some serious consideration since the physical situation is so simplified. This is evidence that the electron-phonon coupling may be much less than predicted by the bare Frölich matrix element of Chapter 7. Comparison of this result to previous work in GaAs is difficult since almost all of those experiments were performed with direct optical injection. These FCA pumping experiments should, therefore, be repeated for bulk GaAs or AlGaAs films. Measuring both ZnSe/ZnMgSSe and GaAs/AlGaAs multiple quantum well samples would also be interesting since much of the carrier dynamics work in III-V materials have been on 2-D systems. A

Ti:sapphire-pumped femtosecond optical parametric oscillator (OPO) would provide both an above-band 775nm probe and a below-band 1.3 μm pump. The probe would not be tunable, but III-V material can be grown in high quality films so rigorous justification of the physical origin of the observed dynamics (i.e. by measuring the spectral dependence) can be somewhat relaxed. A 3-5 μm mid-infrared pump, generated by difference frequency mixing of the OPO signal and idler pulses, would allow the $\Gamma - L$ carrier dynamics to be investigated in the same manner as in Chapter 11.

Bibliography

[1] H. Morkoc, S. Strite, G. B. Gao, M. E. Lin, B. Sverdlov, and M. Burns. "Large-band-gap SiC III-V nitride, and II-VI ZnSe-based semiconductor device technologies". *J. Appl. Phys.*, **76**(3):1363, (1994).

[2] Landolt-Börstein. *Numerical Data and Functional Relationships in Science and Technology*, volume 22a Semiconductors. Springer Verlag, Berlin, 1987.

[3] D. L. Dreifus, B. P. Sneed, J. Ren, J. W. Cook Jr., J. F. Schetzina, and R. M. Kolbas. "ZnSe field-effect transistors". *Appl. Phys. Lett.*, **57**(16):1663, (1990).

[4] A. M. Glass, K. Tai, R. B. Bylsma, R. D. Feldman, D. H. Olson, and R. F. Austin. "Room-temperature optically pumped Cd(0.25)Zn(0.75)/ZnTe quantum well lasers grown on GaAs substrates". *Appl. Phys. Lett.*, **53**(10):834, (1988).

[5] H. Jeon, J. Ding, A. V. Nurmikko, H. Luo, N. Samarth, J. K. Furdyna, W. A. Bonner, and R. E. Nahory. "Room-temperature blue lasing action in (Zn,Cd)Se/ZnSe optically pumped multiple quantum well structures on lattice matched (Ga,In)As substrates". *Appl. Phys. Lett.*, **57**(23):2413, (1990).

[6] J. Ren, K. A. Browers, B. Sneed, J. W. Cook Jr., J. F. Schetzina, and R. M. Kolbas. "ZnSe light-emitting diodes". *Appl. Phys. Lett.*, **57**(18):1901, (1990).

[7] R. M. Park, M. B. Trofer, C. M. Rouleau, J. M. Depuydt, and M. A. Haase. "p-type ZnSe by nitrogen atom beam doping during molecular beam epitaxial growth". *Appl. Phys. Lett.*, **57**(20):2127, (1990).

[8] M. A. Haase, J. Qiu, J. M. DePuydt, and H. Cheng. "Blue-green laser diodes". *Appl. Phys. Lett.*, **59**(11):1272, (1991).

[9] D. C. Grillo, Y. Fan, L. He, R. L. Gunshor, A. Salokatve, M. Hagerott, H. Jeon, A. V. Nurmikko, G. C. Hua, and N. Otsuka. "Pseudomorphic separate confinement heterostructure blue-green diode lasers". *Appl. Phys. Lett.*, **63**(20):2723, (1993).

[10] M. Hovinen, J. Ding, A. V. Nurmikko, G. C. Hua, D. C. Grillo, L. He, J. Han, and R. L. Gunshor. "Degradation of (Zn,Cd)Se quantum well heterostructures for blue/green light emitters under high optical injection". *Appl. Phys. Lett.*, **66**(16):2013, (1995).

[11] H. Cheng, J. M. DePuydt, J. E. Potts, and T. L. Smith. "Growth of p-type ZnSe:Li by molecular beam epitaxy". *Appl. Phys. Lett.*, **52**(2):147, (1988).

[12] M. Ukita, F. Hiei, K. Nakano, and A. Ishibashi. "Band offset at p-ZnTe/p-ZnSe heterointerfaces". *Appl. Phys. Lett.*, **66**(2):209, (1995).

[13] S. M. Sze. *Physics of semiconductor devices.* John Wiley Sons Inc., 1969.

[14] H. Kroemer, W. Y. Chien, J. S. Rockwell, and D. D. Edwall. "Measurement of iso-type heterojunction barriers by C-V profiling". *Appl. Phys. Lett.*, **36**(4):295, (1979).

[15] J. Petruzello, B. L. Greenberg, D. A. Cammack, and R. Dalby. *J. Appl. Phys.*, **63**:2999, (1988).

[16] M. Stoehr, M. Maurin F. Hamdani, J. P. Lascaray, D. Barbusse, B. Fraisse, R. Fourcade, P. Abraham, and Y. Monteil. "Determination of residual strain by reflectivity, X-ray diffraction, and Raman spectroscopy in ZnSe epilayers grown on GaAs (001), InP(001) and GaSb(001) by metal-organic vapor phase epitaxy". *Mat. Sci. Eng.*, **B21**:257, (1993).

[17] G. Bratina, R. Nicolini, L. Sorba, L. Vanzetti, G. Mula, X. Yu, and A. Franciosi. "ZnSe-GaAs heterojunction parameters". *J. Crystal Growth*, **127**:387, (1993).

[18] G. Bratina, L. Vanzetti, R. Nicolini, L. Sorba, X. Yu, A. Franciosi, G. Mula, and A. Mura. "Microscopic control of ZnSe-GaAs heterojunction band offsets". *Physica B*, **185**:557, (1993).

[19] A. Bonnani, L. Vanzetti, L. Sorba, A. Franciosi, M. Lomascolo, P. Prete, and R. Cingolani. "Optimization of interface parameters and bulk properties in ZnSe-GaAs heterostructures". *Appl. Phys. Lett.*, **66**(9):1092, (1995).

[20] J. Rennie, Y. Nishikawa, S. Saito, and G. Hatakoshi. "Operation voltage reduction in ZnSe-based light-emitting diodes due to the use of n-type AlGaAs and CdZnSe buffer regions". *Appl. Phys. Lett.*, **68**(21):2971, (1996).

[21] M. S. Yeganeh, J. Qi, A. G. Yodh, and M. C. Tamargo. "Interface quantum well states observed by three-wave mixing in ZnSe/GaAs heterostructures". *Phys. Rev. Lett.*, **68**(25):3761, (1992).

[22] R. M. Park, H. A. Mar, and N. M. Salansky. *J. Vac. Sci. Technol. B*, **3**:676, (1985).

[23] R. L. Longini. *Solid State Electron.*, **5**:127, (1962).

[24] E. A. Kraut. *J. Vac. Sci. Technol. B*, **1**:643, (1983).

[25] H. H. Farrell, M. C. Tamargo, J. L. De Miguel, F. S. Turco, D. M. Hwang, and R. E. Nahory. ""Designer" interaces in II-VI/III-V polar heteroepitaxy". *J. Appl. Phys.*, **69**(10):7021, (1991).

[26] L. Kassel, H. Abad, J. W. Garland, P. M. Raccah, J. E. Potts, M. A. Haase, and H. Cheng. "Study of undoped and p-doped ZnSe with GaAs and AlAs". *Appl. Phys. Lett.*, **56**(1):42, (1990).

[27] L. Kassel, J. W. Garland, M. A. Haase, and H. Cheng. "Effects of Zn and Ga interdiffusion on ZnSe/n+ GaAs interfaces". *Jap. J. Appl. Phys.*, **9**:A146, (1991).

[28] Prof. Leslie Kolodziejski. private communication.

[29] J. Hermans, V. Wagner, J. Geurts, J. Woitok, J. Sollner, M. Heuken, and K. Heime. "Optical analysis of metalorganic vapor phase epitaxy grown ZnS/ZnSe/GaAs (100) heterostructures: Carrier diffusion and interface sharpness". *J. Vac. Sci. Technol.*, **10**(4):2062, (1992).

[30] O. Pages, M. A. Renucci, O. Briot, and R. L. Aulombard. "Coupled LO-plasmon modes in semi-insulating GaAs of ZnSe/GaAs heterojunctions". *J. Appl. Phys.*, **80**:1128, (1996).

[31] B. O. Seraphin. *Modulation Techniques*, volume 9 of *Semiconductors and Semimetals*, chapter 1, pages 1–125. Academic Press, New York, 1972.

[32] F. H. Pollack. "Modulation spectroscopy as a technique for semiconductor characterization". In *Optical Characterization Techniques for Semiconductor Technology.* Soc. Photo-Optical Engineers, 1981.

[33] M. Cardona. *Modulation Spectroscopy.* Academic Press, New York, 1969.

[34] H. Shen, M. Dutta, L. Fontiadis, P. G. Newman, R. P. Moerkirk, and W. H. Chang. "Photoreflectance study of surface fermi level in GaAs and AlGaAs". *Appl. Phys. Lett.*, **57**(20):2118, (1990).

[35] O. J. Glembocki, B. V. Shanabrook, N. Bottka, W. T. Beard, and J. Comas. "Photoreflectance characterization of GaAs/AlGaAs thin films, heterojunctions, and multiple quantum well structures". In *Spectroscopic Characterization Techniques for Semiconductor Technology II.* Soc. Photo-Optical Instrum. Engineers, 1985.

[36] X. Yin, F. H. Pollack, L. Pawlowicz, T. O'Neill, and M. Hafizi. "Characterization of GaAs/AlGaAs heterojunction bipolar transitors structures using photoreflectance". *Appl. Phys. Lett.*, **56**(13):1278, (1990).

[37] F. Holz. *Phys. Stat. Sol. A*, page 469, 1974.

[38] K. Misawa. "electroreflectance of Si-MOS". *Jap. J. Appl. Phys.*, **15**:1309, (1976).

[39] D. E. Aspnes and A. A. Studna. "Schottky-barrier electroflectance: application to GaAs". *Phys. Rev. B*, **7**(10):4605, (1973).

[40] D. E. Aspnes. "Electric field effects on the optical absorption near thresholds in solids". *Phys. Rev.*, **147**(2):554, (1966).

[41] D. E. Aspnes. "Electric field effects on the dielectric constant of solids". *Phys. Rev.*, **153**(3):153, (1967).

[42] D. E. Aspnes, P. Handler, and D. F. Blossey. "Interband dielectric properties of solids in an electric field". *Phys. Rev.*, **166**(3):921, (1968).

[43] K. Tharmalingam. *Phys. Rev.*, **130**:549, (1963).

[44] D. E. Aspnes. *Handbook of Semiconductors*, volume 2, chapter 4A, pages 111–154. North-Holland, Amsterdam, 1980.

[45] R. J. Elliot. *Phys. Rev.*, **108**:1384, (1957).

[46] W. Franz. *Z. Naturforsch*, **13**:484, (1958).

[47] L. V. Keldysh. *JETP*, **7**:788, (1958).

[48] H. A. Antosiewicz. In Abramowitz and Stegun, editors, *Handbook of Mathematical Functions*, page 435. Nat. Bur. Stds. US, (1964).

[49] X. Yin, F. H. Pollack, G. D. Petit, and J. M. Woodall. "Electromodulation of semiconductors and semiconductor microstructures using a new contactless technique". In *Proceedings of the Society of Photo-Optical Instrumentation Engineers Vol .1678*, page 168. SPIE, (1992).

[50] R. N. Bhattacharya, H. Shen, P. Paryanthal, F. H. Pollack, T. Coutts, and H. Aharoni. "Electroreflectance and photreflectance study of the space-charge region in semiconductors: (In-Sn-O)/InP as a model system". *Phys. Rev. B*, **37**(8):4044, (1988).

[51] R. P.Silberstein and F. H. Pollack. *J. Vac. Sci. Technol.*, **17**:1052, (1980).

[52] H. Shen and F. H. Pollack. "Generalized Franz-Keldysh theory of electromodulation". *Phys. Rev. B*, **42**(11):7097, (1990).

[53] F. H. Pollack and O. J. Glembocki. "Modulation spectroscopy of semiconductor microstructures: an overview". In *Spectroscopic Characterization Techniques for Semiconductor Technology III.* Soc. Photo-Optical Engineers, 1988.

[54] J. D. Dow. "Electroabsorption in semiconductors: the excitonic absorption edge". *Phys. Rev. B*, **1**(8):3358, (1970).

[55] J. Qiu, Q. D. Qian, R. L. Gunshor, M. Kobayashi, D. R. Menke, D. Li, and N. Otsuka. "Influence of GaAs surface stoichiometry on the interface state density of as-grown epitaxial ZnSe/epitaxial GaAs heterostructures". *Appl. Phys. Lett.*, **56**(13):1272, (1990).

[56] B. Weiss, A. G. Choo, and H. E. Jackson. "Photoreflectance characterization of AlGaAs/GaAs structures". In *Proceedings of the Society of Photo-Optical Engineers Vol. 1678*, page 189. SPIE, (1992).

[57] O. J. Glembocki, B. V. Shanabrook, W. T. Beard, and J. Comas. *Appl. Phys. Lett.*, **46**:970, (1985).

[58] A. Badakshan, M. Sydor, K. Alavi, N. Teraguchi, and H. Morkoc. "Application of differential photoreflectance spectroscopy in selective modulation of a layer within multilayer device structures". In *Proceedings of the Society of Photo-Optical Engineers, Vol. 1678*, page 159. SPIE, (1992).

[59] M. Sydor, A. Badakshan, and J. R. Engholm. "Differential photoreflectance from delta-doped structures and GaAs/n-GaAs interfaces". *Appl. Phys. Lett.*, **59**(6):677, (1991).

[60] H. Shen, F. H. Pollack, and R. N. Sacks. "Photoreflectance and photoreflectance excitation spectroscopy of a GaAs/GaAlAs multiple-quantum-well structure". *Phys. Rev. Lett.*, **3487**(6):3487, (1987).

[61] H. K. Yow, P. A. Houston, and M. Hopkinson. "Conduction band discontinuities in GaInP/AlGaInP heterojunctions measured by internal photoemission". *Appl. Phys. Lett.*, **66**(21):2852, (1995).

[62] T. W. Lee, P. A. Houston, X. F. Yang, G. Hill, and M. Hopkinson. "Conduction-band discontinuity in InGaP/GaAs measured using both current-voltage and photoemission methods. *Appl. Phys. Lett.*, **60**(4):474, (1992).

[63] C. Coluzza. "Internally detected electron photoexcitation spectroscopy on heterostructures". *Physica Scripta*, **T45**:192, (1992).

[64] W. Zhou, M. Dutta, H. Shen, J. Pamulapati, B. Bennet, C. H. Perry, and D. W. Weyburne. "Investigation of near interface properties in semi-insulating InP substrates with

epitaxial grown InGaAs and InAlAs by photreflectance". *J. Appl. Phys.*, **73**(3):1266, (1993).

[65] C. Kittel and H. Kroemer. *Thermal Physics*, chapter 13, page 372. W. H. Freeman and Co., 1980.

[66] J. L. House and D. J. Dougherty. private commun.

[67] C. V. Shank, D. H. Auston, E. P.Ippen, and O. Teschke. "Picosecond time resolved reflectivity of direct gap semiconductors". *Solid State Commun.*, **26**:567, (1978).

[68] T. Gong, W. L. Nighan Jr., and P. M. Fauchet. "Hot-carrier coulomb effects in GaAs investigated by femtosecond spectroscopy around the band edge". *Appl. Phys. Lett.*, **57**:2713, (1990).

[69] R. A. Cheville, W. B. Haynes, and N. J. Halas. "Time-resolved reflectivity studies of the GaAs(100)/oxide and GaAs(100)/ZnSe interface". *Appl. Phys. Lett.*, **59**:1476, (1991).

[70] H. Shen, Z. Hang, S. H. Pan, F. H. Pollach, and J. M. Woodall. "Dependence of the photoreflectance of semiinsulating GaAs on temperature and pump chopping frequency". *Appl. Phys. Lett.*, **52**(24):2058, (1988).

[71] H. Haug and S. Schmitt-Rink. "Electron theory of the optical properties of laser excited semiconductors". *Prog. Quant. Electr.*, **9**:3, (1984).

[72] B. K. Ridley. *Quantum Processes in Semiconductors.* Oxford University Press, Oxford, (1988).

[73] Harmut Haug and Stephan W. Koch. *Quantum theory of the optical and electronic properties of semiconductors.* World Scientific, Singapore, second edition, (1990).

[74] Supriyo Datta. *Quantum Phenomena*, volume VIII of *Modular Series on Solid State Devices.* Addison-Wesley, (1989).

[75] Mark Lundstrom. *Fundamentals of Carrier Transport*, volume X of *Modular Series on Solid State Devices.* Addison-Wesley, (1990).

[76] J. A. Valdmanis, R. L. Fork, and J. P. Gordon. *Opt. Lett.*, **9**:522, (1985).

[77] J. Mark, L. Y. Liu, K. Hall, H. Haus, and E. P. Ippen. *Opt. Lett*, **14**:48, (1989).

[78] D. E. Spence, P. N. Kean, and W. Sibbett. *Opt. Lett.*, **16**:63, (1991).

[79] K. Tamura, E. P. Ippen, H. A. Haus, and L. E. Nelson. *Opt. Lett.*, **18**:1080, (1993).

[80] A. Baltuska, Z. Wei, M. S. Pshenichnikov, and D. A. Wiersma. "Optical pulse compression to 5 fs at a 1 MHz repetition rate". *Opt. Lett.*, **22**(2):102, (1997).

[81] Jagdeep Shah. *Ultrafast Spectroscopy of Semiconductors and Semiconductor Nanostructures*, volume 116 of *Solid State Sciences*. Springer-Verlag, 1996.

[82] K. Leo, J. Shah, E. O. Gobel, T. C. Damen, S. Schmitt-Rink, W. Schafer, and K. Kohler. *Phys. Rev. Lett.*, **66**:201, (1991).

[83] E. O. Gobel, K. Leo, T. C. Damen, J. Shah, S. Schmitt-Rink, W Schafer, J. F. Muller, and K. Kohler. *Phys. Rev. Lett.*, **64**:1801, (1990).

[84] K. Leo, T. C. Damen, J. Shah, E. O. Gobel, and K. Kohler. "Quantum beats of light hole and heavy hole excitons in quantum wells". *Appl. Phys. Lett.*, **57**(1):19, (1990).

[85] P. C. Becker, H. L. Fragnito, C. H. Brito Cruz, R. L. Fork, J. E. Cunningham, J. E. Henry, and C. V. Shank. "Femtosecond photon echoes from band-to-band transitions in GaAs". *Phys. Rev. Lett.*, **61**(14):1647, (1988).

[86] C. L. Tang and D. J. Erskine. "Femtosecond relaxation of photo-excited nonequilibrium carriers in AlGaAs". *Phys. Rev. Lett.*, **51**(9):840, (1983).

[87] W. H. Knox, C. Hirliman, D. A. B. Miller, J. Shah, D. S. Chemla, and C. V. Shank. "Femtosecond excitation of nonthermal carrier populations in GaAs quantum wells". *Phys. Rev. Lett.*, **56**(11):1191, (1986).

[88] J. L. Oudar, D. Hulin, A. Migus, A. Antonetti, and F. Alexandre. "Subpicosecond spectral hole burning due to nonthermalized photoexcited carriers in GaAs". *Phys. Rev. Lett.*, **55**(19):2074, (1985).

[89] R. Tommasi, P. Langot, and F. Vallee. "Femtosecond hole thermalization in bulk GaAs". *Appl. Phys. Lett.*, **66**(11):1361, (1995).

[90] F. X. Camescasse, A. Alexandrou, D. Hulin, L. Banyai, D. B. Tran Thoi, and H. Haug. "Ultrafast electron redistribution through Coulomb scattering in undoped GaAs: experiment and theory". *Phys. Rev. Lett.*, **77**(27):5429, (1996).

[91] R. W. Schoenlein, W. Z. Lin, E. P. Ippen, and J. G. Fujimoto. "Femtosecond hot-carrier energy relaxation in GaAs". *Appl. Phys. Lett.*, **51**(18):1442, 1987.

[92] W. H. Knox, D. S. Chemla, G. Livescu, J. E. Cunningham, and J. E. Henry. "Femtosecond carrier thermalization in dense Fermi seas". *Phys. Rev. Lett.*, **61**(11):1290, (1988).

[93] M. T. Portella, J. Y. Bigot, R. W. Schoenlein, J. E. Cunningham, and C. V. Shank. "k-space carrier dynamics in GaAs". *Appl. Phys. Lett.*, **60**(17):2123, (1992).

[94] M. Ulman, D. W. Bailey, L. H. Acioli, F. G. Valle, C. J. Stanton, E. P. Ippen, and J. G. Fujimoto. "Femtosecond tunable nonlinear absorption spectroscopy in AlGaAs". *Phys. Rev. B*, **47**(16):10267, (1993).

[95] P. C. Becker, H. L. Fragnito, C. H. Brito-Cruz, J. Shah, R. L. Fork, J. E. Cunningham, J. E. Henry, and C. V. Shank. "Femtosecond intervalley scattering in GaAs". *Appl. Phys. Lett.*, **53**(21):2089, (1988).

[96] A. F. Levi, J. R. Hayes, P. M. Platzman, and W. Wiegmann. "Injected-hot-electron transport in GaAs". *Phys. Rev. Lett.*, **55**(19):2071, (1985).

[97] M. Heiblum, D. Galbi, and M. Weckwerth. "Observation of single optical phonon emission". *Phys. Rev. Lett.*, **62**(9):1057, (1989).

[98] W. H. Knox, G. E. Doran, M. Asom, G. Livescu, R. Leibenguth, and S. N. G. Chu. "Low-temperature-grown GaAs quantum wells: femtosecond nonlinear optical and parallel-field transport studies". *Appl. Phys. Lett.*, **59**(12):1491, (1991).

[99] R. A. Hopfel, J. Shah, and A. C. Gossard. "Nonequilibrium electron-hole plasma in GaAs quantum wells". *Phys. Rev. Lett.*, **56**(7):765, (1986).

[100] E. M. Conwell and M. O. Vassel. "High-field distribution function in GaAs". *IEEE Transactions on Electron Devices*, **13**(1):22, (1966).

[101] N. Holonyak, R. M. Kolbas, W. D. Laidig, B. A. Vojak, K. Hess, R. D. Dupuis, and P. D. Dapkus. "Phonon-assisted recombination and stimulated emission in quantum-well AlGaAs/GaAs heterostructures". *J. Appl. Phys.*, **51**(3):1328, (1980).

[102] J. Faist, F. Capasso, C. Sirtori, D. L. Sivco, J. N. Baillargeon, A. L. Hutchinson, S. N. G. Chu, and A. Y. Cho. "High power mid-infrared (5 micron) quantum cascade lasers operating above room temperature". *Appl. Phys. Lett.*, **68**(26):3680, (1996).

[103] M. E. Flatte, E. Runge, and H. Ehrenreich. "Coherent exciton lasing in ZnSe/ZnCdSe quantum wells?". *Appl. Phys. Lett.*, **66**(11):1313, (1995).

[104] P. R. Newbury, K. Shahzad, and D. A. Cammack. "Stimulated emission via inelastic exciton-exciton scattering in ZnSe epilayers". *Appl. Phys. Lett.*, **58**(10):1065, (1991).

[105] F. De Rougemont and R. Frey. "Two-level approach to saturation properties in semiconductor materials". *Phys. Rev. B*, 37(3):1237, (1988).

[106] W. Z. Lin, J. G. Fujimoto, E. P. Ippen, and R. A. Logan. "Femtosecond carrier dynamics in GaAs". *Appl. Phys. Lett.*, **50**(19):124, (1987).

[107] S. Das Sarma, J. K. Jain, and R. Jalabert. "Effect of phonon self-energy correction on hot-electron relaxation in two-dimensional semiconductor systems". *Phys. Rev. B*, **37**(9):4560, (1988).

[108] J. Nunnenkamp, J. H. Collet, J. Klebniczki, J. Kuhl, and K. Ploog. "Subpicosecond kinetics of band-edge absorption in Al(0.25)Ga(0.75)As". *Phys. Rev. B*, **43**(17):14047, (1991).

[109] J. Shah, R. C. C. Leite, and J. F. Scott. *Solid State Commun.*, **8**:1089, (1970).

[110] W. Potz and P. Kocevar. "Electron power transfer in pulsed laser excitation of polar semiconductors". *Phys. Rev. B*, **28**:7040, (1983).

[111] H. M. Van Driel. *Phys. Rev. B*, **19**:5928, (1979).

[112] C. J. Stanton and D. W. Bailey. "Femtosecond-pump, continuum-probe nonlinear absorption in GaAs". *Phys. Rev. Lett.*, **65**(2):231, (1990).

[113] M. P. Kesler and E. P. Ippen. "Subpicosecond gain dynamics in AlGaAs lasr diodes". *Appl. Phys. Lett.*, **51**(22):1765, (1987).

[114] C. T. Hultgren, D. J. Dougherty, and E. P. Ippen. "Above and below-band femtosecond nonlinearities in active AlGaAs waveguides". *Appl. Phys. Lett.*, **61**(23):2767, (1992).

[115] J. Shah. Hot carrier effects in quasi-2d polar semiconductors. In J. T. DeVreese, editor, *Physics of the Two-Dimensional Electron GaAs.* Plenum, New York, (1987).

[116] R. Kubo. *Statistical Mechanics.* North-Holland, (1990).

[117] C. A. Coronado, E. Ho, P. A. Fisher, J. L. Houde, K. Lu, G. S. Petrich, and L. A. Kolodziejski. "Gas source molecular beam epitaxy of ZnSe and ZnSe:N". *J. Electron. Mat.*, **23**(3):269, (1994).

[118] J. Z. Zheng, J. W. Allen, H. M. Yates, and J. O. Williams. "The m-center in zinc selenide grown by metalorganic chemical vapour depositon". *J. Crystal Growth*, **117**:358, (1992).

[119] J. Van De Ven. "Selective photoetching of n-GaAs/ZnSe heterostructures". *Materials Letters*, **7**(12):468, (1989).

[120] J. S. Massa. "Photoluminescence decay measurements of n- and p-doped Znse grown by molecular beam epitaxy". *Appl. Phys. Lett.*, **64**(5):589, (1994).

[121] J. Z. Zheng, J. W. Allen, D. E. Spence an W. E. Sleat, and W. Sibbett. "Decay time of the blue luminescence in ZnSe at room temperature". *Apl. Phys. Lett.*, **62**(1):63, (1994).

[122] T. F. Heinz, S. L. Palfrey, and K. B. Eisenthal. "Coherent coupling effects in pump-probe measurements with co-linear, copropagating beams". *Opt. Lett.*, **9**(8):359, (1984).

[123] B. D. Fluegel, A. Paul, K. Meissner, R. Binder, S. W. Koch, and N. Peyghambarian. "Experimental and theoretical investigation of femtosecond carrier relaxation in CdSe". *Solid State Commun.*, **83**(1):17, (1992).

[124] L. Banyai and S. W. Koch. "A simple theory for the effects of plasma screening on the optical spectra of highly excited semiconductors". *Z. Phys. B -Condensed Matter*, **63**:283, (1986).

[125] E. Haga and H. Kimura. "Free carrier infrared absorption in III-V semiconductors IV. Interconduction band transitions". *J. Phys. Soc. Jap.*, **19**(9):1596, (1964).

[126] H. E. Ruda. "Application of free-carrier absorption to N-ZnSe materials characterization". *J. Appl. Phys.*, **61**(8):3053, (1987).

[127] E. W. Van Stryland, M. A. Woodall, H. Vanherzeele, and M. J. Soileau. "Energy band-gap dependence of two-photon absorption". *Opt. Lett.*, **10**(10):490, (1985).

[128] T. D. Krauss and F. W. Wise. "Femtosecond measurement of nonlinear absorption and refraction in CdS, ZnSe, and ZnS". *Appl. Phys. Lett.*, **65**(14):1739, (1994).

[129] C. R. Pidgeon, B. S. Wherret, A. M. Johnston, J. Dempsey, and A. Miller. "Two-photon absorption in zinc-blende semiconductors". *Phys. Rev. Lett.*, **42**(26):1785, (1979).

[130] T. Elsaesser, J. Shah, L. Rota, and P. Lugli. *Phys. Rev. Lett.*, **66**:1757, (1991).

[131] L. H. Acioli, M. Ulman, F. Vallee, and J. G. Fujimoto. "Femtosecond carrier dynamics in the presence of a cold plasma in GaAs and AlGaAs". *Appl. Phys. Lett.*, **63**(5):666, (1993).

[132] R. G. Ulbrich, J. A. Kash, and J. C. Tsang. "Hot-electron recombination at neutral acceptors in GaAs: a CW probe of femtosecond intervalley scattering". *Phys. Rev. Lett.*, **62**(8):949, (1989).

[133] G. Fasol, W. Hackenberg, H. P. Hughes, K. Ploog, E. Bauser, and H. Kano. "Continuous-wave spectroscopy of femtosecond carrier scattering in GaAs". *Phys. Rev. B*, **41**(3):1461, (1990).

[134] J. Shah, B. Deveaud, T. C. Damen, W. T. Tsang, A. C. Gossard, and P. Lugli. "Determination of inter-valley scattering rates in GaAs by subpicosecond luminescence spectroscopy". *Phys. Rev. Lett.*, **59**(19):2222, (1987).

[135] D. Y. Oberli, J. Shah, and T. C. Damen. "Intervalley scattering in GaAs". *Phys. Rev. B*, **40**(2):1323, (1989).

[136] P. N. Saeta, J. F. Federici, B. I. Greene, and D. R. Dykaar. "Intervalley scattering in GaAs and InP probed by pulsed far-infrared transmission spectroscopy". *Appl. Phys. Lett.*, **60**(12):1477, **60**.

[137] J. R. Chelikowski and M. L. Cohen. "Nonlocal pseudopotential calculations for the electronic structure of eleven diamond and zinc-blende semiconductors". *Phys. Rev B*, **14**(2):556, (1976).

[138] R. Markowski, M. Piacentini, D. Debowska, M. Zimmal-Starnawska, F. Lama, N. Zema, and A. Kisiel. "Electronic structure of zincblende ZnSe: theory and experiment". *J. Phys. Condens. Matter*, **6**:3207, (1994).

[139] D. E. Eastman, W. D. Grobman, J. L. Freeouf, and M. Erbudak. "Photoemission spectroscopy using synchrotron radiation. I Overviews of valence-band structure for Ge, GaAs, GaP, InSb, ZnSe, CdTe, and AgI". *Phys. Rev. B*, **9**(8):3473, (1974).

[140] L. Ley, R. A. Pollack, F. R. McFeeley, S. P. Kowalczyk, and D. A. Shirley. "Total valence-band densities of states of III-V and II-VI compunds from x-ray photoemission spectroscopy". *Phys. Rev. B*, **9**(2):600, (1974).

[141] C. S. Menoni, O. Buccafusca, M. C. Marconi, D. Patel, J. J. Rocca, G. Y. Robinson, and S. M. Goodnick. "Effect of indirect Gamma-L and Gamma-X transfer on the carrier dynamics of InGaP/InAlP multiple quantum wells". *Appl. Phys. Lett.*, **70**(1):102, (1997).

[142] W. B. Wang, R. R. Alfano, D. Szmyd, and A. J. Nozik. "Determination of the critical value of Xc for the direct-to-indirect band-gap transition in Al(x)Ga(1-x)As by measuring hot-carrier dynamics in the X-valley". *Phys. Rev. B*, **46**(24):15828, (1992).

[143] P. B. Allen. "Theory of thermal relaxation of electrons in metals". *Phys. Rev. Lett.*, **59**:1460, (1987).

[144] S. D. Brorson, A. Kazeroonian, J. S. Mooders, D. W. Face, T. K. Cheng, E. P. Ippen, M. S. Dresselhaus, and G. Dresselhaus. "Femtosecond room-temperature measurement

of the electron-phonon coupling constant in metallic superconductors". *Phys. Rev. Lett.*, **64**(18):2172, (1990).

[145] M. Combescot and R. Combescot. "Excitonic Stark shift: a coupling to semi-virtual biexcitons". *Phys. Rev. Lett.*, **61**(1):117, (1988).

[146] S. Schmitt-Rink, D. S. Chemla, and H. Haug. "Nonequilibrium theory of the optical Stark effect and spectral hole-burning in semiconductors". *Phys. Rev. B*, **37**(2):941, (1988).

[147] C. Ell, J. F. Muller, K. El Sayed, and H. Haug. "Influence of many-body interactions on the excitonic optical Stark effect". *Phys. Rev. Lett.*, **62**(3):304, (1989).

[148] A. Mysyrowicz, D. Hulin, A. Anotnetti, A. Migus, W. T. Masselink, and H. Morkoc. ""Dressed excitons" in a multiple-quantum-well structure: evidence for an optical Stark effect with femtosecond response time". *Phys. Rev. Lett.*, **56**(25):2748, (1986).

[149] W. H. Knox, D. S. Chemla, D. A. B. Miller, J. B. Stark, and S. Schmitt-Rink. "Femtosecond AC Stark effect in semiconductor quantum wells : Extreme high and low-intensity limits". *Phys. Rev. Lett.*, **62**:1189, (1989).

[150] M. Joffre, D. Hulin, J. P. Chambaret, A. Migus, and A. Antonetti. "Dynamics and Fourier transform studies of the excitonic optical Stark effect". *IEEE J. Quant. Electron.*, **25**(12):2505, (1989).

[151] N. Peyghambarian, S. W. Koch, M. Lindberg, B. Fluegel, and M. Joffre. "Dynamic Stark effect of exciton and continuum states in CdS". *Phys. Rev. Lett.*, **62**(10):1185, (1989).

[152] D. Hulin, A. Mysyrowicz, A. Antonetti, A. Migus, W. T. Masselink, H. Morkoc, H. M. Gibbs, and N. Peyghambarian. "Ultrafast all-optical gate with subpicosecond ON and OFF times". *Appl. Phys. Lett.*, **49**(13):749, (1986).

[153] J. Paye and D. Hulin. "Monochromatic all-optical gate with 1 ps response time". *Appl. Phys. Lett.*, **62**(12):1326, (1993).

[154] B. R. Mollow. *Phys. Rev. A*, **4**:1666, (1971).

[155] P. Meystre and M. Sargent III. *Elements of Quantum Optics*, chapter 5. Springer-Verlag, 1990.

[156] M. Combescot. "Polarization effects for the excitonic optical Stark effect at all detunings". *Solid State Commun.*, **68**(1988):471, (1988).

[157] M. Combescot and R. Combescot. "Optical Stark effect of the exciton: Biexcitonic origin of the shift". *Phys. Rev. Lett.*, **40**(6):3788, (1989).

[158] N. Peyghambarian, S. H. Park, S. W. Koch, and A. Jeffrey. "Room temperature excitonic optical nonlinearities of molecular beam epitaxially grown ZnSe films". *Appl. Phys. Lett.*, **52**(3):182, (1988).